Wind loads assessment on double-skin facades

Sylvain Aguinaga

To cite this version:

Sylvain Aguinaga. Wind loads assessment on double-skin facades. CSTB - Centre scientifique et technique du bâtiment. 2023. hal-04628424

HAL Id: hal-04628424
https://cstb.hal.science/hal-04628424v1

Submitted on 28 Jun 2024

CSTB
le futur en construction

Multi-criteria evaluation of products

Wind loads assessment on double-skin facades

AGUINAGA Sylvain

2023 programme

Distribution : Public

Scientific and technical centre for the building industry
Head office > 84 avenue Jean Jaurès - Champs-sur-Marne - 77447 Marne-la-Vallée cedex 2 - France
Tel: +33 (0)1 64 68 82 82 - www.cstb.fr
Marne-la-Vallée / Paris / Grenoble / Nantes / Sophia Antipolis

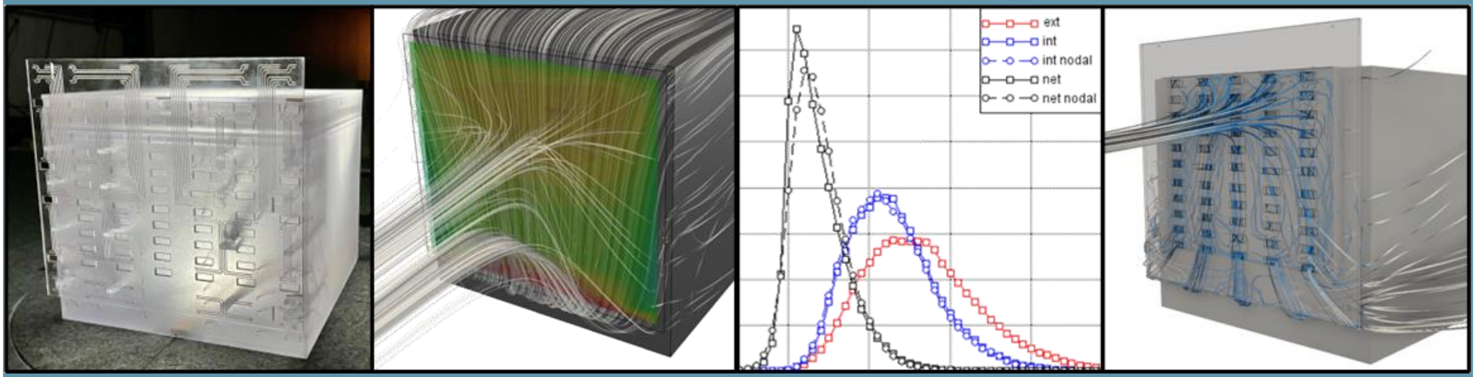

CSTB
le futur en construction

Multi-criteria evaluation of products

Wind loads assessment on double-skin facades

AGUINAGA Sylvain

Centre Scientifique et Technique du Bâtiment, DC2A, Nantes

Strategic Action Area : Buildings and cities in the face of climate change

30/11/23

Keywords:

Wind loads, double-skin facades, atmospheric boundary layer turbulence, numerical simulation, wind tunnel simulation

Foreword:

This report was originally written in French. It was translated using mainly the DeepL Pro algorithm. Any help or comment to improve this translation is welcome.

To cite this report:

AGUINAGA. S, *Wind loads assessment on double-skin facades,* CSTB, 2023

TABLE OF CONTENTS

1 INTRODUCTION: CONTEXT AND STRATEGY OF THE STUDY

1.1 DOUBLE-SKINNED FACADE AND WIND LOADS ASSESSEMENT

This study concerns double-skin facades. These are facade elements detached from the main facade of the building, and therefore exposed to the open air on both sides. They differ from acroteria and other feathered facades, which are also exposed to the wind on both sides, in that the double-skin facade remains at a close distance from the building facade, thus forming an air gap.

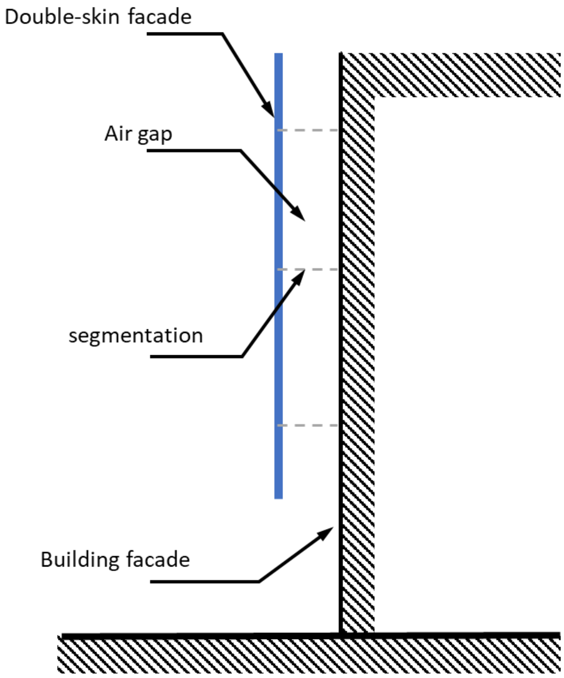

Figure 1 - Double-skin facade terminology

These facades have several functions. They can have an aesthetic purpose, to dress up the facade of the building. But they are also, and above all, used to regulate the building's temperature. In winter, the air space can capture solar energy through the greenhouse effect, to heat the building. In summer, on the other hand, the air gap can act as an aeraulic engine, via natural convection, to cool the building.

There are many different types of double-skin facade, and we refer the reader to Vaglio's thesis work [1] who proposes a classification of the different possible geometric configurations.

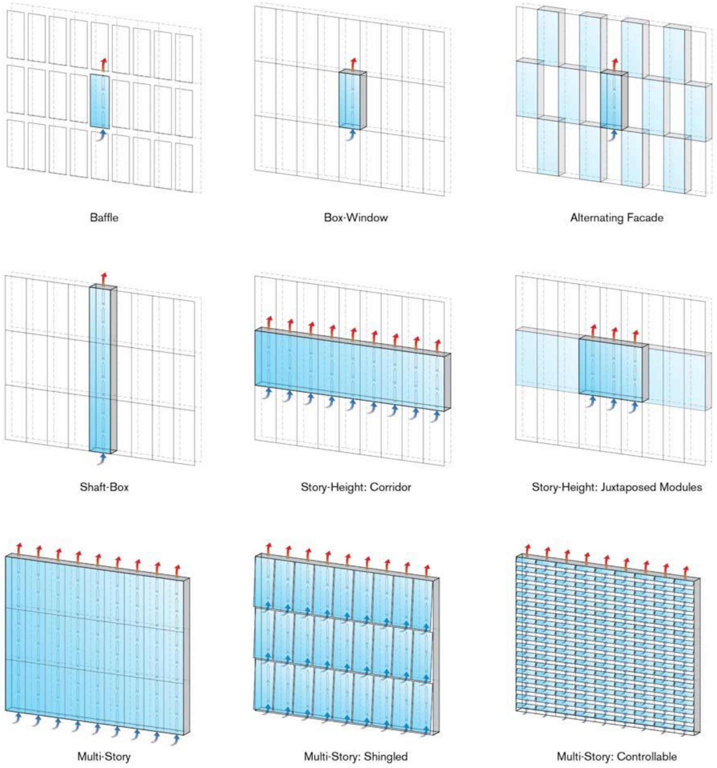

Figure 2 - Different types of double-skin facade according to Vaglio [1]

A key parameter of the double-skin facade will be the segmentation of the air space by overlaps. These overlaps will have a significant impact on the way air can circulate in the air space.

The other key parameter in the geometry of the double-skin facade will be its porosity. Depending on how the facade is constructed - glass, perforated sheeting, interlocking tiles, etc. - its air permeability will vary greatly.

This study looks at the design of wind loads on double-skin facades, with a view to assessing their resistance to a fifty-year storm. This is an increasingly important engineering issue, as more and more buildings are now equipped with double-skin facades.

The force exerted by the wind on the double-skin facade will result from the difference between the pressure p_{ext} applied by the wind on the external face of the facade, and the pressure p_{int} applied to the inside of the facade. The differential of these two pressures will be noted:

$$p_{net} = p_{ext} - p_{int}$$

If $p_{ext} > p_{int} \Rightarrow p_{net} > 0$ we consider the double-skinned facade in compression.

If $p_{ext} < p_{int} \Rightarrow p_{net} < 0$ we consider the double-skinned facade in tear-off (pull-out).

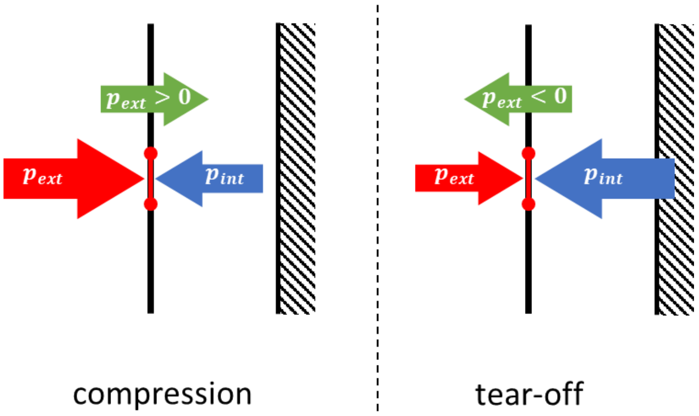

Figure 3 - Terminology and sign conventions for pressure differentials

In most cases, these pressures will be expressed as pressure coefficients:

$$c_p = \frac{p}{p_{dyn\_ref}} = \frac{p}{\frac{1}{2}\rho U_{ref}^2}$$

With p_{dyn_ref} a reference dynamic flow pressure, associated with a reference velocity U_{ref} taken upstream of the building (see §3.6 for more details).

The difficulty in assessing the pressure differential will lie mainly in measuring the pressure on both sides of the facade synchronously.

The importance of synchronising this measurement is explained by the very large fluctuations in the pressure signals. These fluctuations are generated by the scales of atmospheric boundary layer turbulence. These scales are of the same order of magnitude as, or even larger than, the size of the building. Thus, within the same flow, instationnarities on the scale of the building, generated by its own wake, and instationnarities on the scale of the Atmospheric Boundary Layer will coexist. This superposition of dynamics makes it particularly complex to estimate peak pressures, induced by the greatest instationnarities (on all scales combined), which can be more than twice the mean pressure.

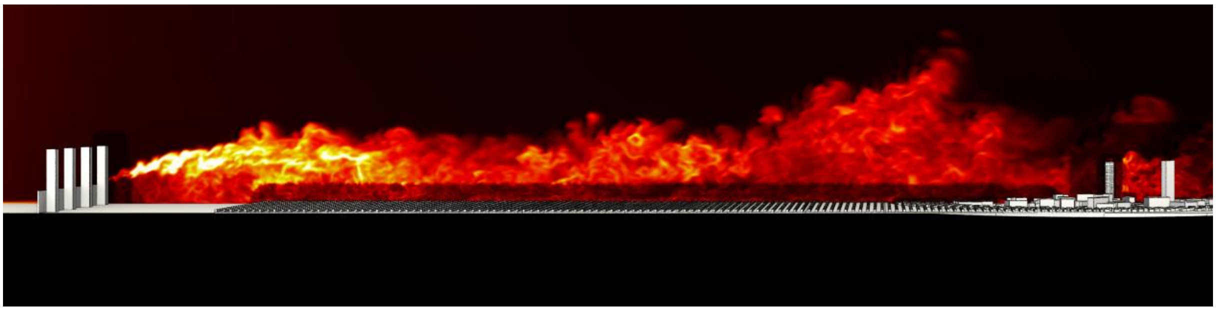

Figure 4 - Illustration of atmospheric boundary layer turbulence (source unknown)

So, depending on how these pressure fluctuations are propagated within the air gap, there can be very significant variations in the pressure differential p_{net} over time which must be captured as accurately as possible.

The sizing of the double-skin facade in the wind will therefore essentially consist of determining the correct instantaneous pressure balance of the air space, according to the strong pressure fluctuations that will apply at its various openings.

This balancing will depend on the specific characteristics of the double skin, but also on the way in which the flow is structured around the building, and thus generates pressure differences across the air space. Without going into too much detail about the mechanisms underlying this balancing for the moment, the Figure 5 illustrates two very different balancing configurations.

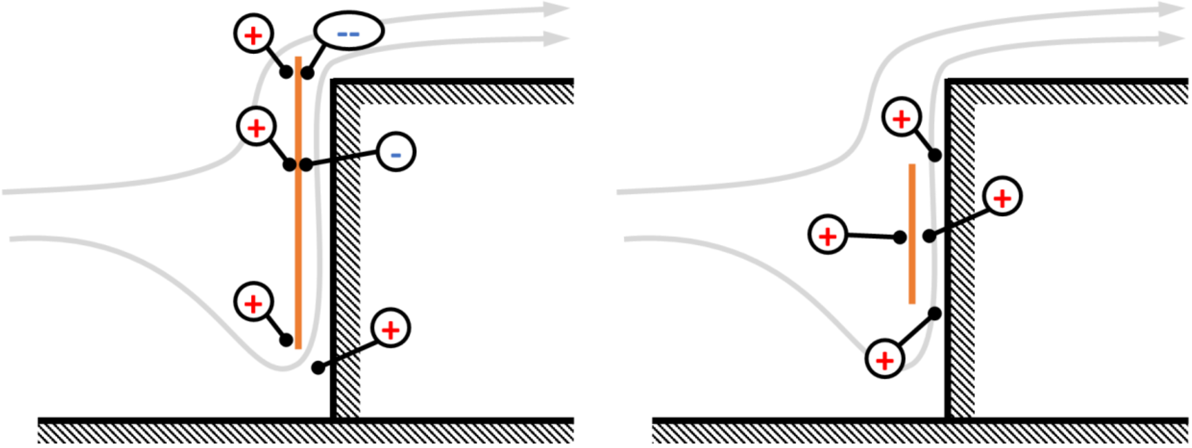

Figure 5 - illustration of two extreme cases of air gap pressure balancing

In the configuration on the left, the facade extends slightly above the roof. Bypassing the feathered part of the double skin will generate negative pressures at the top of the air space. At the foot of the facade, the stagnation point of the wind flow will create positive pressures, and we can therefore expect the air space to balance out at an intermediate pressure, which will certainly be negative. In this way, the air gap would be in negative pressure, whereas the double skin is positioned facing the wind, which may seem counter-intuitive at first sight. The negative pressure on the inside will then combine with the positive pressure on the outside, significantly increasing the forces applied to the double skin compared with a normal facade.

In the configuration on the right, where the double skin does not rise to the top of the building, we can expect the pressures at the terminals of the air space to be similar, and close to the stagnation pressure exerted by the wind on the whole facade. The pressure in the air space will therefore balance out at a value close to that applied to the facade as a whole, and especially close to the value applied to the external face of the double skin. The forces on each face will then compensate, leading to a net force that is certainly very low, which may also seem counter-intuitive for a facade element placed on the windward face of the building.

This first example illustrates that small geometric variations can lead to very large variations in wind loads on the double-skin facade.

1.2 A BRIEF REVIEW OF THE ACADEMIC STATE OF THE ART

Initially, we propose to carry out a rapid bibliographical review of the state of the art on the subject. The main aim is to position this study in relation to work already carried out in the academic world. The state of the art on the wind load assessment of double-skin facades is fairly limited.

The first significant study on the subject dates back to 1994 and was proposed by Gerhardt & Janser [2]. Their study, mainly based on wind tunnel tests, highlights the problem of pressure balancing in a perforated skin, depending on the geometry of the air gap and the dimensions of the building, which will modify the field of pressures applied to the building facade and at the terminals of the air gap. The study also includes field measurements carried out on a building in Berlin, showing good agreement with the wind tunnel results. The study focuses on average pressure differentials on the facade, and does not explore the effects of instationnarity.

The second widely cited study on the subject dates from 2008, and is proposed by Marques da Silva & Gloria Gomes [3]. This study, carried out on a wind tunnel model, highlights the pressure balancing of the air space in a large, solid, non-overlapped double-skin facade. In particular, they point out the low pressures in the air space, as described in the previous paragraph. In particular, the authors highlight the effects of wind direction on the pressure balance of the air space, as well as the effect of extending the double skin onto the other facades of the building. Here again, the unsteady aspect is not addressed.

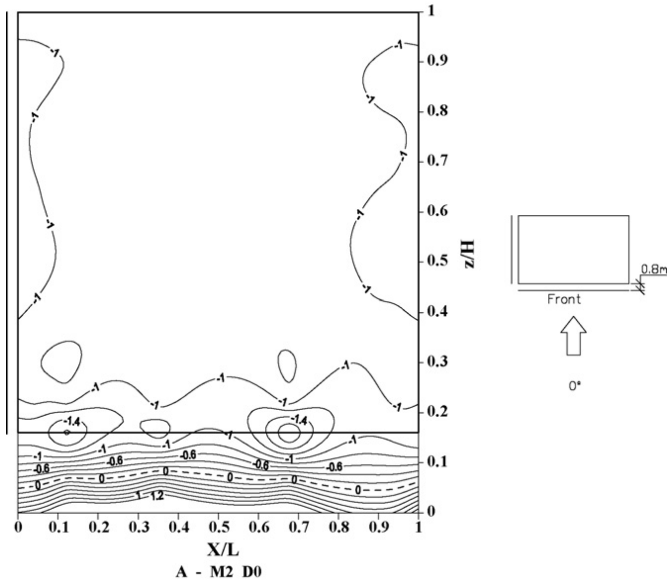

Figure 6 - Mapping of the pressure field on the facade of a building protected by a double skin from Marques da Silva & Gloria Gomes 2008 [3].

Vaglio's thesis work [1] is also an excellent reference for illustrating the problem of the wind loads assessement of double-skin facades. His work includes an interesting literature review and a detailed description of the various existing double-skin topologies, illustrated by a review of a very large number of buildings around the world equipped with such facades. Vaglio also presents an initial attempt to model the flow in a double-skin using CFD (Computational Fluid Dynmics) numerical simulation, studying in particular the impact of the geometry of the facade and its porosity. The model comes up against the inherent limitations of this type of modelling and does not take into account the unsteadiness effects of atmospheric boundary layer turbulence. Vaglio concludes his work with interesting and pragmatic recommendations for the design of double-skin facades in order to optimise the forces generated by the wind.

More recent works in the literature include those by Jafari and Alipour [4] in 2021 which attempt to optimise the geometry of a double-skin facade in order to reduce the overall stresses of the building. Their work is based on CFD simulations, combined with genetic optimisation algorithms. They do not focus on the design of the skin itself, but only on its impact on the overall loads. Hu et al [5] proposed a similar study in 2017 using measurements on wind tunnel models. In particular, they explore the impact of the presence of a double-skin facade, placed on the windward side of the building, on the dynamic response of global loads by taking into account aeroelastic phenomena at the scale of the building. Hu et al [6] used this geometry again in 2019, this time focusing on loads on the facades. Their measurements show that the presence of the double skin will largely modify the wind loading on the facade, as Marques da Silva and Gloria Gomes had shown. Their pressure measurements were supplemented by PIV flow velocity measurements near the facade. Although they measure the spectrum of the pressure signal on the facade, they do not assess the impact of the double skin on peak loads.

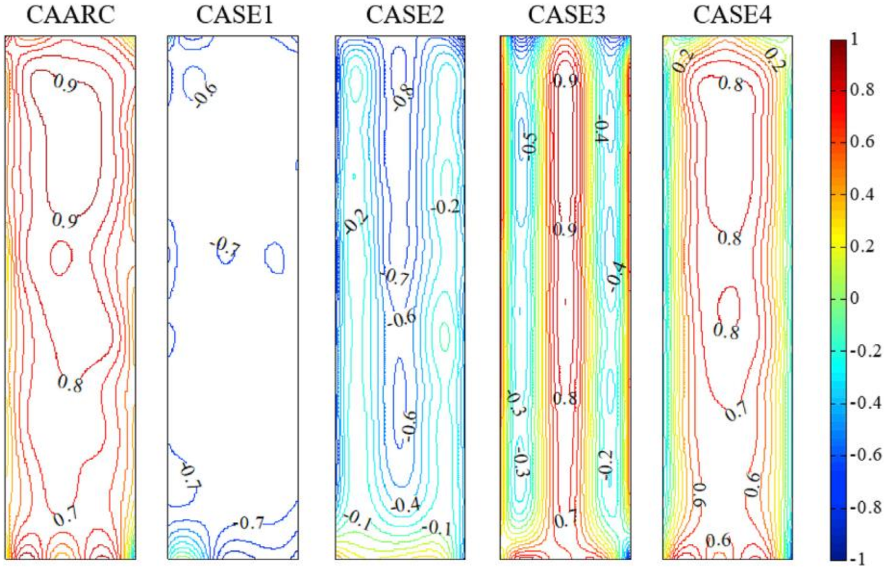

Figure 7 - Change in wind loading of the facade due to the presence of a double-skinned facade according to Hu et al. [6]

Kemper & Fledmann [7] presented a very interesting study in 2019 on porous double-skin facades of the grid type. The study is fairly comprehensive, with a characterisation of the pressure losses in the grid on a dedicated bench, and comparison of the results with a field experiment. The study then considers a wind tunnel model to measure the loads on a porous double skin covering the entire facade of a building. The measurements are then used to map the net differential loads on the facade. The authors also explore the question of peak loads induced by the largest eddies of turbulence in the Atmospheric Boundary Layer, but only by extrapolating average loads using the rules of the Eurocode [8].

Pomaranzi et al [9] proposed a similar study in 2020, with wind tunnel measurements of loads on a porous facade. The authors consider two different model scales in order to measure the impact of this parameter on the modelling. This study is particularly interesting in that the authors focus on the evaluation of unsteady loads on the double skin, in particular by plotting the distribution of the pressure signal (PDF Probability Density Function) on each side of the facade. These plots make it possible to highlight the difference in dynamics on either side of the facade.

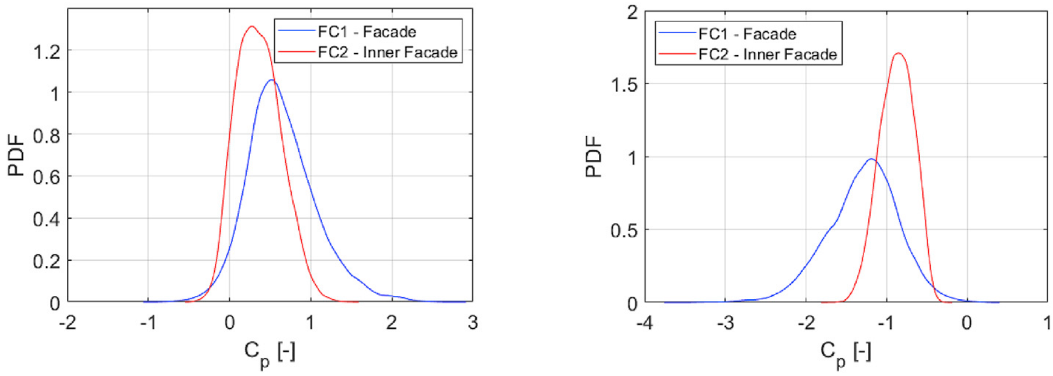

(a) (b)

Figure 8 -PDF of the pressure signal on either side of the double-skin facade, after Pomaranzi et al. [9]

To show that the subject is still topical, we might mention the very recent work by Skvorc and Kozmar [10] dating from 2023. The study looks at the impact of a variable-porosity skin on the local and global loads of a tower. It is based on a wind tunnel experiment in which several types of wind, urban or rural, are considered.

1.3 ENGINEERING ISSUES

The previous paragraph has therefore shown that the academic world is interested in the various problems caused by the presence of a double-skin facade on a building. We now propose to return to the engineering problem that prompted this study, the wind resistance of the double skin itself, and to see what technical means are available to address it.

1.3.1 Regulatory approach

Double-skin facades are only briefly dealt with in the Eurocode (§7.2.10) [8]. The rules for "pressure exerted on facades comprising several walls" do not allow the complexity of the flows generated by double-skin facades to be taken into account. The Eurocode also specifies that these rules "do not apply when air inlets connect the air space with faces of the building other than the face on which the wall is located".

In order to dimension the double-skin facades currently being built, the technical inspectors rely on a document entitled *"Fiche Technique n°45 Tableaux des Pressions de vent W50 applicables aux facades légères et déterminées selon l'Annexe Nationale NF EN 1991-1-4/NA*" *[Technical Data Sheet No. 45 Tables of Wind Pressures W50 applicable to lightweight facades and determined in accordance with National Annex NF EN 1991-1-4/NA].* [11] which, as its name suggests, is itself based on the results of the Eurocode.

This sheet has also been included in the RAGE programme (Règle de l'Art Grenelle Environnement 2012) [12]. These sheets recommend sizing based on a pressure coefficient $c_{p_{net}} = -1.5$. This value seems to result from a combination of a pull-out coefficient $c_{p_{ext}} = -1.3$ specified on the outer face of the double skin, corresponding to the maximum pull-out of a conventional facade, and a value of $c_{p_{int}} = +0.2$ prescribed in the air space, a value which appears to be taken from the conventional pressure balance of the interior of a building. This reasoning is representative of the limitations of the interpretation of Eurocode values. Although this $c_{p_{net}}$ results from an assembly of coefficients taken from the Eurocode, it is not at all representative of the reality of air flows circulating around the double skin.

In fact, the regulatory approach, as it stands, does not seem to be able to provide a complete response to the engineering problem.

1.3.2 Atmospheric Boundary Layer wind tunnel measurement

The Atmospheric Boundary Layer wind tunnel is currently the tool best able to reproduce the instabilities of wind flows and their impact on the wind loads of buildings and structures. The main obstacles to its use are the cost of the study, the time required to carry it out, and the availability of test facilities. The metrology associated with the measurement of peak pressures is mature, and makes it possible to offer reliable assessments of peak loads on building facades. However, measuring wind loads on double-skin facades in a wind tunnel is not without its difficulties.

These difficulties are mainly inherent in the scale of the building models that are tested in the wind tunnel. This scale is chosen according to the size of the building and its immediate environment. It generally varies between 1/100 and 1/300. At these scales, an air gap 20cm thick will in practice be less than 2mm in size on the model. The difficulty then lies in measuring the pressure in such a small space. The pressure taps fitted to the models have a diameter of 1.6mm, which is about the same as the thickness of the air gap. Then there are the pneumatic connections that transmit the pressure signals to the sensors. Their presence can create significant obstructions, which will alter the flow and pressure balance of the air gap.

Consequently, the measurements of double-skin facades currently carried out in wind tunnels only concern sections of buildings reproduced on a large scale. These simulations are mainly concerned with the local behaviour of double-skin facade elements, particularly when these are perforated. They cannot reproduce the effects of pressure balancing on large double-skin facades on the scale of the building. Also, and above all, these sectional models cannot reproduce the interaction of the building with all the scales of turbulence in the Atmospheric Boundary Layer, which will strongly influence the peak loads on the facade.

1.3.3 Numerical simulation in fluid mechanics

Numerical simulation in fluid mechanics, also known as CFD (Computational Fluid Dynamics), is not subject to these problems of scale. It can therefore be seen as an attractive solution for measuring pressure differentials across the elements of double-skin facades. It is capable of modelling the volume of air between the building facade and the double-skin facade, and thus simulating the pressure balancing of the air space as a function of the flow pattern at building scale.

For industrial applications, simulations are generally based on a mean flow approach (RANS Reynolds Average Navier Stokes) where the effects of turbulence on the mean flow are mimicked by a turbulence model. In this case, CFD is unable to correctly reproduce the effects of unsteadiness of the flow, and to measure peak loads on facade elements. This is why CSTB only offers pre-assessment of wind loads using numerical simulation.

In order to overcome the lack of information on the unsteadiness of the wind with the average approaches, we generally resort to techniques taken from the regulatory approach, which allow us to estimate peak loads by extrapolating the average loads using a multiplication factor based on the turbulence of the upstream wind. The approach is similar to that proposed by Kemper and Feldmann [7]. However, this technique either results in loads that are too conservative, in the case of high average pressure coefficients, or not sufficiently safe, in the case of low average pressure coefficients.

A study report issued by an engineering consultancy reported zero wind loads on the elements of a double-skin facade with high porosity. In fact, pressure balancing of the air space results in a mean value of zero for $c_{p_{net}}$ on the elements at the centre of the facade. However, extrapolation to the peaks of a zero mean coefficient by a multiplying coefficient ultimately results in a zero peak coefficient. The simulation is not wrong in itself, but in its interpretation of the result, the Design Office should have emphasised that this result was inherent in the limitations of the modelling used, and proposed more conservative loads.

The mirage that CFD can compensate for the shortcomings of the normative approach means that there is a risk that many CFD-oriented design offices will jump into the breach, in order to be able to respond to the increasing demands of technical inspectors and project managers. Without the necessary hindsight, this can lead to problems with the undersizing of double-skin facade elements. Some design offices are nevertheless proposing to address this problem by using unsteady numerical simulations known as "large-eddies" simulations (LES, DES, etc.) to overcome the limitations of averaged RANS approaches. This being the case, the calculation times for these simulations are reduced in order to meet the industrial requirements of the project. In fact, as they stand, the results of these simulations are certainly not reliable enough to correctly measure peak loads on a double-skin facade.

In conclusion, CFD is a very interesting tool for anticipating the impact of geometric configurations inducing high loads on double-skin facade elements. In particular, it is a formidable teaching tool for understanding these flows, which sometimes lead to counter-intuitive phenomena. However, in an industrial context, it is not capable of correctly measuring the peak loads exerted by wind on double-skin facade elements.

This limitation of CFD is not specific to double-skin facades alone, but applies to the overall wind design of buildings and structures. This is why the numerical simulation approach is complementary to the measurement of wind loads in an Atmospheric Boundary Layer wind tunnel.

1.4 STUDY STRATEGY

This study is then positioned in relation to the academic state of the art, and the engineering problem that has just been outlined, with the following objectives:

-to improve our knowledge of the problem of the wind loads assessment of double-skin facades, in addition to the academic work mentioned above. It will focus in particular on the mechanisms of pressure balancing of the air gap, taking into account the unsteady aspect induced by the large-scale turbulence of the Atmospheric Boundary Layer.

-to provide some answers to the engineering problem of estimating peak net loads generated by large-scale turbulence in the Atmospheric Boundary Layer. The aim is to overcome the limitations mentioned in the previous paragraph.

The study is structured around a reference experiment in an Atmospheric Boundary Layer wind tunnel. A model of a parallelepiped reference building is reproduced on a scale of 1:100, and immersed in a flow representative of wind in an urban environment. The relatively large scale of the model avoids the pitfall of geometric representativeness of the air gap mentioned above. The model is therefore designed to be as modular as possible, so that the impact of geometric variations in the double skin on the pressure balance of the air gap can be easily studied. The model is then instrumented with pressure sensors, enabling pressure fluctuations to be traced across the entire double-skin facade.

Firstly, a detailed analysis of the results of the wind tunnel measurements will be carried out, exploring the impact of geometric variations in the double-skin facade, in order to illustrate the physical mechanisms at work in the pressure balancing of the air space. The analysis of the measurements is supported by visualisations of the flows using numerical simulations.

Secondly, an attempt will be made to model this pressure balancing using a nodal numerical approach, in order to reproduce the pressure fluctuations inside the air space, based solely on measurements of the pressure fluctuations outside the double-skin facade. As well as providing interesting information about the physics underlying pressure balancing, this methodology could pave the way for new methods of designing double-skin facades for complex building geometries. It would therefore be an interesting way of solving the engineering problem of wind loads assessment of double-skin facades.

The final part of the study aims to establish a framework for the practical application of the results obtained, with a view to addressing the engineering problem of the wind dimensioning of double-skin facades.

2 TOTAL PRESSURE, STATIC PRESSURE, PRESSURE LOSSES AND PRESSURE BALANCING

Since the problem of wind load assessment on double-skin facades is mainly based on the issue of balancing the pressure of the air space, it seems important, as a preamble to the study, to recall and explain the concepts of total pressure, static pressure and pressure losses.

2.1 TOTAL PRESSURE AND STATIC

Total pressure is the sum of static and dynamic pressure :

$$p_{tot} = p_{stat} + p_{dyn}$$

Static pressure is what will generate the forces on the facades, and therefore the quantity to be taken into account for wind dimensioning purposes.

Dynamic pressure is directly linked to flow velocity U and its density ρ by the relation :

$$p_{dyn} = \frac{1}{2}\rho U^2$$

The total pressure is therefore :

$$p_{tot} = p_{stat} + \frac{1}{2}\rho U^2$$

The formula is similar to that traditionally used in mechanics to characterise total energy as the sum of potential energy and kinetic energy. Static pressure can therefore be equated with the potential energy of flow.

In a hydraulic analogy, static pressure can be seen as the height of a drop of a watercourse, and velocity as the flow of the watercourse.

In an analogy with electricity, static pressure can be seen as an electrical voltage and speed as an electrical current.

Bernoulli's theorem can then be used to propose an initial, highly simplified relationship between pressure and velocity, using an analogy with the conservation of total mechanical energy, saying that total pressure is conserved. Thus, between two points A and B in a flow :

$$p_{tot\_A} = p_{tot\_B}$$

$$p_{stat\_A} + \frac{1}{2}\rho U_A^2 = p_{stat\_B} + \frac{1}{2}\rho U_B^2$$

We can illustrate this theorem with two examples of applications. The first is the stagnation point of a flow on the facade of a building. At a distance, and considering zero static pressure (pressure reference), we assume that the total pressure is equal to the dynamic pressure. At the stopping point, the wind speed is zero. The dynamic pressure is then totally reflected in the static pressure, creating a force exerted by the wind on the facade.

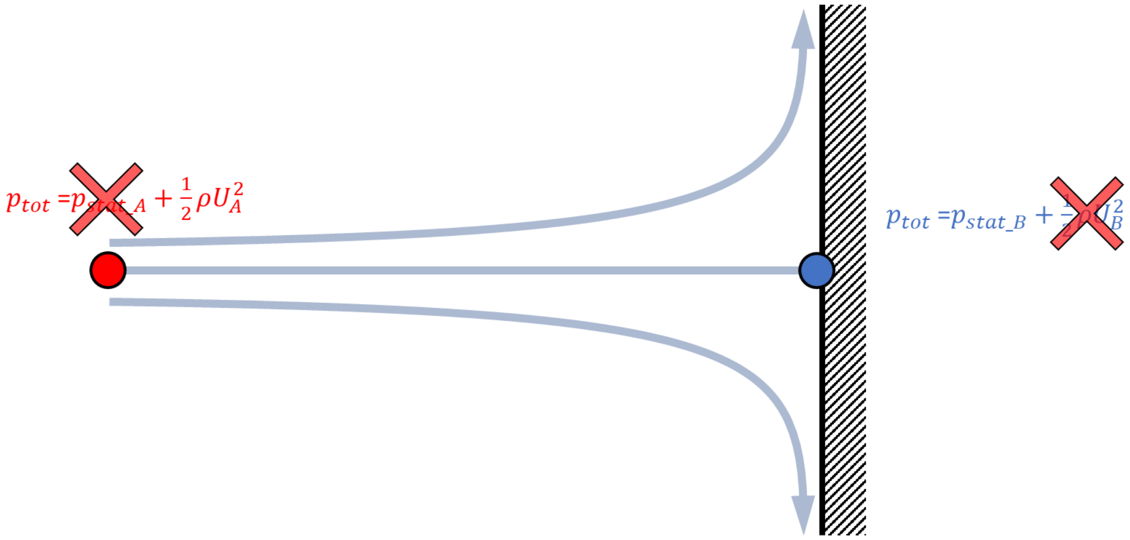

Figure 9 of total pressure at a stagnation point

The second example is flow in a channel of constant cross-section. By virtue of the fundamental assumption of conservation of mass in the flow, the velocity in the channel is conserved ($S_A = S_B \Rightarrow U_A = U_B$). A direct application of Bernoulli's theorem would therefore lead to conservation of the static pressure in the channel :

$$p_{tot\_A} = p_{tot\_B} \Longrightarrow p_{stat\_A} = p_{stat\_B}$$

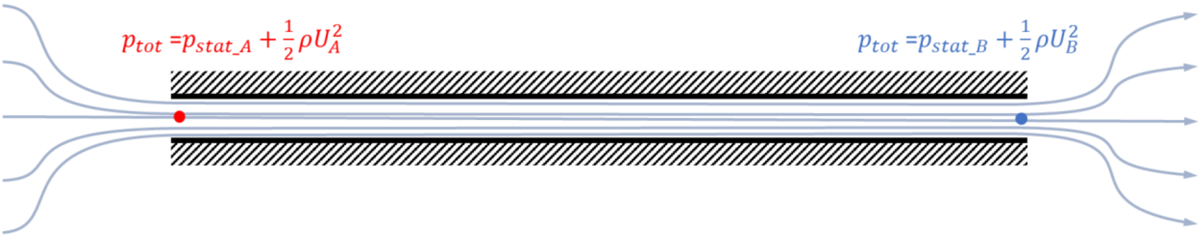

Figure 10 Conservation of total pressure in a pipe

2.2 PRESSURE LOSSES

Bernoulli's theorem is practical and provides a simple explanation of many fluid mechanics phenomena. However, it is based on the strong assumption that the fluid is perfect. However, given the viscosity of a fluid, energy will be lost as a result of friction at the walls or significant variations in velocity at the inlet and outlet of the channel. These energy losses can be expressed as head losses in the equation for the conservation of total pressure:

$$p_{tot\_A} = p_{tot\_B} + \Delta p_{loss}$$

Pressure losses in a channel are often modelled by a quadratic relationship to the flow velocity, coupled with a pressure loss coefficient :

$$\Delta p_{loss} = \frac{1}{2}\xi\rho U^2$$

In an analogy with electricity, the pressure drop coefficient can then be likened to an electrical resistor which dissipates energy by the Joule effect. The change in total pressure across the tube then becomes :

$$p_{tot\_A} = p_{tot\_B} + \frac{1}{2}\rho\xi U^2$$

In a pipe with a constant cross-section ($S_A = S_B$) and due to the conservation of the flow rate ($U_A = U_B$) :

$$\Rightarrow p_{stat\_A} - p_{stat\_B} = \frac{1}{2}\rho\xi U^2$$

So the static pressure difference across the channel will be proportional to the pressure drop coefficient and the square of the velocity (quadratic relationship). It can be seen as the driving energy required to overcome the energy losses generated by the viscosity of the fluid. The greater the pressure difference across the channel, the greater the velocity in the channel.

2.3 PRESSURE BALANCING

This relationship between head loss and velocity in the pipe can then be applied to determine the evolution of pressure along the length of the pipe. The Figure 11 discretizes the previous channel into 4 points. The pressure at these 4 points will change between the value p_{stat_A} and p_{stat_B} as a result of head losses in each section of the channel (friction losses), but also of head losses at the engulfment and discharge of the channel (so-called singularity head losses). The change in pressure in the channel will then be the result of pressure equalisation, which depends on the pressure losses in each section and the establishment of the flow in the pipe.

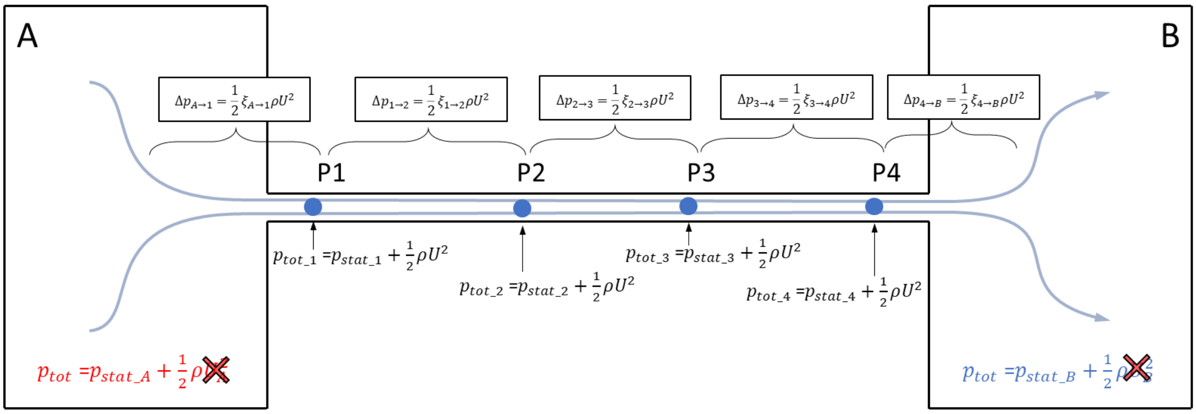

Figure 11 - change in pressure as a result of pressure losses in a channel

For example, the Figure 12 and the Table 1 show simulations of the evolution of pressure in a channel with a cross-section of 0.01m², subjected to a pressure differential of 100Pa. 4 simulations are carried out by varying the cross-sectional area of the inlet and outlet of the channel, leading to 4 different scenarios for the evolution of pressure in the pipe.

#simu	PA (Pa)	PB (Pa)	section A (m²)	section B (m²)	P1 (Pa)	P2 (Pa)	P3 (Pa)	P4 (Pa)	velocity(m/s)
1	100	0	0.01	0.01	65	56	47	46	1.50
2	100	0	0.01	0.005	97	96	95	95	0.49
3	100	0	0.005	0.01	8	7	6	6	0.53
4	100	0	0.005	0.005	56	55	54	54	0.37

Table 1 - evolution of static pressure in a channel

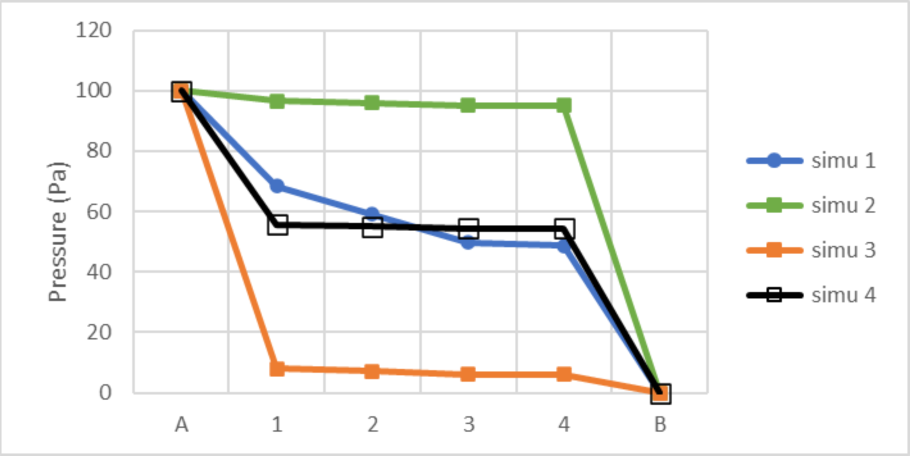

Figure 12 -Evolution of static pressure in a channel

If the inlet and outlet cross-sections are identical, the pressure in the channel will equalise at an average value of the pressures at its terminals, around 50 Pa. In the case where the inlet and outlet cross-sections are small (simulation 4), inlet/outlet pressure losses will severely restrict the flow in the channel. The pressure is then virtually constant in the channel (no friction losses due to low flow). When the inlet and outlet cross-sections are the same size as the channel, the diagram shows a continuous variation in pressure in the pipe due to frictional losses along the entire length of the pipe. When one of the two inlet/outlet sections is smaller than the other, the analysis shows that the pressure in the channel will equalise at a value close to that of the larger section.

Four very different configurations of channel pressure balance can be observed, simply by modifying the inlet/outlet cross-sections of the channel.

This example illustrates the mechanisms that will be at work in pressure balancing problems, which are at the heart of the analysis of wind loads on double-skin facades.

3 REFERENCE EXPERIMENT

The purpose of this section is to describe the reference experiment used to understand the mechanisms of pressure balancing in the air space and the generation of loads on a double-skin facade.

3.1 MODEL CONFIGURATION AND ENVISAGED MODULARITIES

The reference experiment is based on a double-skin facade affixed to one of the facades of a cubic building measuring 40m on each side. This building is reproduced as a 1:100 scale model. The model measures 40cm on each side. We will differentiate hereafter between the scale of the model and the Real Scale (RS). In its reference configuration, the double-skin facade covers the entire width of the building facade and extends 5 m from the ground to the top of the building facade. It is clear of the building wall by a distance of 2m Real Scale, i.e. 20mm at model scale. The double-skin facade and the building it backs onto have several geometric modularities.

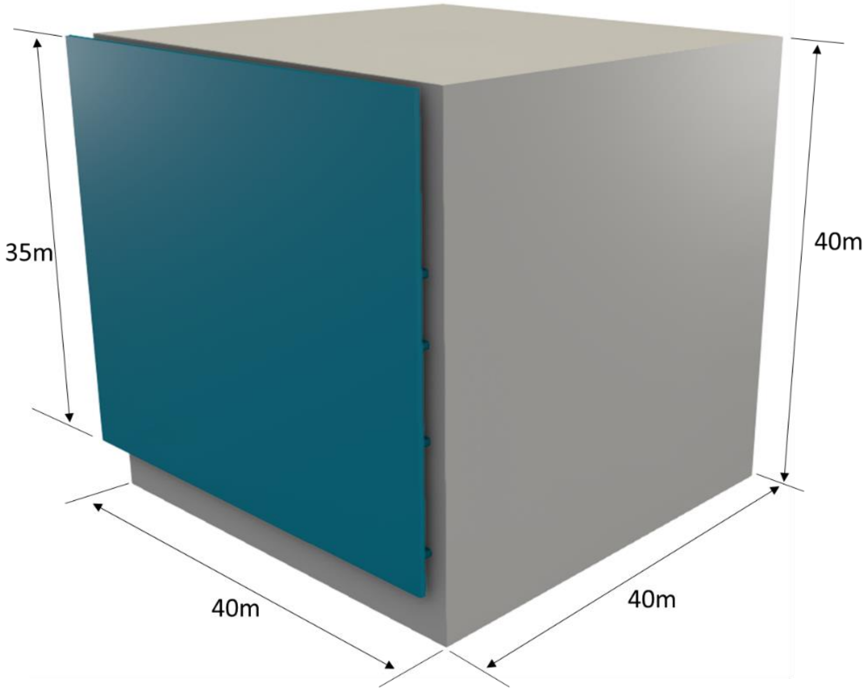

Figure 13 - reference model configuration

The first modularity is based on the height of the building, which can either be lowered to a height of 35m, with the double skin overhanging the roof by 5m, or raised to a height of 45m, with the double skin facade stopping 5m from the top of the building facade. The basic configuration is referred to as "level", the other two are referred to as "low" and "high" respectively, as illustrated Figure 14.

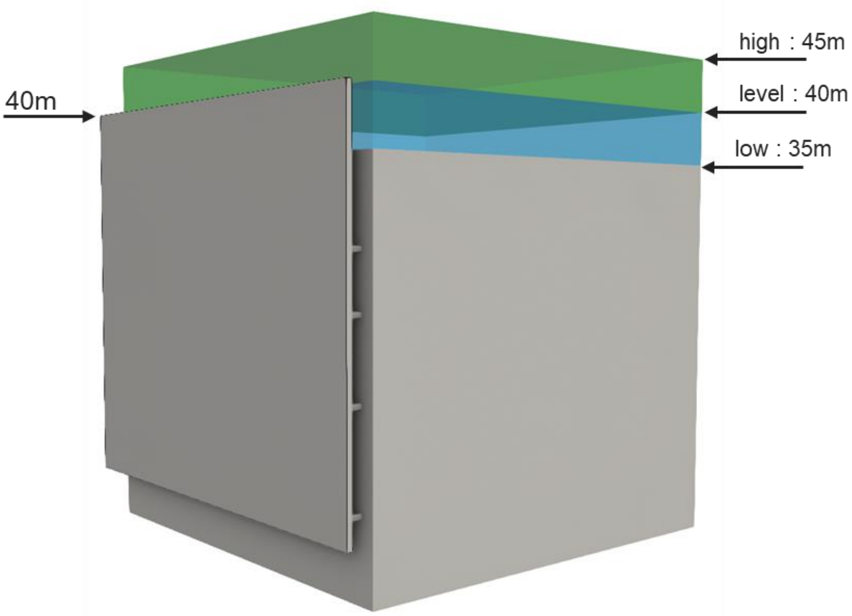

Figure 14 - modularity of building height

The second modularity concerns the thickness of the air gap, which can be continuously adjusted. 4 thicknesses were studied: 50cm, 1m, 2m and 3m, as illustrated below Figure 15

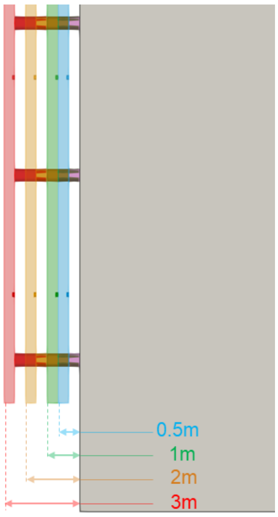

Figure 15 - modularity of air space thickness

The porosity of the double-skin facade can also be simulated by arranging holes across the facade. Each hole can be blacked out independently, opening up a wide range of possibilities for the design of this porosity. In this study, the holes were arranged to create a distributed porosity of 15% and 8% of the double-skin surface. A third configuration was also studied with a porosity equivalent to 3% of the double-skin surface, but extremely localised at the top and bottom of the facade, as shown in Figure 16.

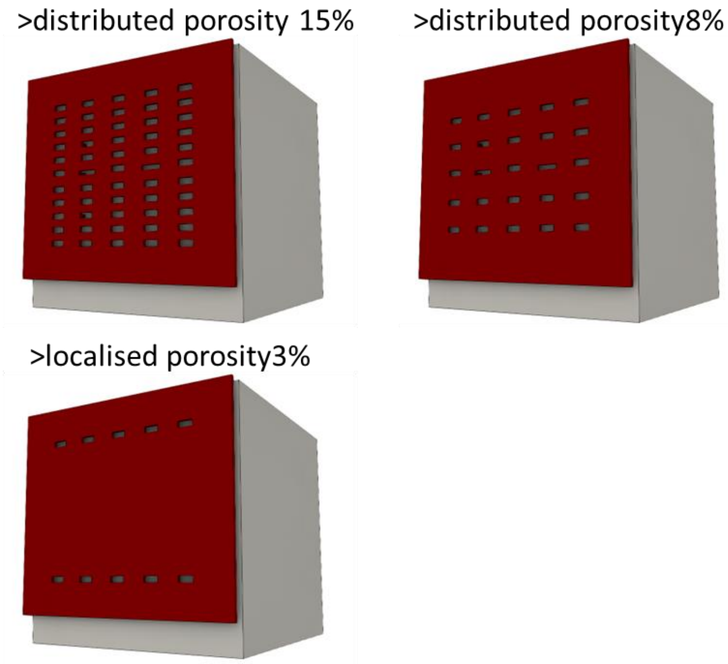

Figure 16 - modularity of porosity

The air gap can then be segmented across its entire thickness, as shown in Figure 17. The purpose of this segmentation is to compartmentalise the air gap in a sealed way, modifying its pressure balance.

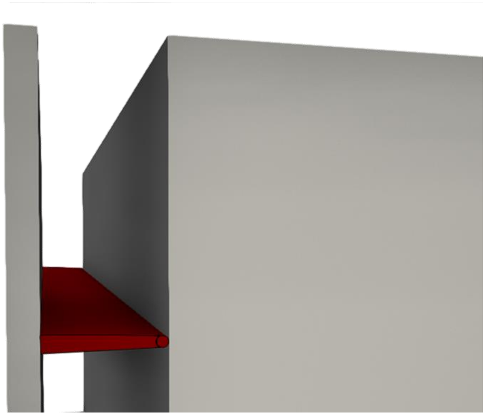

Figure 17 - air gap segmentation principle

The segmentation can be carried out vertically as shown in Figure 18. Dividing blades are placed at a distance of 5m from each edge of the facade, and run the full height of the double-skin facade.

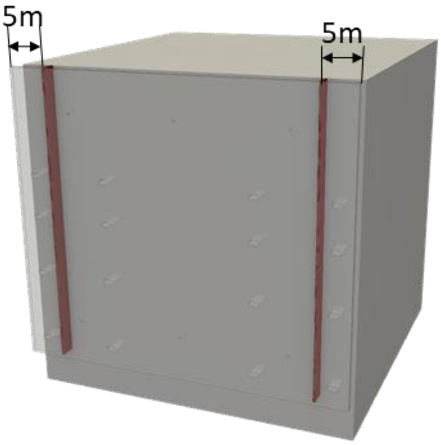

Figure 18 - vertical segmentation

The segmentation can then be carried out horizontally. Two configurations were studied, as shown in Figure 19. The first imposes a separation running the full width of the facade, located at a height of 5m from the lower limit of the double-skin facade. The second configuration places the separation at a distance of 5m from the upper part of the double-skin facade.

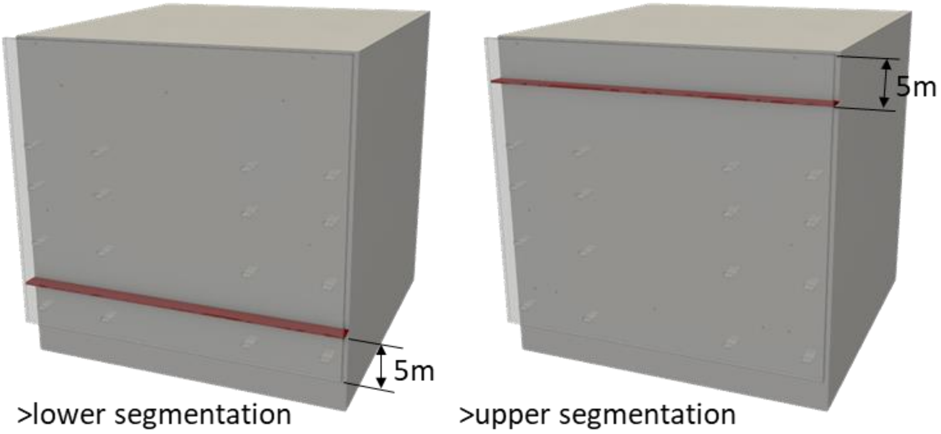

Figure 19 - horizontal segmentation

The porosity of these horizontal segments can be adjusted by creating openings leading to porosities of 8% or 15%, as shown below Figure 20.

Figure 20 - porosity of vertical segmentation

A final configuration known as "perimeter segmentation" allows part of the double-skin facade to be segmented on these 4 sides, as shown below. Figure 21. This configuration can be particularly interesting when associated with a porous double-skin facade.

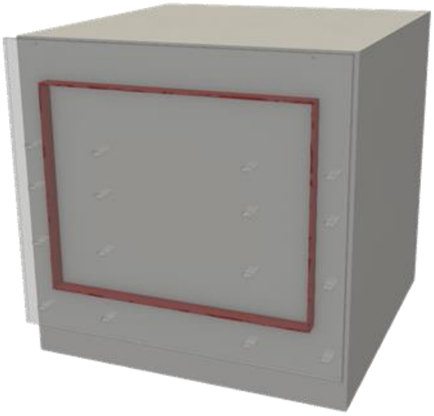

Figure 21 - segmentation around the perimeter

A final modularity enables the double-skin facade to be extended to all 4 facades of the building, in a configuration known as peripheral double-skin.

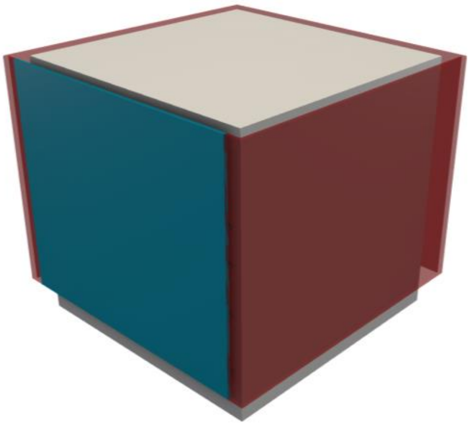

Figure 22 - peripheral double-skin

These modularities can be combined with each other to generate a very large number of geometric configurations. A nomenclature principle was then defined to easily describe each of the geometric configurations tested. It is presented Figure 23.

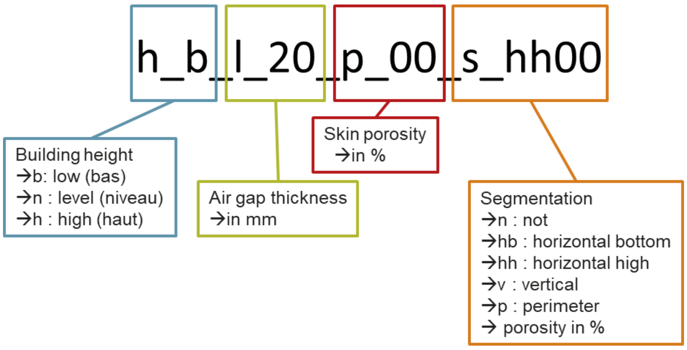

Figure 23 - nomenclature principle used to describe a geometric configuration based on a combination of modularities

A total of 45 different geometric configurations were studied, and are listed in the Table 2.

# config	Building height	Air gap thickness (m Real Scale)	Skin porosity	Segmentation
1	low	2	full	no
2	level	2	full	no
3	high	2	full	no
4	low	2	full	horiz high full
5	level	2	full	horiz high full
6	high	2	full	horiz high full
7	low	2	full	horiz low full
8	level	2	full	horiz low full
9	high	2	full	horiz low full
10	low	2	full	vertical
11	level	2	full	vertical
12	high	2	full	vertical
13	low	2	full	horiz high porous 08%
14	high	2	full	horiz high porous 08%
15	low	2	full	horiz high porous 15%
16	high	2	full	horiz high porous 15%
17	high	0.5	full	no
18	level	0.5	full	no
19	low	0.5	full	no
20	level	1	full	no
21	high	1	full	no
22	level	3	full	no
23	high	3	full	no
24	low	peripheral	full	no
25	high	peripheral	full	no
26	low	2	full	perimeter
27	high	2	full	perimeter
28	low	2	8% porous	perimeter
29	high	2	8% porous	perimeter
30	low	2	15% porous	perimeter
31	high	2	15% porous	perimeter
32	low	2	15% porous	no
33	high	2	15% porous	no
34	level	2	15% porous	no
35	low	2	8% porous	no
36	high	2	8% porous	no
37	level	2	8% porous	no
38	high	2	3% porous	no
39	level	2	3% porous	no
40	high	2	3% porous	vertical
41	low	2	3% porous	vertical
42	level	2	3% porous	vertical
43	high	2	15% porous	vertical
44	low	2	15% porous	vertical
45	level	2	15% porous	vertical

Table 2 - list of geometric configurations investigated

3.2 WIND MODEL FOR DIMENSIONING WIND LOADS

In order to bring this reference experiment closer to the industrial application framework for the wind dimensioning of buildings, it was decided to base the model of the wind incident on the building in accordance with Eurocode [8] and its French National Annex NF EN 1991-1-4/NA.

The natural wind is a signal that fluctuates over time: it varies in intensity and direction. The instantaneous wind speed can be expressed as :

$$u(t) = U + u'(t)$$

where U is the average speed over the observation period $T$and $u'(t)$the fluctuation in speed around this average.

Turbulence is characterised by the standard deviation σ of the longitudinal fluctuation in wind speed $u'(t)$over the period Taccording to the expression

$$\sigma = \sqrt{\frac{1}{T}\int_0^T u'^2(t)dt} = \sqrt{\overline{u'^2}}$$

The turbulence intensity is then given by the expression

$$I = \frac{\sigma}{U}$$

The average speed and turbulence data vary with height. This distribution is a function of the roughness of the ground and its topography, and is therefore characteristic of the 'history' of the wind.

The increase in average velocity with height can be modelled for a height z above a minimum value z_{min} by a logarithmic law expressed by the expression

$$U = k_r \ln\left(\frac{z}{z_0}\right) V_{b,0} \text{ for } z > z_{min}$$

Where z is the altitude expressed in metres, z_0 is the site roughness parameter, $z_{0,II}$ is the roughness parameter for category II terrain, k_r is the roughness-dependent terrain factor defined by : $k_r = 0.19\left(\frac{z_0}{z_{0,II}}\right)^{0.07}$ and $V_{b,0}$ is the average speed measured at the reference weather station at a height of 10 metres. For $z < z_{min}$the value at z_{min} is retained.

The turbulence gradient can be modelled by the relation

$$I(z) = \frac{k_l}{\ln\left(\frac{z}{z_0}\right)}$$

Where the turbulence coefficient k_l is expressed by the formula :

$$k_l = 1 - 2.10^{-4}(log(z_0) + 3)^6$$

The average velocity profile can then be used to define an average dynamic pressure exerted by the wind such that :

$$\overline{p_{dyn}} = \frac{1}{2}\rho U^2$$

With ρ the air density taken to be 1.225kg/m^3 in accordance with the French National Annex to the Eurocode.

The Eurocode then proposes a modelling of peak pressures based directly on the turbulence intensity of the wind is defined as :

$$\widehat{p_{dyn}} = (1 + 7I)\,\overline{p_{dyn}}$$

The French National Annex to the Eurocode proposes a wind map for selecting a value for the reference speed with a 50-year return period $V_{b,0}$ depending on the location of the project. For the purposes of this study, we will choose $V_{b,0} = 24m/s$ which is, for example, the value prescribed for the city of Paris.

This velocity is measured in a flat, uncluttered area with a type II roughness at an altitude of 10 m above ground level. For the purposes of this study, we will choose an urban environment assimilated to roughness IIIb as defined in the Table 3 taken from the French National Annex to the Eurocode. This table also provides the values of z_0 values depending on the nature of the site. These roughness values can then be used, from the above formulae, to transpose the reference wind speed $V_{b,0}$ for any altitude and any type of roughness.

Class	**Nature of the land**	z_0	z_{min}
0	Sea or coastal zone exposed to sea breezes; lakes and bodies of water crossed by the wind over a distance of at least 5km.	0.005	1
II	Open country, with or without a few isolated obstacles (trees, buildings, etc.) separated from each other by more than 40 times their height.	0.05	2
IIIa	Countryside with hedgerows; vineyards; hedged farmland; scattered settlements	0.20	5
IIIb	Urbanised or industrial areas; dense hedged farmland; orchards	0.50	9
IV	Urban areas where at least 15% of the surface area is occupied by buildings with an average height of more than 15m, forests	1	15

Table 3 : Terrain roughness parameters

For the purposes of this study, and by defining a reference height $h_{ref} = 40m$ for a roughness IIIb environment, we find the following reference values:

$$\overline{U}(z = h_{ref}) = 23.5\text{m/s}$$
$$I(z = h_{ref}) = 21\%$$
$$\overline{p_{dyn}}(z = h_{ref}) = 338\text{Pa}$$
$$\widehat{p_{dyn}}(z = h_{ref}) = 835\text{Pa}$$

3.3 ATMOSPHERIC BOUNDARY LAYER WIND TUNNEL

The aim of this model experiment is to study the evolution of the pressure balance of the air space in the double-skin facade, taking into account the natural unsteadiness of the wind generated by the turbulence of the Atmospheric Boundary Layer. To do so, the model is placed in the test section of the CSTB's Atmospheric Boundary Layer wind tunnel.

3.3.1 NSA wind tunnel

The CSTB's NSA (Nouvelle Soufflerie Atmosphérique) wind tunnel is a so-called Atmospheric Boundary Layer wind tunnel. This type of wind tunnel is characterised by very long test sections in which roughnesses are placed, obstacles that generate turbulence representative of the Atmospheric Boundary Layer.

The test section is 4m wide by 2m high (adjustable to 2.5m) and 14m long. It is equipped with a turntable at its centre, enabling the model to be placed at different wind directions. The maximum speed in the test section is 20m/s.

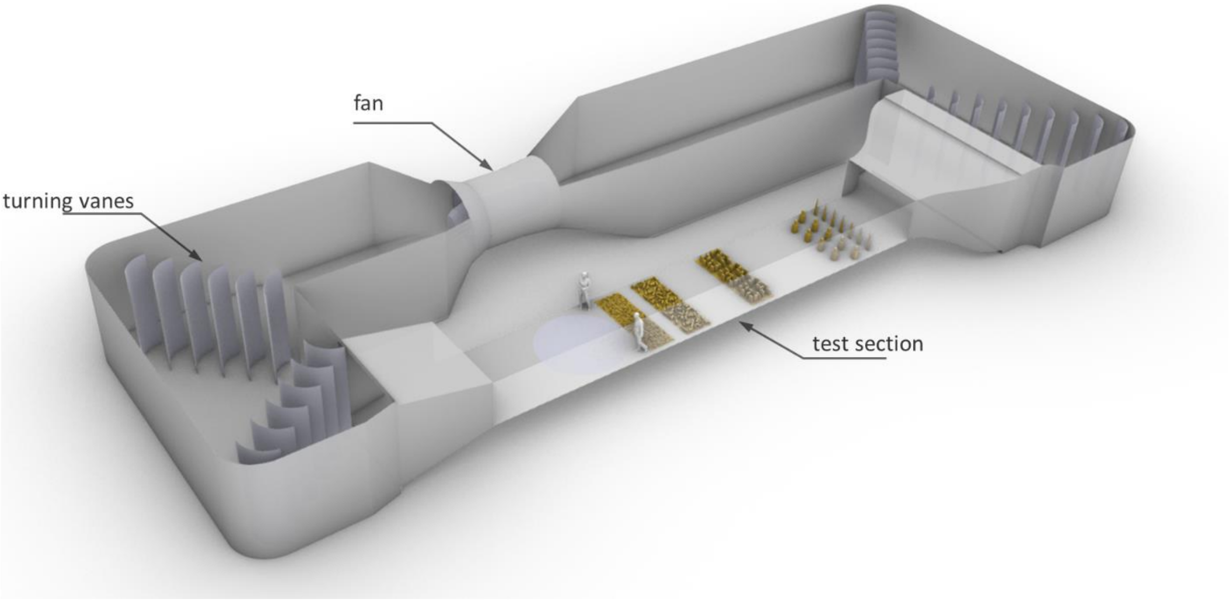

Figure 24 - schematic of the CSTB's Atmospheric Boundary Layer Wind Tunnel

3.3.2 Wind velocity and turbulence gradient

The long length of the test section means that roughness of different sizes can be placed upstream of the model to generate turbulence that is representative of natural wind. The turbulence thus created is a superposition of vortices of different sizes and different intensities. The large roughnesses are positioned furthest upstream and will generate large eddies that will persist over time. Conversely, small roughnesses will create small eddies that will disappear more quickly. The aim is then to position all of these roughnesses along the entire length of the vein so as to combine the different sizes of vortex at the same point on the model.

In order to reproduce the turbulence characteristic of the site studied, from sea winds to urban winds, on the desired scale, the arrangement of these roughnesses will differ from one project to another. It is therefore necessary, prior to the tests, to measure the mean velocity gradient and turbulent intensity to ensure that it complies with the Eurocode profile required for the project in question. We will therefore try to find the values of the wind model described in §3.2.

The velocity gradient is measured using a "fast" Pitot tube at a high acquisition frequency to obtain information on the turbulence of the flow. It is carried out at the centre of the test section, at the point where the model will be positioned, in the absence of the model. This characterisation ensures that the desired wind profile is established at the model. The gradient is measured iteratively, adapting the size and position of the roughness to obtain the desired mean velocity and turbulence gradients.

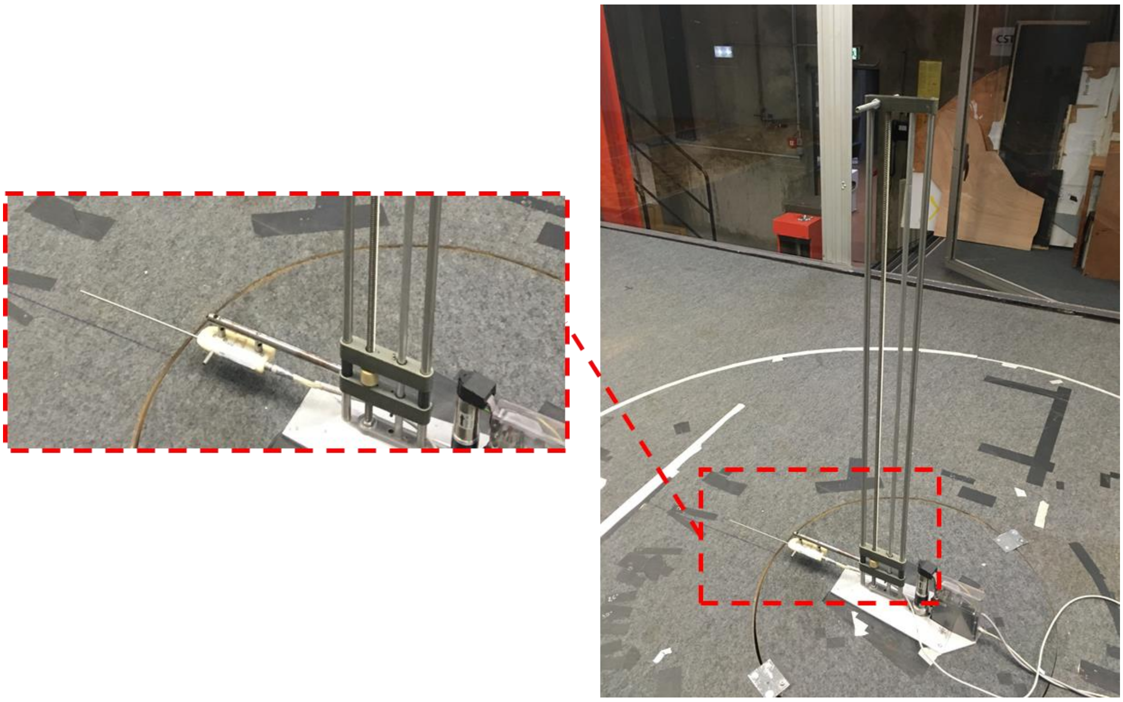

Figure 25 - Measurement of velocity gradient and turbulence using a fast pitot on a robotic support

The Figure 26 shows the roughness layout used to generate the wind profile on the model.

Figure 26 - Roughness upstream of the model

The Figure 27 shows the peak dynamic pressure profile measured at the centre of the test section. It also shows the interpolation of a Eurocode roughness IIIb profile. This interpolation makes it possible to calculate a crossover coefficient between the dynamic pressure measured in the wind tunnel and the Real Scale (RS) dynamic pressure. The Figure 28 also shows the associated mean velocity and turbulent intensity profiles. It compares the measured profiles with those proposed by the Eurocode for rural (rugo II) or urban (rugo IIIb) roughness. The comparison confirms that the gradient generated in the wind tunnel corresponds to that of an urban environment.

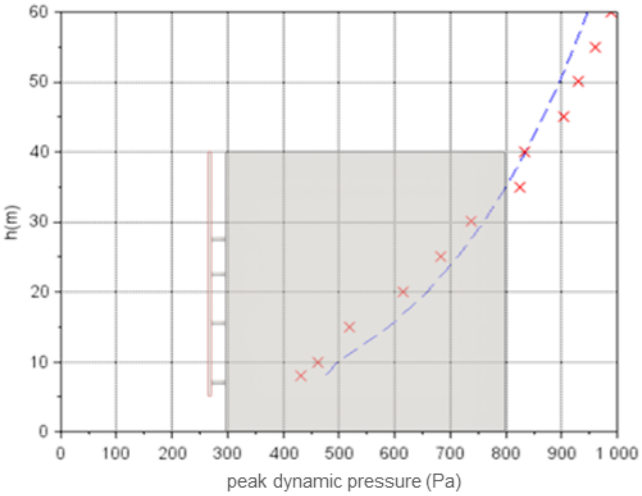

Figure 27 - Peak dynamic pressure gradient measured in the wind tunnel

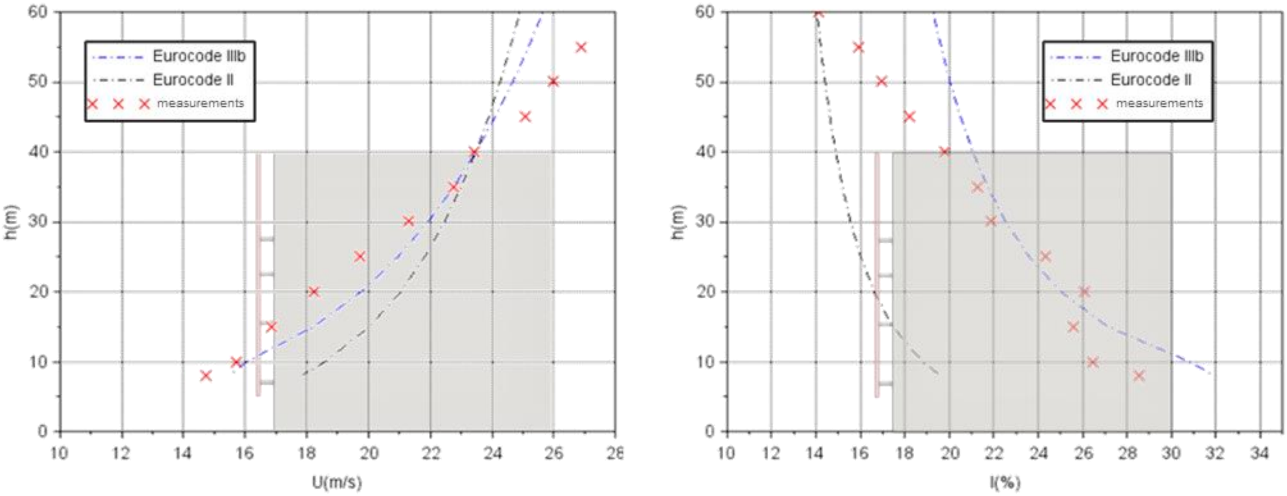

Figure 28 - Velocity and turbulence gradients measured in the wind tunnel - Comparison with Eurocode profiles for open country (rugo II) and urban areas (rugo IIIb)

During the tests, the wind speed is recorded by a Pitot tube fixed to the ceiling above the model, free from the aerodynamic disturbances generated by the model. This Pitot tube is also present during the gradient measurements. These measurements can then be used to deduce an calibration coefficient that enables a reference speed to be deduced at reference height of the model (40m RS) from the speed measured by the Pitot tube on the wind tunnel ceiling during the tests. For the purposes of these tests, this calibration coefficient is equal to 0.588.

3.4 MOCK-UP AND METROLOGY

3.4.1 Building's mock-up

The mock-up of the building was produced on a scale of 1:100 in the CSTB workshop. It is made of frosted Plexiglas sheets. It is fixed directly to the floor of the turntable of the test section as shown in Figure 29. The upper part of the model is removable, and a set of spacers of different heights allows the height of the building to be adjusted.

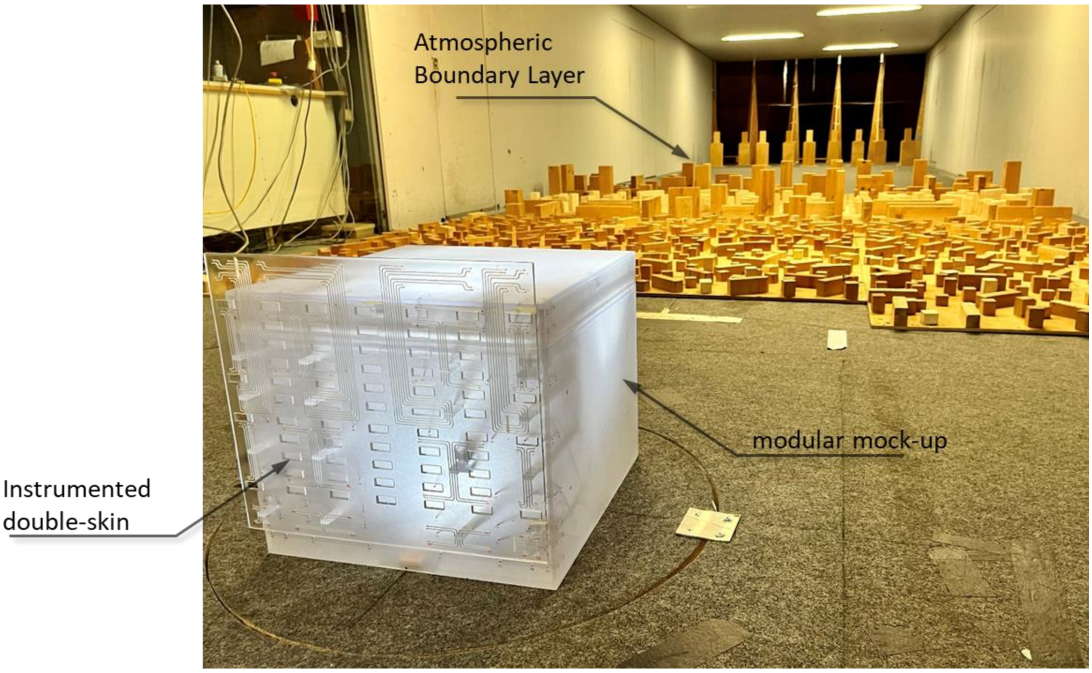

Figure 29 - wind tunnel model of the building and its double-skin facade

The model of the double-skin, as well as those of the segments, were produced by 3D printing in a transparent resin using a stereolithography printing technique. The double-skin facade is fitted with 16 rods that slide in bores machined into the facade of the building, enabling the thickness of the air space in the double-skin to be continuously adjusted.

3.4.2 Location of pressure taps

The model is equipped with 240 pressure taps which are distributed as follows Figure 30 :

- 64 pressure taps on the external face of the double-skin facade
- 64 pressure taps on the internal face of the double-skin facade
- 112 pressure taps on the facade of the building

On the double-skin facade, the internal and external pressures are located at the same points on the facade, forming 64 doublets of taps that measure an instantaneous pressure difference on either side of the double skin. Pressure taps are also positioned on the facade of the building, opposite the pressure taps located on the double-skin facade. These will show whether there is a pressure difference (mean and/or instantaneous) in the thickness of the air space.

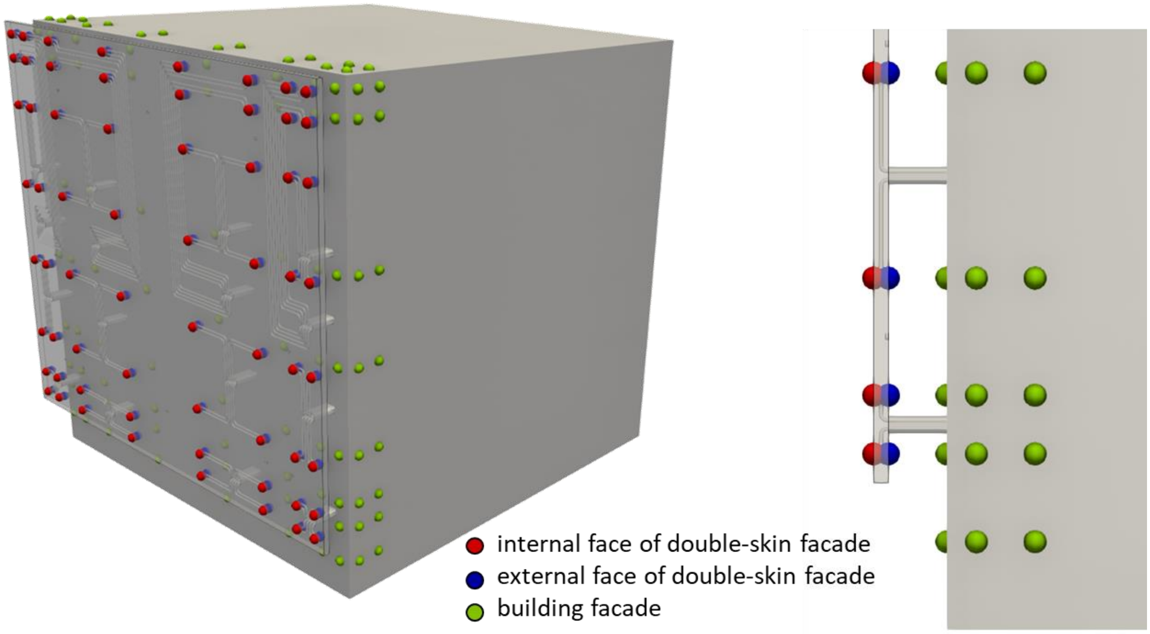

Figure 30 - distribution of pressure taps on the building

3.4.3 Pressure sensors and pneumatic lines

The pressure at the end of each pressure tap is measured using PSI synchronous pressure transducers (see Figure 31). These enable 32 pressure channels to be measured synchronously at a sampling frequency of 512 Hz. 8 sensors with 32 channels are therefore used here to acquire the 240 pressure taps on the model. The pressure is then transmitted from the taps to the sensors via pneumatic connections made from 1.5 m long vinyl tubes with an internal diameter of 1.4 mm. A deconvolution function is then used to take into account the propagation of the pressure wave in these tubes, and thus correct the frequency response of the pressure signal acquired by the sensors.

Figure 31 - 32-channel PSI pressure sensor

To ensure that the pneumatic tubes connected to the pressure taps on the double-skin facade do not disturb the flow in the air space, they were 3D printed directly into the thickness of the facade mock-up. The 128 pneumatic connections are then routed inside the building model through the 16 facade support rods. At the end of the support rods, the pressure signal is transmitted to the pressure sensors using standard vinyl tubes.

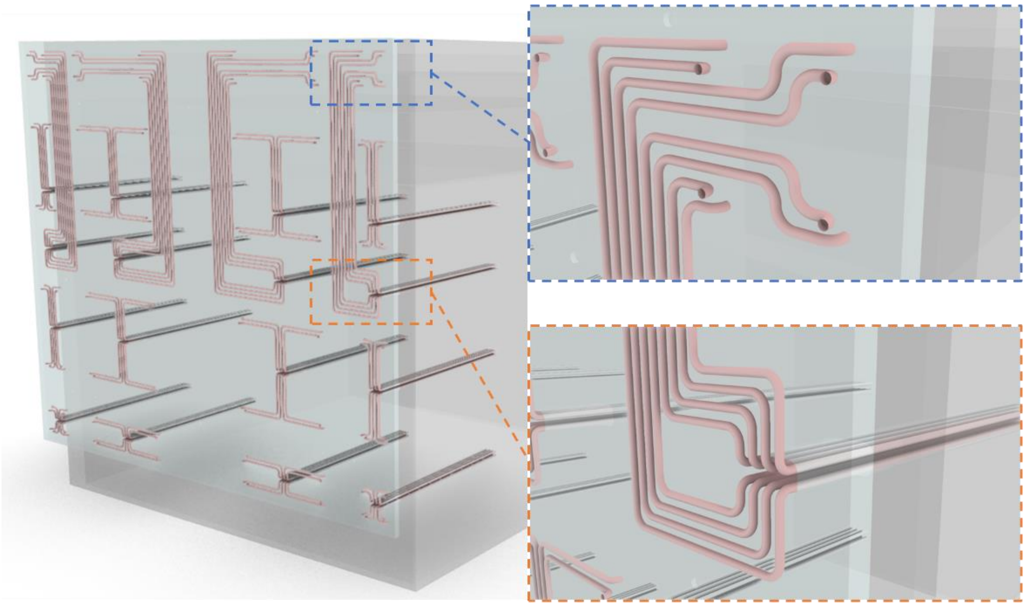

Figure 32 - CAD of the 3D printed pneumatic connections in the model of the double-skin facade

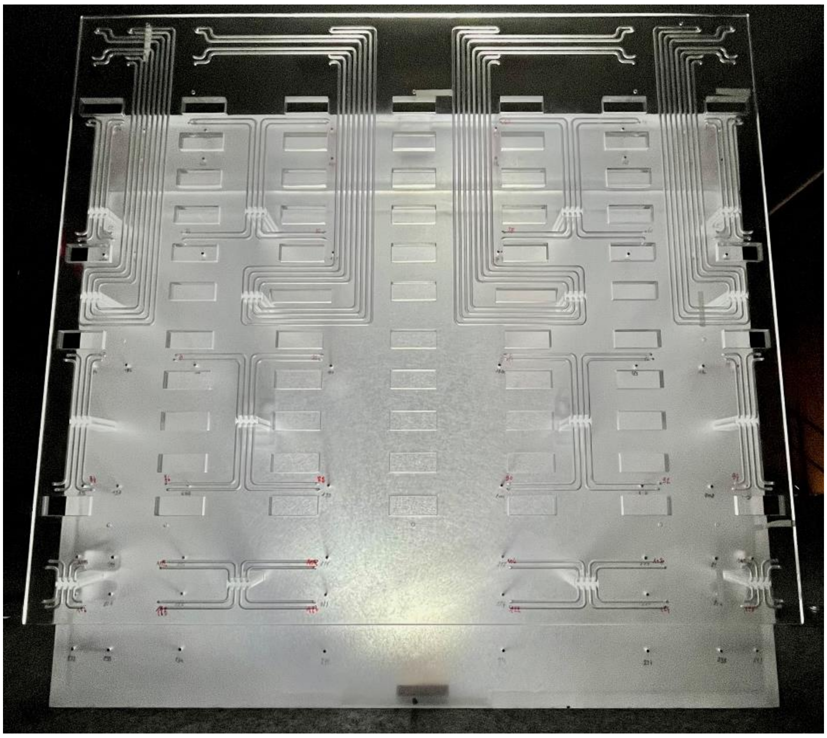

Figure 33 - photo of the complete 3D-printed pneumatic circuit

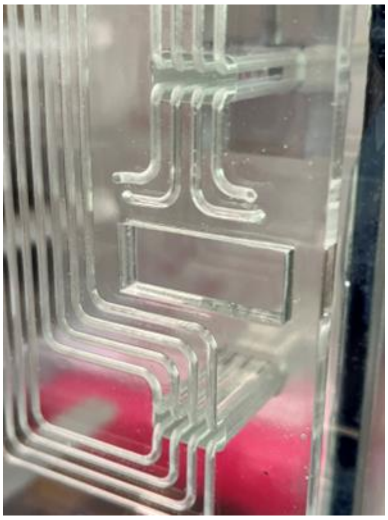

Figure 34 Detail view of the 3D-printed pneumatic circuit, with the pressure taps on the front, and the pressure routing via the support rods.

The 3D printing of the pneumatic connections means a low obstruction of the air space, thanks to the mere presence of the 16 support rods, without impacting on the aerodynamics of the air gap. Although this means that the flow remains highly representative, the use of these 3D printed connections is not without risks:

- risk of pneumatic connections becoming blocked during 3D printing of the model
- risk that the succession of bends and the lengthening of the pneumatic circuit could disrupt the dynamics of the pressure signal

The resolution of the new 3D printers ensures that tubes with a diameter of 1.5mm are not completely blocked when the part is printed. They also make it possible to produce very clean bends with a large diameter of curvature, which limits the problems of pressure wave propagation in the pneumatic circuit.

The Figure 35 plots the time signals from two pressure taps located in the air gap in the middle of the double-skin facade. The "blue" tap corresponds to the internal tap of the double-skin facade, with a pressure signal transported through a 3D-printed pneumatic connection. The "red" tap corresponds to the tap on the facade of the building, with a pressure signal carried by a simple traditional pneumatic connection. The acquisition was carried out for a geometric configuration where the two pressure taps are supposed to see the same signal. Plotting the time signals shows that the two signals are indeed superimposed. The spectral analysis carried out over the entire length of the acquisition, together with the probability density (PDF) of the pressure values, also shows that the two signals are identical. This means that the 3D-printed pneumatic connection does not interfere in any way with the acquisition of the pressure signal.

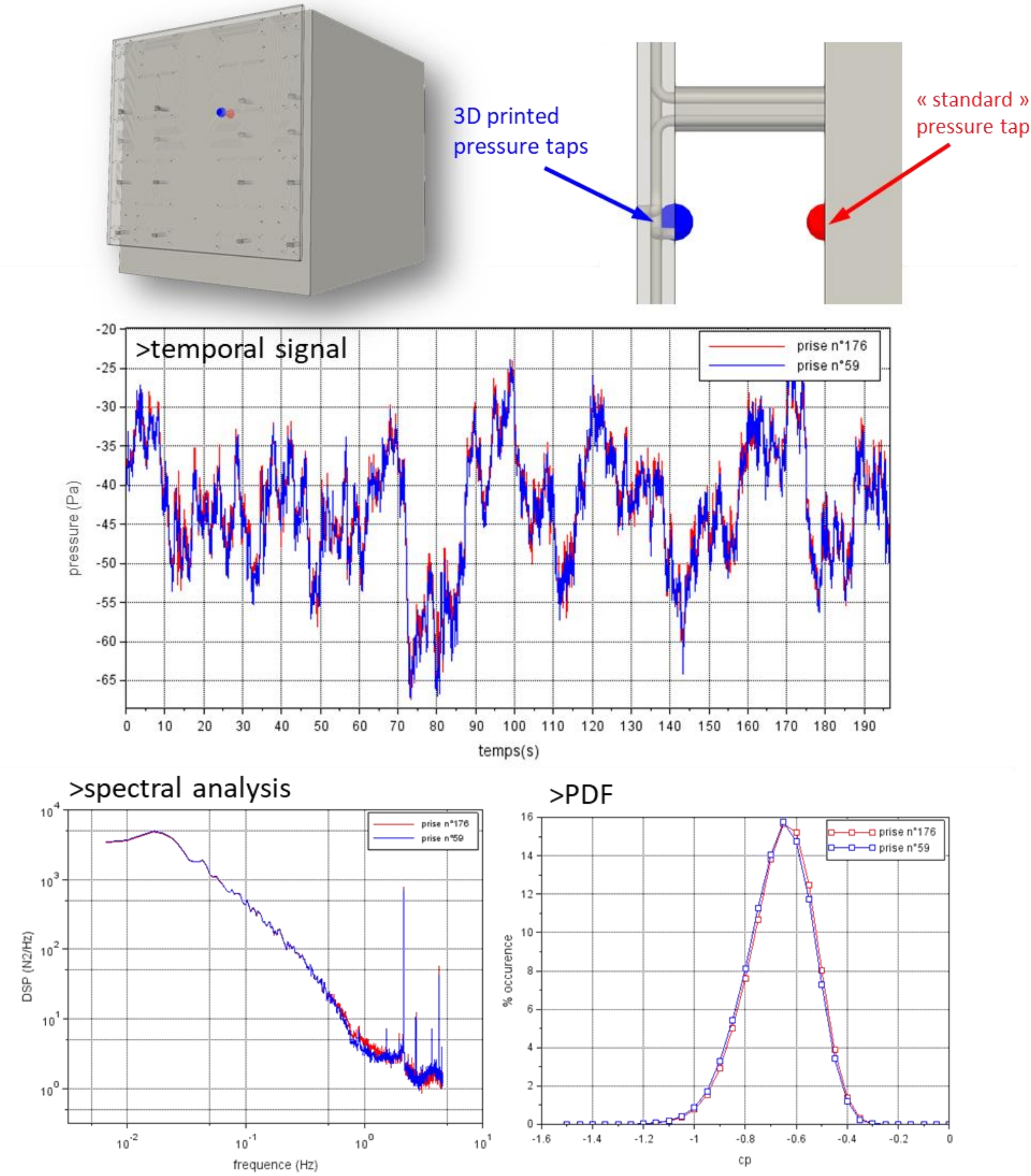

Figure 35 - comparison of the pressure signals carried by a 3D printed pneumatic connection and a "traditional" pneumatic connection

3.5 REAL SCALE EXTRAPOLATION AND MEASUREMENT OF PEAK FORCES

The pressure on the facade is measured at a frequency of 512 Hz for a duration of 5 minutes at wind tunnel scale. In order to transpose the flow dynamics from the model scale to the real scale, it is necessary to define a geometric scale and a velocity scale. These two scales will then also be used to define a time scale.

The geometric scale is defined by the scale of the model:

$$s_{geo} = \frac{h_{RS}}{h_{model}} = 100$$

The velocity scale is the ratio between the wind velocity at the reference height (here 40m) measured in the wind tunnel and that prescribed by the Eurocode:

$$s_{velocity} = \frac{U_{RS,z=40m}}{U_{model,z=40m}}$$

The aim of these tests is to reach a speed of 10m/s at the top of the building.

The geometric and velocity scales are therefore imposed by the wind tunnel simulation parameters. They can then be used to deduce a time scale:

$$s_{time} = \frac{t_{RS}}{t_{model}} = \frac{s_{geo}}{s_{velocity}}$$

The Table 4 summarises the different scaling factors for a wind speed of 10m/s at the top of the building:

model scale		100
wind speed at 40m	model (m/s)	10.0
	RS (m/s)	23.5
velocity scale		2.4
time scale		43
Acquisition time	model (mn)	5
	RS (mn)	**213**
acquisition frequency	model (Hz)	512
	RS (Hz)	**12.0**

Table 4 - Scaling factors and extrapolation of characteristic quantities to the Real Scale for the model

The table shows that the Real Scale acquisition time is 3.5 hours. We generally try to reproduce a storm lasting more than 2 hours to ensure statistical convergence of the peak values. In addition, it can be seen that the acquisition frequency is greater than 10Hz, which makes it possible to discretise the gust events we are trying to measure, which have a characteristic duration of 3s on the Real Scale.

The Figure 36 shows the time signal, extrapolated to Real Scale, of the pressure measured on the outer face of the double skin during a test. The time plot shows very strong fluctuations in the value of the pressure, with peaks 2.5 times higher than the mean value. In order to obtain a representative value for these peaks, the signal is broken down into blocks of 10mn Real Scale, the duration generally used in climatology to establish the average wind speed. The maximum and minimum pressure values are then recorded in each block. The peak value is then taken to be equal to the average of the peaks recorded in each 10-minute block.

In terms of notation, we distinguish between mean pressure, noted as $\bar{p}$ from the peak pressure noted $\hat{p}$

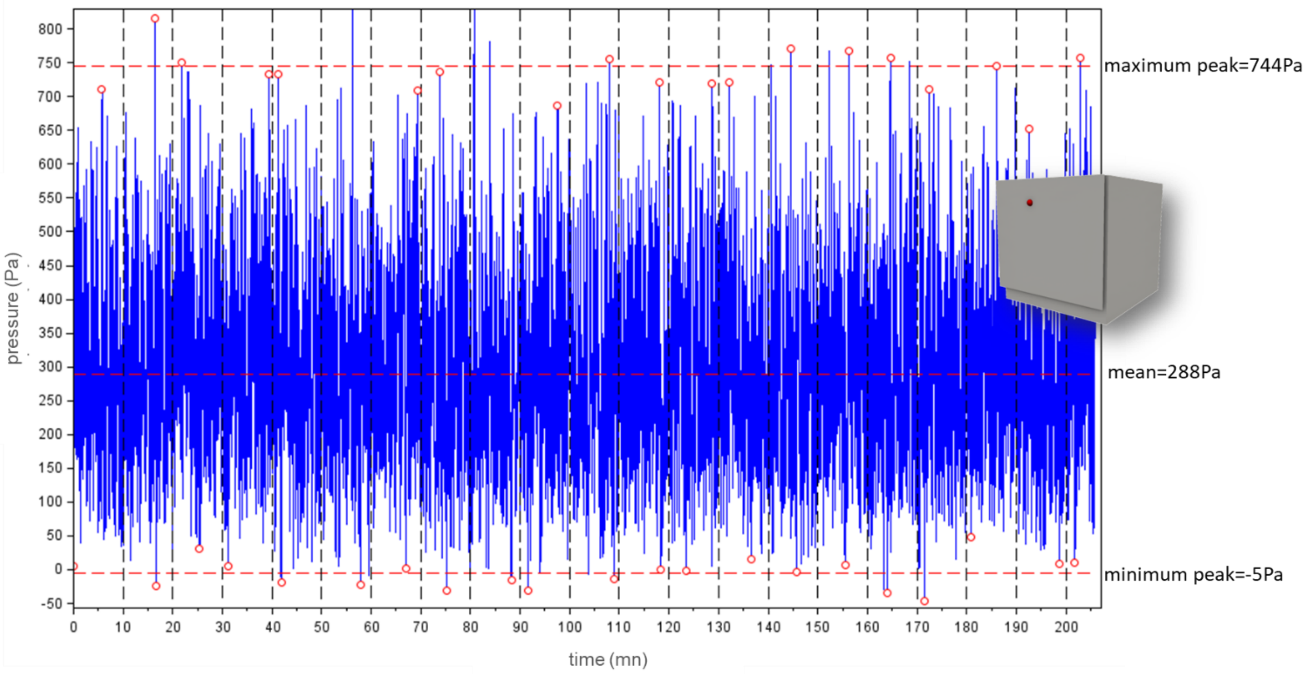

Figure 36 - Pressure signal, transposed into Real Scale, measured at the centre of the external face of the double-skin facade

3.6 MEAN AND PEAK PRESSURE COEFFICIENTS

The pressure on the facades will vary according to the structure of the flow around the building, as well as the reference dynamic wind pressure upstream of the building. It can generally be seen that at a given point on the facade, the pressure varies linearly with the dynamic pressure upstream. The pressure a given position can then be written as :

$$p = c_p \cdot p_{dyn}$$

c_p is then called the pressure coefficient. This coefficient does not generally depend on the dynamic pressure upstream, but only on the shape of the building and the way the flow is structured around it. This can be very practical, as the pressure on the facade can be extrapolated for various wind speeds.

Unless otherwise stated, the pressure coefficients in this study will be expressed on the basis of the reference dynamic pressure $p_{dyn_{ref}}$ evaluated at the reference height $h_{ref} = 40m$.

A distinction is made between the mean pressure coefficient $\overline{c_p} = \frac{\overline{p}}{\overline{p_{dyn_{ref}}}}$ and the peak pressure coefficient $\widehat{c_p} = \frac{\hat{p}}{\widehat{p_{dyn_{ref}}}}$. In the tests, the mean dynamic pressure $\overline{p_{dyn_{ref}}}$ is measured via the Pitot tube on the ceiling of the wind tunnel combined with the adjustment coefficient obtained by measuring the velocity gradient (see §3.3.2). As this Pitot tube cannot measure velocity fluctuations at the reference height, the reference peak dynamic pressure is obtained from the proposed extrapolation of the Eurocode

$$\widehat{p_{dyn_{ref}}} = \left(1 + 7I\left(h_{ref}\right)\right) \cdot \overline{p_{dyn_{ref}}}$$

The gradient measurements in section §3.3.2 showed that this approximation was fully justified.

The Eurocode [8] does not differentiate between the mean value and the peak value of the pressure coefficient, which implies that $\overline{c_p} = \widehat{c_p}$. This is generally observed for simple geometries, when the peak pressures on the building are solely due to fluctuations in the large-scale turbulence of the Atmospheric Boundary Layer. This is no longer necessarily the case for more complex geometries, where the interaction of large-scale turbulence and turbulence at the building scale can create different dynamics.

In the case of the double-skin facade, we will also be interested in the instantaneous pressure differentials between the pressure exerted on the outer face of the skin p_{ext} and the inner face p_{int}. This differential is noted $p_{net} = p_{ext} - p_{int}$

An associated pressure coefficient $c_{p_{net}}$ and an mean value $\overline{c_{p_{net}}}$ and peak value of this coefficient $\widehat{c_{p_{net}}}$

If on average $\overline{c_{p_{net}}} = \overline{c_{p_{ext}}} - \overline{c_{p_{int}}}$, because of the difference in dynamics on either side of the skin $\widehat{c_{p_{net}}} \neq \widehat{c_{p_{ext}}} - \widehat{c_{p_{int}}}$. The average of the differential value is equal to the differential of the average values, but the peak of the differential is not necessarily equal to the differential of the peak values.

3.7 SIMILARITY AND DEPENDENCE ON REYNOLDS NUMBER

The use of the pressure coefficient allows the forces on the facade to be extrapolated to the Real Scale, and for several different reference dynamic pressures. This extrapolation is based on the assumption that the coefficient itself is independent of scaling effect, as well as the reference dynamic pressure.

This is true if the flow respects the so-called similarity rules. The flow is considered similar if the Reynolds number $Re = \frac{UD}{\upsilon}$ is conserved, with υ the kinematic viscosity of air and D a characteristic dimension of the flow. To obtain a similar flow, reducing the scale to 1/100 would require blowing 100 times faster on the model, which is impossible in practice.

However, it turns out that above a certain Reynolds number, the pressure coefficients become independent of it, opening the door to their use for extrapolation to Real Scale and for all wind speeds.

This is particularly true for sharp-edged geometries, which fix the position of the detachments driving the flow structure. Similarity issues generally concern rounded surfaces where the position of the detachments will vary as a function of the Reynolds number.

In order to ensure that the pressure coefficient is independent of the Reynolds number, a measurement was carried out for several different wind speeds. The configuration chosen was that of a tall building with no segmentation. The analysis of the pressure field on the facade will be studied §4.2.3. The Figure 37 plots the mean and peak net pressure coefficients. It shows that in both cases, the results are identical for the 3 wind speeds investigated, thus demonstrating that the pressure coefficient is independent of the Reynolds number. In addition, the figure shows that although the mean and peak pressure coefficients are different for the two geometric configurations, the ratio between the two seems to be conserved for the 3 flow speeds. The flow dynamics are therefore also similar for the 3 wind speeds investigated.

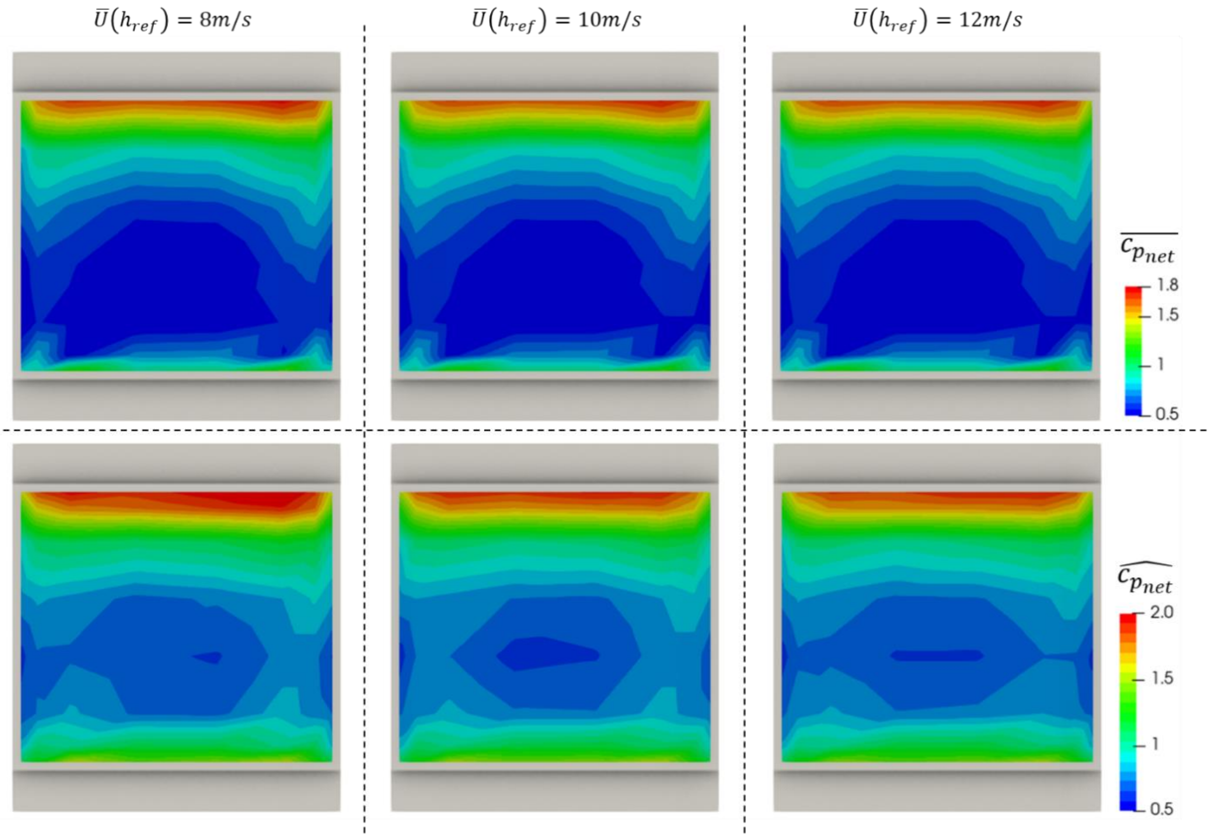

Figure 37 - average and peak net pressure coefficient on the double-skin facade as a function of wind velocity

This ensures that the pressure coefficients can be used to extrapolate loads to Real Scale, and for different flow speeds.

4 WIND LOADS ON THE DOUBLE-SKIN FACADE

This section now describes the evolution of wind loads on the double-skin facade as a function of the different geometric modularities investigated. Each of these parameters proved to have a significant influence on the loading of the facade. It is therefore quite difficult to decide in which order the analysis of each of these parameters should be presented. For pedagogical purposes, it was decided to present the configurations in an order of increasing complexity of the flow structure in the air gap, thus allowing the different mechanisms at work in the pressure equalisation of the air gap to be understood.

4.1 VERTICALLY SEGMENTED SKIN

The analysis begins with a double-skin facade configuration with vertical segmentations. In this configuration, the double-skin facade is open on two sides, with an opening at the foot of the facade, and an opening at the top of the facade. The air gap can then be likened to a flat channel for which each end of the channel is subjected to a different pressure, imposed by the structure of the flow bypassing the building.

4.1.1 Reference case

Initially, the analysis is based on a building configuration with a standard roof height of 40m. The upper end of the double-skin facade is then at roof edge level. The Figure 39 plots the mean pressure coefficients measured on the external face $\overline{c_{p_{ext}}}$internal $\overline{c_{p_{int}}}$ as well as the mean pressure differential noted $\overline{c_{p_{net}}}$.

On the outside, the pressure coefficient $\overline{c_{p_{ext}}}$ is positive and varies from almost zero in the lower corners to a value of 0.8 in the centre of the facade. It remains above 0.5 over a large part of the facade. The figure clearly shows the increase in pressure with altitude due to the upstream wind gradient. The pressure loading of this facade is entirely consistent with what we would expect for this type of geometry.

Inside the air space the pressure coefficient $\overline{c_{p_{int}}}$ is negative. The area bounded by the vertical segmentation is clearly visible. Between the two segments, the pressure is almost uniform in the air space, with a pressure coefficient of -0.5. At the foot of the facade, the pressure lowers rapidly to a value of -1.4. Outside the segmentation, depressions are higher than inside the air space, reaching a peak of -1.

The mean pressure differential map $\overline{c_{p_{net}}}$ combines the characteristics of the two previous maps. The coefficient is positive over the entire facade. The combination of a positive pressure on the external face and a negative pressure on the internal face therefore results in a compression force pushing the double-skin facade towards the facade of the building. Once again, there is a clear separation induced by the presence of the segments. Initially, we will only be interested in the internal part framed by the two segments, the external part then behaving like an acroterion. The pressure coefficient $\overline{c_{p_{net}}}$ peaks at 1.3 on the upper part of the facade and decreases with altitude to a value of 0.9. It rises rapidly at the foot of the facade to a value of 1.4.

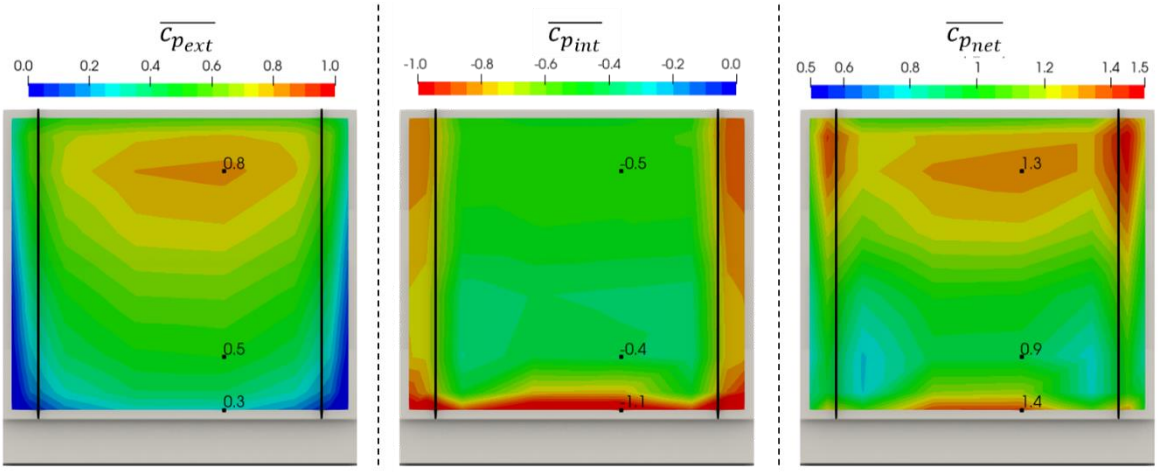

Figure 38 Pressure coefficient map on the double-skinned face, external, internal and differential (configuration h_n_l_20_p_00_s_vert)

The Figure 39 plots the flow around the facade obtained from a CFD numerical simulation. It shows the flow arriving on the facade, creating a stagnation point at the very point where the pressure is at its maximum on the outer face of the double skin. The flow then bypasses the facade via the sides and the top of the building. The flow enters the air space through the opening at the foot of the facade, and exits through the opening at the edge of the roof. The figure also shows the pressure coefficients measured on the facade of the building, at the foot of the facade and at the edge of the roof. The pressure at the opening at the foot of the facade is therefore positive, while the pressure at the opening at the top of the facade is negative. It is therefore logical to observe a flow in the air space propagating from the positive pressure towards the negative pressure.

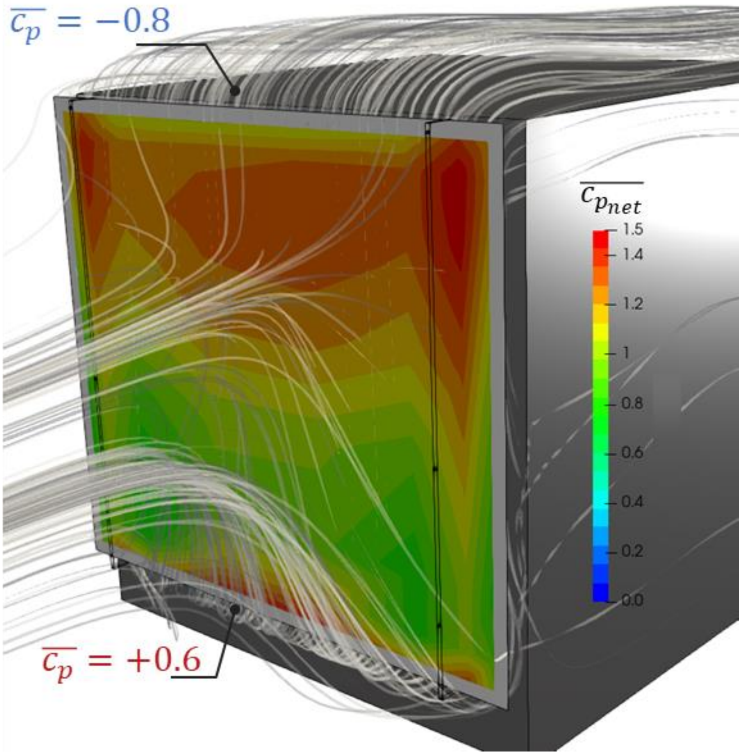

Figure 39 flow structure around the double-skin from a numerical simulation and differential load mapping $\overline{c_{p_{net}}}$ measured in a wind tunnel (configuration h_n_l_20_p_00_s_vert)

The Figure 41 plots a vertical profile of the mean pressure coefficient on the double-skin facade (noted DSF), internal $\overline{c_{p_{int}}}$ external $\overline{c_{p_{ext}}}$ and net $\overline{c_{p_{net}}}$ as well as the pressure on the building facade (BF). The figure shows that the mean pressure measured on the facade of the building is identical to that measured on the inside of the double-skinned facade, except for the measurement point at the foot of the facade. Apart from this point, the static pressure appears to be homogeneous throughout the thickness of the air space. The figure shows that the pressure profile inside the air space $\overline{c_{p_{int}}}$ equilibrates to a uniform value over the entire upper part of the facade, equal to -0.5. This value lies between the pressure values measured at the ends of the air space (+0.6 at the bottom and -0.8 at the top), but still seems closer to that measured at the top of the facade. Attempts at modelling using nodal approaches will be presented §5 will show that the value of this pressure can be obtained quite simply by considering the pressures at the ends of the air space, the head loss coefficients at the inlet and outlet of the channel, and the dynamic pressure induced by the flow in the air gap.

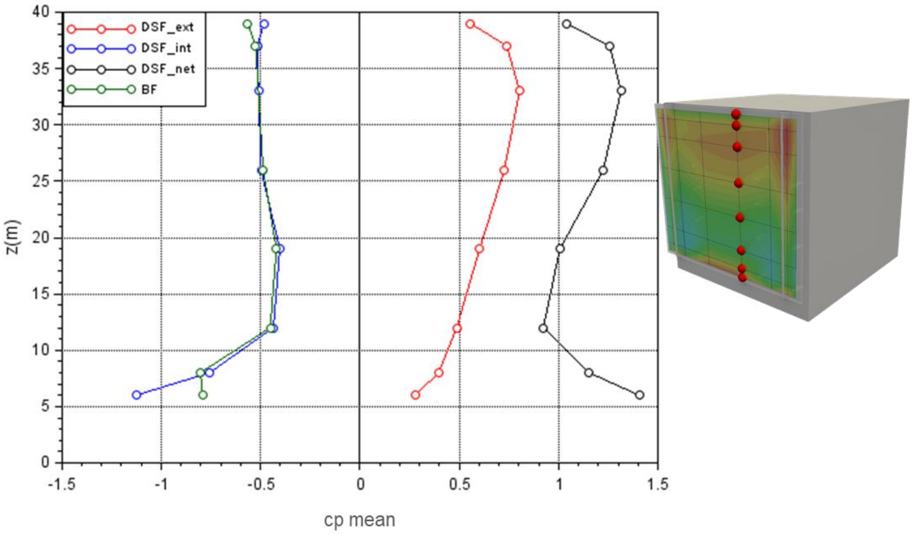

Figure 40 - profile of the average pressure coefficient on the inner, outer and net double-skin facade (DSF) and on the building facade (BF) (configuration h_n_l_20_p_00_s_vert)

The figure again shows a significant increase in the negative pressure at the foot of the air gap. To understand this phenomenon, the Figure 41 shows cross-sections of the pressure field and velocity field obtained by CFD numerical simulation. It highlights the entrenchment of the flow inside the air gap. At the entrance to the air space, as a result of the bend in the flow, the velocity is no longer uniform across the thickness of the gap, and an overspeed is created, leading to a drop in static pressure. The figure also shows that this drop in pressure is greater on the side of the double-skinned facade than on the side of the building facade (effect of detachment inside the bend). The observations from the numerical simulations and wind tunnel measurements therefore appear to be consistent with each other. The sudden change in pressure in the air gap at the foot of the facade therefore seems to be induced by the local aerodynamics of the entanglement of the flow in the air gap. This effect can also be seen in the measurements by Marques Da Siva & Gomes [3] or the simulations by Vaglio [1].

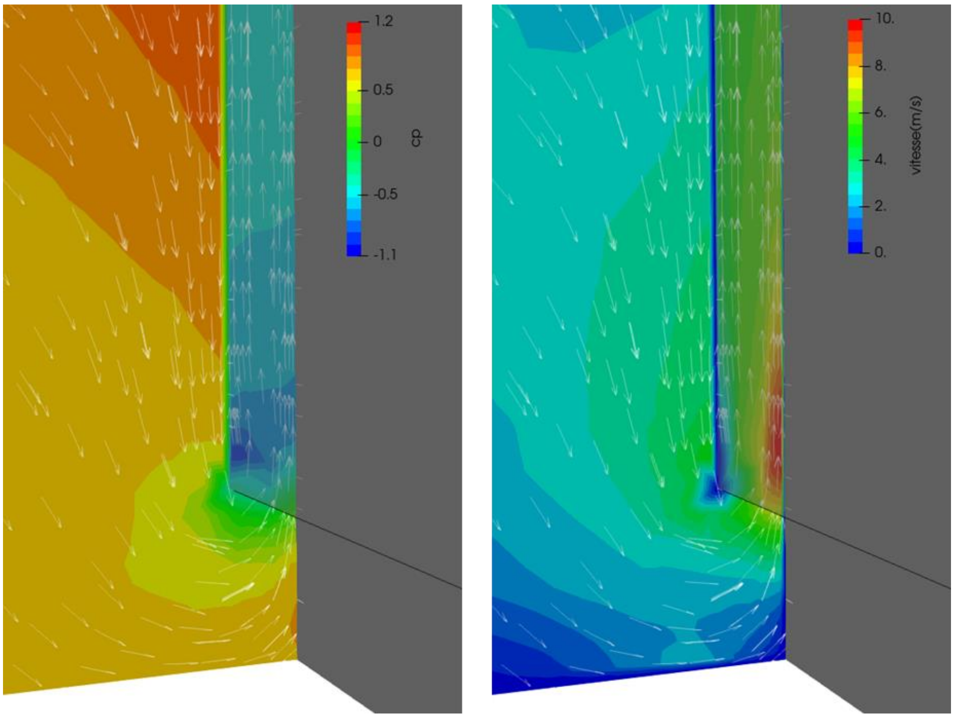

Figure 41 - cross-section of the pressure field (left) and velocity field (right) at the low inlet of the air space, obtained from a numerical simulation (configuration h_n_l_20_p_00_s_vert)

The Figure 40 shows that the evolution of the mean pressure differential $\overline{c_{p_{net}}}$ is controlled by the external pressure $\overline{c_{p_{ext}}}$ on the upper part of the facade (the internal pressure being constant), and by the internal pressure $\overline{c_{p_{int}}}$ on the lower part of the facade (the internal pressure evolving faster than the external pressure).

The Figure 42 shows the vertical profile of pressure coefficients from Figure 40 but with the addition of the peak values, minimum and maximum, of the pressure coefficients. The Figure 43 plots the PDF of the pressure signal measured at 3 points on the profile, in order to analyse the signal in more detail.

The profiles then show that the peak pressure coefficients are roughly equal to the mean pressure coefficients, indicating that the peaks are globally correlated with fluctuations in the large-scale turbulence upstream of the building.

On the outside, the peak pressure coefficients $\widehat{c_{p_{ext}}}$ are slightly higher than the mean pressure coefficients $\overline{c_{p_{ext}}}$. The associated PDFs show fairly similar dynamics over the 3 measurement points, with a distribution close to that of a Gumbel distribution.

For internal pressure, the peak pressure coefficients $\widehat{c_{p_{int}}}$ are very close to the average pressure coefficients $\overline{c_{p_{int}}}$ on the upper part of the facade. At the foot of the facade, the peak pressures are higher in absolute value than the mean pressures. The value of the peak pressure on the facade of the building is now much closer to that on the inner facade of the double skin. Turbulence therefore "stirs" the pressure inhomogeneity in the thickness of the air space. The PDFs show a much higher dynamic at the foot of the facade than in the central part of the double-skin facade. Thus, at the centre of the double-skin facade, the flow dynamics seem to be directly linked to large-scale turbulence, whereas at the foot of the facade the higher dynamics also seem to be explained by turbulence generated locally by the entanglement of the flow in the air space.

The value of the peak pressure differential $\widehat{c_{p_{net}}}$ is slightly lower than the average value $\overline{c_{p_{net}}}$ on the upper part of the facade. This can be explained by a desynchronisation of the peaks generated by the large-scale turbulence inside and outside the air space. The Figure 44 shows the temporal pressure signals inside and outside the air gap at a point taken from the centre of the facade. It shows that although the pressure fluctuations on either side of the facade are generally correlated, the peaks may not occur at exactly the same time. This decorrelation of the peaks is not due to the propagation time of the pressure information in the air gap, but to the fact that the pressures at the terminals of the air gap are not completely synchronous with each other. Consequently, the resulting pressure balance will not be completely synchronous with the pressure exerted on the outside face either.

On the other hand, the value of the peak pressure differential is higher than the average value at the foot of the facade. This is due to the entanglement of the flow in the air gap, which generates higher dynamics and peak values.

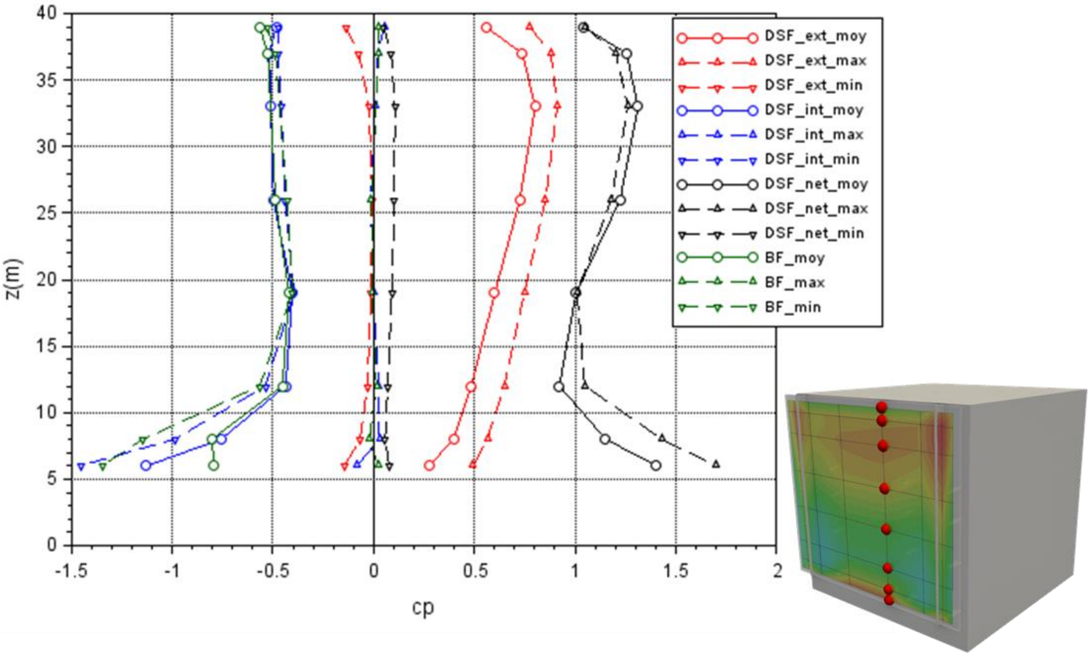

Figure 42 profile of the average and peak pressure coefficient on the internal, external and net double skin facade (DSF) and on the building facade (BF) (configuration h_n_l_20_p_00_s_vert)

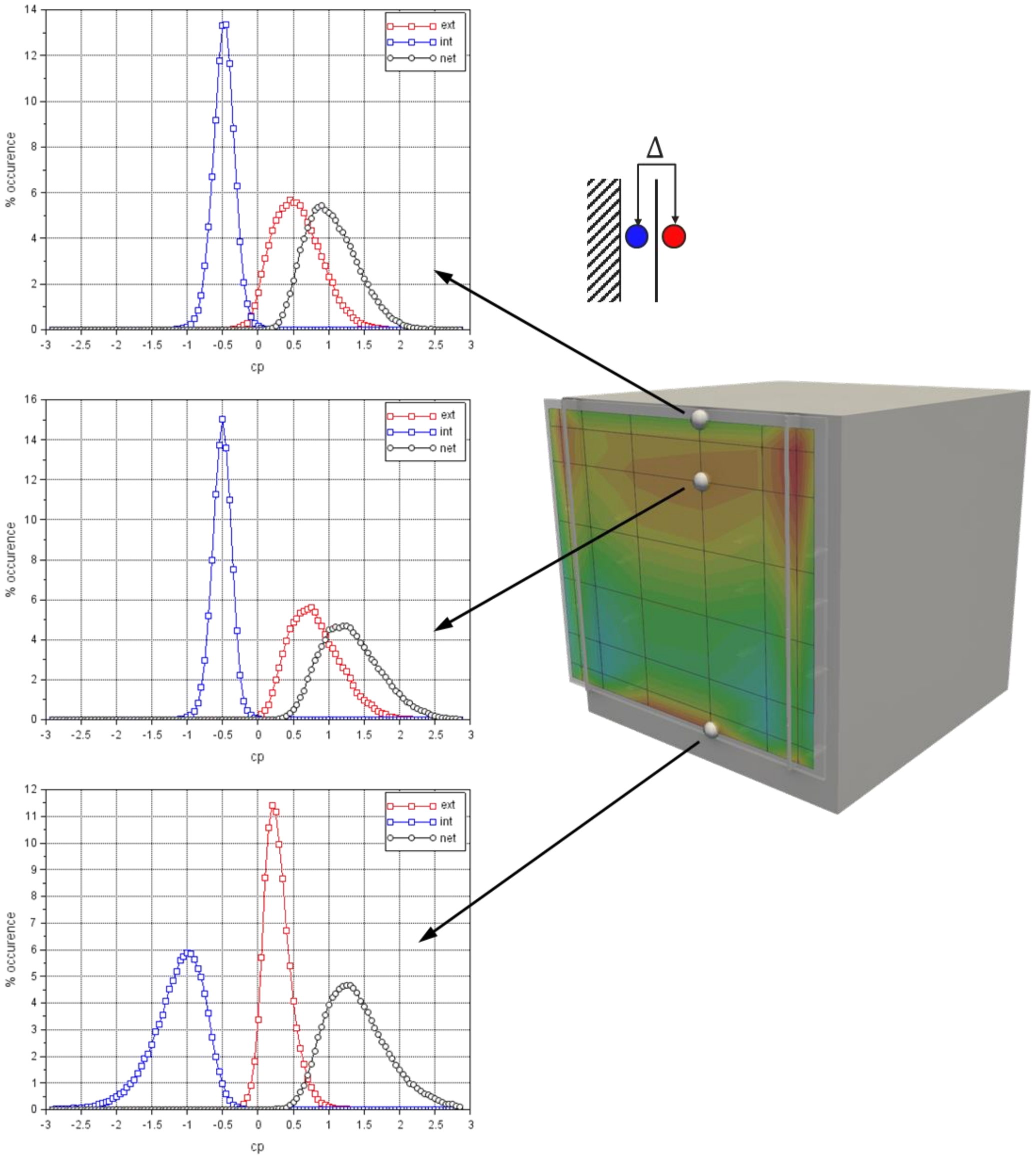

Figure 43 - PDF of the pressure coefficient, interior, exterior and net, at three points of the double-skin facade (configuration h_n_l_20_p_00_s_vert)

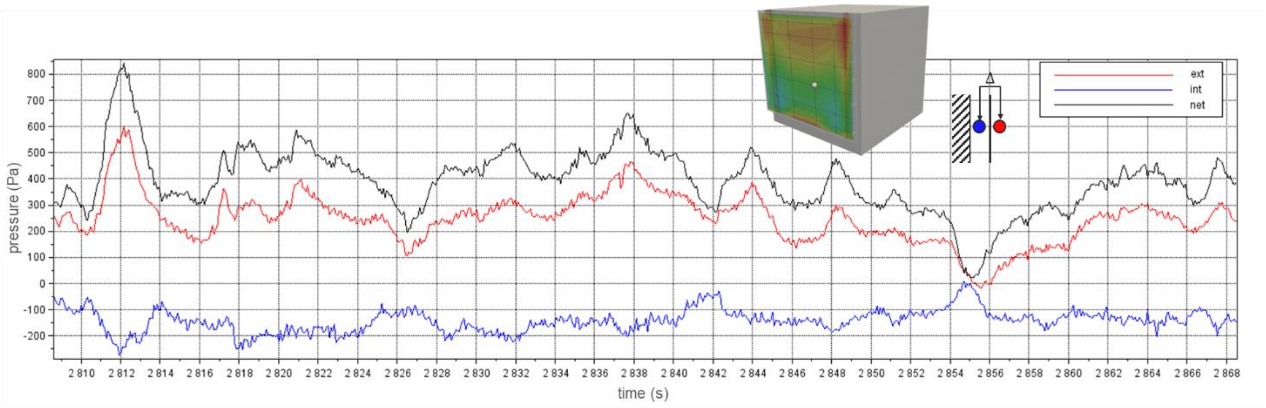

Figure 44 - extract of time signals for pressure, interior, exterior and net, at one point on the double-skin facade (configuration h_n_l_20_p_00_s_vert)

To sum up, for this first configuration studied, the analysis shows that the pressure in the air space is mainly controlled by a balancing of the pressure at the boundaries of the double-skin facade, resulting in a negative pressure, homogeneous in thickness and over most of the facade. It leads back to the rather counter-intuitive configuration; described in the literature, of an air space depressurised by a "chimney effect" when the facade of the building is facing into the wind.

The outer face of the double skin is then in compression, while the inner face is simultaneously in negative pressure. The contributions add up, and the net differential leads to a higher compression than that which would be applied to a single facade.

The pressure difference across the double-skin also generates a flow in the air gap, which, through an overspeed effect at the entry point, generates an even higher negative pressure, leading to a significantly higher stress at the foot of the facade.

4.1.2 Effect of building height

We now propose to study the influence of a first geometric parameter, which in this case is the height of the building. This is increased by 5m Real Scale. The upper end of the double-skin now stops below the edge of the roof. The Figure 45 plots the average pressure coefficients measured on the outer face $\overline{c_{p_{ext}}}$inner face $\overline{c_{p_{int}}}$ as well as the average pressure differential noted $\overline{c_{p_{net}}}$.

On the outside, the mapping of the pressure coefficient $\overline{c_{p_{ext}}}$ is very similar to that obtained with the previous geometric configuration. The pressure coefficient at the stagnation point is slightly higher. As the building is higher, the upstream wind gradient will induce a higher dynamic pressure on the windward side. By keeping a reference dynamic pressure at 40m high to establish the pressure coefficient, it is therefore normal to find a slightly higher pressure coefficient with a 45m high building.

On the inside of the air space, the mapping of the pressure coefficient $c_{p_{int}}$ is completely different from that observed in the previous configuration. Between the two segmentations, the pressure field is homogeneous over almost the entire facade and equilibrates at a pressure that is now positive. The behaviour is therefore the opposite of that observed in the previous geometric configuration. The Figure 46 plots the structure of the flow around the double-skinned facade in this configuration, and presents the pressure coefficients measured on the facade of the building, at the boundaries of the air gap. In contrast to the previous case, the upper end of the air gap is now at overpressure. The pressure coefficient is slightly higher than that measured at the foot of the facade. We can therefore expect a flow to be established in the air space, but this time from top to bottom. Given the lower pressure difference across the air gap, the flow rate of this flow will also be lower than in the previous configuration.

The mapping of the mean pressure differential $\overline{c_{p_{net}}}$ is also very different from the previous geometric configuration. This time the average net pressure coefficient, although remaining positive, is much lower, and even cancels out in the middle of the facade. The pressure therefore balances out on average on either side of the facade, leading to a zero mean load, which at first glance might seem rather counter-intuitive for a facade positioned facing into the wind.

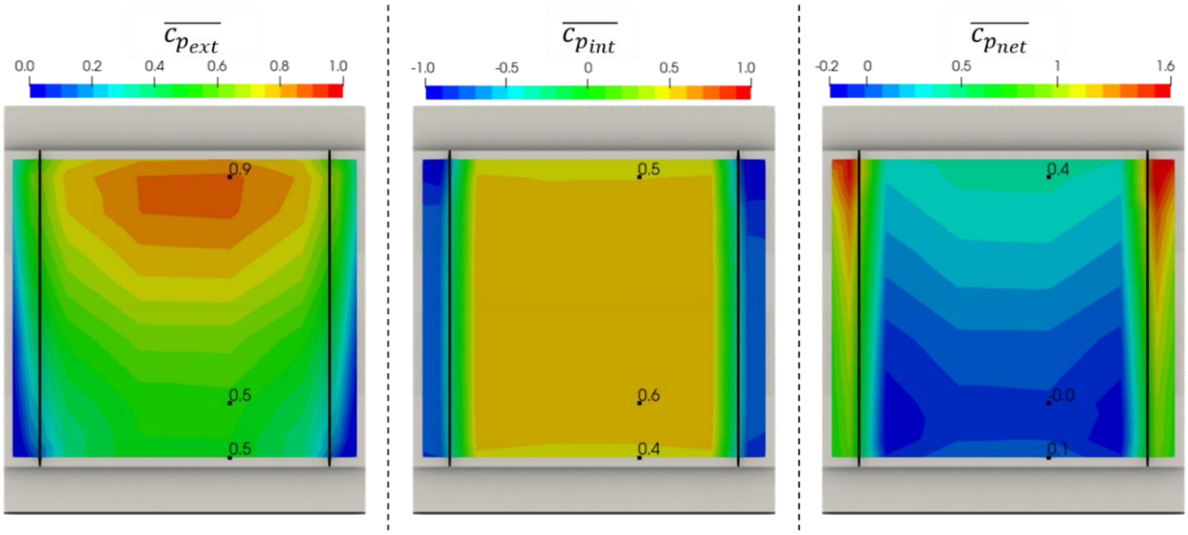

Figure 45 - Pressure coefficient map on the double-skinned face, external, internal and differential (configuration h_h_l_20_p_00_s_vert)

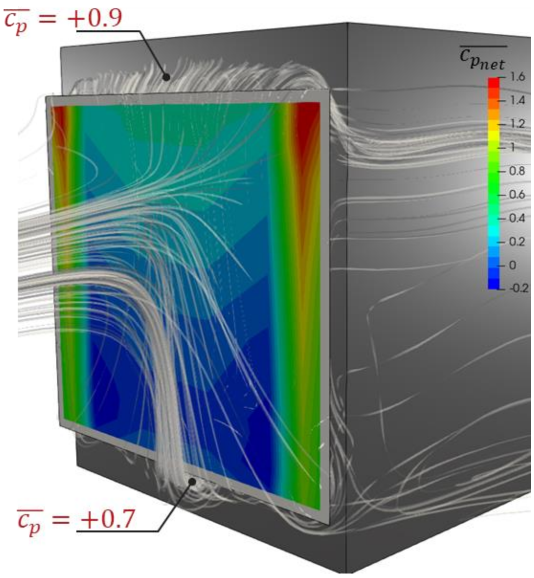

Figure 46 - flow structure around the double skin from a numerical simulation and differential load mapping $\overline{c_{p_{net}}}$ measured in the wind tunnel (configuration h_h_l_20_p_00_s_vert)

The Figure 41 plots a vertical profile of the average pressure coefficient on the double-skin facade (noted DSF), internal, external and net, as well as the pressure on the building facade (noted BF).

The figure again shows that the pressure coefficient on the facade of the building is identical to that on the inside of the double skin. The pressure in the air space $\overline{c_{p_{int}}}$ balances out at the centre of the blade at a value of 0.55. It is therefore lower than the values measured at the ends of the air space. Attempts at modelling using the nodal approach §5 will again show that this value can be obtained by taking into account the pressures at the boundaries of the air space, the pressure losses associated with the engulfment and discharge of the flow, as well as the dynamic pressure induced by the flow in the air gap. The latter partly explains why the static pressure in the air knife is lower than the static pressures at the air gap's boundaries. Note the lower pressures at the ends of the air space, which are certainly again induced by acceleration effects when the flow in the air space becomes entangled/receded.

The pressure profile on the outside of the double skin facade $\overline{c_{p_{ext}}}$ is again driven by the upstream pressure gradient, and is very similar to that measured for the previous geometric configuration.

The profile of the average pressure differential $\overline{c_{p_{net}}}$ is mainly driven by the upstream pressure. The figure shows that part of the double-skin facade even passes under negative pressure, which may seem even more counter-intuitive for a double-skin facade mounted facing into the wind.

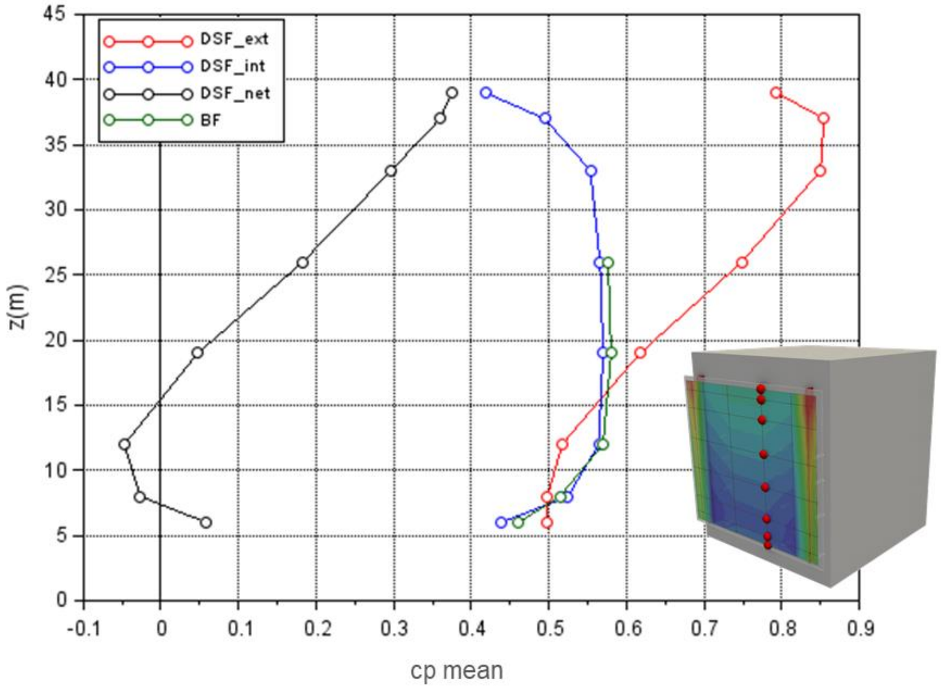

Figure 47 - profile of the average pressure coefficient on the inner, outer and net double-skin facade (DSF) and on the building facade (BF) (configuration h_h_l_20_p_00_s_vert)

The Figure 48 repeats the plot of the vertical profile of the pressure coefficients, but with the addition of the values of the peak coefficients, minimum and maximum. For ease of reading, the measurements on the facade of the building are not presented, but are again identical to those measured on the inside of the double-skin facade. The Figure 50 plots in parallel the PDF of the pressure signal measured at 3 points of the profile in order to analyse the dynamics of the signal. As in the previous configuration, the external peak pressure coefficient $\widehat{c_{p_{ext}}}$ is greater than the mean pressure coefficient $\overline{c_{p_{ext}}}$. Unlike the previous geometric configuration, the internal peak pressure coefficients $\widehat{c_{p_{int}}}$ are also greater than the average coefficient $\overline{c_{p_{int}}}$. Plotting the PDFs at the centre of the facade shows that the pressure distributions on the external and internal faces are extremely close. However, the distribution of the pressure differential is not zero, and takes the form of a Gaussian centred around a zero value. So even though the dynamics of the pressure signals appear identical on both sides of the facade, the fact that they are not necessarily synchronised with each other can lead to non-zero instantaneous pressure differentials. The Figure 49 shows an extract of the temporal pressure signals at the centre of the facade. The figure shows that the slight shift, in value and time, of the pressure fluctuations on either side of the double-skin leads to non-negligible pressure differential values. Once again, this decorrelation of the peaks is not due to the propagation time of the pressure information in the air gap, but to the fact that the pressures at the terminals of the air gap are not completely synchronous with each other.

The plot of the peak pressure differential $\widehat{c_{p_{net}}}$ shows values much higher than the mean value $\overline{c_{p_{net}}}$, both for minimum and maximum values. This means that even if the average force is low, the peak value will not be negligible, and will alternate between compression and pull-out forces.

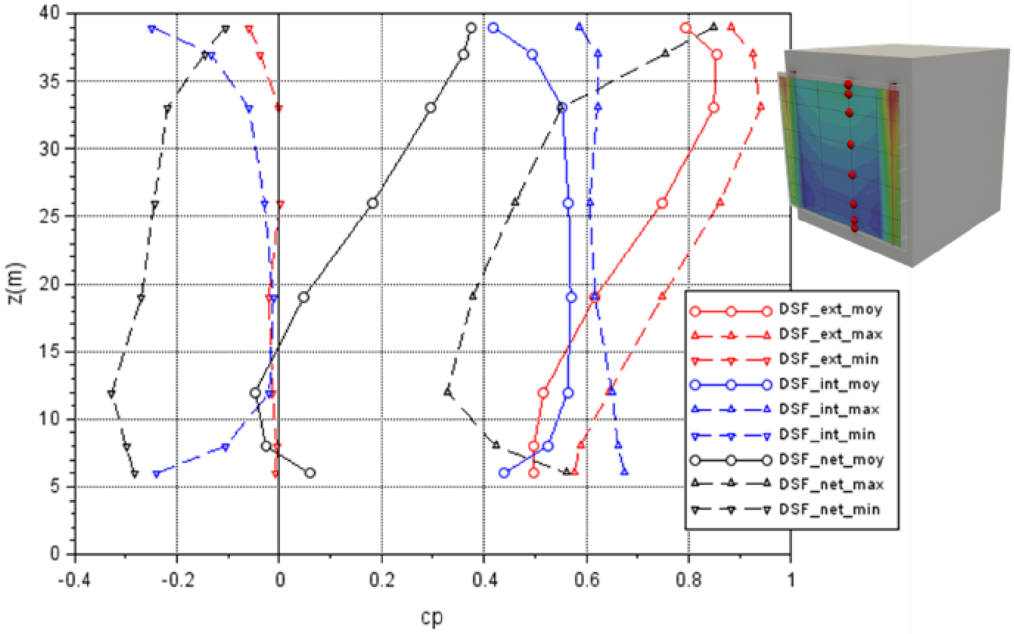

Figure 48 - profile of the average and peak pressure coefficient on the internal, external and net double skin facade (configuration h_h_l_20_p_00_s_vert)

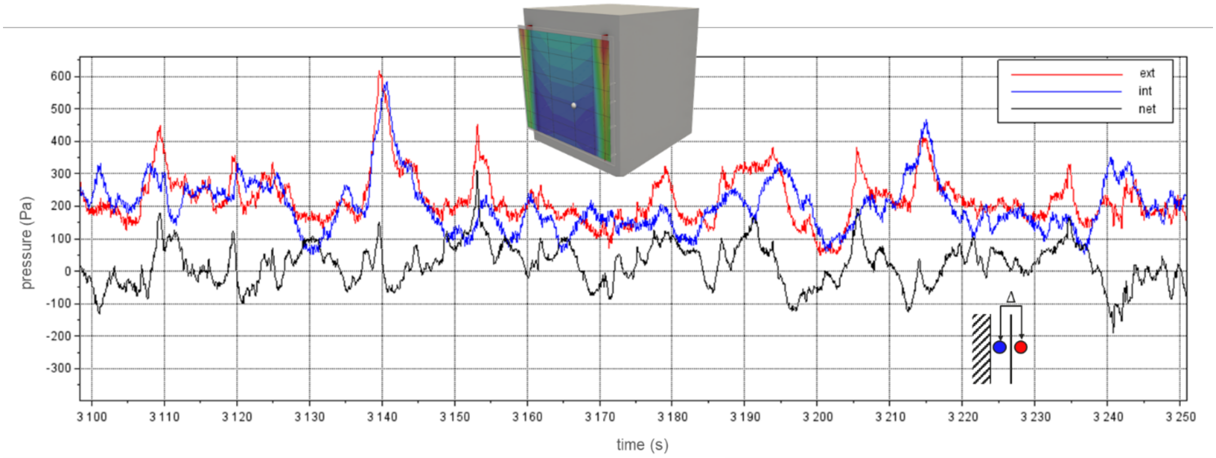

Figure 49 - extract of the time signals for pressure, internal, external and net, at a point on the double-skin facade (configuration h_h_l_20_p_00_s_vert)

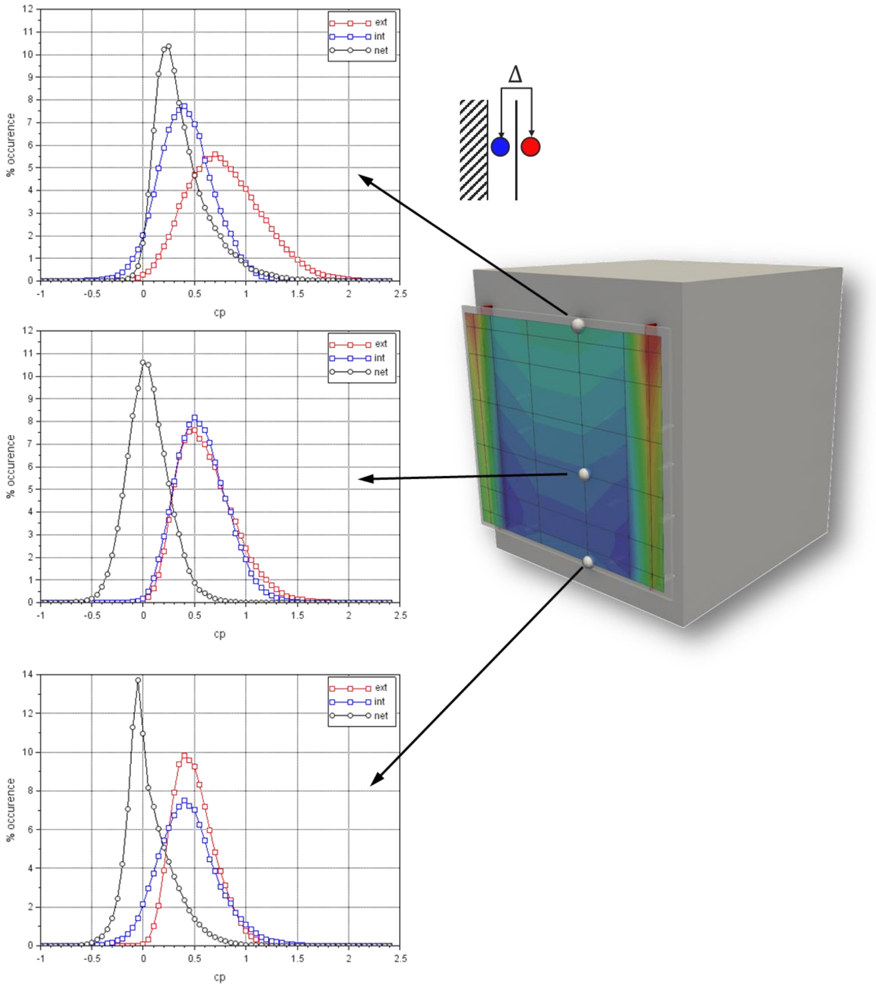

Figure 50 - PDF of the pressure coefficient, internal, external and net, at three points on the double-skin facade (configuration h_h_l_20_p_00_s_vert)

The analysis shows that simply changing a geometric parameter, in this case shifting the end of the double-skin 5m below the edge of the building, radically changes the pressure balance of the air gap, and ultimately the wind loads applied to the double-skin facade. The analysis also shows the importance of taking into account the dynamics of the turbulence of the Atmospheric Boundary Layer, which can lead to peak loads that are very different from the average loads.

We now propose to study the opposite geometric configuration, i.e. reducing the height of the building by 5m. The Figure 51 plots the average pressure coefficients measured on the outer face $\overline{c_{p_{ext}}}$inner face $\overline{c_{p_{int}}}$ as well as the average pressure differential noted $\overline{c_{p_{net}}}$. This time, the plot is quite similar to that of the reference configuration, where the roof edge was level with the upper end of the double-skin facade. On the external face, the pressure coefficient is identical to the reference configuration. On the internal face, the pressure coefficient also shows a similar evolution, but with slightly lower pressures than in the reference case. The result is a slightly higher differential pressure coefficient.

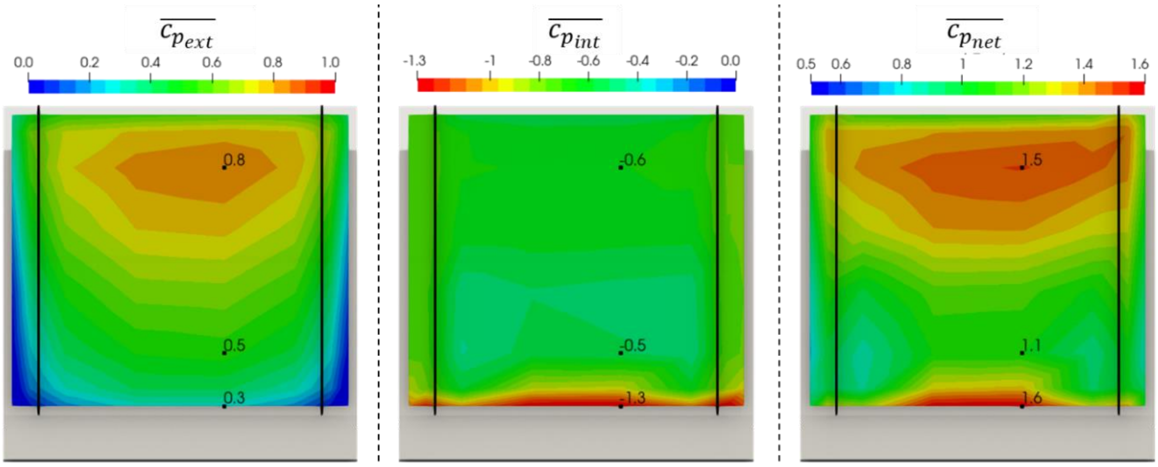

Figure 51 - Pressure coefficient map on the double-skinned face, external, internal and differential (configuration h_b_l_20_p_00_s_vert)

The Figure 52 plots a vertical profile of the average pressure coefficient on the double-skin facade, internal, external and net, comparing the values obtained with a low or level roof. It again shows a superimposition of the external pressure coefficients $\overline{c_{p_{ext}}}$. If, at the very top of the double-skin facade, the internal pressure coefficient $\overline{c_{p_{int}}}$ is identical for both configurations, the rest of the profile shows lower pressure (-0.2) for the low building. These lower pressures can be explained by the emergent part of the double-skin, which generates a wake downstream. This wake will reduce the pressure over the entire exposed part of the internal face, a reduction which is then propagated throughout the air space. The profile of the mean pressure differential $\overline{c_{p_{net}}}$ logically shows an identical shift of +0.2, increasing the wind loads on the facade.

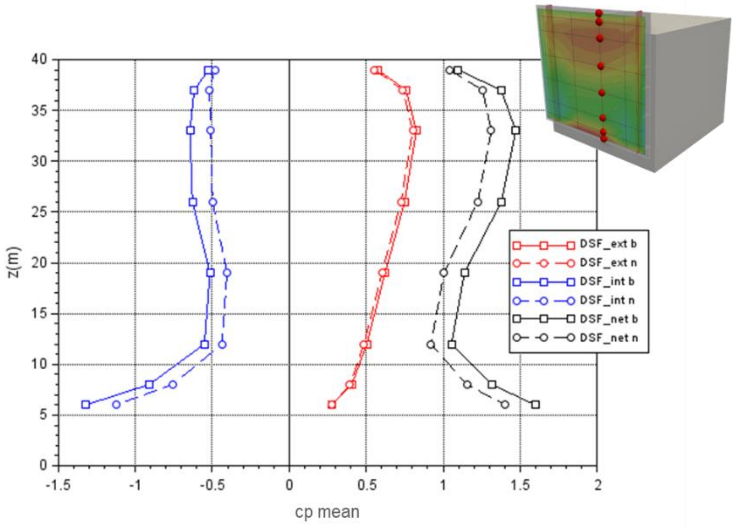

Figure 52 - profile of the mean pressure coefficient on the internal, external and net double-skin facade (DSF), comparison of low building (b) and level (n) (configuration h_b_l_20_p_00_s_vert and h_n_l_20_p_00_s_vert)

The Figure 53 plots the vertical profile of the peak coefficients, minimum and maximum, for the configuration with a low building. A behaviour quite similar to the reference configuration can be observed. It should be noted, however, that the peak values of the pressure in the air space $\widehat{c_{p_{int}}}$ are lower in absolute value than the mean value, whereas in the reference configuration, the two values were equal.

This can be explained by the presence of the wake of the emerging part of the double skin, which by its own dynamics will influence the pressure balance, and thus contribute to a certain decorrelation of the peak effects inside the air gap. This decorrelation effect of the internal pressures is then added to that of the external pressures, and leads to a higher decorrelation of the peak coefficient of the pressure differential $\widehat{c_{p_{net}}}$ than that observed for the reference configuration.

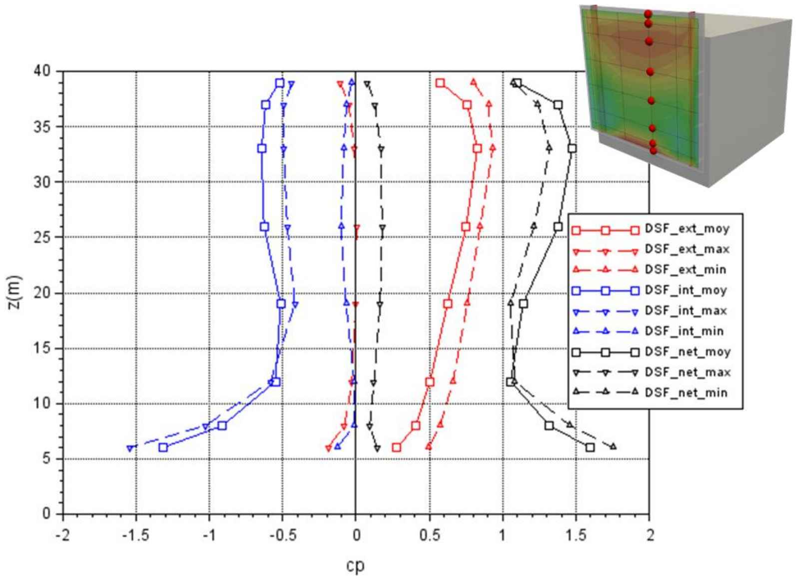

Figure 53 - profile of the mean and peak pressure coefficient on the internal, external and net double skin facade (configuration h_b_l_20_p_00_s_vert)

Although this geometric variation has a less spectacular impact on the pressure balance of the air space than an increase in the height of the building, it once again demonstrates a certain sensitivity to the dynamics of pressure balance.

4.2 OPEN SKIN ON ALL 4 SIDES

The analysis now focuses on a more complex configuration, aeraulically speaking, as it exposes all 4 sides of the air gap to the open air, without any overlap.

4.2.1 Reference case

We return to the reference case of the previous paragraph, i.e. with a 40m high building. The double-skin is flush with the edge of the roof, but also with the side edges of the building. Only the lower end remains 5m above the ground. The Figure 54 plots the mean pressure coefficients measured on the outer face $\overline{c_{p_{ext}}}$inner face $\overline{c_{p_{int}}}$ as well as the mean pressure differential noted $\overline{c_{p_{net}}}$.

On the outside of the double-skin facade, the pressure coefficient is mapped in a very similar way to that obtained with the vertical segments. $\overline{c_{p_{ext}}}$ is quite similar to that obtained with the presence of the vertical segments.

On the inside of the double-skin facade, the mean pressure coefficient $\overline{c_{p_{int}}}$ is once again almost homogeneous across the entire facade. The pressure coefficient is negative and of the order of -0.7, compared with -0.5 with the presence of the vertical segments. The Figure 55 plots the structure of the flow around the double-skin facade in this configuration and presents the pressure coefficients measured on the facade of the building, at the ends of the air gap. The ends of the air gap are in negative pressure on 3 out of the 4 edges of the double-skin facade, with a pressure coefficient of -0.7 on the sides, and -0.8 on the upper part. The pressure coefficient at the foot of the facade remains equal to +0.7. A flow will therefore be established by penetrating through the lower edge of the air space, and extracting through the

3 other edges. Compared to the configuration with vertical segments, this has two consequences:

-a preponderance of negative pressure surfaces compared to positive pressure surfaces at the boundaries of the air gap. This explains why the pressure is balanced at a lower value at the centre of the air space.

-a higher flow rate through the air gap, due to a greater pressure differential.

This explains the pressure coefficient of -1.7 at the foot of the facade, compared with -1.4 in the configuration with vertical segmentation. The higher flow rate therefore generates greater acceleration and lower static pressures.

The mapping of the average coefficient of pressure differential $\overline{c_{p_{net}}}$ shows that the facade is in compression overall, with an average value of +1.5 at the centre of the facade. At the foot of the facade, the value of the coefficient rises locally to +2.

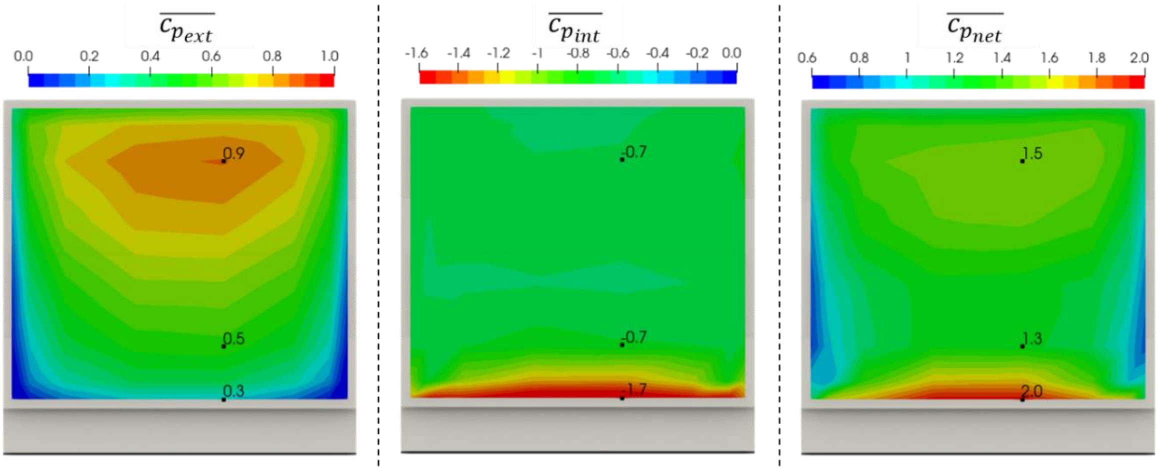

Figure 54 - Pressure coefficient map on the double-skinned face, external, internal and differential (h_n_l_20_p_00_s_n configuration)

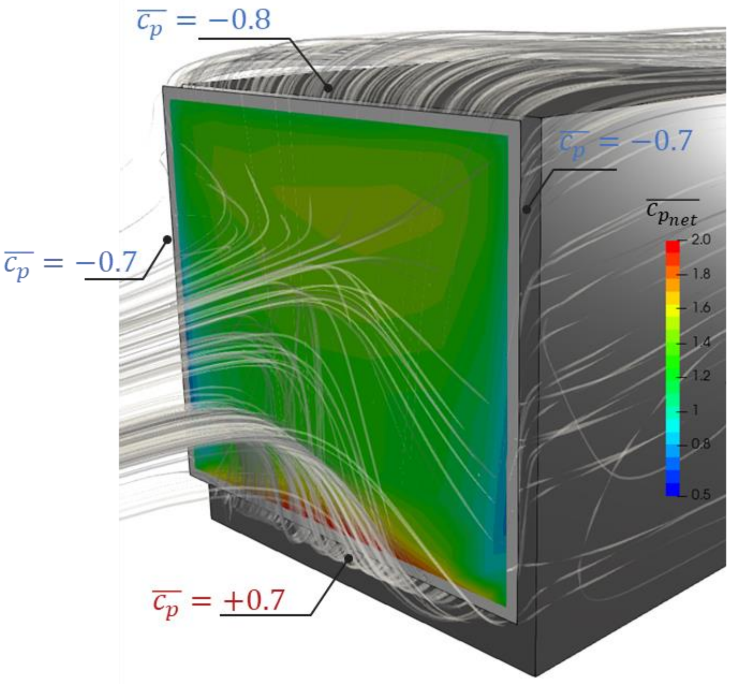

Figure 55 - flow structure around the double skin from a numerical simulation and differential load mapping $\overline{c_{p_{net}}}$ measured in a wind tunnel (configuration h_n_l_20_p_00_s_n)

The Figure 56 plots a vertical profile of the mean pressure coefficient on the double-skin facade, internal, external and net, comparing the values obtained in this configuration with those obtained with vertical segmentation. Once again, the profile shows that the pressure coefficient on the external face of the double skin $\overline{c_{p_{ext}}}$ is identical in both configurations. The figure also shows that the pressure in the air gap $\overline{c_{p_{int}}}$ is again lower than in the configuration with vertical segmentation. The internal pressure profile $\overline{c_{p_{int}}}$ is similar in both configurations, but with a more pronounced shift at the foot of the facade, probably due to a higher air flow entering the air space, reinforcing the drop in static pressure caused by acceleration effects.

The profile of the mean pressure differential $\overline{c_{p_{net}}}$ profile is also quite similar to that of the configuration with vertical segmentation, but with a more marked increase in loads at the foot of the facade, due to the reduction in pressure inside the air space.

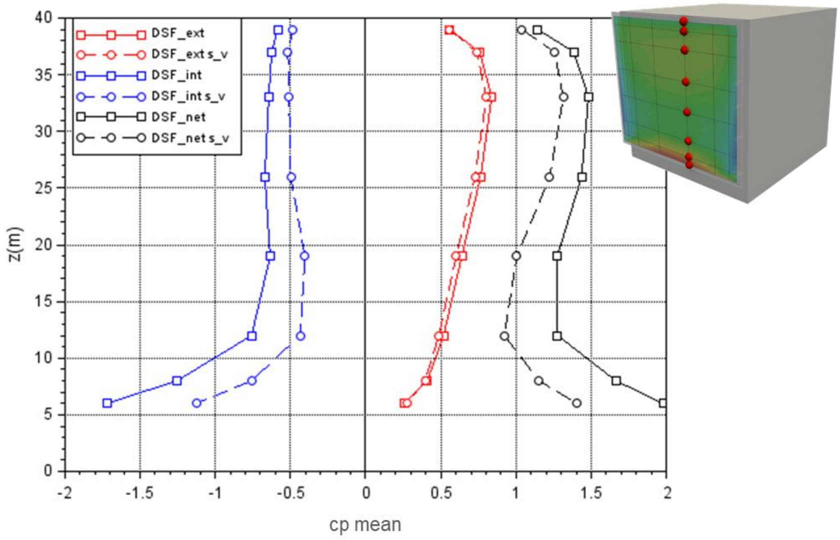

**Figure 56 - profile of the mean pressure coefficient on the inner, outer and net double-skin facade (DSF), comparison with and without vertical segmentation (s_v)
(configuration h_n_l_20_p_00_s_n and h_n_l_20_p_00_s_vert)**

The Figure 57 plots the vertical profile of the peak coefficients, minimum and maximum, for the configuration without segmentation. A behaviour quite similar to the configuration with vertical segmentation can be observed. It should be noted, however, that the peak values of the pressure in the air gap $\widehat{c_{p_{int}}}$ are lower in absolute value than the mean value, whereas in the configuration with vertical segmentation, the two values were equal. This can be explained by a reinforcement of the decorrelation of the peaks inside the air gap, due to the fact that it is open on all 4 sides.

This effect of decorrelation of the peaks inside the air gap has a direct impact on the peak value of the pressure differential $\widehat{c_{p_{net}}}$ which is lower than the mean value. This decorrelation of the peak coefficient is even more marked than for the configuration with vertical segmentation.

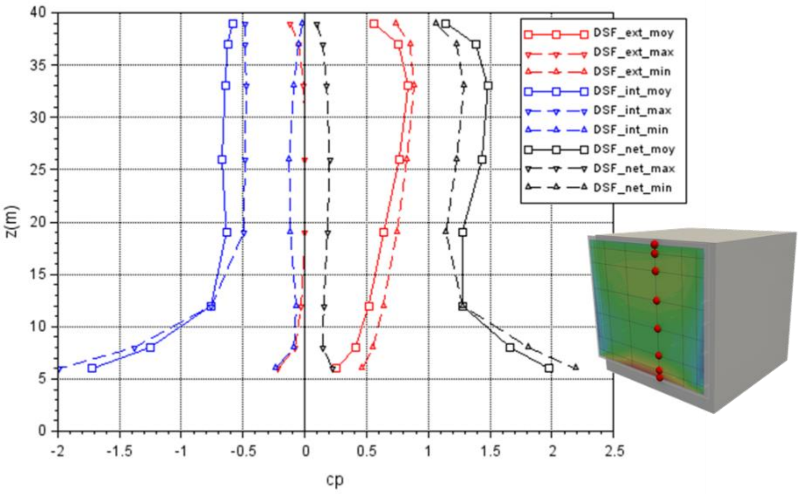

Figure 57 - profile of the mean and peak pressure coefficient on the internal, external and net double skin facade (configuration h_n_l_20_p_00_s_n)

The absence of vertical segmentations therefore has a fairly limited impact on the evolution of wind loads on the double-skin facade, although we can once again observe an interesting impact on the dynamics of wind loads.

4.2.2 Effect of wind direction

So far, the analysis has focused on a wind direction of 0°, i.e. a wind direction perpendicular to the double-skin facade, putting the outer face of the double-skin in compression. As the wind can arrive in any direction, the analysis now proposes to study the effect of the wind direction on the pressure balance of the air space. This analysis is carried out with the previous geometric configuration, i.e. no segmentation and a level building.

The Figure 58 plots the mean pressure coefficients measured on the outer face $\overline{c_{p_{ext}}}$internal $\overline{c_{p_{int}}}$ as well as the mean pressure differential noted $\overline{c_{p_{net}}}$ for 8 different wind directions, from 0° to 180°.

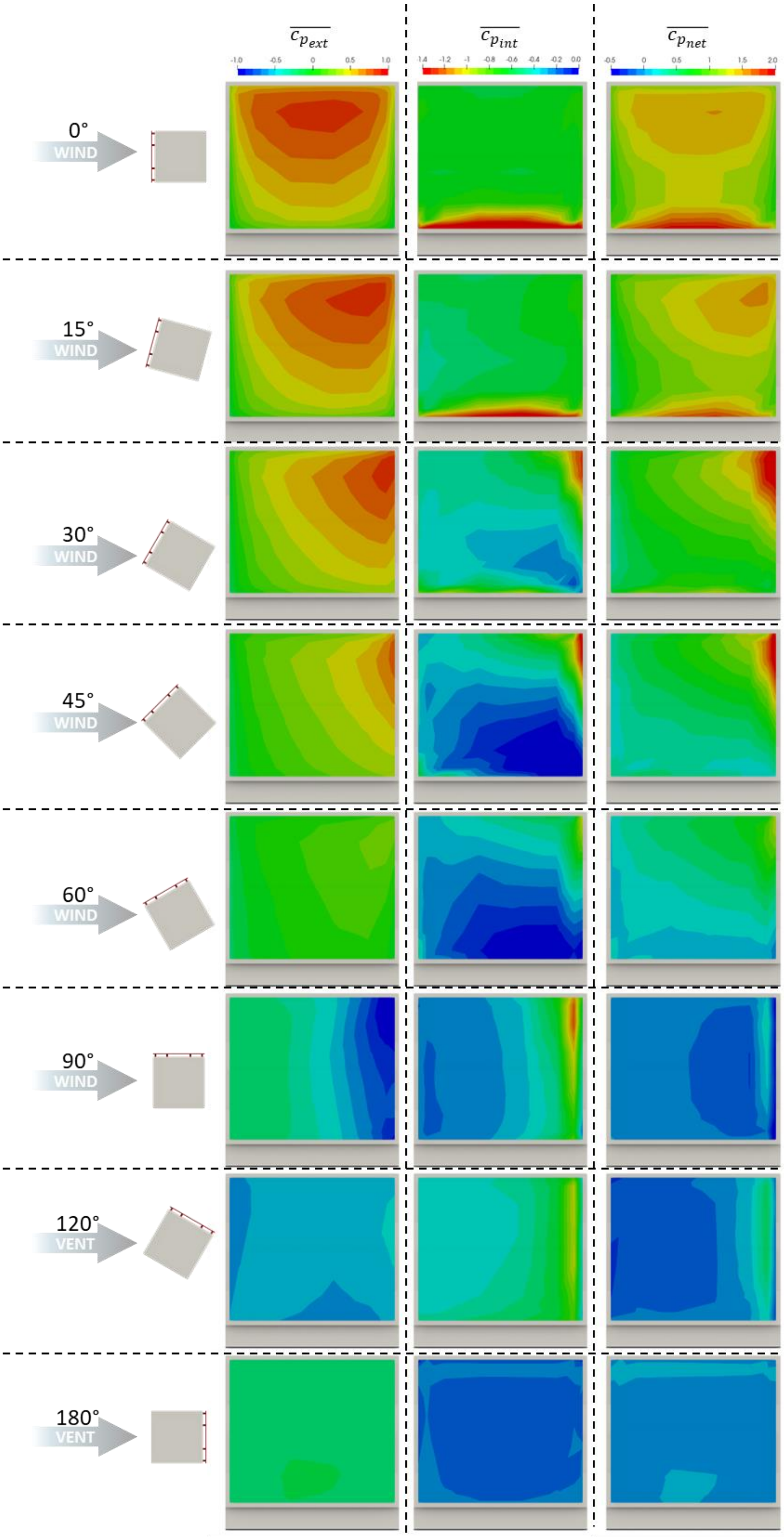

Figure 58 - Mean pressure coefficients for different wind directions (configuration h_n_l_20_p_00_s_n)

The 0° and 15° wind directions show similar wind loads, with a slight shift in the stagnation point on the exterior facade for the 15° direction. This offset is reflected in the net pressure differentials $\overline{c_{p_{net}}}$.

The 30° and 45° wind directions are fairly similar to each other, and show a break with the first two. On the outside, the pressure field $\overline{c_{p_{ext}}}$ shows a more pronounced shift from the stagnation point towards the windward edge of the facade. Inside the air gap, the pressure field $\overline{c_{p_{int}}}$ becomes more inhomogeneous. The Figure 59 compares the structure of the flow around the double-skin facade for a direction of 0° and 30°, and presents the pressure coefficients measured on the facade of the building, at the boundaries of the air gap.

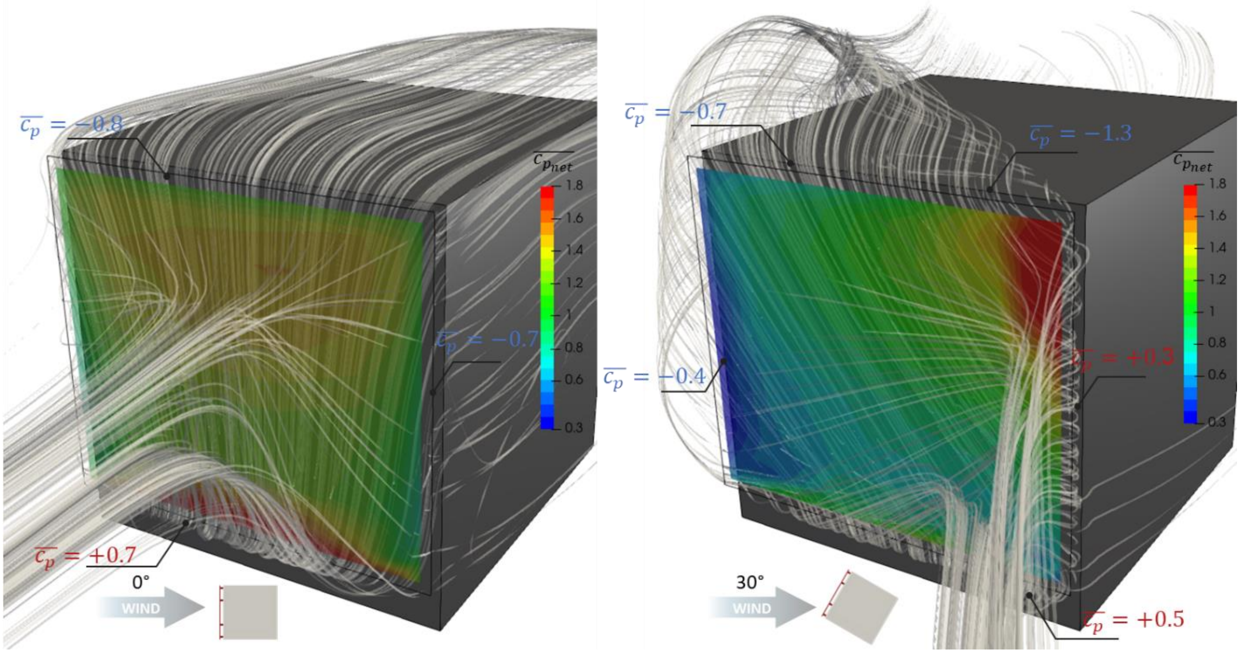

Figure 59 flow structure around the double skin from a numerical simulation and differential load mapping $\overline{c_{p_{net}}}$ measured in a wind tunnel, for wind directions of 0° and 30° (configuration h_n_l_20_p_00_s_n). (configuration h_n_l_20_p_00_s_n)

For a 30° wind direction, the side of the building facing into the wind has a positive pressure coefficient, while at the same time, the negative pressure on the windward side of the roof increases. A flow will then be established in the air gap between this high-pressure zone and this low-pressure zone. The acceleration of the flow as it rushes into the air space explains the very low pressure zone observed on the windward side of the internal face. The pressure at the foot of the facade remains positive, while at the same time there is a negative pressure on the leeward side. A flow can then also be established between these two openings, although the flow rate will be lower, due to a smaller pressure differential. The entrapment of the flow at the foot of the facade therefore also explains the persistence of a low pressure zone in the air space at the foot of the facade. The flow in the air gap will therefore be structured in two parts: a first flow with high dynamics, between the lateral windward opening and the roof, and a second less dynamic flow, between the foot of the facade and the lateral leeward opening. Between these two flows there is a much less dynamic zone. This results in a zone where the negative pressures are significantly less marked in the air space at the centre of the facade.

This structuring of the flow in the air space is reflected in the pressure differential $\overline{c_{p_{net}}}$ where a zone of high compression is found at the windward lateral opening, which is a combination of the high negative pressure inside the air gap and the stagnation point on the external face. At the foot of the facade, the pressure differential is lower due to the lower pressure on the external face, and the much lower entrapment of the flow in the air gap.

For a direction of 60°, the structure of the pressure field changes again with a much lower pressure on the outer face of the double skin $\overline{c_{p_{ext}}}$. In the air space, there is a windward zone with a pressure coefficient $\overline{c_{p_{int}}}$ of the order of -1. This corresponds to a residual flow established between the lateral windward opening and the opening at the top of the facade. In this zone, the pressure differential coefficient $\overline{c_{p_{net}}}$ is of the order of 1, and remains much lower on the rest of the facade.

With a 90° direction, the wind flow is parallel to the double-skin facade and will therefore generate less stress on the facade. However, on the windward side, bypassing the building will lower the pressure on both the outer and inner faces of the cladding. As the negative pressure is not the same on both sides of the double skin, the result is a pressure differential that changes sign rapidly as it moves away from the windward edge. However, the value of this differential remains fairly low. A similar behaviour can be observed for an angle of 120°.

For a direction of 180°, the facade is completely immersed in the wake of the building. The inner and outer faces of the double-skin facade are then both in negative pressure, with a comparable pressure coefficient of around -0.2, resulting in a pressure differential of almost zero.

Analysis of the mean pressure fields showed that the highest double-skin loads occurred for wind directions between 0° and 45°. However, previous analyses have shown that unsteadiness effects can lead to non-negligible peak pressure differentials $\widehat{c_{p_{net}}}$ pressure differentials, even when the mean differential $\overline{c_{p_{net}}}$ was low. In this sense the Figure 60 and the Figure 61 respectively show the maximum (corresponding to peak compression) and minimum (corresponding to peak tearing) peak pressure coefficients of the pressure differential recorded for each wind direction.

Analysis of the figures shows that the conclusions drawn for peak pressure fields appear to be the same as those drawn for mean pressure fields. For peak compressions, the double-skin is more particularly stressed for wind directions from 0° to 45°. For a wind direction of 60°, the peak compression on the upper corner of the facade is more pronounced than the mean pressure coefficient would suggest. The highest peak pull-outs were obtained for wind directions of 60°, 120° and, more particularly, 90°, where the two faces of the double-skin were in negative pressure, but with quite different dynamics. Finally, it should be noted that for a direction of 180°, the values of the peak pressure coefficient remain very low.

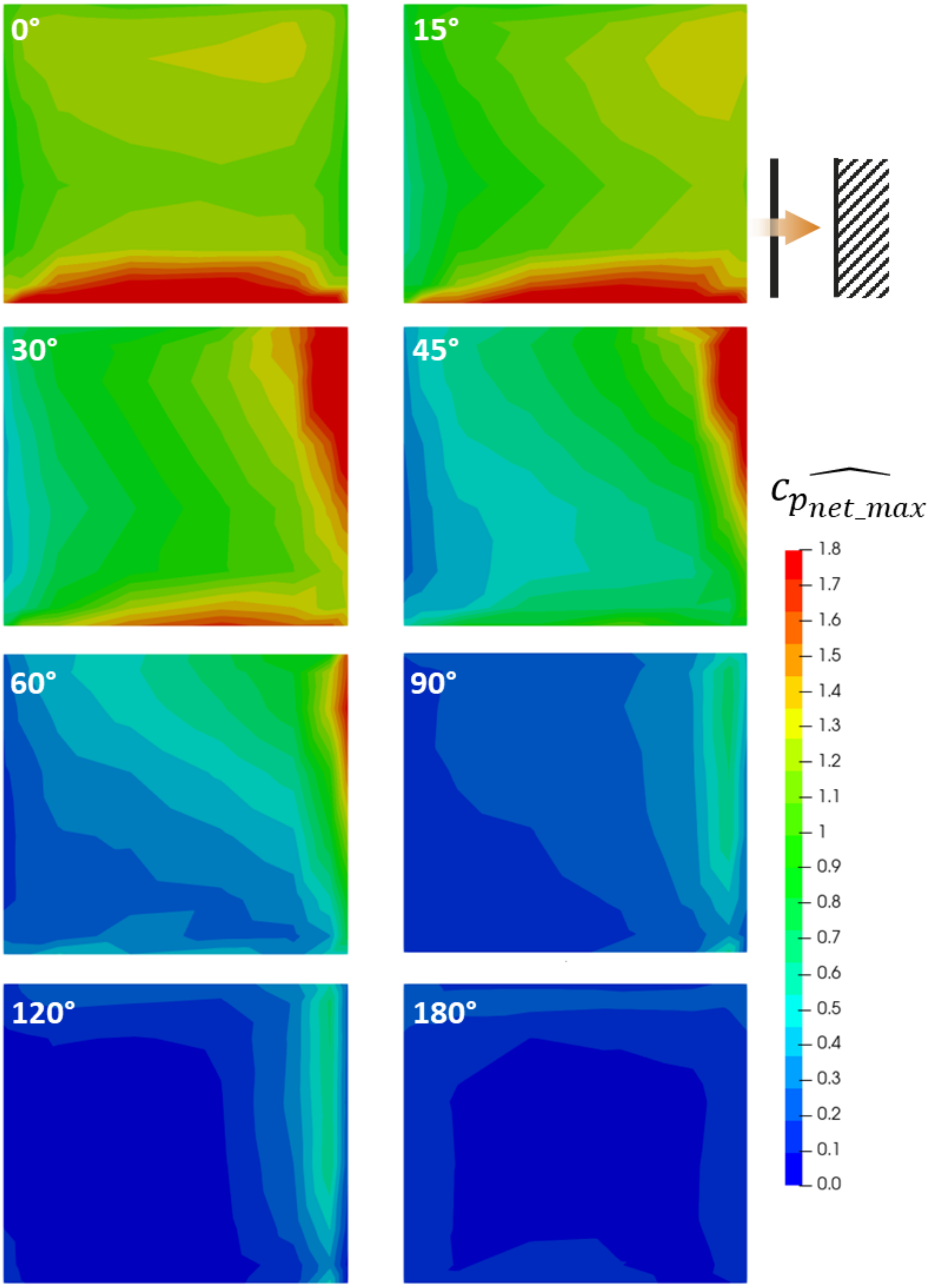

Figure 60 - Maximum peak pressure differential coefficient mapping (peak compressions) for each wind direction (configuration h_n_l_20_p_00_s_n)

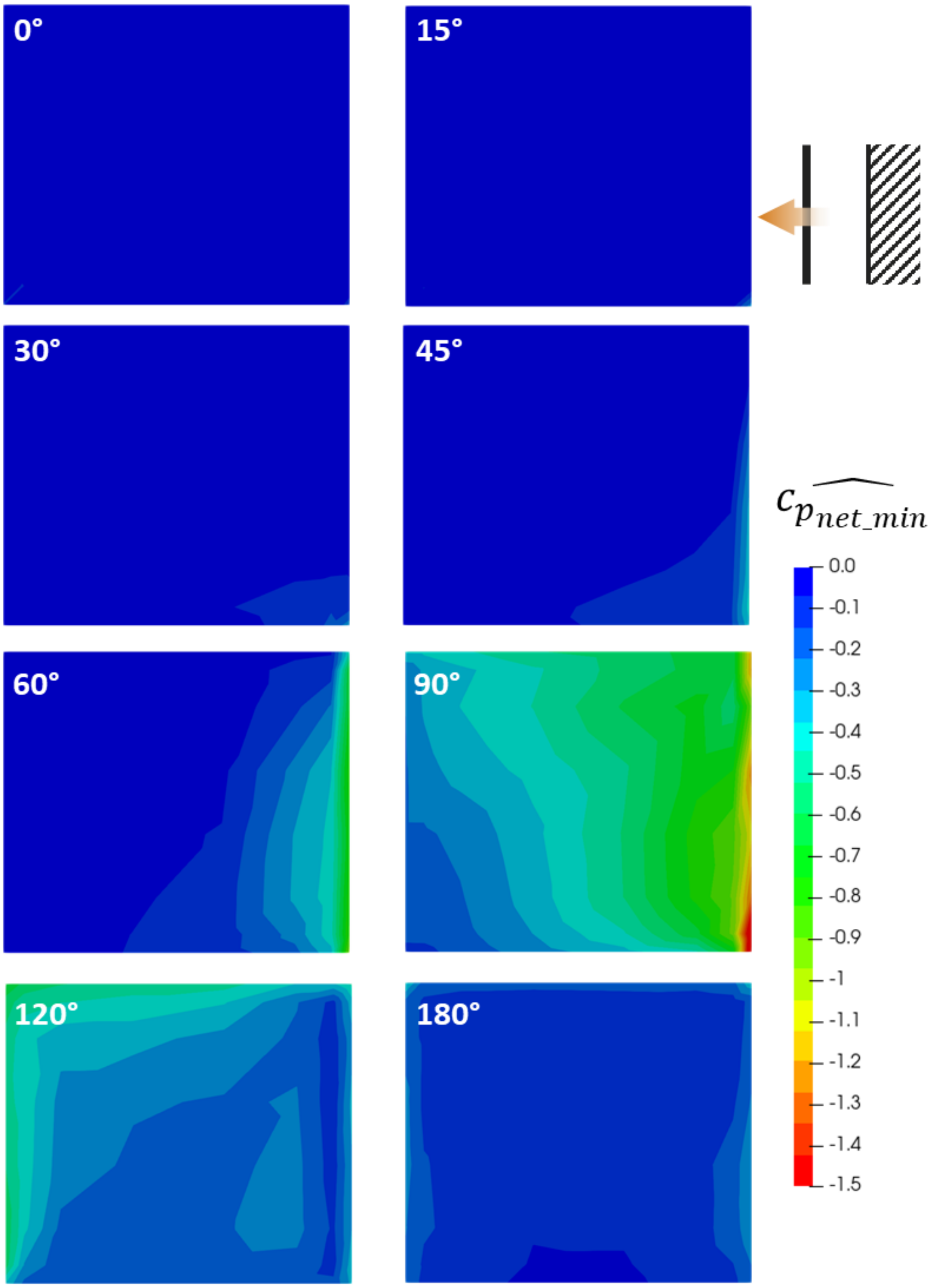

Figure 61 - Mapping of the coefficient of minimum peak pressure differential (peak pull-outs) for each wind direction (configuration h_n_l_20_p_00_s_n)

The Figure 62 summarises these maps by proposing a peak differential pressure coefficient, maximum and minimum, for all wind directions combined. The pressure fields in the figure are symmetrical.

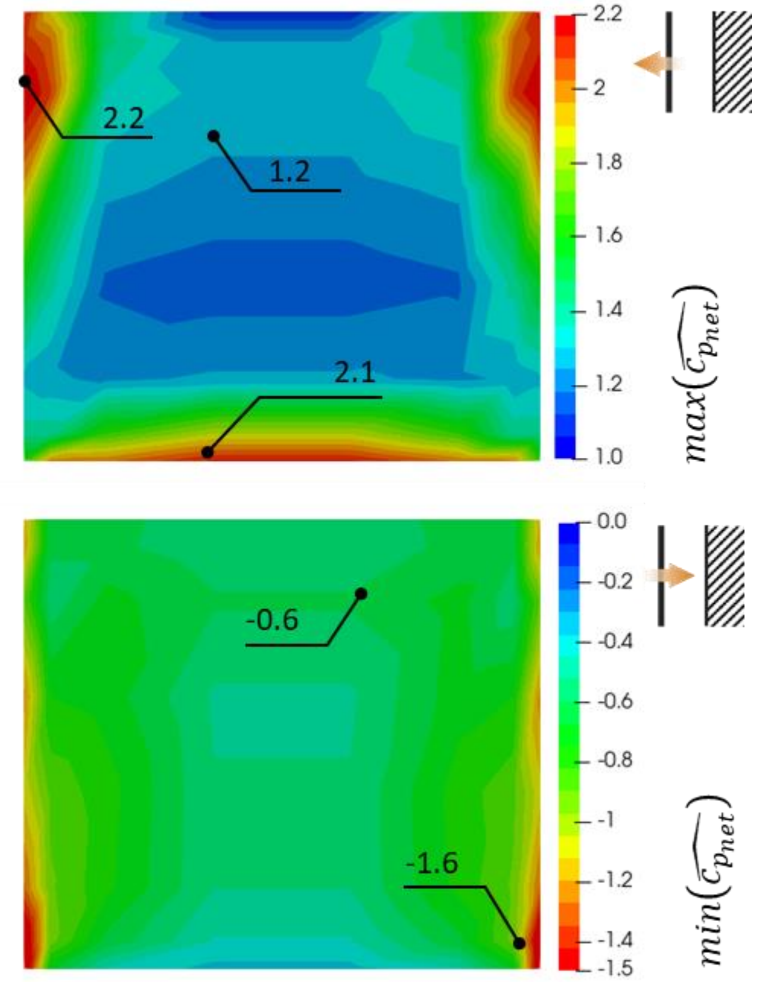

Figure 62 - mapping of the peak pressure differential coefficient for all wind directions combined, top: maximum (peak compression) bottom: minimum (peak pull-out) (configuration h_n_l_20_p_00_s_n).

The figure allows us to conclude that, for this geometric configuration, the double-skin facade is much more stressed in compression than in pull-out. For compression, the differential pressure coefficients rise to a value of 2.2 at the foot of the facade, as well as on the upper part of the lateral edges. The coefficient then gradually decreases to a value of 1.2 at the centre of the facade. For pull-outs, the maximum peak value is -0.6 over the vast majority of the facade. It rises very locally to a value of -1.6 at the edges.

The Figure 63 plots the maximum differential pressure coefficient for all directions combined, considering only the 3 wind directions 0°, 30° and 60°. It compares it with that calculated previously for 8 wind directions. The 2 maps are extremely similar and seem to show that the maximum stresses on the double-skin facade are generated for wind directions between 0° and 60°.

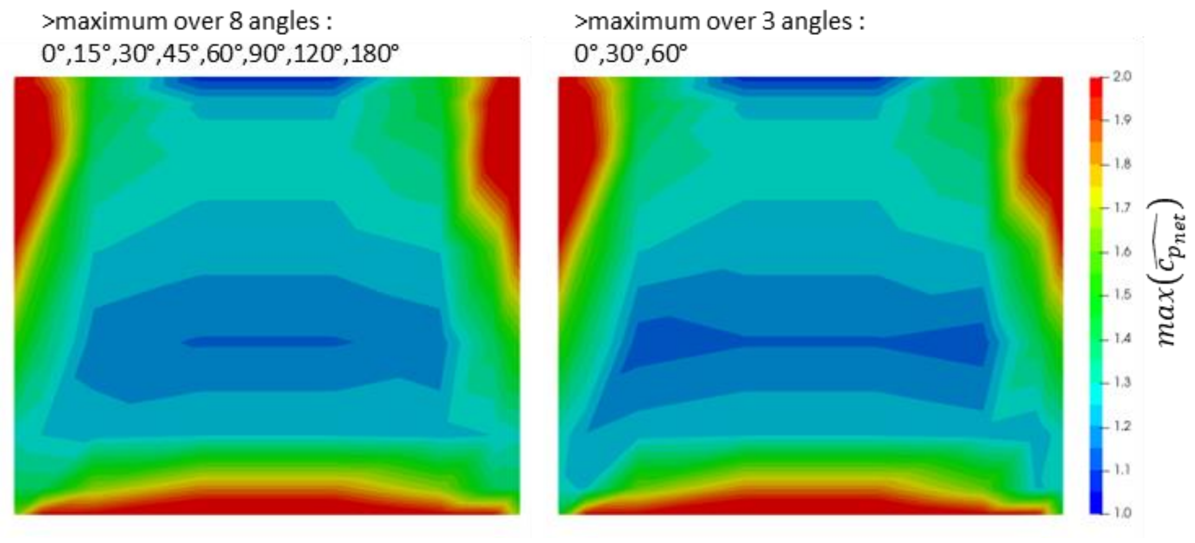

Figure 63 - mapping of the peak pressure differential coefficient for all wind directions combined: influence of the number of directions considered
(configuration h_n_l_20_p_00_s_n).

4.2.3 Effect of building height

We now propose to study the influence of building height on this configuration without segmentation. The analysis is carried out directly on the maps of the peak pressure differential $\widehat{c_{p_{net}}}$ all wind directions combined, as presented in the previous paragraph. The directions analysed are the same as before, 0°, 15°, 30°, 45°, 60°, 90°, 120° and 180°. The Figure 64 and Figure 65 respectively show the maps of peak compression and peak pull-out for all wind directions combined and obtained for the 3 building heights.

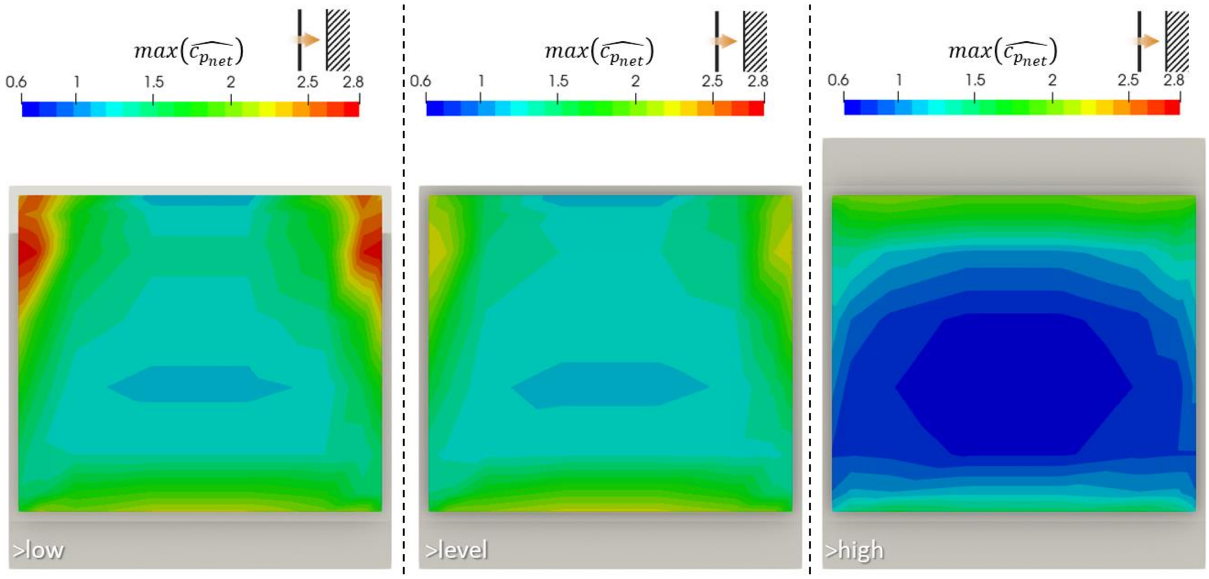

Figure 64 - mapping of the coefficient of maximum peak pressure differential (peak compressions) for all wind directions combined as a function of building height

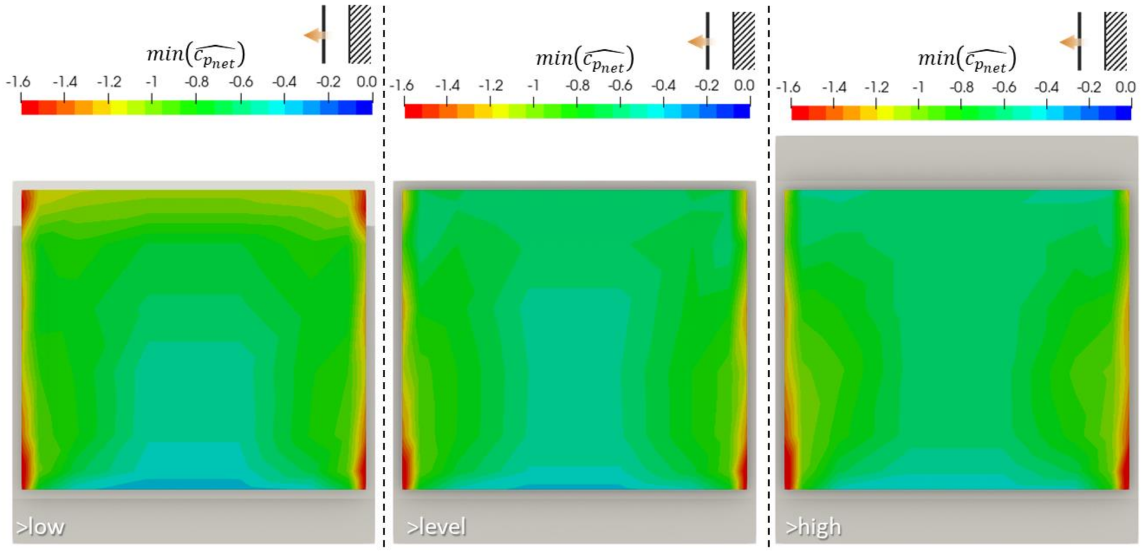

Figure 65 - Mapping of the coefficient of minimum peak pressure differential (peak tearing) for all wind directions combined as a function of building height

The Figure 65 shows that the maps of peak pull-outs are identical for the 3 building heights. There is just a slight difference at the top corners of the facade, with higher pull-outs for a low building. The impact of the height of the building on the pull-outs is therefore slight.

The same cannot be said for the peak compression maps. The map obtained for a low building is very similar to that obtained for a building at level, apart from significantly higher values at the upper corners of the facade. The Figure 66 plots the flow structure in a low building configuration for a wind direction of 0° and 30°. For the 0° direction, the flow structure is very similar to the one presented here Figure 59 for a level building, with the flow entering at the foot of the facade and evacuating via the other 3 sides of the facade. At an angle of 30°, as in the case of the level building, the flow rushes in through both the lateral wind opening and the foot of the facade. One can also note a vortex, generated by bypassing the windward edge of the double skin, and developing on the scale of the emerging part of the facade. These vortices are known to be very energetic, and induce very low pressures on the facades. This explains the very high pressure differential on the upper corner of the facade, induced by this vortex, which generates a very high negative pressure on the inner face of the double skin. This mechanism is very similar to the one that generates the very high loads on the acroteria at the edge of the roof.

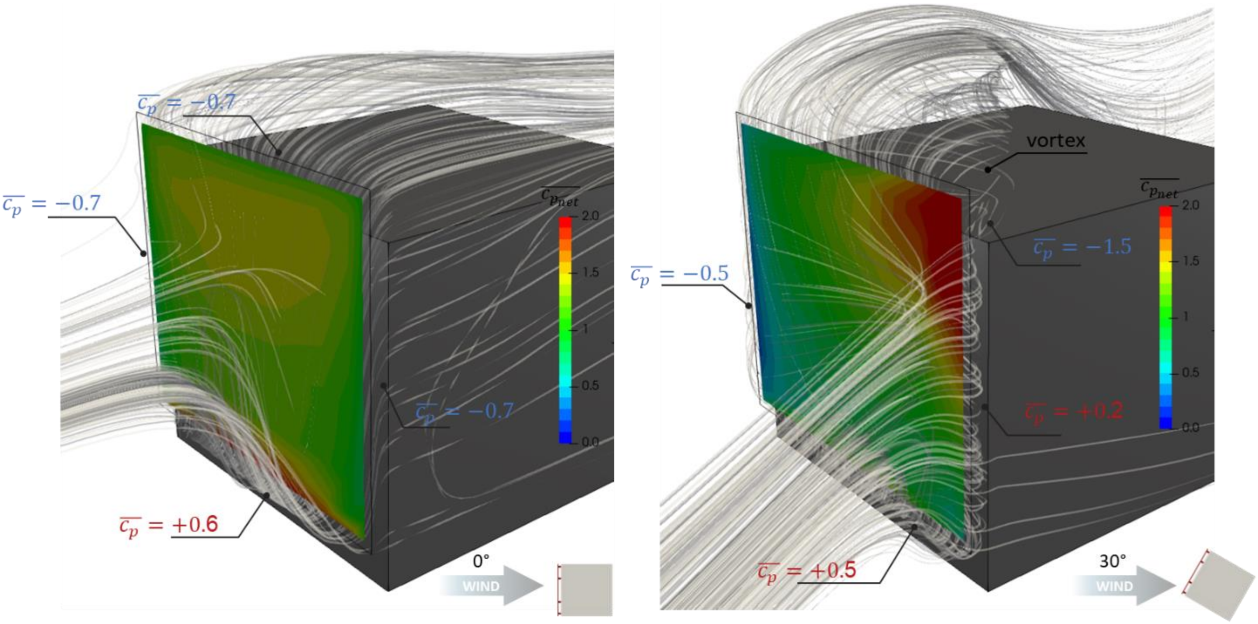

Figure 66 - flow structure around the double skin from numerical simulation and differential load mapping $\overline{c_{p_{net}}}$ measured in a wind tunnel, for wind directions of 0° and 30° (configuration h_b_l_20_p_00_s_n). (configuration h_b_l_20_p_00_s_n)

As in the case of the configuration with vertical segmentation, the increase in the height of the building leads to a very significant reduction in the wind loads on the double-skin facade. Peak compressions remain high at the top and bottom of the facade, at around +2, then decrease to a value of +0.6 at the centre of the facade. The Figure 67 plots the structure of the flow around the double-skin for two wind directions of 0° and 30°. For a wind direction of 0°, the flow enters at the top and bottom of the facade, which are at high pressure, and then exits through the side openings, which are at low pressure. The air space is therefore divided between a flow coming from the top of the facade and from the bottom of the facade. At the centre of the facade, between these two flows, the dynamics are very low, which explains why the loads are lower. For a 30° wind direction, the flow rushes in from the top and bottom of the facade. It also rushes in through the upper part of the lateral windward opening, which is now at high pressure. The flow then evacuates only through the leeward side opening, which is now the only one under negative pressure. This configuration therefore creates a higher circulation in the air space on the upper windward corner of the double-skin facade, which explains why the loads are higher at this point.

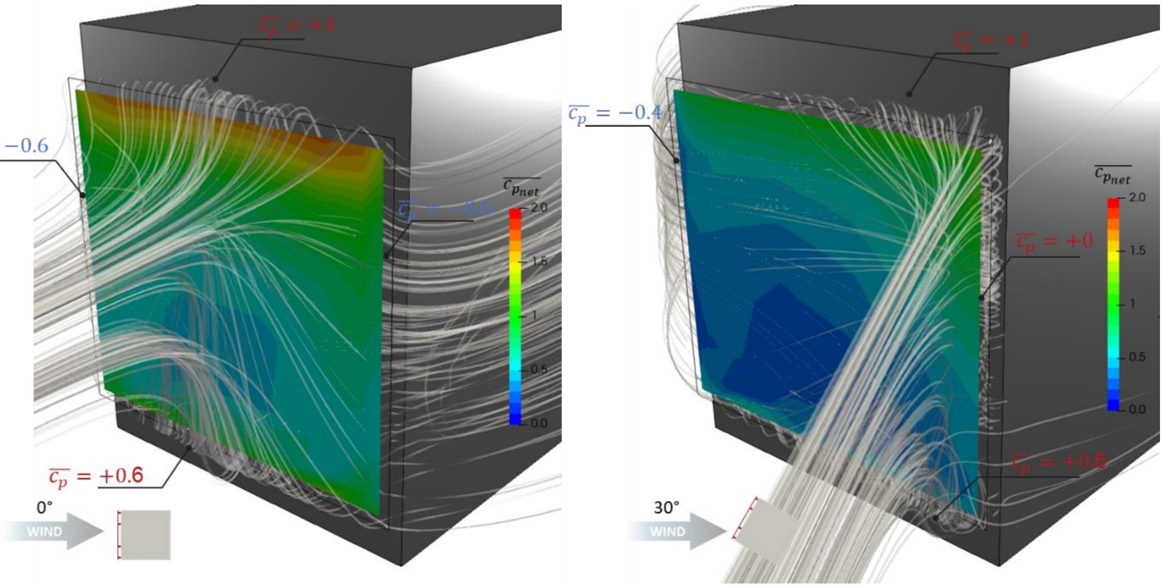

Figure 67 - Flow structure around the double skin from numerical simulation and differential load mapping $\overline{c_{p_{net}}}$ measured in the wind tunnel, for wind directions of 0° and 30° (configuration h_h_l_20_p_00_s_n)

The effects of wind direction on these open double-skin facades illustrate the link between the wind loads on the double-skin and the way in which the flow is structured within the air space. This flow is itself dependent on the pressures imposed on the boundaries of the air space by the wind flow at the scale of the building.

The effects of wind direction were not presented for double-skin facades with vertical segmentations, although they were tested as part of this study. Given that lateral openings have no longer any impact on the pressure balance of the air space, the effect of wind direction is much less marked in the presence of vertical segmentations. The wind load for a 0° direction is therefore representative of a wind load for all wind directions combined.

4.3 HORIZONTALLY SEGMENTED SKIN

The study will now examine the repercussions of the presence of horizontal segmentation on the pressure balancing of the air space and wind loads.

4.3.1 Solid segmentations

Initially, we consider solid segmentations, as opposed to porous segmentations as presented in Figure 20. The Figure 68 shows the plot of the average pressure differential $\overline{c_{p_{net}}}$ on the double-skin facade for a direction of 0°, and for three heights of the building. Measurements will be taken with a horizontal segmentation, either high or low (5 m from the edge of the double skin in both cases), and compared with the configuration without segmentation. In addition, the Figure 69, Figure 70 and Figure 71 show the internal and external pressure profiles and the corresponding differential for the 3 building heights respectively.

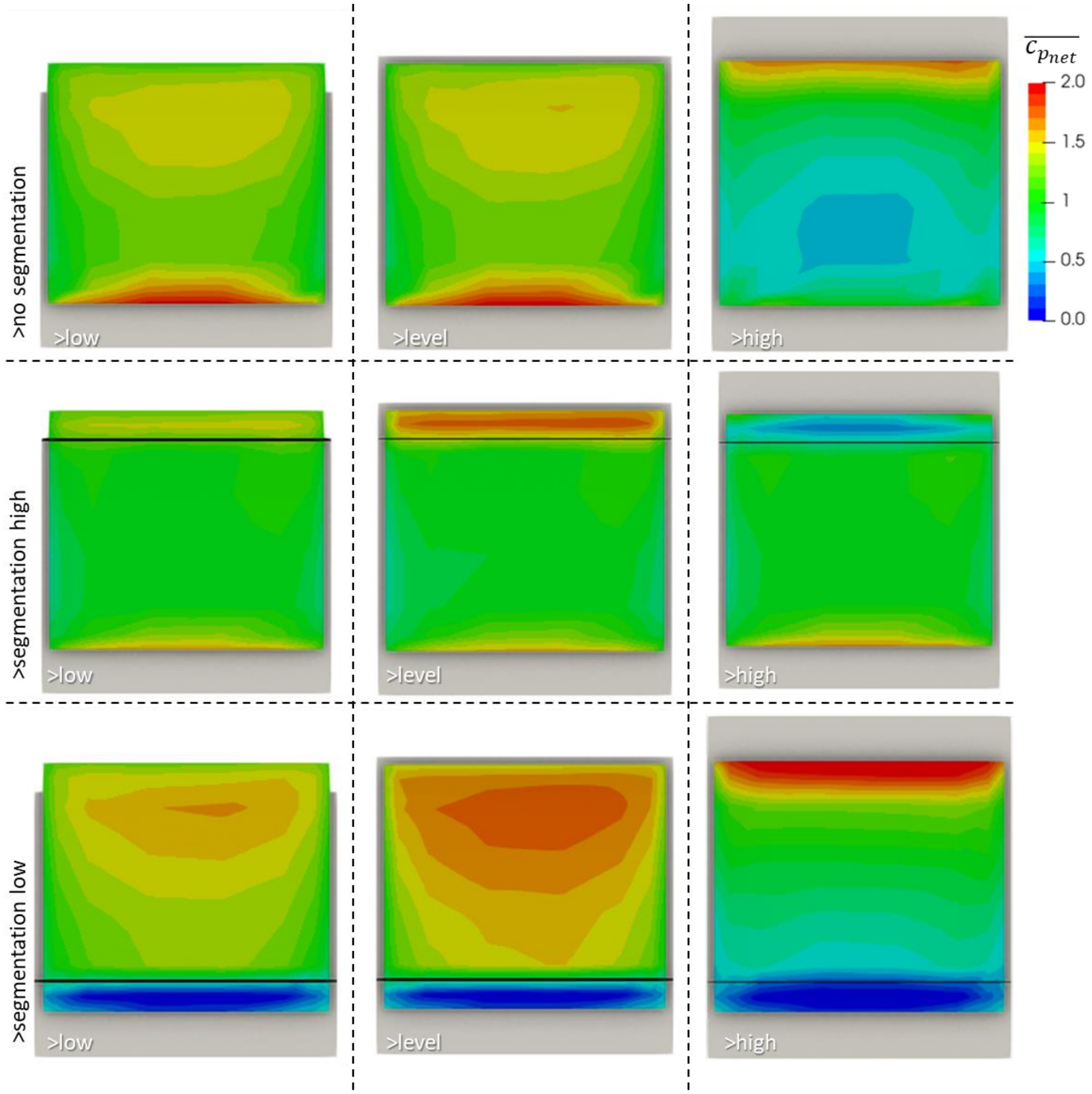

Figure 68 - Mean pressure coefficients $\overline{c_{p_{net}}}$ for a direction of 0°, three building heights and two types of horizontal segmentations

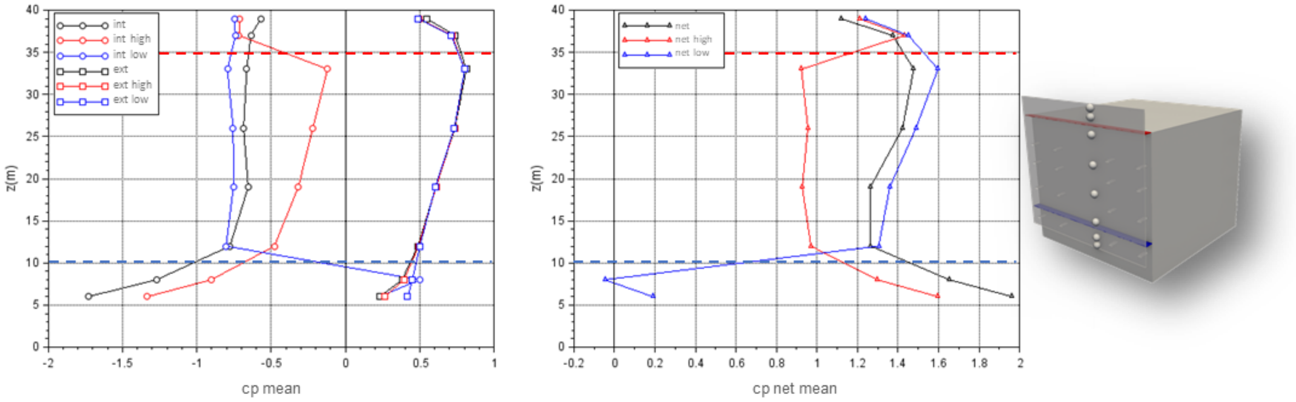

Figure 69 - profile of the mean pressure coefficient on the internal, external and net double-skin facade, for a low building with two configurations of horizontal segmentations

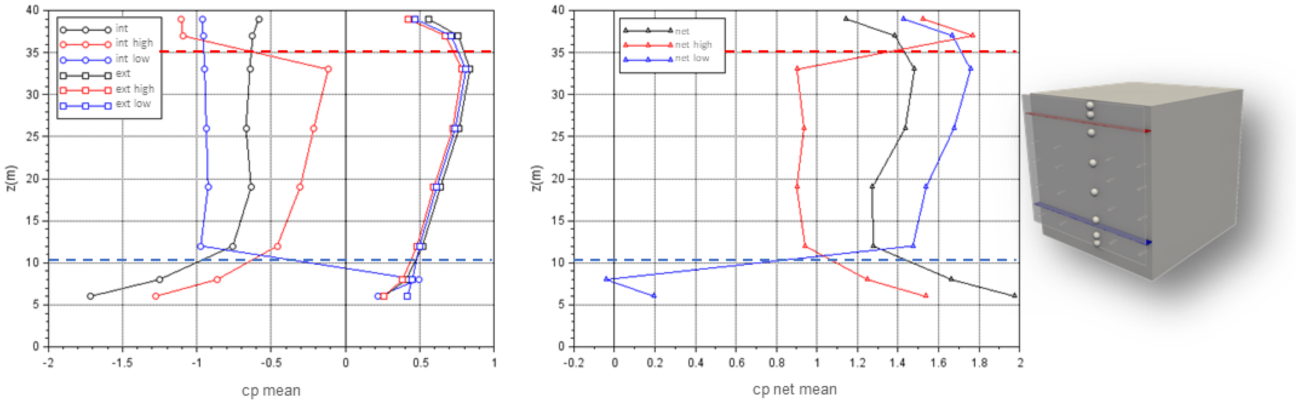

Figure 70 - profile of the mean pressure coefficient on the inner, outer and net double-skin facade, for a level building with two configurations of horizontal segmentations

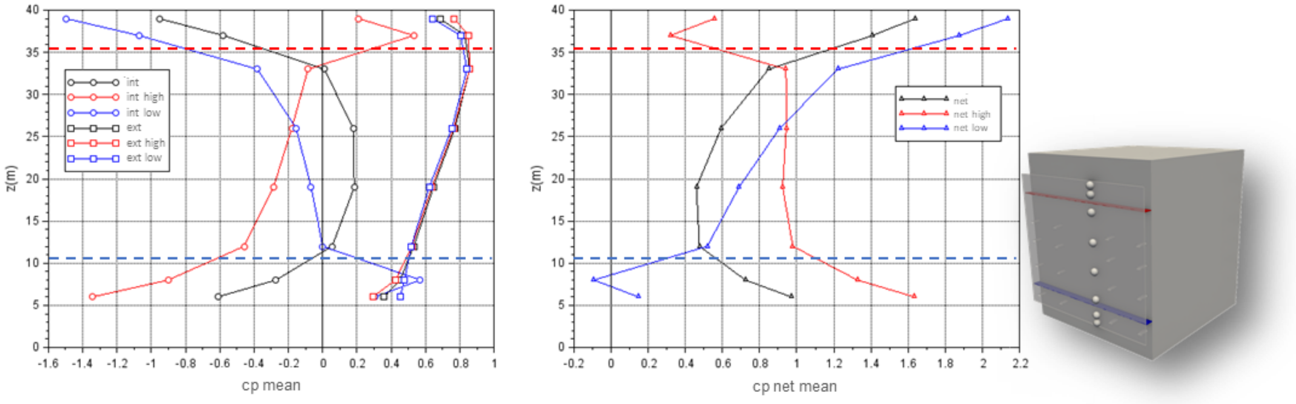

Figure 71 - profile of the mean pressure coefficient on the internal, external and net double-skin facade, for a tall building with two configurations of horizontal segments

The figures show that these horizontal segmentations have a very significant impact on the wind loads on the double-skin facade.

For low and level buildings, high segmentation will reduce wind loads on the double skin. It will cut off access to low pressure at the top of the facade. As a result, for one side with high pressure at the foot of the facade, there are only 2 sides with low pressure, compared with 3 sides in the configuration without segmentation. This has the effect of reducing the negative pressure inside the air space. We can therefore observe a shift in the average internal pressure profile $\overline{c_{p_{int}}}$. This translates directly into a reduction in net loads $\overline{c_{p_{net}}}$. High segmentation, on the other hand, will lead to an increase in loads for the high building. It will have the effect of cutting off access to high pressure at the top of the facade. In the configuration without segmentation, there were 2 sides with high pressure for 2 sides with low pressure. With the high segmentation, there is only one side with high pression for 2 sides with low pressure. This lowers the pressure inside the air gap and increases the flow entering it. The internal pressure profile $\overline{c_{p_{int}}}$ and net differential $\overline{c_{p_{net}}}$ profiles show a significant increase in loads at the foot of the facade due to the flow being trapped in the air gap.

For low and level buildings, the presence of a segmentation at the foot of the facade will increase wind loads. In this configuration, the segmentation cuts off access to the high pression opening at the foot of the facade, and the 3 remaining openings of the air space are therefore under low pressure. The result is lower pressure in the air space, and therefore a higher net differential. It should be noted that this increase in loads is greater for the level building than for the low building. For the high building, the segmentation at the foot of the facade also leads to an increase in loads. As with the low segmentation, cutting off access to a section with high pressure reduces the pressure in the air space. In this configuration, air is drawn in much more strongly at the top of the facade, resulting in higher loads on the upper part of the facade.

Once again, the analysis shows that the evolution of wind loads on the double-skin facade can be easily linked to the pressures imposed at the facade boundaries, and to the flow they will generate in the air space.

4.3.2 Porous segmentations

We now propose to study the effect of variable porosity on these segments. In this case, it is arranged in the form of holes distributed along the entire length of the segmentation as shown in Figure 20. They can, for example, represent air intake hatches at the top of a double-skin facade.

The Figure 72 and the Figure 73 show a plot of the internal and external pressure profiles, and the corresponding differential, associated respectively with a low building and a high building, for a configuration with a high segmentation of the double-skin. The figure shows a slight variation in pressure balance with increasing porosity. It can be seen that the profile is much closer to the balance obtained with solid segmentation than with a configuration without segmentation. This suggests that the profiles will approach the profile without segmentation as the porosity of the segmentation increases. However, the measurements seem to indicate that the arrangement of reduced porosity in the segmentation has little impact on the pressure balance of the air gap. This balancing will continue to be determined mainly by the open sections of the air space, whose surface area is much greater than that of the porosities in the segmentation.

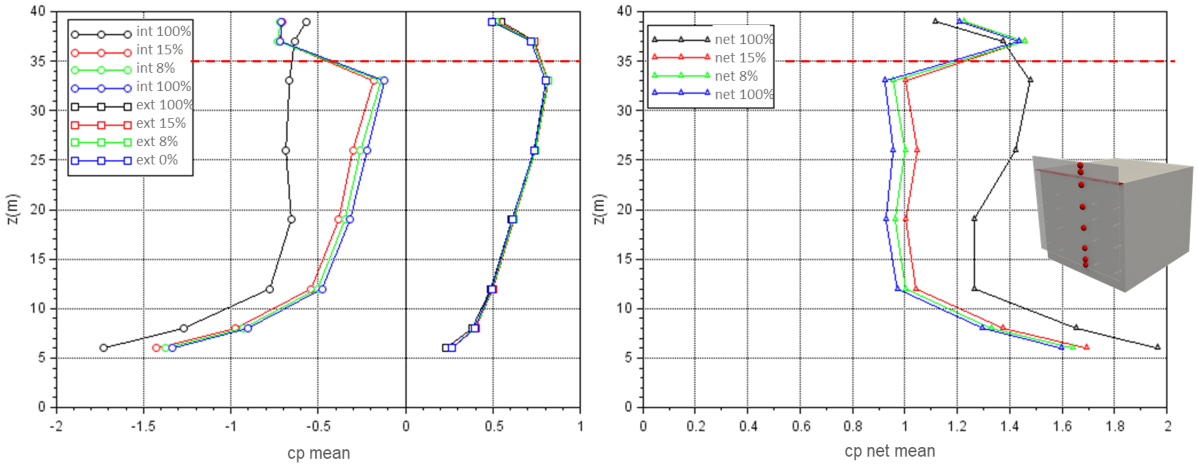

Figure 72 - profile of the mean pressure coefficient on the internal, external and net double-skin facade, for a low building with a high segmentation with variable porosity

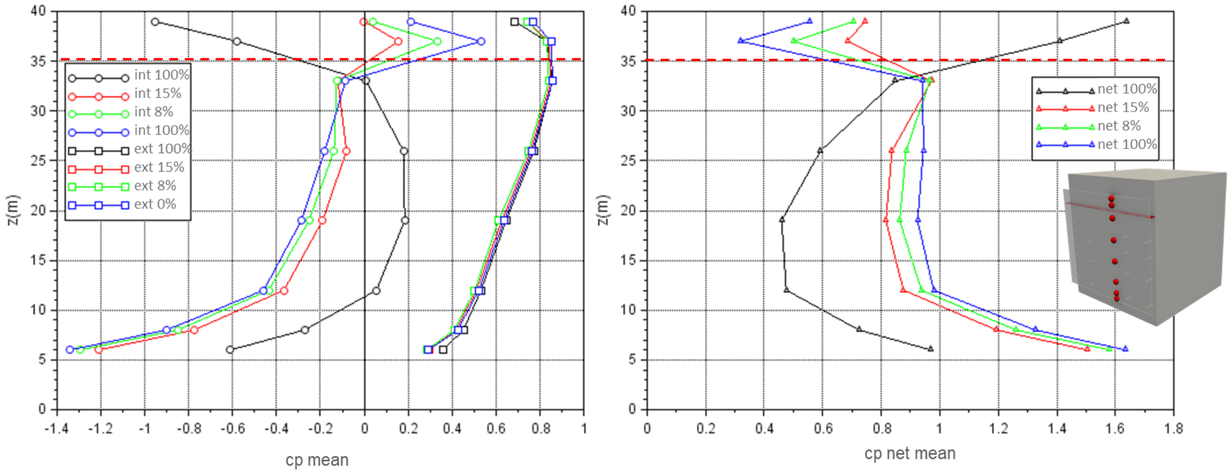

Figure 73 - profile of the mean pressure coefficient on the internal, external and net double-skin facade, for a tall building with a high segmentation with variable porosity

4.4 EFFECT OF THE THICKNESS OF THE AIR SPACE

The study will now examine the effect of the thickness of the air space on the wind loads of the double-skin. The model makes it possible to continuously adjust the thickness of the air space in the absence of segmentations (segmentations were only carried out for a single thickness of the air space).

The Figure 74 maps the average pressure differential $\overline{c_{p_{net}}}$ on the double-skin facade, for a level building and a wind direction of 0°. Measurements are taken for 4 air gap thicknesses: 50 cm, 1m, 2m and 3m Real Scale. In addition, the Figure 75 plots the profiles of the mean internal and external pressures and the net differential for the 4 thicknesses of the air space.

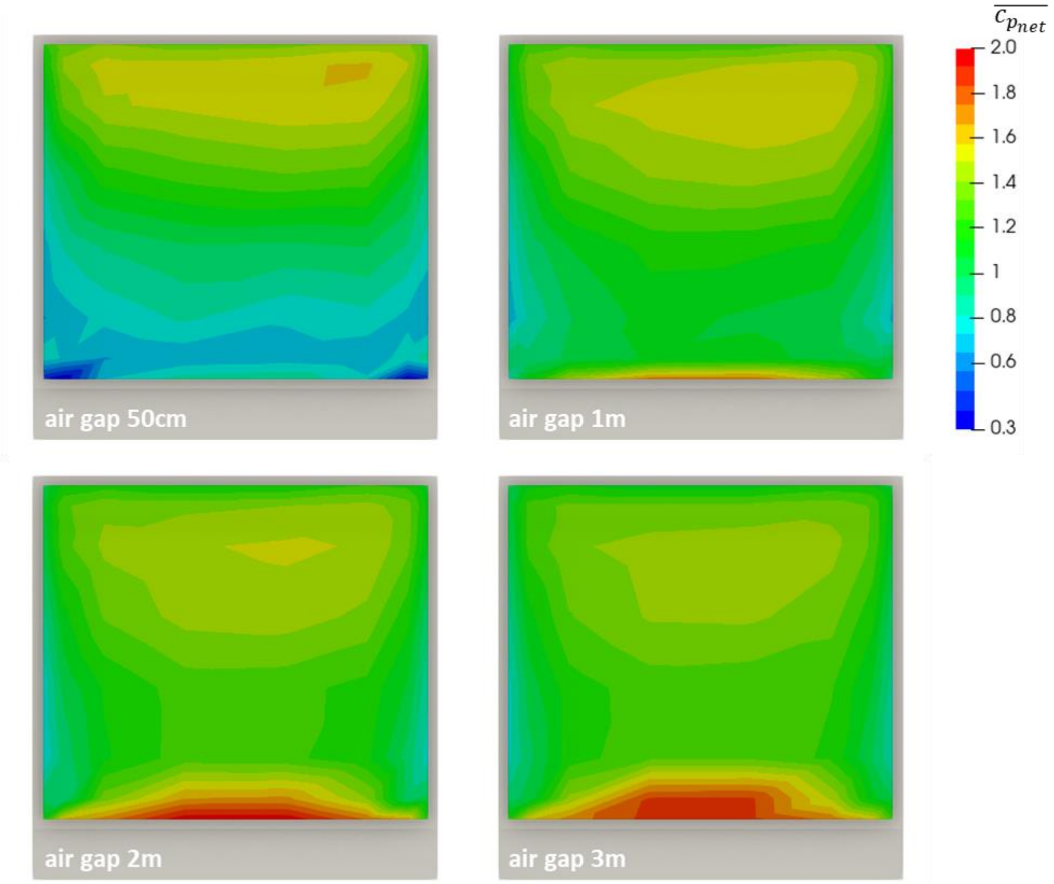

Figure 74 - Mean pressure coefficients for different blade thicknesses and a wind direction of 0° (configuration h_n_l_XX_p_00_s_n)

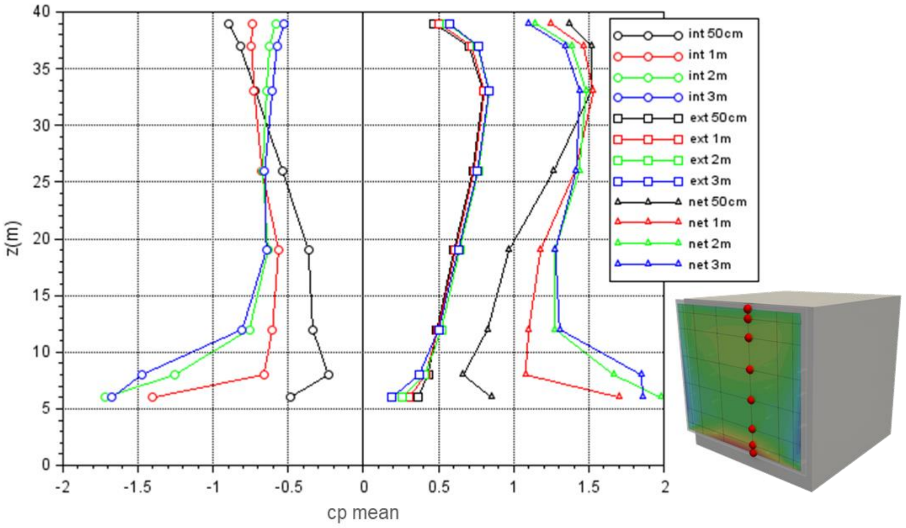

Figure 75 - profile of the average pressure coefficient on the internal, external and net double-skin facade (DSF), for three air space thicknesses (configuration h_n_l_XX_p_00_s_n)

The figures show that the thickness of the air space has a significant impact on the wind loads of the double-skin facade. Generally speaking, reducing the thickness of the air space leads to a reduction in loads. The loads measured for a thickness of 2m and 3m are fairly similar, and seem to indicate that the loads will not increase for air space thicknesses greater than 2m.

As the thickness of the air space decreases, the internal pressure profile $\overline{c_{p_{int}}}$ shows that, in absolute terms, the negative pressure decreases in the lower part of the air gap and increases in the upper part. This behaviour seems to suggest a limitation of the flow entering the air gap as its thickness decreases. Thus, as the flow velocity inside the air gap decreases, the static pressure drop generated by the dynamic pressure of the flow also weakens. The pressure profile inside the air space then tends to get a little closer to the values of the static pressure at the air space's openings. The decrease in the flow rate entering the air gap is due to the increase in pressure losses at the bottleneck and at the discharge of the flow. As a caricature, it is more "difficult" for the flow to enter the air gap because of its narrowness, so it "prefers" to pass through the outside of the facade.

The change in internal pressure $\overline{c_{p_{int}}}$ with the reduction in the thickness of the air space leads to a slight increase in the net pressure differential $\overline{c_{p_{net}}}$ on the upper part of the facade, and a significant reduction in loads on the lower part.

The thickness of the air space has a slight influence on the external pressure coefficient $\overline{c_{p_{ext}}}$ at the foot of the facade. This effect can be explained by a change in the flow entering the air space, as shown in Figure 41. The reduction in the inflow rate of the air space will affect the structure of the flow which bypasses the lower edge of the facade, and thus impact on the pressure on its outer face.

This configuration therefore highlights the effect of the dynamic pressure of the flow in the air gap, and its significant repercussion on the static pressures measured on the inside of the double-skin. Here, at identical pressures at the boundaries of the air space, the flow rate in the air gap is only controlled by the pressure losses at the point where the flow enters/exits.

The Figure 76 plots the average pressure differential on the double-skin facade, for a tall building and a wind direction of 0°. Measurements are taken for 4 air gap thicknesses: 50 cm, 1m, 2m and 3m. In addition, the Figure 77 plots the profiles of the mean internal and external pressures and the net differential for the 4 thicknesses of the air space.

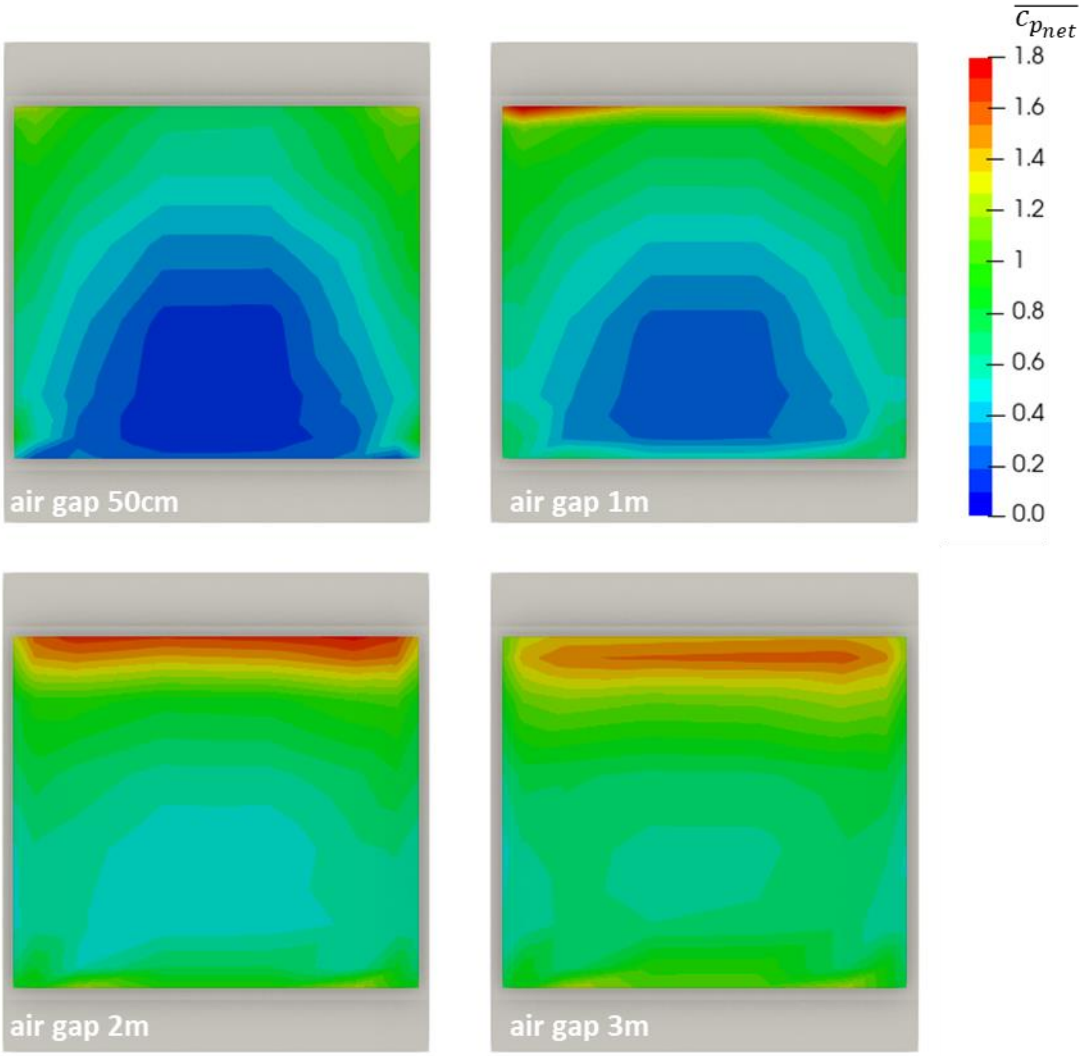

Figure 76 - Mean pressure coefficients for different blade thicknesses and a wind direction of 0° (configuration h_h_l_XX_p_00_s_n)

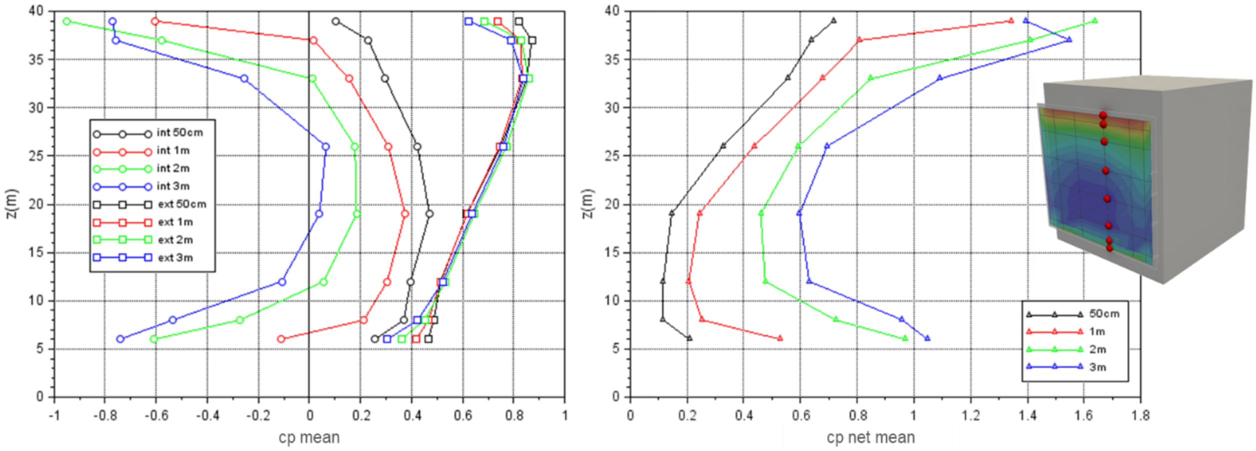

Figure 77 - profile of the mean pressure coefficient on the internal, external and net double-skin facade (DSF), for three air space thicknesses (configuration h_h_l_XX_p_00_s_n)

Once again, the reduction in the thickness of the air space has a significant influence on the wind loads of the double-skin facade. Contrary to the previous case, the thickness of 2m no longer seems to constitute a limit value for the increase in loads, since for a thickness of 3m, the loads are greater than those obtained for a thickness of 2m. Once again, we can see that the pressure on the inside of the facade $\overline{c_{p_{int}}}$ increases as the thickness of the blade decreases. This phenomenon can again be attributed to a reduction in the flow rate entering the air space due to an increase in the pressure drop at the inlet/outlet of the channel. The pressure in the air gap will then equilibrate to a value closer to the static pressures at the air gap boundaries.

This analysis therefore confirms that the thickness of the air space is also a first-order parameter for wind loads on the double-skin facade.

4.5 POROSITY EFFECT OF THE DOUBLE-SKIN FACADE

The study now looks at the case of a porous double-skin facade. This configuration is representative, for example, of facades made up of non-adhering panels, creating distributed porosity, or of facades in which vents are regularly installed.

In the reference experiment, the model of the double-skin facade is fitted with a series of rectangular holes that allow the porosity of the facade to be modulated at will.

4.5.1 Uniform porosity

Initially, we are interested in the case of uniformly distributed porosity on the facade, excluding a 5m edge where the facade remains solid. Two configurations are studied. In the first case, all the openings are open, creating a porosity of 15% in the porous zone at the centre of the facade. A second configuration was studied in which every second hole was blocked, creating a distributed porosity of 8% in the centre of the facade. These two configurations were presented Figure 16.

Initially, we are interested in the effect of the porosity of the skin on the level building, without segmentation and for a wind direction of 0°. The Figure 78 plots the mean pressure coefficients measured on the outer face $\overline{c_{p_{ext}}}$ inner face $\overline{c_{p_{int}}}$ as well as the mean pressure differential noted $\overline{c_{p_{net}}}$ for the two porosities studied, and compares them to a configuration with a solid skin. The Figure 79 plots the internal and external pressure profiles and the corresponding differential. It also records the peak values of the pressure signal. The porous part of the facade is delimited by red (8%) or blue (15%) horizontal dotted lines.

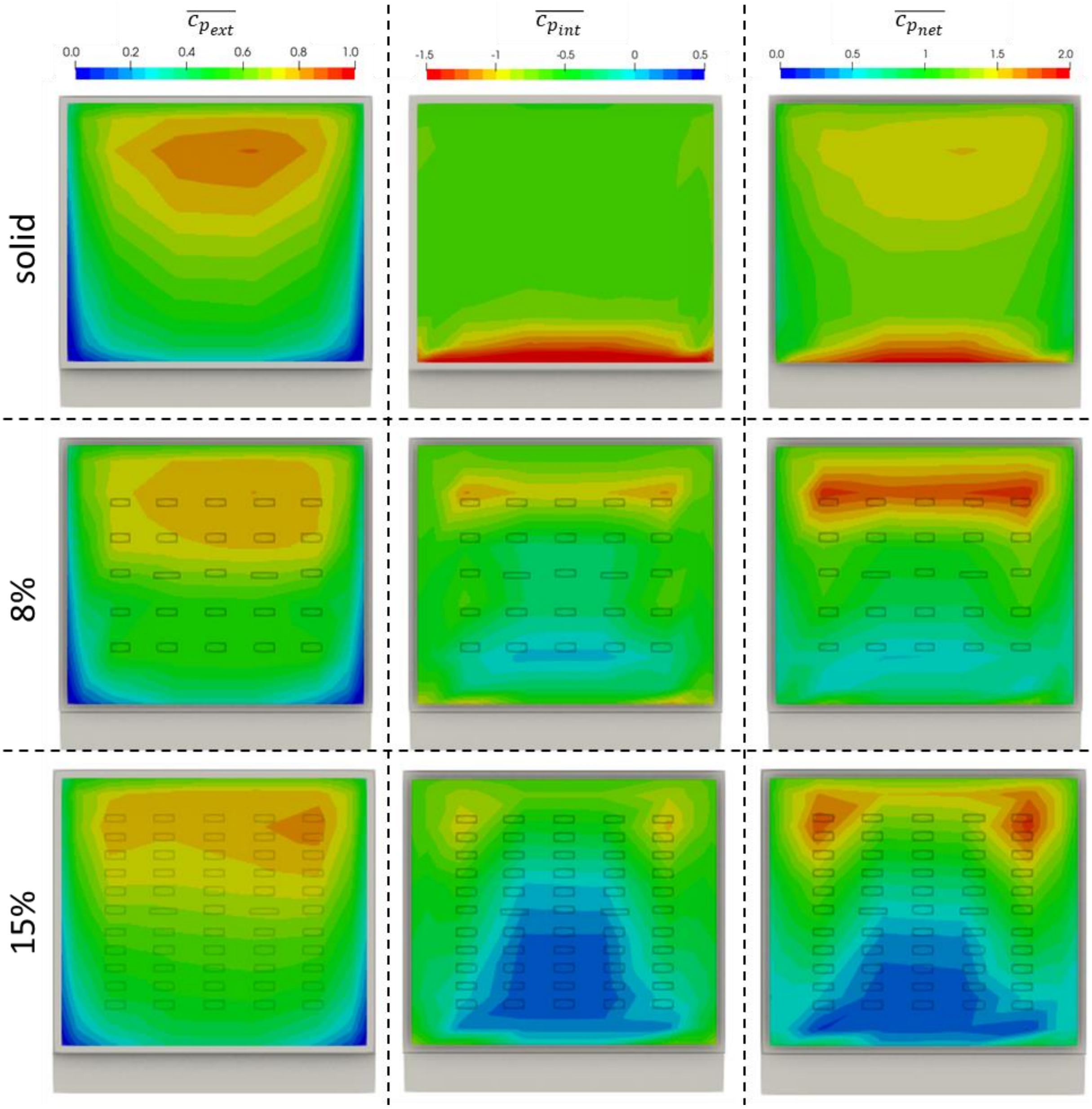

Figure 78 - mean pressure coefficients for a level building with a variable porosity skin (configuration h_n_l_20_p_XX_s_n)

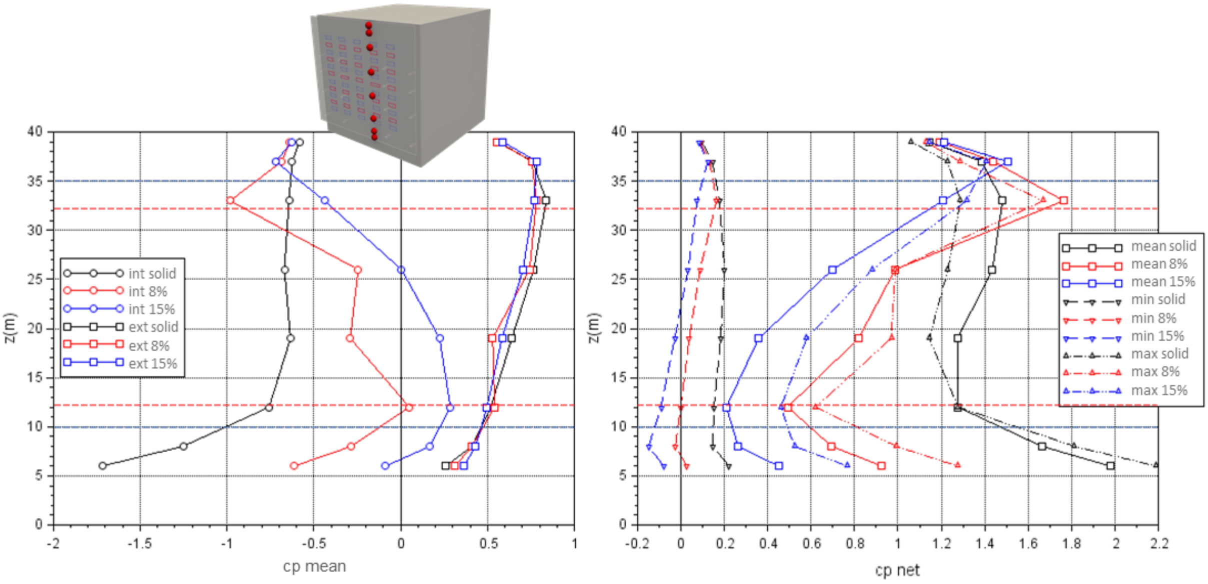

Figure 79 - profile of the mean pressure coefficient on the internal and external double skin facade, and mean and peak net, for a level building with a skin of variable porosity (red 8%, blue 15%) (configuration h_n_l_20_p_XX_s_n)

Firstly, the maps show the impact of porosity on the external pressure coefficient $\overline{c_{p_{ext}}}$. It decreases slightly as porosity increases, and the stagnation point imprint spreads over a larger area.

The changes are much more marked for the internal pressure coefficient $\overline{c_{p_{int}}}$. The maps and profiles show a change in the pressure balance of the air space, with pressure levels increasing and getting closer and closer to the value of the pressure on the outside of the facade. The effect is much more marked on the lower part of the facade than on the upper part. At the bottom of the facade, for a porosity of 15%, the pressure even changes sign and becomes positive.

At the very top of the facade, the pressure in the air space $\overline{c_{p_{int}}}$ remains very low. This zone corresponds to the 5m edge with no porosity. It constitutes a sealed channel linking the low pressures at the opening at the top of the facade, and the high pressures on the external face through the porosities. We can therefore assume that a flow is generated, rushing through the pores to reach the top of the facade. This flow then induces low pressure in the air space according to the mechanism described before.

The mapping of pressure differentials $\overline{c_{p_{net}}}$ appears to be copied on that of the internal pressure coefficient $\overline{c_{p_{int}}}$. Overall, there is a significant reduction of double-skin loads as porosity increases. For a porosity of 15%, the mean loads at the foot of the facade are almost zero. The profiles again show that although the mean coefficient $\overline{c_{p_{net}}}$ is close to 0, this is not the case for the peak coefficient $\widehat{c_{p_{net}}}$ which remains above 0.5 at the foot of the facade. Once again, there are areas of high load at the upper edge, due to the flow being engulfed in the air space in this area, which has no porosity.

The Figure 80 and the Figure 81 show the same information for a configuration with a tall building.

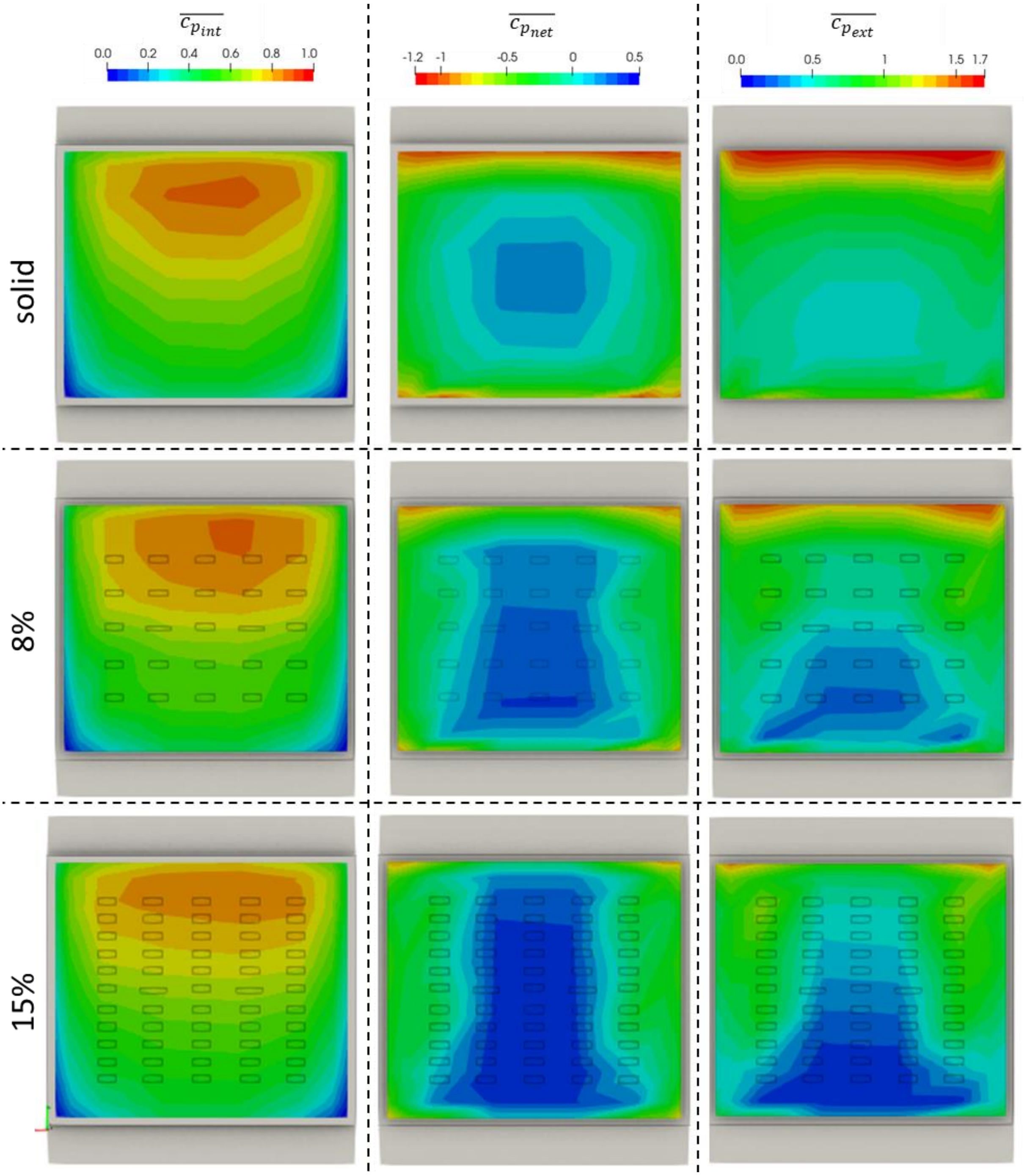

Figure 80 - mean pressure coefficients for a tall building with a variable porosity skin (configuration h_h_l_20_p_XX_s_n)

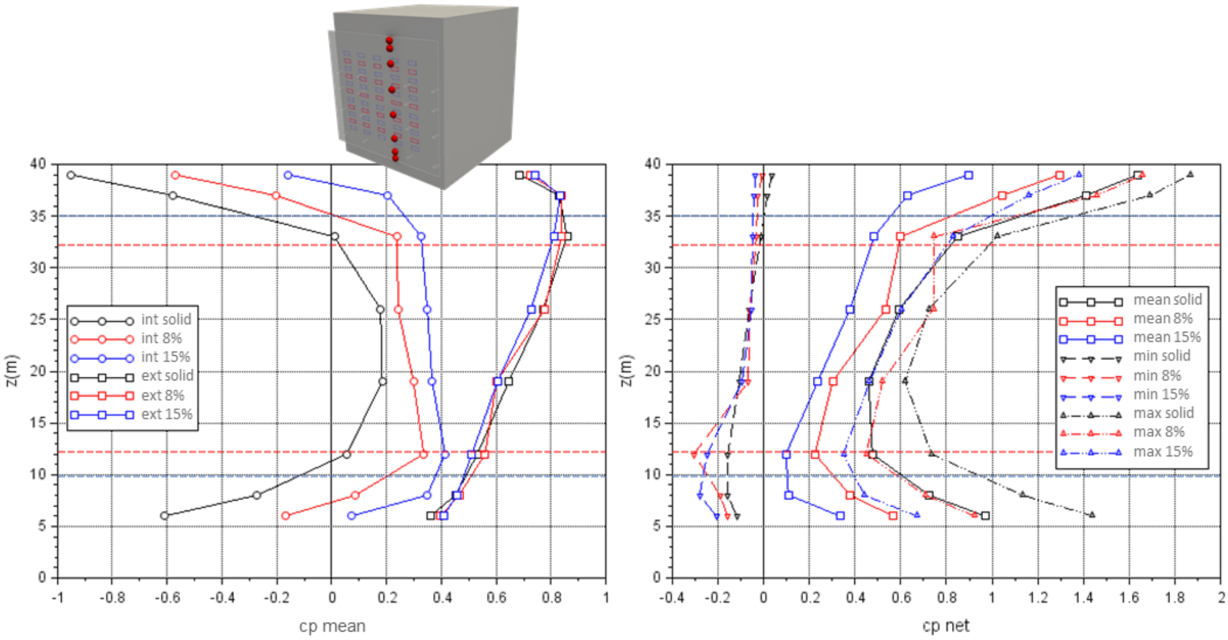

Figure 81 - profile of the mean pressure coefficient on the internal and external double skin facade, and mean and peak net, for a tall building with a variable porosity skin (configuration h_h_l_20_p_XX_s_n)

Once again, the analysis shows a significant change in the pressure balance of the air space as the porosity of the skin increases. The profiles show that the increase in porosity again leads to an increase in pressure in the air gap $\overline{c_{p_{int}}}$ in this case associated with a uniform profile. The result is a reduction in net loads $\overline{c_{p_{net}}}$. This reduction is less marked than for the configuration of the building at level. This can be explained by the fact that the pressure differences between the inside and outside of the facade were already lower with a solid skin. This absence of high-pressure differentials may also explain why we do not find very high loads at the solid edges of the façade as in the case of building at level.

The Figure 82 plots the profiles of the pressure coefficients in a final configuration, with an at level building equipped with vertical segmentations.

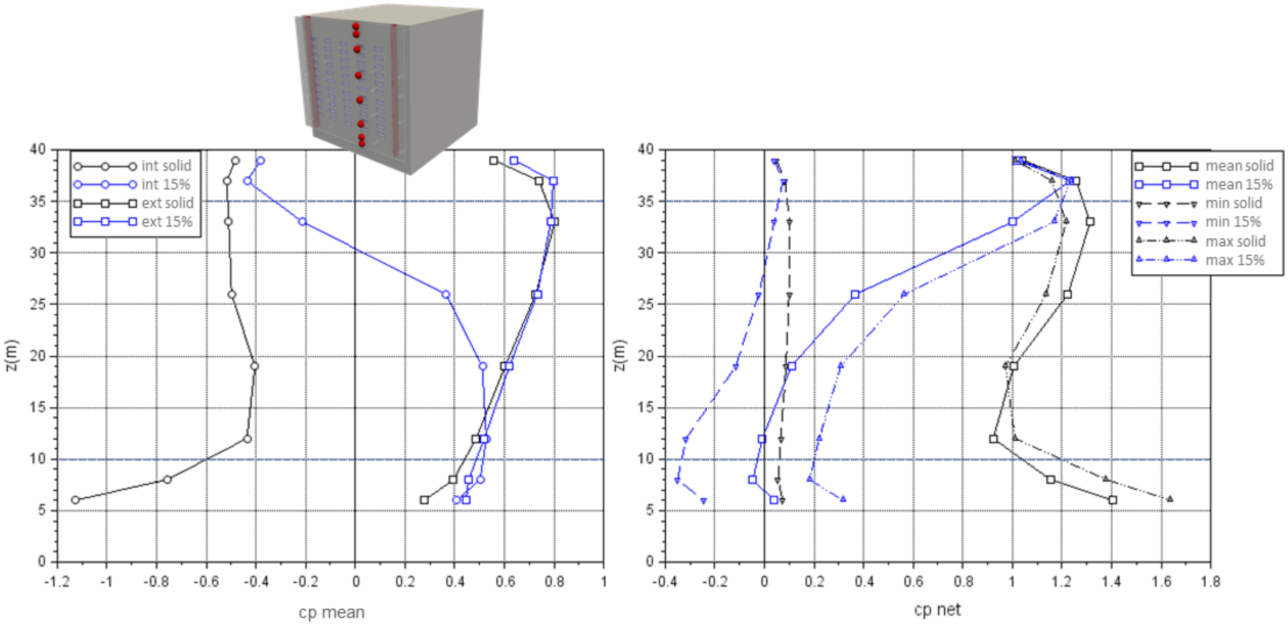

Figure 82 - profile of the mean pressure coefficient on the internal and external double-skin facade, and mean and peak net, for a level building, with vertical segmentation with 15% porosity (configuration h_n_l_20_p_XX_s_vert)

The effect of porosity in this configuration is even more marked. At the foot of the facade, the average pressure in the air space $\overline{c_{p_{int}}}$ becomes higher than that of the external face $\overline{c_{p_{int}}}$.

Thus, whereas the foot of the facade was in strong compression with a solid skin, it is in slight pull-out with a porous skin. Admittedly, the average loads remain low, particularly compared with the associated peak loads, but the shift in pressure balance due to the porosity generates a fairly spectacular and counter-intuitive effect on wind loads.

This latest analysis confirms that the effect of the porosity of the double skin has a first-order effect on the pressure balance of the air space, and will drastically change the wind loads on the double skin facade.

4.5.2 Localised porosity

The study now focuses on a case where the porosity of the double skin is no longer uniformly distributed over the surface, but localised. In this case, only the openings on the highest and lowest rows of the facade are left open, as shown in Figure 16. Porosity is then reduced to 3%, but concentrated at the ends of the facade. Initially, the configuration is that of a level building, equipped with vertical segmentations for a 0° direction. The Figure 83 plots the mean pressure coefficients measured on the external face $\overline{c_{p_{ext}}}$, internal $\overline{c_{p_{int}}}$, as well as the mean pressure differential noted $\overline{c_{p_{net}}}$ with this localised porosity, and compares them to a configuration with a solid skin. The Figure 84 plots the internal and external pressure profiles and the corresponding differential. It also records the peak values of the pressure signal. The porous part of the facade is located by horizontal dotted lines.

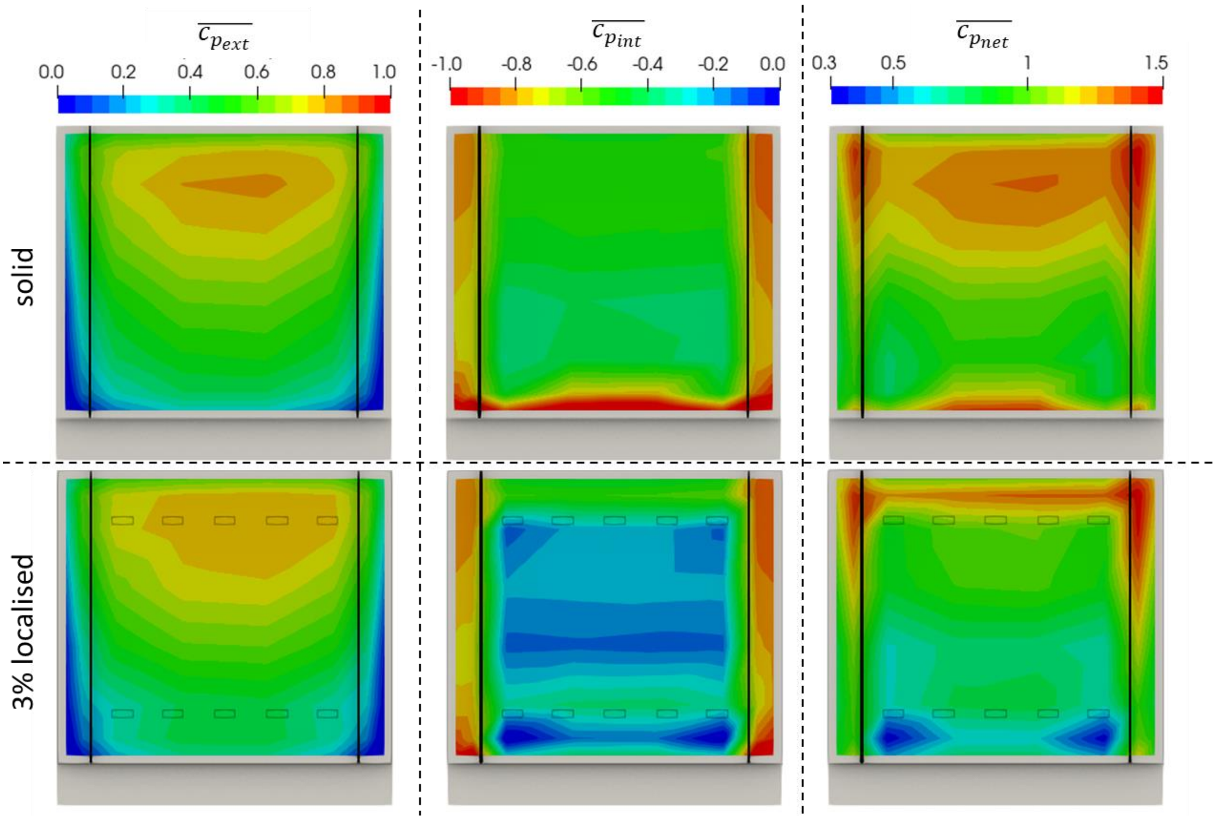

Figure 83 - Mean pressure coefficients for a level building with vertical segmentation and a skin with localised porosity (configuration h_n_l_20_p_XX_s_vert)

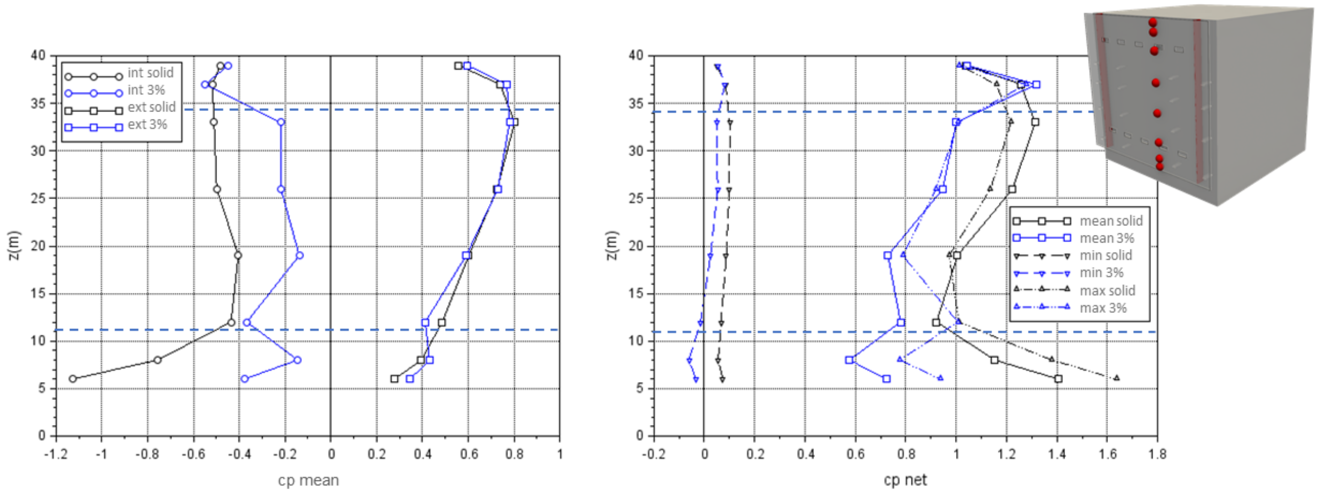

Figure 84 - profile of the mean pressure coefficient on the internal and external double skin facade, and mean and peak net, for a level building with vertical segmentation and a skin with localised porosity (configuration h_n_l_20_p_XX_s_vert)

Analysis of the figures shows that this localised porosity is enough to significantly change the pressure balance of the air space. The most marked change occurs at the foot of the facade, where the very low pressure zone induced by the flow engulfing the air space has virtually disappeared. More generally, the pressure inside the air gap $\overline{c_{p_{int}}}$ is higher, thus contributing to a reduction in net loads $\overline{c_{p_{net}}}$ across the entire double-skin facade. At the very top of the facade, as in the case of distributed porosity, there are locally high loads on the edge without porosity. Once again, this is due to the flow being channelled locally into the air space, as the porosity enables the high pressures on the external face of the double skin to be directly connected to the low pressures at the very top of the air space.

The Figure 85 and the Figure 86 show the same analysis for a configuration with a tall building, still equipped with vertical segmentations.

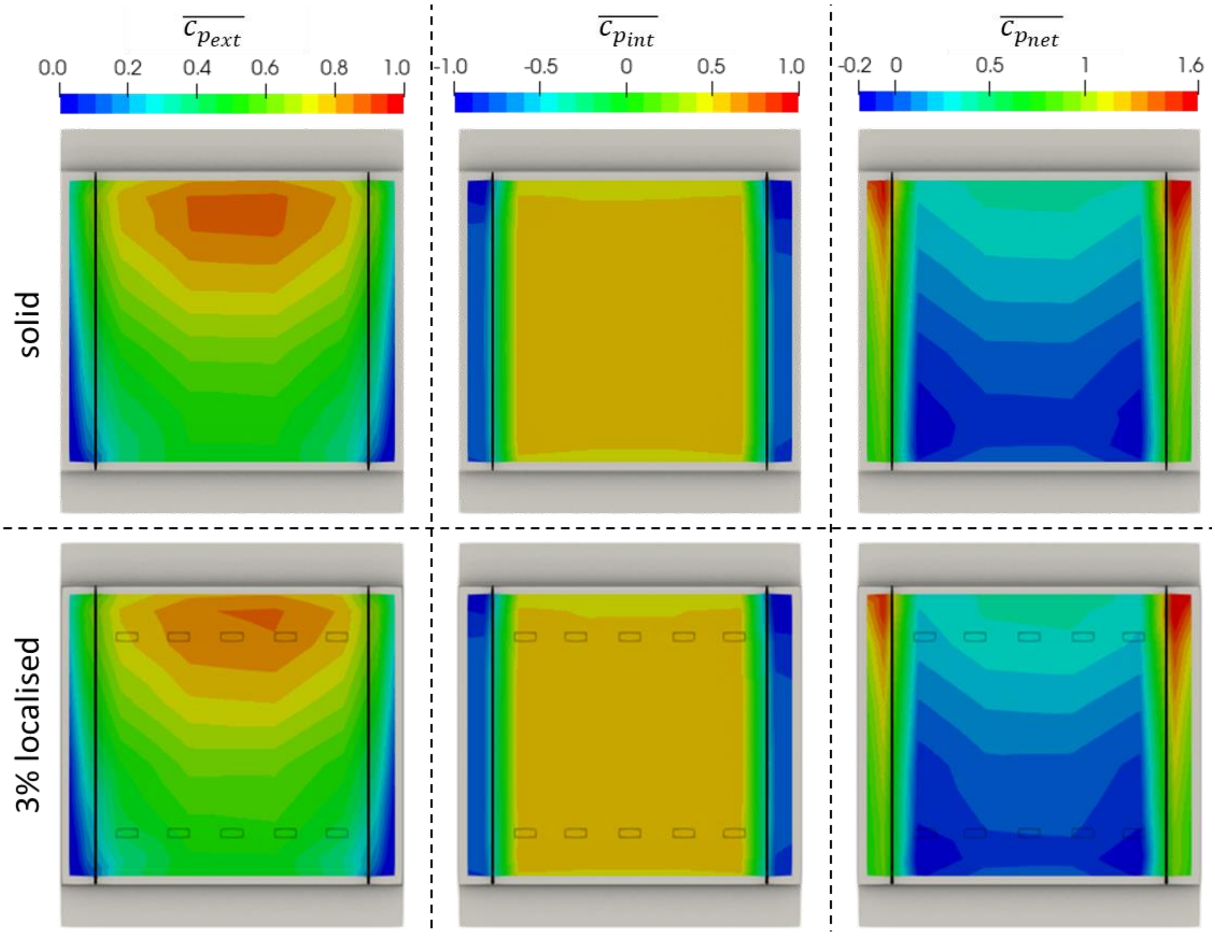

Figure 85 - Mean pressure coefficients for a level building with vertical segmentation and a skin with localised porosity (configuration h_h_l_20_p_XX_s_vert)

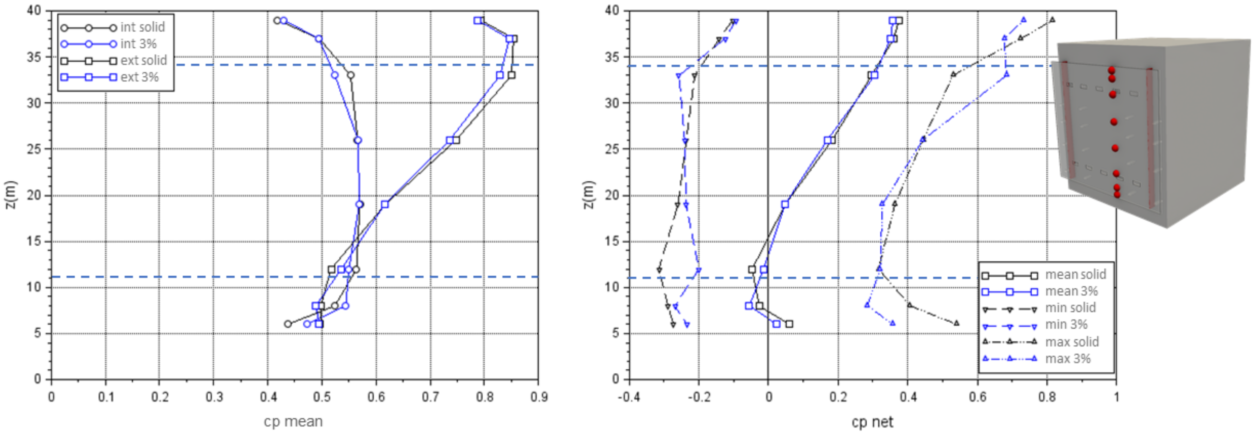

Figure 86 - profile of the mean pressure coefficient on the internal and external double-skin facade, and mean and peak net, for a tall building with vertical segmentation and a skin with localised porosity (configuration h_n_l_20_p_XX_s_vert)

The analysis shows that for this configuration, localised porosity has very little impact on the pressure equilibrium of the air gap. The profiles of the mean pressure coefficients are virtually superimposed. There is just a slight decrease in the peak pressure differential at the foot of the facade. As with distributed porosity, the pressure differential between the internal and external faces was already lower in this configuration with a solid skin. This may explain why the influence of porosity is less marked than with a level building.

This last analysis shows that the effect of the porosity will depend heavily on the way it is arranged, but also on the other parameters of the pressure balance of the air gap.

4.5.3 Fully cut porous skin

We are now interested in the case of a double skin entirely overlapped on these 4 sides. It is representative of double-skins that would be arranged in the form of independent cells. Firstly, we consider a non-porous double skin. The Figure 87 plots the mean pressure coefficients measured on the outer face $\overline{c_{p_{ext}}}$inner face $\overline{c_{p_{int}}}$ as well as the mean pressure differential noted $\overline{c_{p_{net}}}$ for a solid skin that has been completely intersected, and this for two building configurations: low and high. The Figure 84 shows the internal and external pressure profiles and the corresponding differential. The boundary of the intersected zone is shown as a blue dotted line.

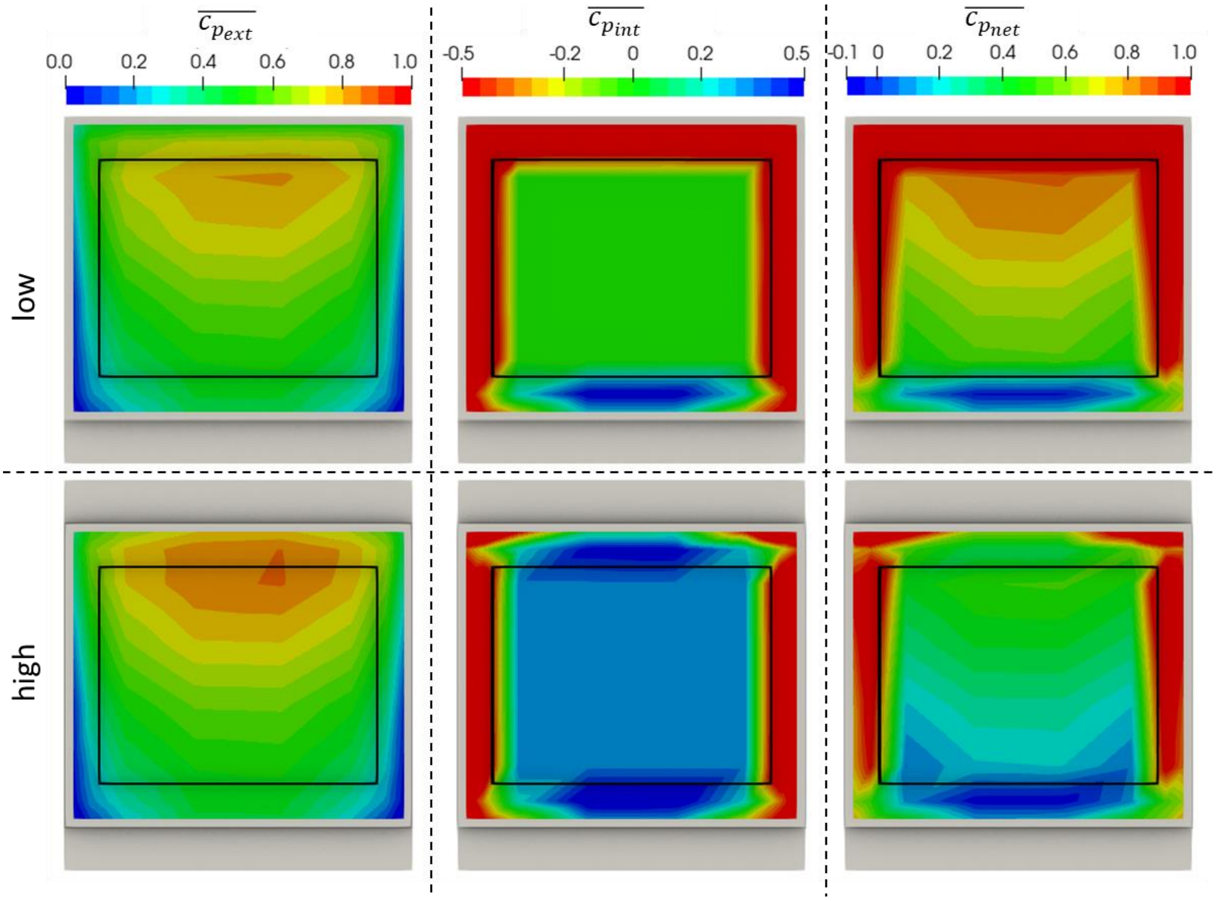

Figure 87 - Mean pressure coefficients for a low and high building fitted with a full skin that is fully overlapped (configuration h_x_l_20_p_00_s_p)

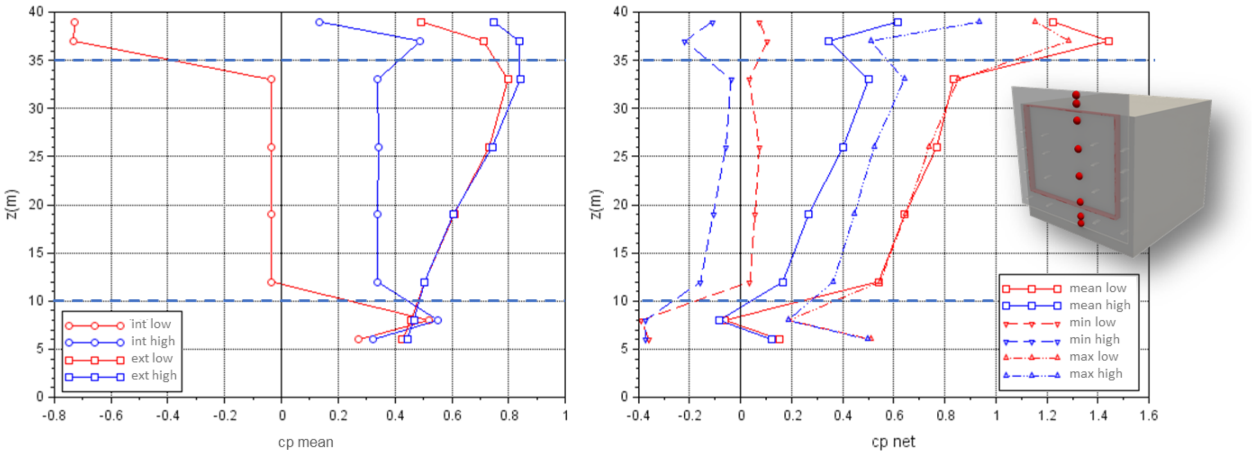

Figure 88 - profile of the mean pressure coefficient on the internal and external double skin facade, and mean and peak net, for a low and high building fitted with a fully overlapped solid skin (configuration h_x_l_20_p_00_s_p)

Analysis of the figures shows that the overlap on the 4 sides results in perfect homogenisation of the mean pressure $\overline{c_{p_{\imath nt}}}$ inside the air gap. The profile of the pressure differential $\overline{c_{p_{net}}}$ on the double-skin facade is then directly modelled on that of the external pressure $\overline{c_{p_{ext}}}$ subtracted from the uniform value of the pressure inside the air space $\overline{c_{p_{\imath nt}}}$.

As the skin is completely intersected, we might have expected the pressure inside the air space to be equal to the static pressure of the test section of the wind tunnel, and therefore to obtain a zero pressure coefficient in the intersected air space. But not only is this pressure coeffcient not zero, it is also different in the two building configurations studied. It is close to 0 and slightly negative for the low building, and around +0.35 for the high building. The overlaps are fitted with an O-ring on one of their edges, to ensure a watertight seal with the building facade. They are attached to the double-skinned facade by two tenons, but there is no device to ensure a seal between the overlap and the inside face of the double skin. This raises the suspicion that there are leaks all along the perimeter of the overlap. The pressure inside the air space will be balanced by the average pressure of the leaks around the perimeter of the overlap. This equalisation takes place almost instantaneously. The Figure 89 plots the pressure signal for two pressure taps positioned on the inside face of the double skin, and located diametrically opposite each other in the overlap zone. The figure shows that the pressure signals are perfectly equal. The pressure fluctuates homogeneously throughout the entire intersected zone. These fluctuations are induced by the pressure fluctuations at the edge of the overlap, due to the turbulent structures of the Atmospheric Boundary Layer.

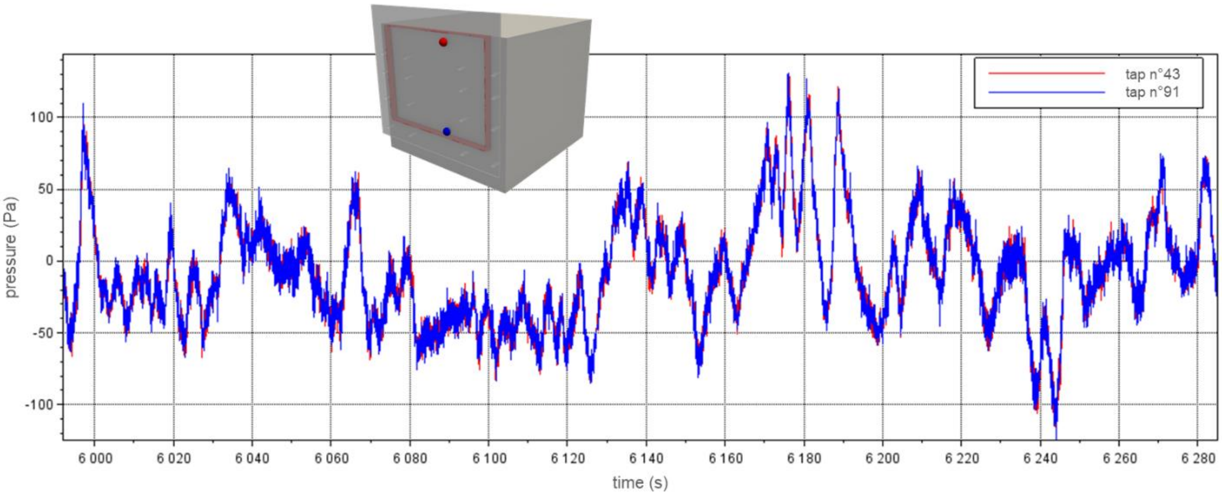

Figure 89 - extract of the temporal pressure signals at two points in the air gap (configuration h_b_l_20_p_00_s_p)

The pressure balancing of the air space in the overlapped zone will therefore be very different depending on how the leaks in the segmentation affect this balancing. This is therefore a fairly random parameter which can have a major impact on the loads on the double skin. This configuration can therefore prove problematic when it comes to accurately dimensioning wind loads on the double skin.

We are now interested in the case of a completely cut and porous skin. A uniformly distributed porosity of 8% and 15% is tested, as studied in §4.5.1. The Figure 90 and Figure 92 plot the mean pressure coefficients measured on the facade for a high building and a low building respectively, for two different porosities, and compare them with the case of a solid skin presented previously. The Figure 91 and Figure 93 show the corresponding profiles.

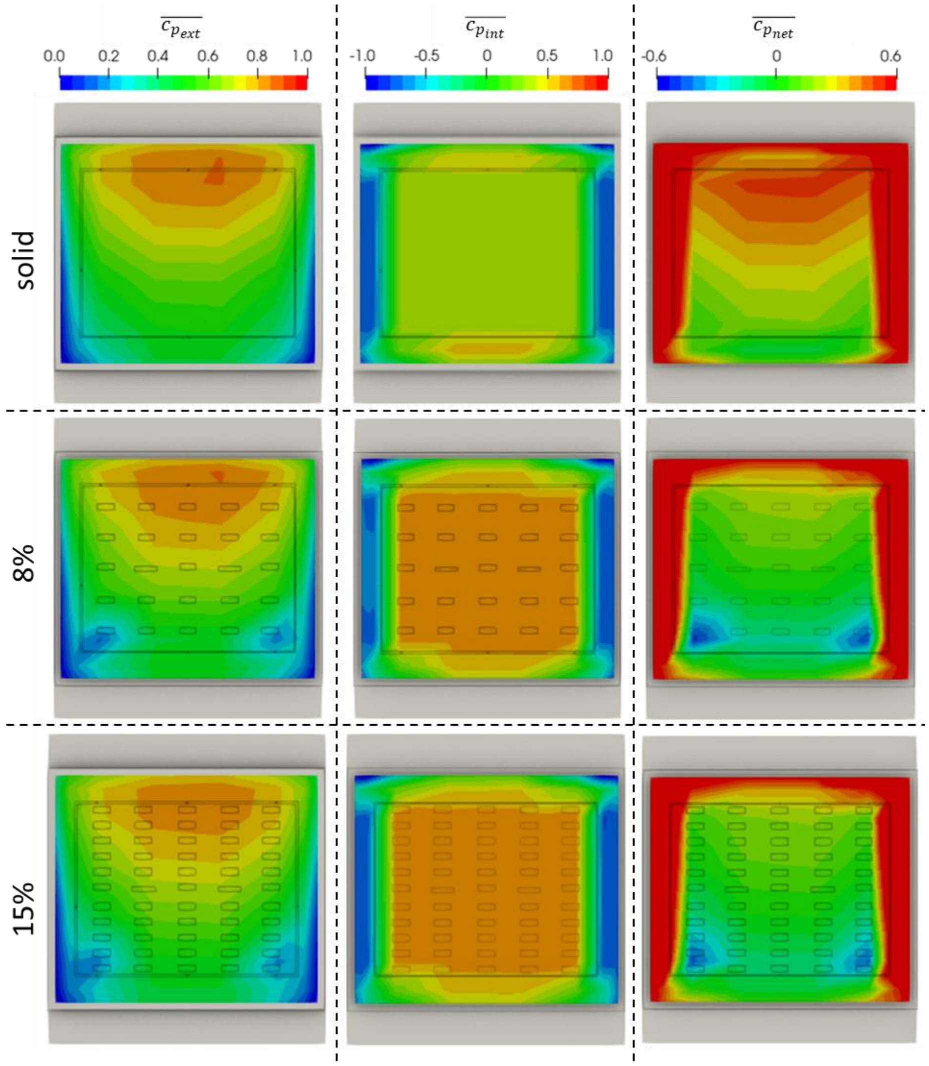

Figure 90 - mean pressure coefficients for a tall building fitted with a fully overlapped variable porosity skin (configuration h_h_l_20_p_xx_s_p)

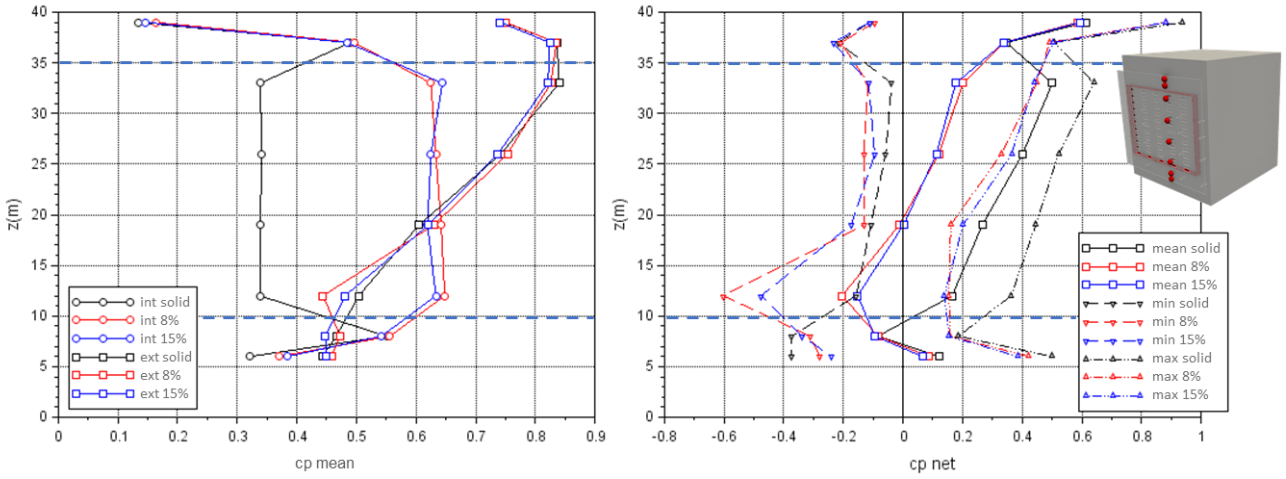

Figure 91 - profile of the mean pressure coefficient on the internal and external double-skin facade, and mean and peak net, for a tall building fitted with a fully overlapped variable porosity skin (configuration h_h_l_20_p_xx_s_p)

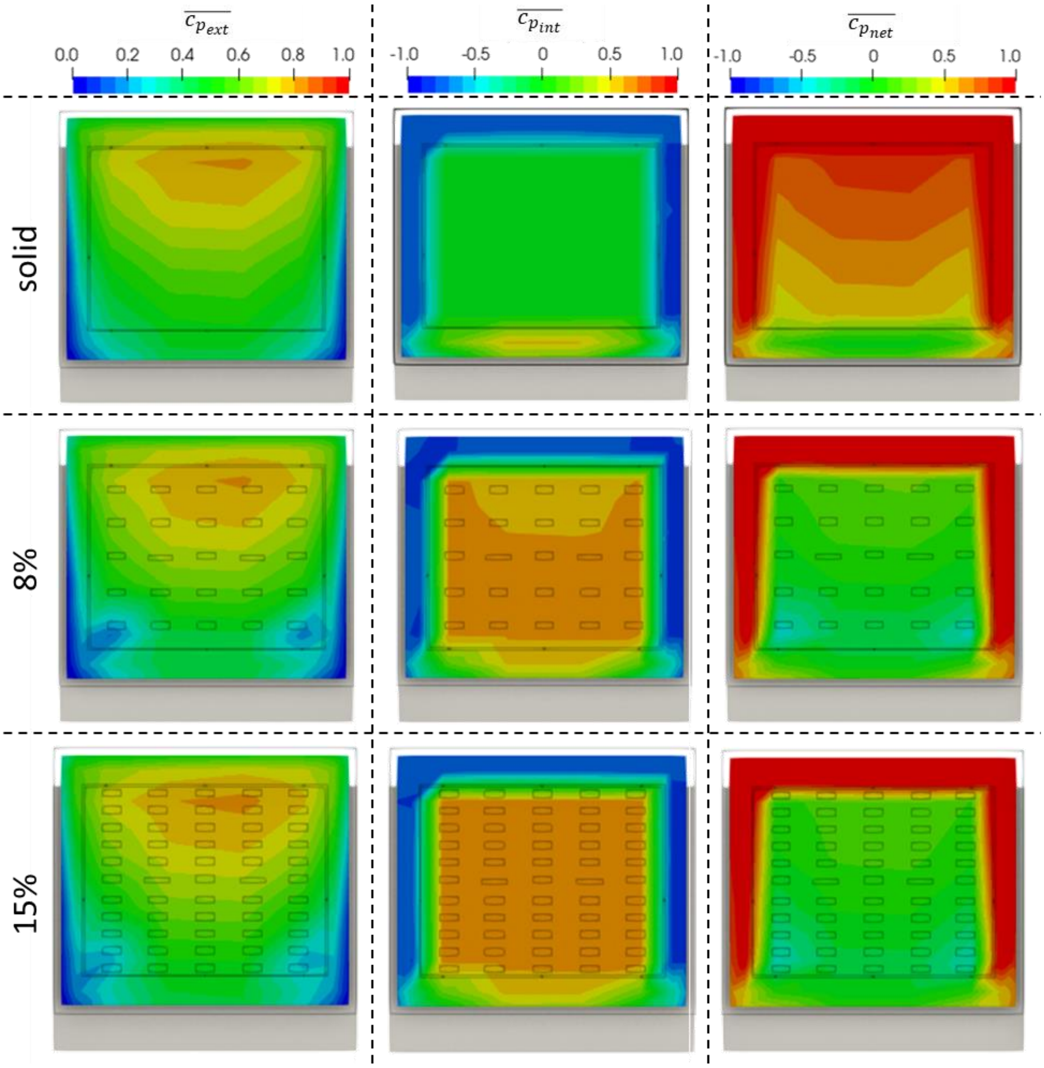

Figure 92 - mean pressure coefficients for a low-rise building fitted with a fully overlapped variable porosity skin (configuration h_h_l_20_p_xx_s_p)

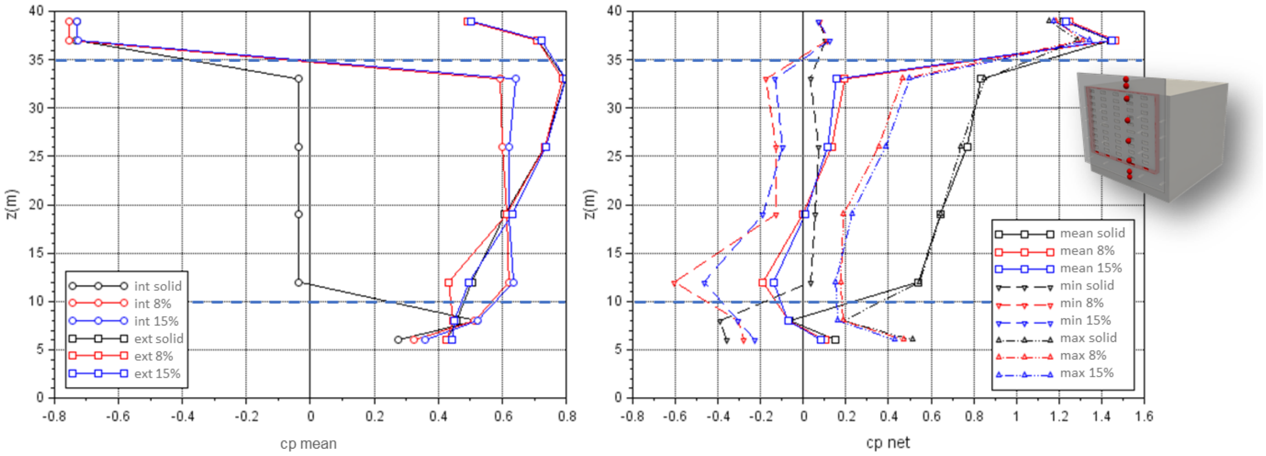

Figure 93 - profile of the mean pressure coefficient on the internal and external double-skin facade, and mean and peak net, for a low-rise building fitted with a fully overlapped variable porosity skin (configuration h_b_l_20_p_xx_s_p)

The figures show that in both configurations, the presence of porosity will once again change the pressure balance in the intersected air gap. The pressure $\overline{c_{p_{int}}}$ remains relatively homogeneous throughout the intersected zone. The Figure 94 plots, by analogy with Figure 89, the pressure signal for two pressure taps positioned on the inside face of the double skin and located diametrically opposite each other in the overlapped zone.

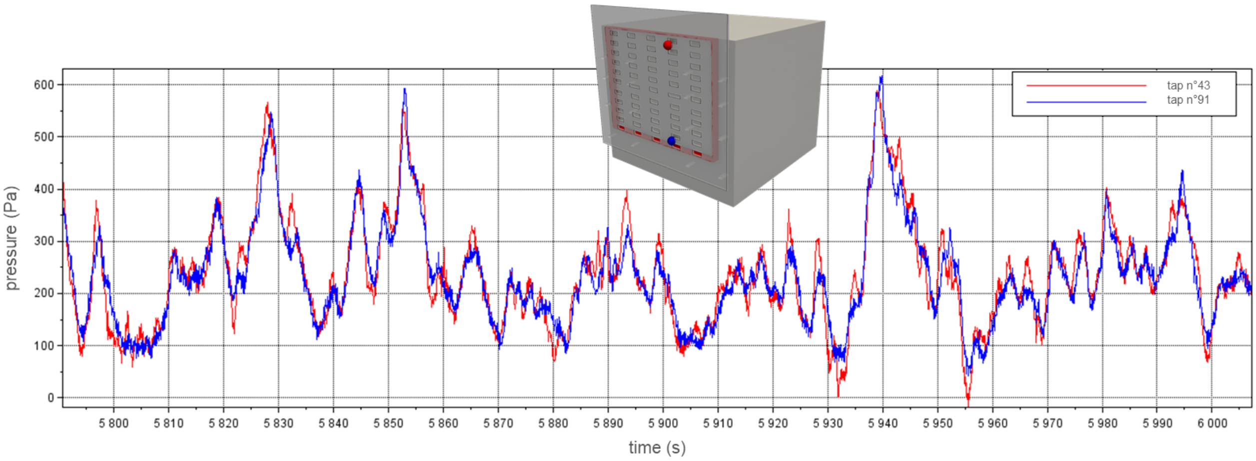

Figure 94 - extract of the temporal pressure signals, at two points of the air gap (configuration h_b_l_20_p_15_s_p)

Once again, the signals are close, showing that spatial homogenisation on the scale of the intersected zone occurs almost instantaneously over time. It should be noted, however, that the signals are less synchronous than what was observed with a solid skin, which shows that there are still slight variations in pressure equalisation at the scale of the intersected zone.

The value at which the pressure $\overline{c_{p_{int}}}$ sets in the air space is identical for the two porosity values, and for the two building heights. The pressure in the air space is in fact equal to the average value of the pressure $\overline{c_{p_{ext}}}$ on the external face of the intersected zone. Given the pressure gradient on the external face (higher at the top than at the bottom), the internal pressure $\overline{c_{p_{int}}}$ will be lower than the external pressure $\overline{c_{p_{ext}}}$ on the upper part of the intersected zone, and the internal pressure $\overline{c_{p_{int}}}$ will be higher than the external pressure $\overline{c_{p_{ext}}}$ on the lower part.

In terms of average pressure differential $\overline{c_{p_{net}}}$ the result is that the upper part of the cut zone is slightly in compression, while the lower part of the cut zone is slightly in pull-out. The average values $\overline{c_{p_{net}}}$ are low, but the peak values $\widehat{c_{p_{net}}}$ are higher, and can be negative or positive.

To illustrate this dynamic, the Figure 95 plots the PDFs of the internal, external and net pressure signals at 3 points on the facade for a configuration with a low building.

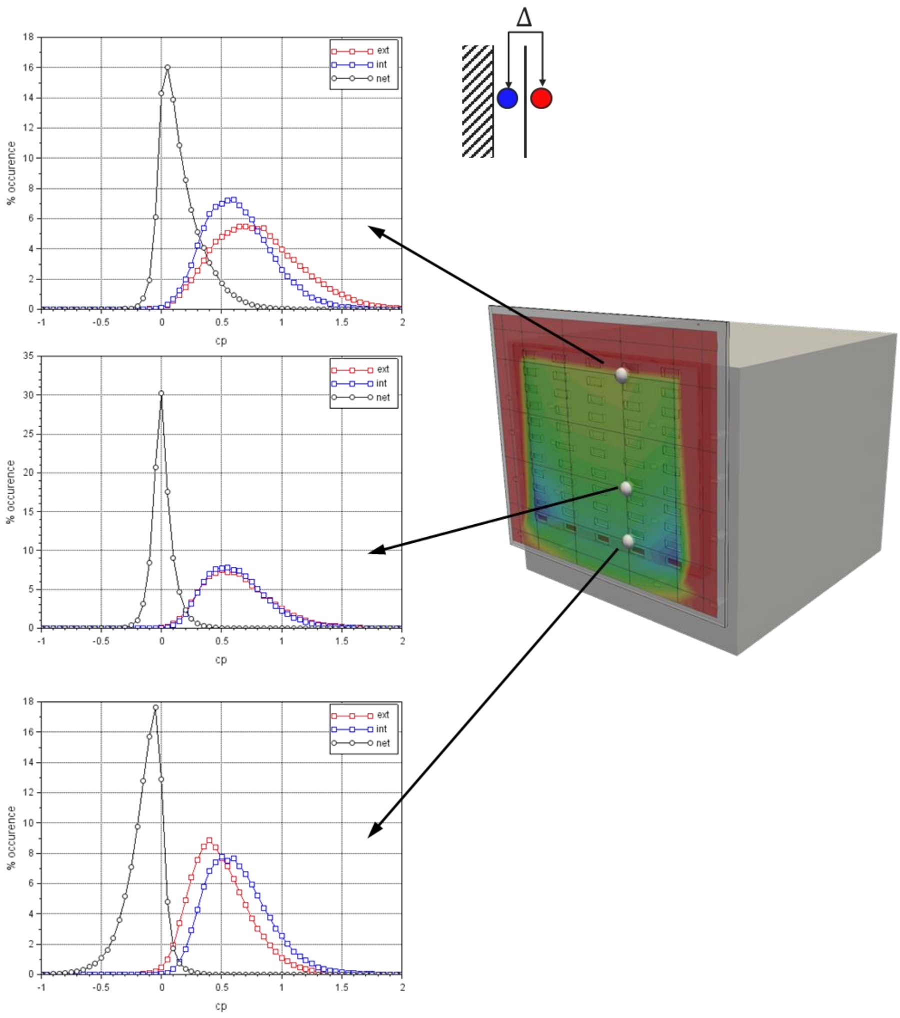

Figure 95 - PDF of the pressure coefficient, interior, exterior and net, at three points of the double-skin facade (configuration h_b_l_20_p_15_s_p)

The figure shows that the internal pressure PDF $\overline{c_{p_{int}}}$ are identical at the 3 measurement points, highlighting a homogeneous dynamic throughout the intersected zone, in agreement with the temporal pressure signals seen Figure 94. The external pressure PDF $\overline{c_{p_{ext}}}$ changes between the upper and lower parts of the intersected zone, due to the wind gradient upstream of the building. The offset between the external pressure PDF and the internal pressure PDF therefore seems to shape the pressure differential PDF $\overline{c_{p_{net}}}$. At the centre of the intersected zone, it can be seen that the external and internal pressure PDFs are almost superimposed. The pressure differential PDF is then very narrow and centred on a value close to 0, indicating that the facade will be alternately in compression and pull-out. On the upper part of the intersected zone, the PDF of the pressure differential is off-centre towards positive values, which seems to indicate that the facade will most often be in compression. On the other hand, in the lower part of the intersected zone, the PDF of the pressure differential shifts towards negative values, showing that the facade will mainly be in pull-out.

The profiles in Figure 93 show that the peak values $\widehat{c_{p_{net}}}$ are close for the two values of the double-skin porosity, as well as for the two building heights. The influence of the porosity ratio on pressure equalisation therefore appears to be fairly slight.

The Figure 96 plots the mean pressure coefficients measured on the outer face $\overline{c_{p_{ext}}}$internal $\overline{c_{p_{int}}}$as well as the average pressure differential noted $\overline{c_{p_{net}}}$ for a 15% porous skin, fully intersected, for two building configurations: low and high. The Figure 97 shows the corresponding pressure profiles. The figures are therefore similar to Figure 87 and Figure 88 but this time with a 15% porous skin.

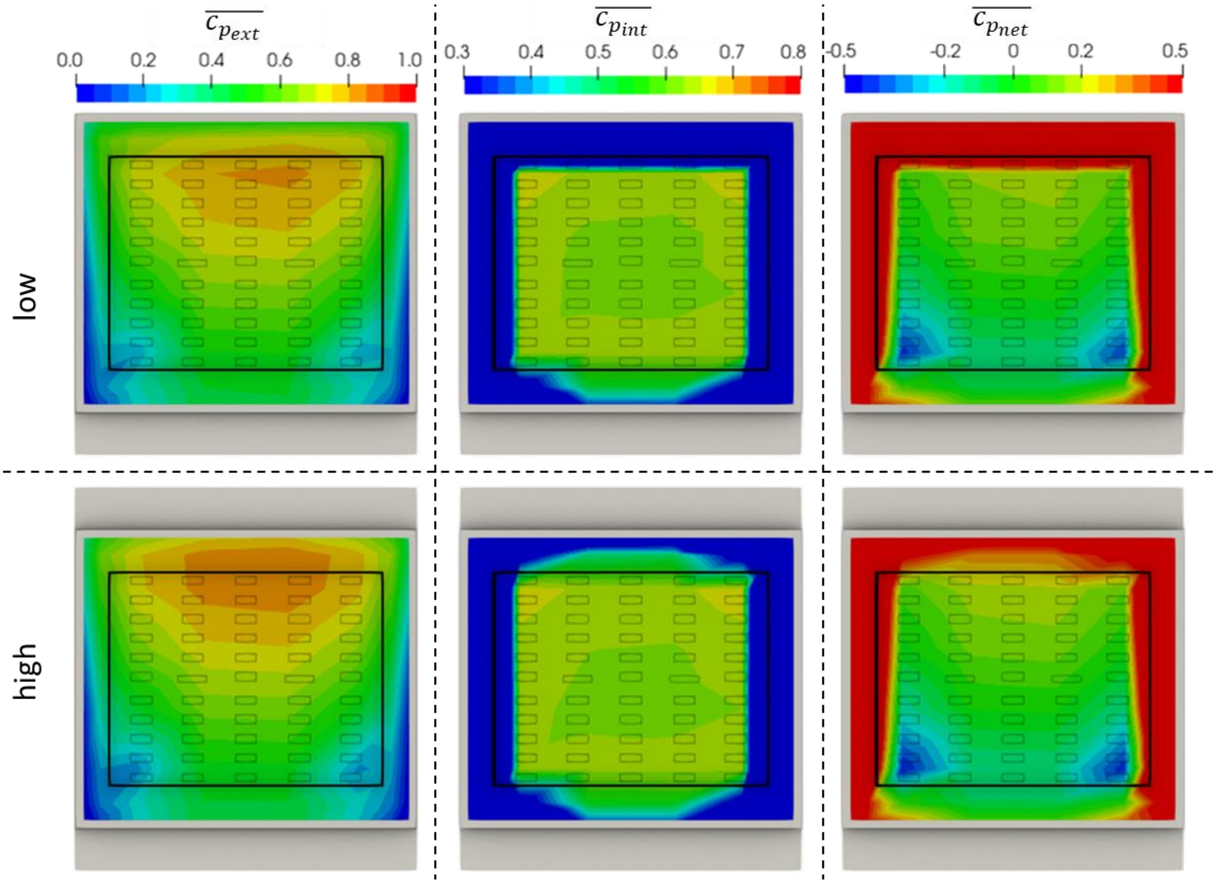

Figure 96 - Mean pressure coefficients for a low and high building fitted with a 15% porous skin that is fully overlapped (configuration h_x_l_20_p_15_s_p)

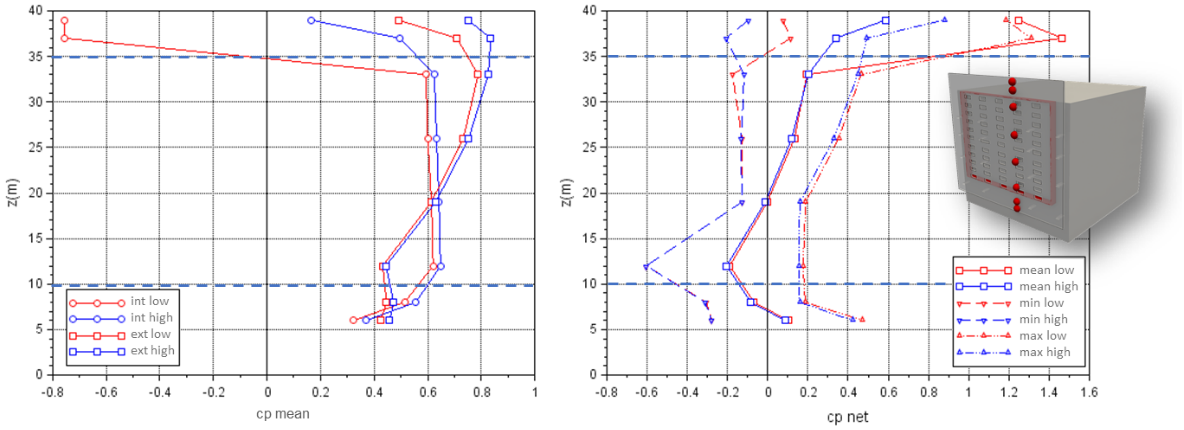

Figure 97 - profile of the mean pressure coefficient on the internal and external double skin facade, and mean and peak net, for a low (red) and high (blue) building fitted with a 15% porous skin that is fully overlapped (configuration h_x_l_20_p_15_s_p)

Contrary to what was observed for a solid skin that was completely cut back, the pressure profiles in the cut-back zone are identical here for both building heights. The pressure balance is not only identical on means values, but also for the peak values. This therefore seems to indicate that, for a double-skinned facade that is fully intersected and porous, pressure balancing will take place solely on the basis of the pressure dynamics on the external face of the intersected zone, independently of the flow on the rest of the double-skinned facade. This is a strong assumption that can be useful for the design of large double-skin facades.

The mapping of the average pressure differential $\overline{c_{p_{net}}}$ shows two higher pull-out zones on the lower corners of the cut zone. These pull-out zones are thought to be linked to a flow forming in the air gap and resulting from the external pressure difference between the top and bottom of the cut zone. This flow is illustrated by a numerical simulation Figure 98. It would rush into the air gap over the upper part of the cut zone, and escape from the lower part, a priori preferentially from the sides, in a manner consistent with the pull-outs observed on the pressure differential map.

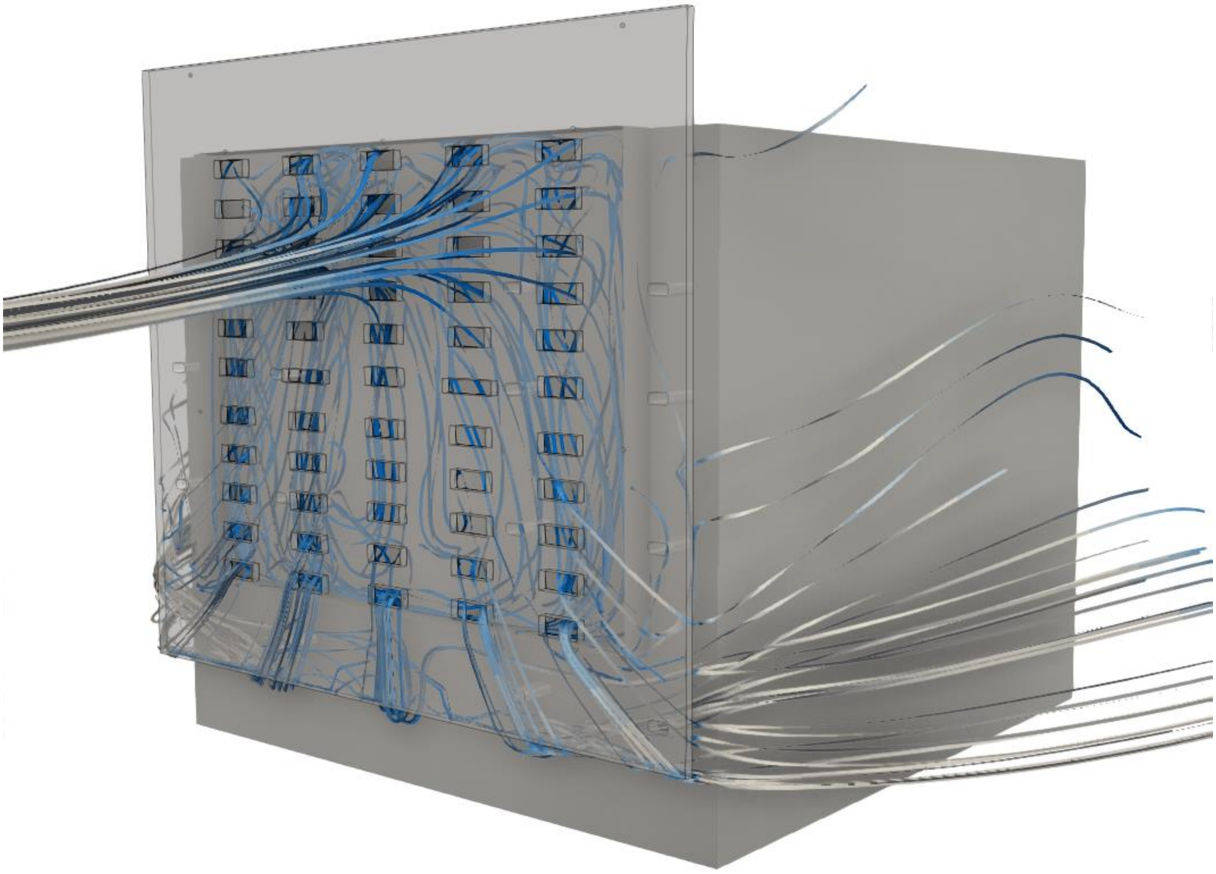

Figure 98 - flow structure within the intersected zone from a numerical simulation (configuration h_b_l_20_p_15_s_p)

This configuration is interesting because the low dependence on porosity and flow around the building means that the pressure balance of the air space and wind loads can be well controlled. This configuration is in fact described in §7.2.10 of the Eurocode [8] with the notion of :

"Walls and roofs with an impermeable inner wall (envelope) and a permeable outer wall with an approximately uniformly distributed permeability.

In this case, the Eurocode proposes the following approximation for the peak differential:

$\widehat{c_{p_{net}}} = \frac{2}{3}\overline{c_{p_{ext}}}$ for compressions

$\widehat{c_{p_{net}}} = -\frac{1}{3}\overline{c_{p_{ext}}}$ for pull-outs

The Figure 99 again plots the profile of the pressure differential over a fully cut and 15% porous skin, comparing it with the design proposed by the Eurocode.

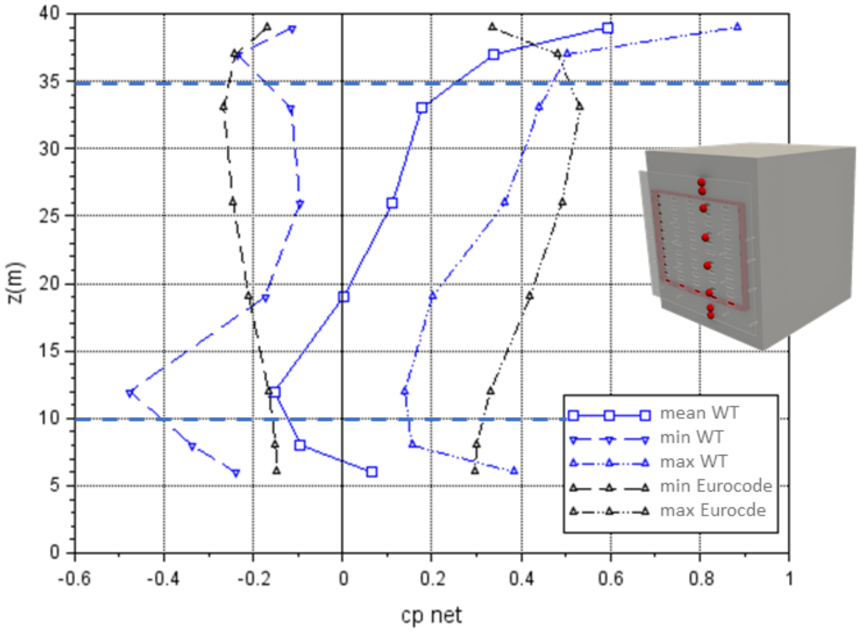

Figure 99 - comparison of peak differential measurements with the values proposed by the Eurocode (configuration h_h_l_20_p_15_s_p)

The figure shows that the values proposed by the Eurocode are of the same order of magnitude as the peaks actually measured, while remaining slightly conservative, which is generally the case with the dimensioning proposed by the Eurocode. However, it should be noted that the Eurocode design slightly underestimates the peak pull-out at the foot of the facade, compared with what was actually measured in the wind tunnel.

4.6 PERIPHERAL SKIN

The study now focuses on the case of a double skin propagating on all four facades of the building, without any overlap, as illustrated in Figure 22. The analysis of the previous measurements showed that the pressure in the air gap would equilibrate according to the pressures imposed by the external flow at is boundaries. In the case where this air gap crosses all the facades, we can wonder how the pressure will balance when part of the facades will be in compression, while the other part of the facades will be in depression. Can pressure fluctuations propagate from one facade to another? And disrupt the pressure balance of the air space?

The analysis begins with the case of a tall building. The Figure 100 studies the dynamics of pressure balancing at the centre of the double-skin facade by plotting the PDF of the internal and external pressures, as well as the net differential. The analysis is carried out for 3 wind directions, and the results are compared with the case of a double-skin facade limited to a single facade.

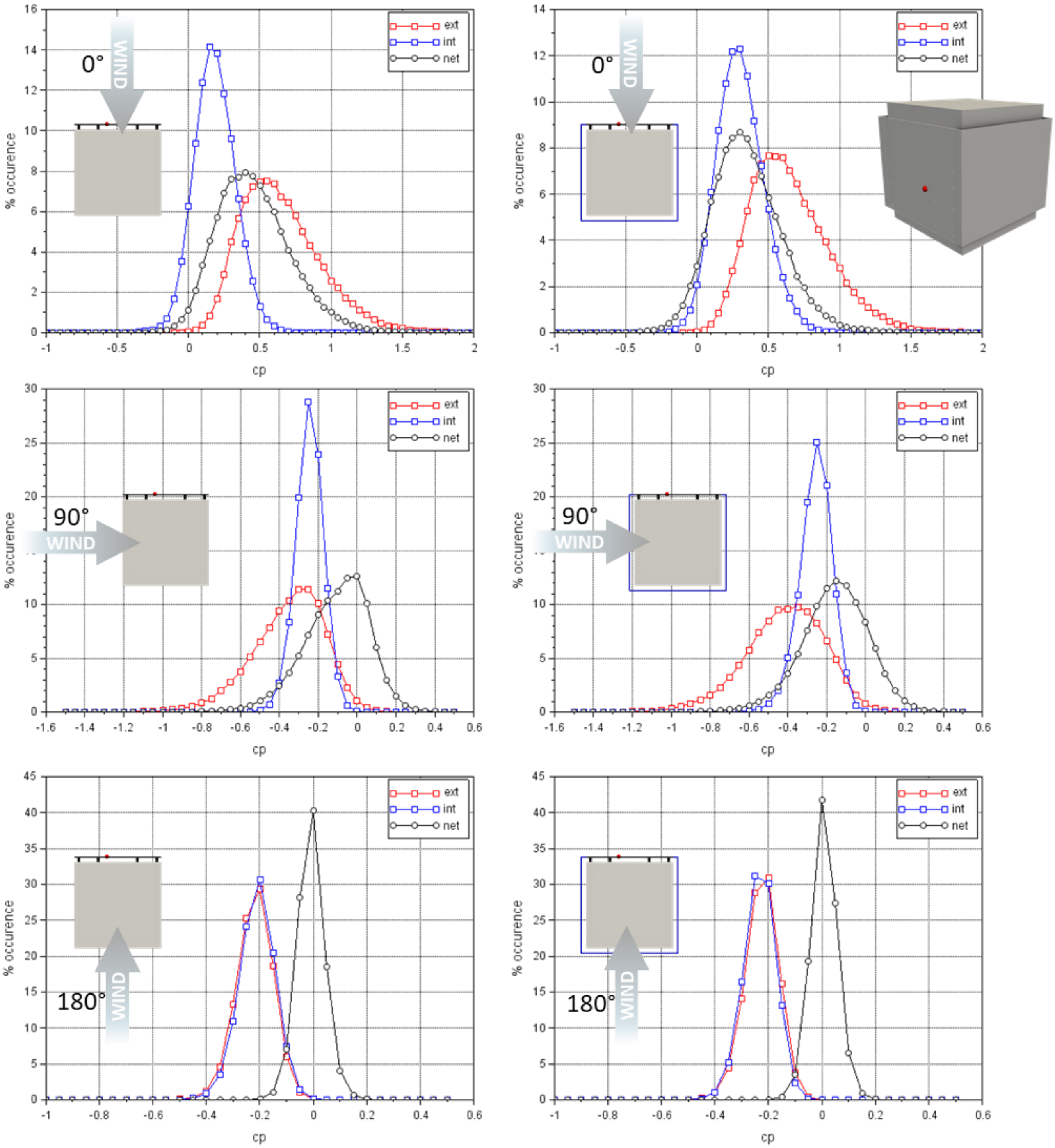

Figure 100 - PDF of the pressure coefficient, interior, exterior and net, at one point of the double-skin facade for a tall building, for 3 wind directions, with (right) and without (left) perimeter skin

Generally speaking, the figures do not show any major change in the pressure dynamics in the air gap due to the presence of the peripheral skin, for any of the 3 wind directions.

For a direction of 0°, the internal pressure PDF $c_{p_{int}}$ is slightly off-centre towards positive pressures in the presence of the peripheral skin. This can be explained by the fact that the peripheral skin will cut off access to negative pressures on the lateral edges of the double skin, according to the same principle as the vertical segmentations. This increases the pressure level in the air space, and lowers the net loads $c_{p_{net}}$.

For a 90° wind direction, the internal pressure PDF $c_{p_{int}}$ is only slightly affected by the presence of the peripheral skin. Slight variations, observed on both the internal pressure $c_{p_{int}}$ and external pressure $c_{p_{ext}}$ of the double skin facade can be attributed to the change in geometry induced by the presence of the perimeter skin. This may indeed have an impact on the way the flow is structured along the facade for this wind direction where the flow is grazing. In any case, there is no evidence of positive pressure fluctuations that could have propagated from the upwind facade.

Finally, for a wind direction of 180°, the PDFs are identical for both configurations. Here again, this comparison shows that, a priori, there are no pressure fluctuations that could propagate from facades where the pressure would be much lower, or on the contrary, much higher.

The Figure 101 and the Figure 102 respectively plot the peak compression and peak pull-out, all wind directions combined, for a low and high building, fitted with a solid skin, without segmentation, with and without a peripheral skin.

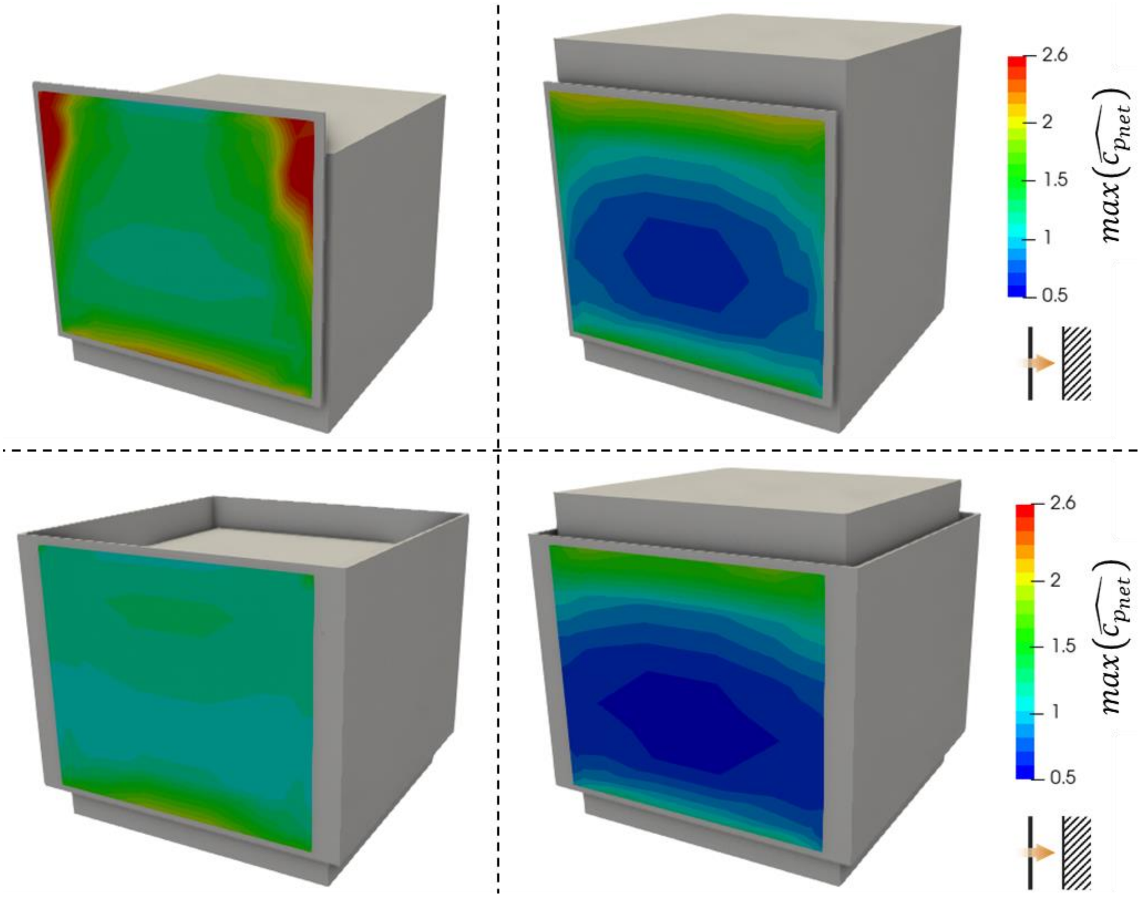

Figure 101 - mapping of the maximum peak pressure differential coefficient (peak compressions) for all wind directions combined, for a low and high building, with and without peripheral skin

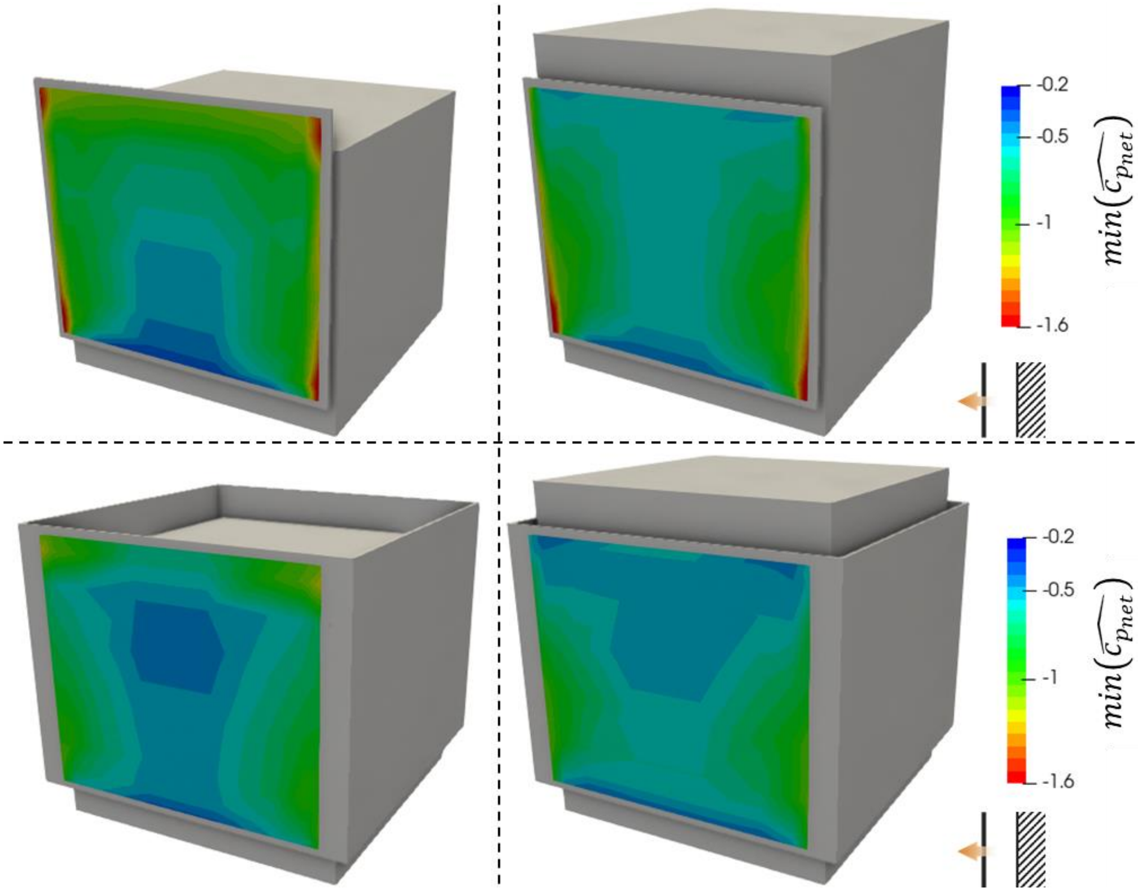

Figure 102 - Mapping of the coefficient of minimum peak pressure differential (peak pull-outs) for all wind directions combined, for a low and high building, with and without peripheral skin

Analysis of the maps shows that the presence of a peripheral skin leads to a reduction in loads at the edges of the double skin. This reduction is observed for both the low and high building configurations. This can be explained by the disappearance of configurations where the flow rushes in through the lateral edges of the double skin, and generates strong accelerations in the air space, thus generating very high net loads (see §4.2.3). At the centre of the facade, the loads are only slightly modified by the presence of the peripheral skin. Once again, these maps of peak loads do not highlight the possibility of pressure fluctuations coming from other facades, which could propagate in the air space to significantly affect the peak loads of the double-skin facade.

4.7 SUMMARY ON WIND LOADS

This study highlighted the very high variability of wind loads on the double-skin facade according to the different geometric modularities that were investigated. For example, for the same double skin 35m high by 40m wide leaning against the facade of a building, the wind loads will depend very strongly on the geometry of the building, the direction of the wind, the presence of segmentations, the thickness of the air space and the porosity of the double skin. All these parameters will have a comparable influence, and the different combinations of these parameters will lead to different results in terms of balancing and pressure dynamics in the air space.

4.7.1 Maximum loads for all configurations

The first step is to look at the maximum peak loads that have been measured on the double-skin facade in order to provide as conservative a picture as possible of the loads that can be exerted on this facade. The Figure 103 maps the maximum and minimum peak pressure differential coefficients obtained for all wind directions and for all the geometric configurations investigated.

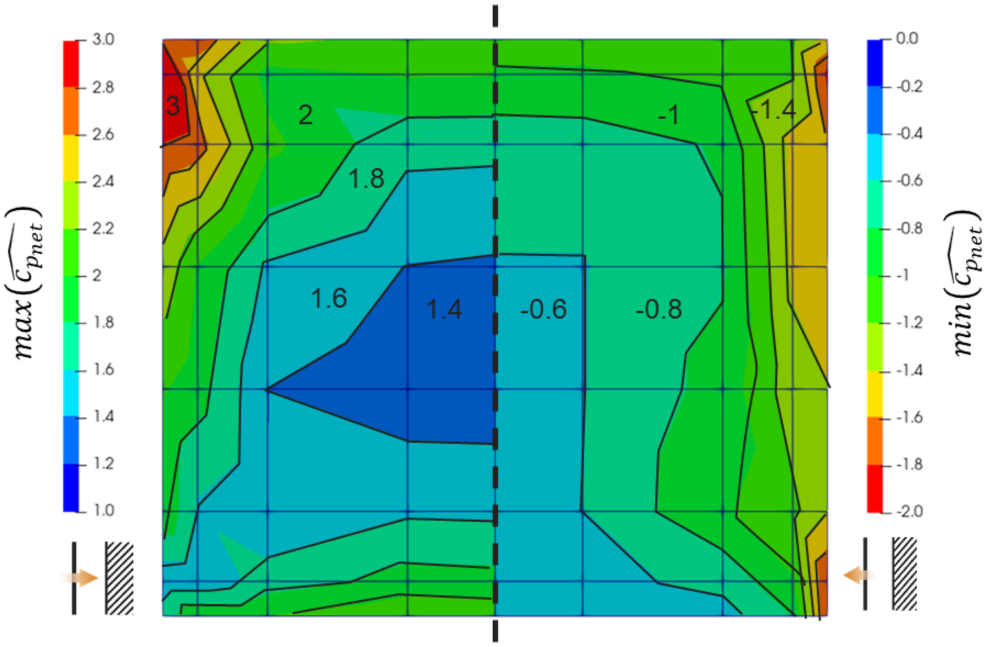

Figure 103 - Coefficient of maximum (peak compression) and minimum (peak pull-out) peak pressure differential, all wind directions and geometric configurations combined

This mapping shows firstly that, for the geometric configurations considered in this study, the double-skin facade is subject to greater compressive stress than pull-out stress. Peak compressions will vary between +1.4 and +3, while peak pull-outs will vary between -0.6 and -1.8. On a "classic" facade, it is the pull-outs that are more important.

The highest peak pull-out essentially corresponds to local detachments at the edge of the facade, for configurations where the flow is grazing the facade. These detachments will generate high pressure differentials as shown in Figure 58. At the centre of the facade, the maximum peak pull-out corresponds to the strongest pressure fluctuations when the pressure is balanced on average on either side of the skin, as shown for example Figure 95.

The highest peak compressions, of the order of +3 and observed on the upper corner of the facade, correspond to flow configurations with a low building, where the facade is then feathered in relation to the roof of the building, as shown in Figure 66. The double-skin facade can then be likened to an acroterion. The pressure coefficient measured on the double-skinned facade is actually in agreement with the values that could be proposed by the Eurocode [8] for these objects. Apart from these zones, which are very localized at the edges of the facade, there is a more extensive zone at the periphery of the facade with coefficients between +2 and +2.4. These correspond to zones where the flow will rush into the air space, and where the acceleration of the flow will lower the pressure on the inside of the double skin, increasing the net loads. At the centre of the facade, the coefficient decreases to +1.4. This lower value is partly explained by the decrease in pressure on the external face of the facade, due to the dynamic pressure gradient upstream of the building.

So one of the difficulties in generalising the results of this study will be to determine what conditions the transition from a zone where the coefficient is of the order of +2 to a zone where the coefficient is of the order of +1.5.

In any case, this load case, taking all configurations together, shows that the recommendations of the SNFA sheet [11] which are included in the RAGE [12] program, do not conservatively cover some of the configurations tested in this study, since the net peak loads far exceed the +1.5 value proposed by these documents.

4.7.2 Pressure balancing mechanisms

The measurements carried out in this study have enabled us to gain a better understanding of the mechanics of pressure balancing in the air gap. It seems difficult to be exhaustive about everything that can happen, given that the combination of different parameters can generate so many different situations. However, we can try to summarise the mechanisms at work on the basis of a few main principles:

1) the air space will balance itself according to the pressures applied to all its openings

2) this balancing takes place almost instantaneously

3) If there is a sufficient difference in pressure between two openings in the air gap, this will generate a flow from the highest pressure to the lowest pressure.

4) in which case the dynamic pressure of this flow will have an impact on the static pressure of the inner face of the double skin, and consequently on the wind loads

5) in which case the rushing flow in the air gap can generate local accelerations that significantly increase wind loads.

The reference experiment enables the pressure balance of the air space to be characterised directly by measuring the pressure on the inside of the double skin. If the model does not allow the pressure in the air space to be measured directly, the pressure balance can be characterised by :

1) determining the instantaneous pressures at each opening in the air gap

2) determining the flow generated in the air gap and its impact on the pressure balance of the skin

3) the determination of potential local effects at the level of flow entanglements in the air gap

The first point can be addressed quite easily by judiciously placing pressure taps on a model in an Atmospheric Boundary Layer wind tunnel, and recording the pressure signals synchronously.

The second point will be the subject of attempts at modelling using a nodal approach, which will be detailed in the following section.

5 NODAL MODELLING

The problem of dimensioning double-skin facades wind loads is therefore essentially based on balancing the pressure of the air space and determining the instantaneous pressure within it, synchronously with the pressure applied to the external face of the double skin.

Given the thinness of the air gap, the flow in the latter can be assimilated to that of a plane channel in the case of segmented double-skins, or a 2D flow in the absence of segmentation. The idea would then be to use simple nodal approach modelling, which is much faster in terms of calculation time than CFD approaches, in order to determine the instantaneous pressure balance in the air gap, based solely on the pressure signals measured at its boundaries. The principle is illustrated Figure 104.

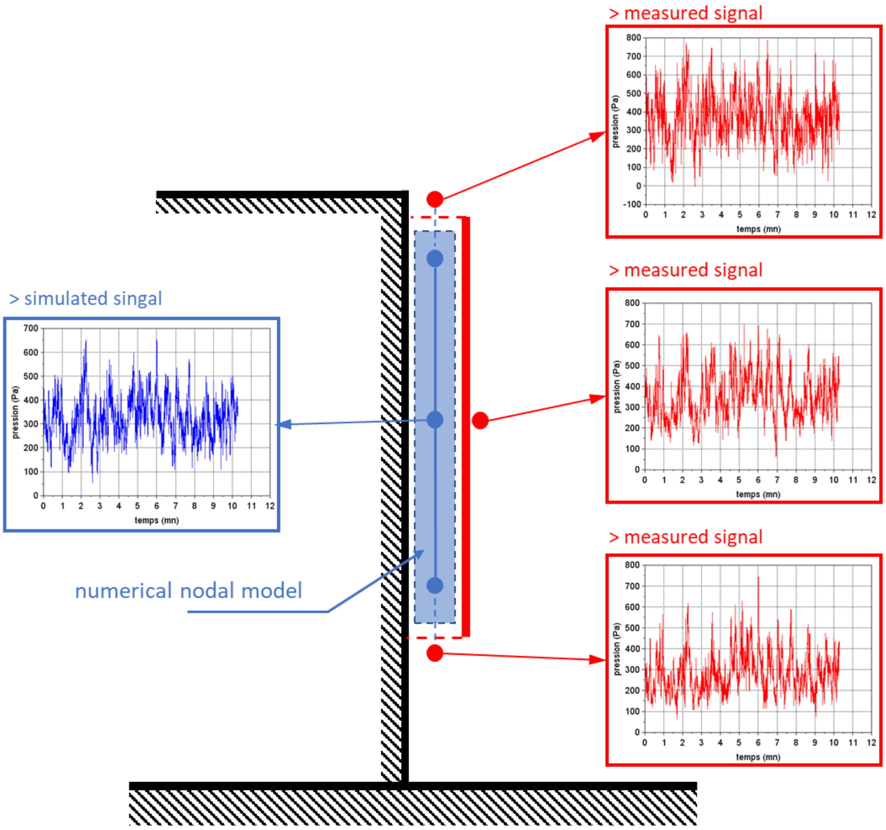

Figure 104 - principle of using the nodal approach to determine the instantaneous pressure balance in the air gap

This principle would thus provide a "virtual measurement" of the pressure inside the air gap for models which, for reasons of scale, would not allow the pressure in the air gap to be measured directly. In order to assess the relevance of this approach, we propose to apply it to the reference experiment, and to compare the results thus obtained with the measurements made in the wind tunnel.

5.1 NODAL APPROACH AND CODE MATHIS

The nodal approach is classically used for aeraulics problems, i.e. the study of confined flows propagating in a series of ducts. The aeraulic network is then discretised in the form of nodes (hence the name nodal) connected together by branches. These branches are used not only to model the channelling of flow through the ducts from one node to another, but also to model the pressure losses caused by the circulation of air in the ducts. Depending on the type of connection between the nodes, different types of pressure loss models can be applied.

Thus the channel problem described in §2.2 can be simplified by a nodal network as shown in Figure 105. The network consists of 4 nodes (in blue) and 2 boundary conditions (in red). The various nodes are connected by branches in which friction losses (so-called linear losses) are modelled. The end nodes are linked to the boundary conditions by branches reflecting singular head losses caused by the flow becoming entangled in the channel, or by backflow to the outside.

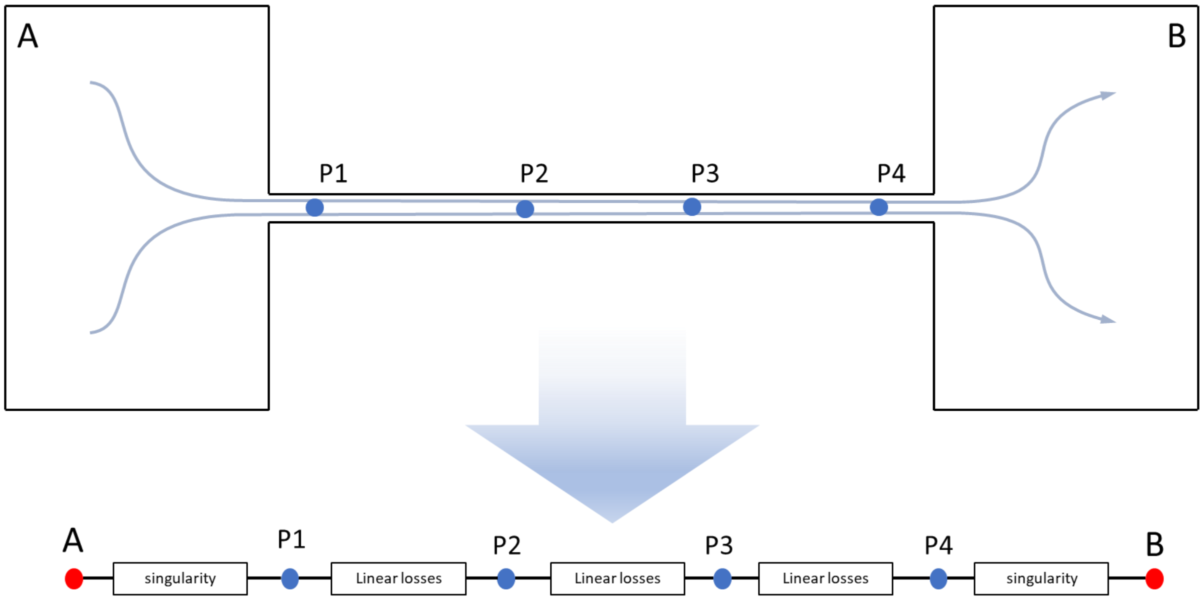

Figure 105 -modelling of a channel connected to two pressurised volumes

The §2.2 showed how the pressure inside the duct varied greatly depending on the inlet cross-sections, and the resulting pressure balance. This calculation is carried out using a nodal calculation code, which solves the conservation of mass and mechanical energy in the aeraulic network.

The MATHIS nodal code is used in this study. This open source code was developed at the CSTB by François Demouge (https://gitlab.com/CSTB/mathis). The MATHIS calculation code was developed to take into account the thermal and aeraulic problems of building ventilation networks. In the context of this study, the code is mainly used for its ability to reproduce instantaneous pressure balancing in an aeraulic network. It is important to emphasise here that the aim of this study is not to validate the MATHIS code, which has already been the subject of several validation campaigns, but rather the ability of a nodal approach to determine the pressure balancing of the air gap with a view to the wind loads assessment of a double-skin facade. It is not the tool itself that is being evaluated, but rather its suitability for this purpose.

5.2 NODAL MODEL OF THE AIR GAP

5.2.1 Discretisation of the air gap

The aim is to set up a nodal model to study the pressure balance of the air space in the double-skin facade of the reference experiment. The Figure 106 and Figure 107 show a visualisation of the nodal model thus constructed in 2D and 3D respectively, superimposed on the geometry of the facade. The model is made up of 64 nodes (in blue) distributed at the locations of the pressure taps in the model experiment.

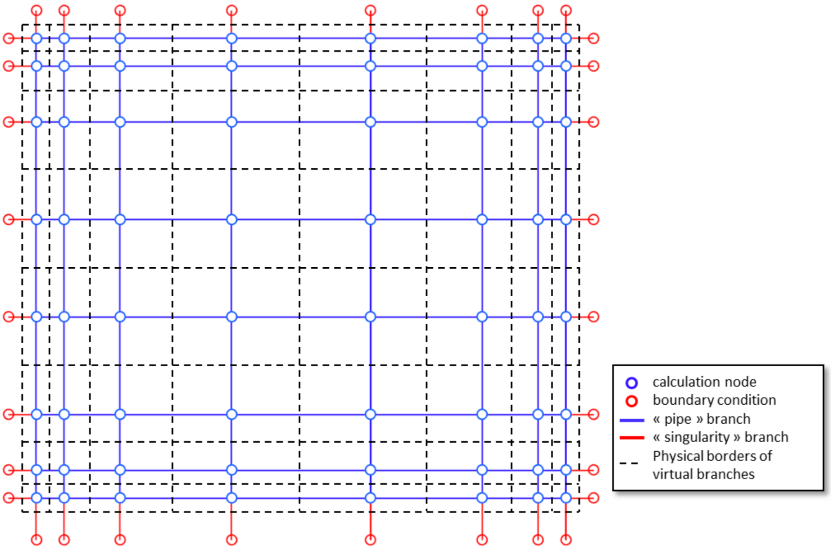

Figure 106 - 2D visualisation of the nodal model of the air gap in the double-skin facade

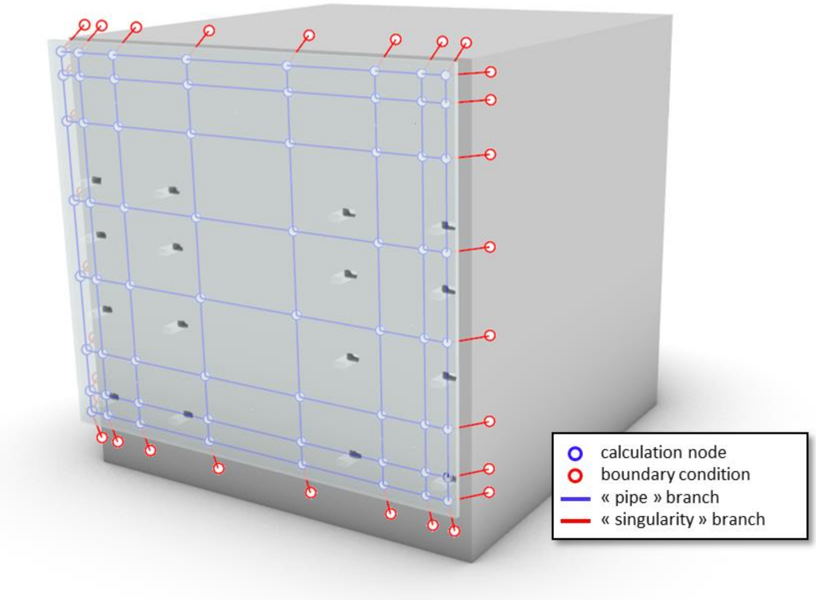

Figure 107 - 3D visualisation of the nodal model of the air gap in the double-skin facade

At the periphery of the model, the end nodes are linked to 32 boundary condition nodes (in red). These boundary conditions correspond to the pressure taps located on the facade of the building, outside the air gap. For the lower edge, they correspond to the pressure taps located at the foot of the facade. For the lateral edges, they correspond to the pressure taps located on the two lateral sides of the building. For the upper edge, they correspond either to the pressure taps located on the roof for a level building, or to the pressure taps located on the top of the facade for a tall building.

On these boundary conditions (in red), we will prescribe the pressure signal that was measured in the wind tunnel. On the calculation nodes (in blue), we will read the pressure calculated by the nodal model, and compare it with the pressure actually measured in the wind tunnel.

The calculation nodes are interconnected by branches (in blue on the figures) arranged along a vertical and horizontal axis. In these branches, defined as "PIPE" types in the MATHIS code, a linear head loss law representing friction is prescribed [13]. To do this, a pipe cross-section and surface roughness are defined. The cross-section of the duct is defined by the thickness of the air gap and the sum of the two half-distances separating the neighbouring nodes. The duct considered in this way is represented by the dotted lines in Figure 106. The surface roughness is considered negligible and taken to be equal to 1µm.

The calculation nodes at the periphery are connected to the boundary conditions by branches (in red) defined as "SINGULARITY" types in the MATHIS code [13]. These branches are used to simulate the loss of head generated by the engulfment or backflow of the flow in the channel. They will prescribe a loss of head in the form of a quadratic law of velocity as seen in §2.2

$$\Delta p_{singu} = \frac{1}{2}\xi\rho U^2$$

The coefficient ξ will vary according to the direction of flow in the branch. If the flow enters the air gap $\xi = 0.5$. If the flow leaves the air gap $\xi = 1.5$. These values, classically used in aeraulic simulations of tunnel ventilation [14] have also been the subject of a sensitivity study, not presented in this report.

5.2.2 Calculation of the static pressure in the air gap

The calculation is carried out on a scale model. The calculation time step is that of the pressure signal acquisition in the wind tunnel, i.e. 0.00195s (512Hz). The simulation is carried out in isothermal mode. All other code parameters are set to default values. The simulation is carried out over a period of 300s, i.e. the entire acquisition time of the wind tunnel signal. The calculation therefore represents 153600 time steps. The simulation requires 3.5 hours of calculation (an equivalent unsteady CFD calculation would require several days).

The calculation code then provides, for each time step, the total pressure calculated at each calculation node. The relevant information for wind loads assessment is the static pressure on the inside of the double skin: $p_{stat} = p_{tot} - \frac{1}{2}\rho U^2$. It is therefore necessary to go back to the flow velocity at each node. The nodes are mathematical objects without volume, which do not allow a notion of speed to be determined directly. It is therefore necessary to consider the flows calculated in each of the branches connected to the node. The Figure 108 represents the four branches connected to the calculation node, distinguishing between the two horizontal branches noted as H, from the two vertical branches noted V. Let S_H and S_V be the cross-sections of the horizontal and vertical branches respectively.

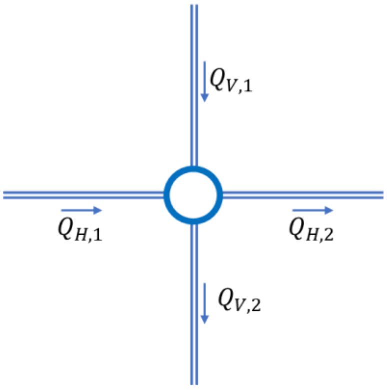

Figure 108 -flows in the four branches connected to a calculation node

For each node, we define a horizontal speed U_x and a vertical speed U_y:

$$U_x = \frac{1}{2}\left(\frac{Q_{H,1} + Q_{H,2}}{S_H}\right)$$

$$U_y = \frac{1}{2}\left(\frac{Q_{V,1} + Q_{V,2}}{S_V}\right)$$

In this way, the process also provides a notion of the directivity of the flow in the air space. The norm of the velocity calculated in this way is then defined $U = \sqrt{U_x^2 + U_y^2}$

This calculation of velocity and static pressure is done in post-processing of the MATHIS simulations. The 'virtual' pressure signals thus calculated at each node are then stored and processed in the same way as the pressure signals measured in the wind tunnel.

5.2.3 Intrinsic limitations of the model

Before analysing the results obtained with this model, we can highlight some of its intrinsic limitations in relation to the physical mechanisms it is designed to model.

By design, the model assumes a constant and uniform velocity in each of the branches. However, analysis of wind tunnel measurements has shown that in certain parts of the air gap, particularly where the flow is embedded in the gap, the velocity can be very inhomogeneous in the thickness of the air gap.

Another limitation concerns the modelling of boundary conditions based on measured pressures, which in this case are static pressures. However, the calculation code expects a total pressure for these boundary conditions. In other words, depending on the flow configuration at the air space boundaries, the model does not necessarily take into account the dynamic pressure of this flow. This can lead to a bias in the modelling because a certain "inertia" of the flow in the air gap induced by the building-scale flow is not taken into account.

Finally, the singular head loss coefficients prescribed at the inlet/outlet branches are not necessarily representative of the local flow topology, depending on how the air gap flow separates/joins the flow at building-scale.

5.3 RESULTS

The aim of this section is to present the results of the model on certain configurations tested in the wind tunnel, in order to assess the model's ability to predict the unsteady pressure equilibrium of the air gap.

5.3.1 Vertically segmented skin

The reference case is a vertically segmented skin. This configuration is the one that most closely resembles a flat channel, to which a pressure differential is applied at each of its ends. It should therefore be particularly suitable for nodal modelling. Initially, we consider a level building as studied in §4.1.1.

The Figure 109 plots the profile of the pressure coefficient calculated by the nodal approach in the air space, and compares it with the values measured on the inside of the double skin and on the building.

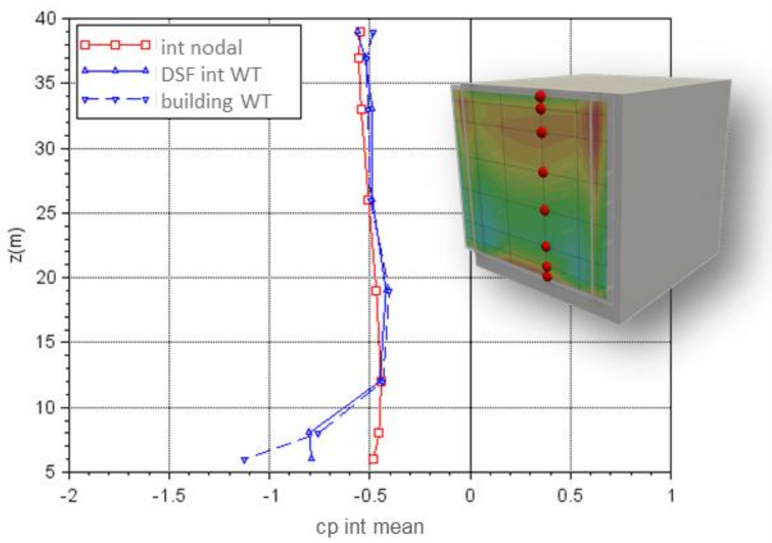

Figure 109 - profile of the mean internal pressure coefficient obtained by calculation, compared with the pressure measured on the inside of the double skin and on the building wall (configuration h_n_l_20_p_00_s_vert)

The figure shows a good match between the pressure value calculated by the nodal model and the value measured in the wind tunnel. In this geometric configuration, where the pressure is almost uniform in the air space, the pressure balancing will essentially be based on the pressure values at the air space boundaries and the pressure drop coefficients chosen at the inlet and outlet. The fact that the model is balanced at the correct pressure value means that the choice made regarding the values of the pressure drop coefficients prescribed at the inlet and outlet of the domain is ratified.

Nevertheless, the figure shows a significant difference at the foot of the facade between the values calculated by the model and those measured. While the pressure drops sharply in the measurements, it remains constant in the model. The analysis of the measurements had shown that this drop in pressure was induced by an acceleration in the engulfment of the flow in the air space. The Figure 41 shows a velocity field obtained from CFD simulations, which revealed a high degree of velocity inhomogeneity in the thickness of the air gap. The nodal calculation cannot represent this inhomogeneity, and therefore cannot translate the pressure drop it induces. This is therefore a first limitation of the approach in the reproduction of these strong pull-outs.

The Figure 110 plots an extract of the time signal of the internal pressure in the air space calculated at each time step of the simulation, and compares it with the signal measured in a wind tunnel. It also plots the net pressure differential obtained by subtracting the value calculated in the air space from the synchronous value measured on the outer face of the double skin. The plot is made at a point located in the centre of the facade.

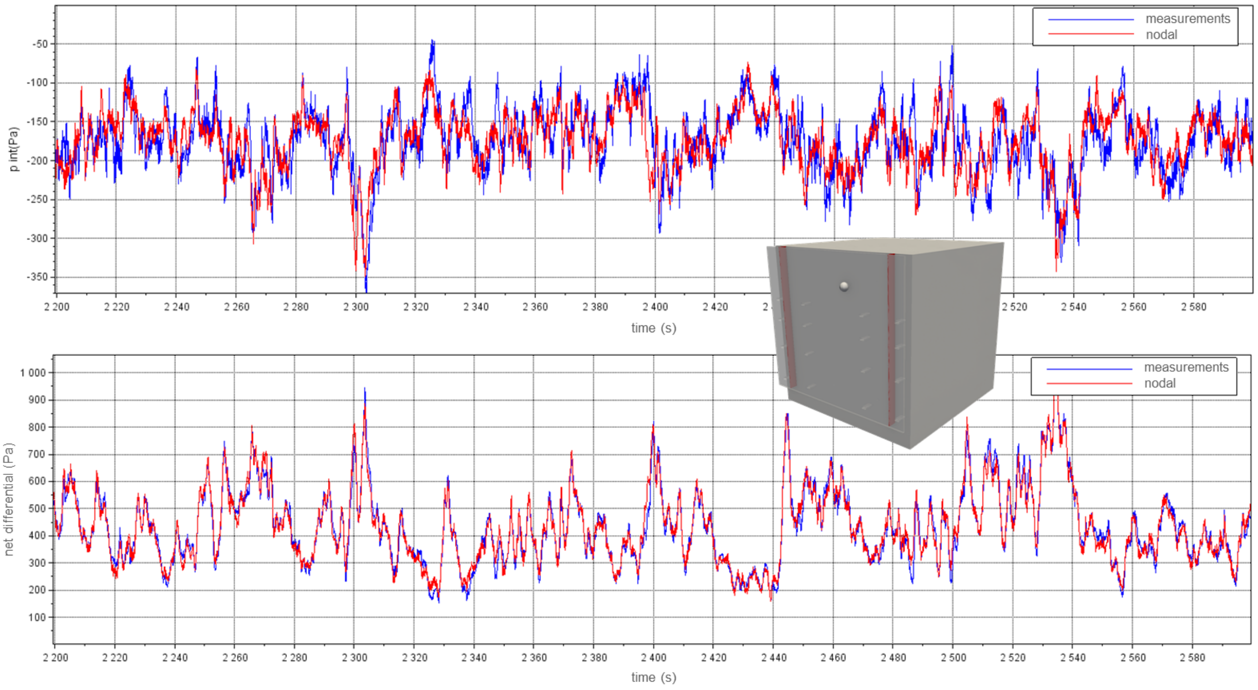

Figure 110 - extracts of the time signals for internal pressure (top) and net differential (bottom) calculated by the model at the centre of the facade, compared with wind tunnel measurements (configuration h_n_l_20_p_00_s_vert)

The figure shows that the calculated internal pressure signal follows the strongest fluctuations in the pressure signal measured in the wind tunnel relatively well. Smaller-scale fluctuations are not necessarily all reproduced well. Fluctuations in the pressure differential signal appear to be much better reproduced. This is partly due to the fact that the fluctuations are mainly induced by the external pressure signal, which is identical in the generation of the two signals being compared. That said, it shows the model's ability to reproduce the pressure variation on either side of the double-skin facade synchronously.

The Figure 111 plots the internal pressure profile and the net differential, mean and peak, calculated by the nodal model, and compares them with the values measured in the wind tunnel.

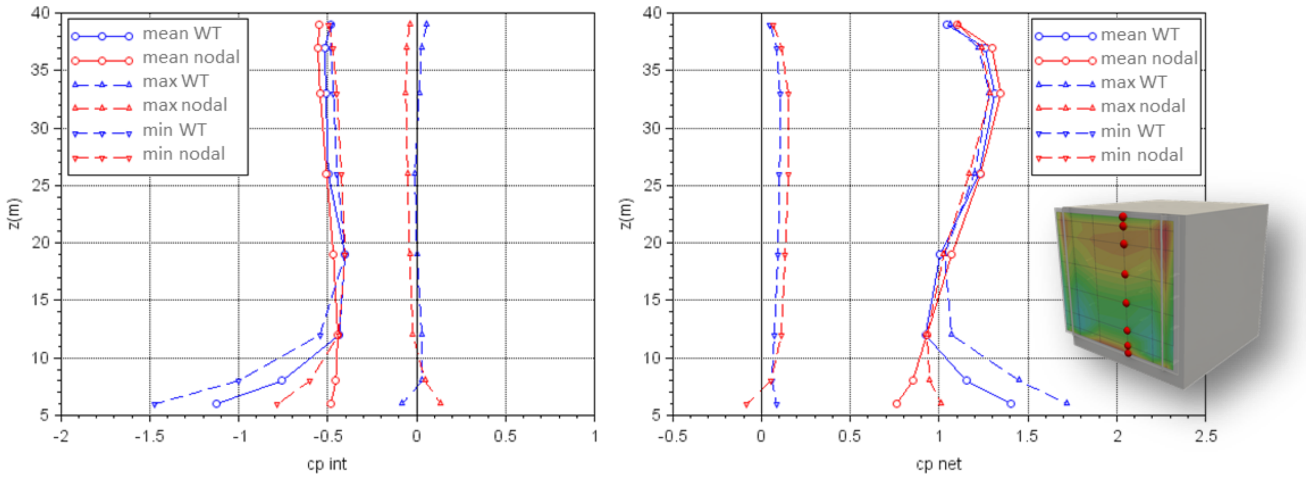

Figure 111 - average and peak pressure coefficient profile, interior on the left and net on the right, comparison of calculated and measured values (configuration h_n_l_20_p_00_s_vert)

The figure shows that the peak values simulated by the nodal approach are in very good agreement with the values measured in the wind tunnel. The prediction of these peak values is even better than that of the mean values. It can also be seen that the peak values for the pressure differential are also in very good agreement. This indicates that the pressure fluctuations between the inside and outside of the air space are well reproduced in a synchronous manner by the nodal approach, and induce peak differentials identical to those measured in the wind tunnel. At the foot of the facade, there is a discrepancy with the measurements, which is again explained by the inability of the nodal model to translate the acceleration of the flow as it becomes embedded in the air space.

The Figure 112 provides a more in-depth analysis of the dynamic aspect by plotting the PDFs of the calculated pressure signals and comparing them with the wind tunnel measurements. The analysis is carried out at 3 points on the facade.

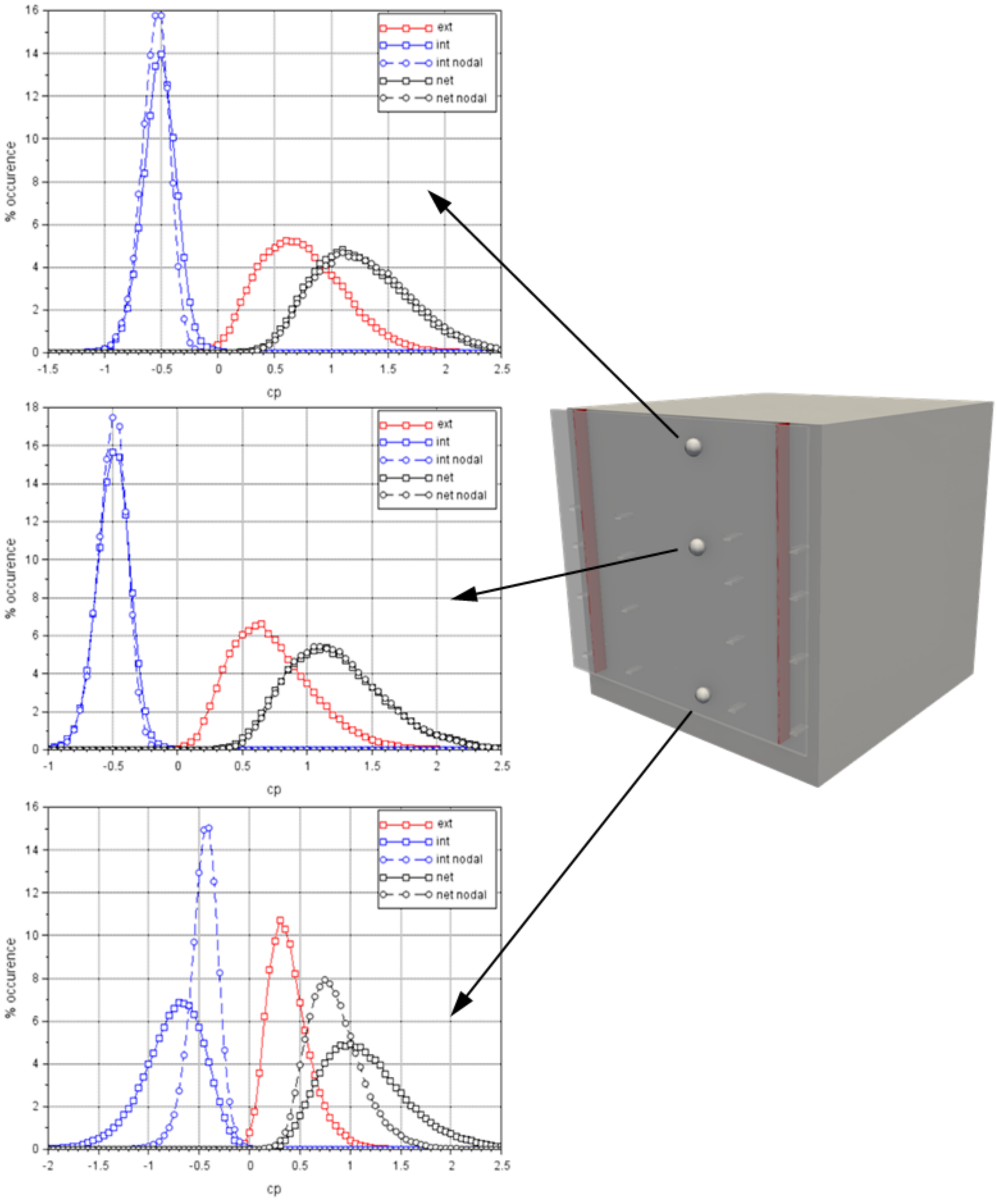

Figure 112 - PDF of the pressure coefficient, interior, exterior and net, at three points of the double-skin facade, comparison of calculated and measured values (configuration h_n_l_20_p_00_s_vert)

At the centre of the facade, the figure shows a superimposition of both the internal pressure PDF and the pressure differential PDF. Once again, this shows that at the centre of the facade, the dynamics of the pressure balance are perfectly reproduced by the nodal model in a synchronous manner, making it possible to reproduce a pressure differential dynamic that is very similar to that measured in the wind tunnel.

At the top of the facade, the calculated PDFs are again fairly close to those measured in the wind tunnel, although there is a slight difference in the internal pressures. At the foot of the facade, on the other hand, the dynamics of the internal pressure signals and the net differential are not at all in agreement with the measurements. This is further evidence of the inability of the nodal model to reproduce the flow dynamics at the entrance to the air gap.

In order to take better account of the engulfment of the flow at the foot of the facade, we propose to modify the model by reducing the cross-section of the channels in the first branches at the foot of the facade. The aim is to mimic the inhomogeneity of the flow by artificially accelerating it. The thickness of the air gap is thus reduced to 2/3 of the initial thickness in the first branches at the foot of the facade, in agreement with the observations made on the cross-sections of the velocity field obtained by CFD. The Figure 113 shows the mean and peak pressure profiles thus obtained.

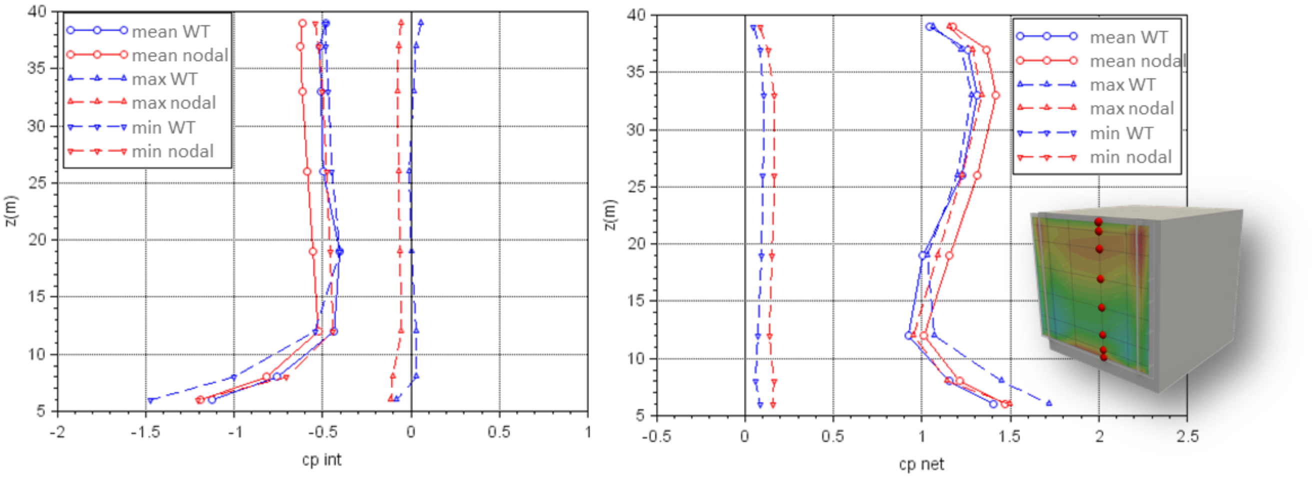

Figure 113 - profile of the mean and peak pressure coefficient, interior on the left and net on the right, comparison of calculated and measured values, model modified at the foot of the facade (configuration h_n_l_20_p_00_s_vert)

The figure shows a significant improvement in the pressure profile on the lower part of the facade. However, this is to the detriment of pressure balancing in the rest of the air space, since the pressure inside the air space becomes lower than that measured in the wind tunnel. Thus the modification of the model at the foot of the facade must certainly go hand in hand with a modification of the pressure drop coefficient at the entrance to the air space, a modification that remains to be determined.

The figure also shows that the peak values at the foot of the facade, although higher than those observed before the model was modified, are still lower than those measured in the wind tunnel. The Figure 114 shows the PDFs of the signals calculated by the modified nodal model.

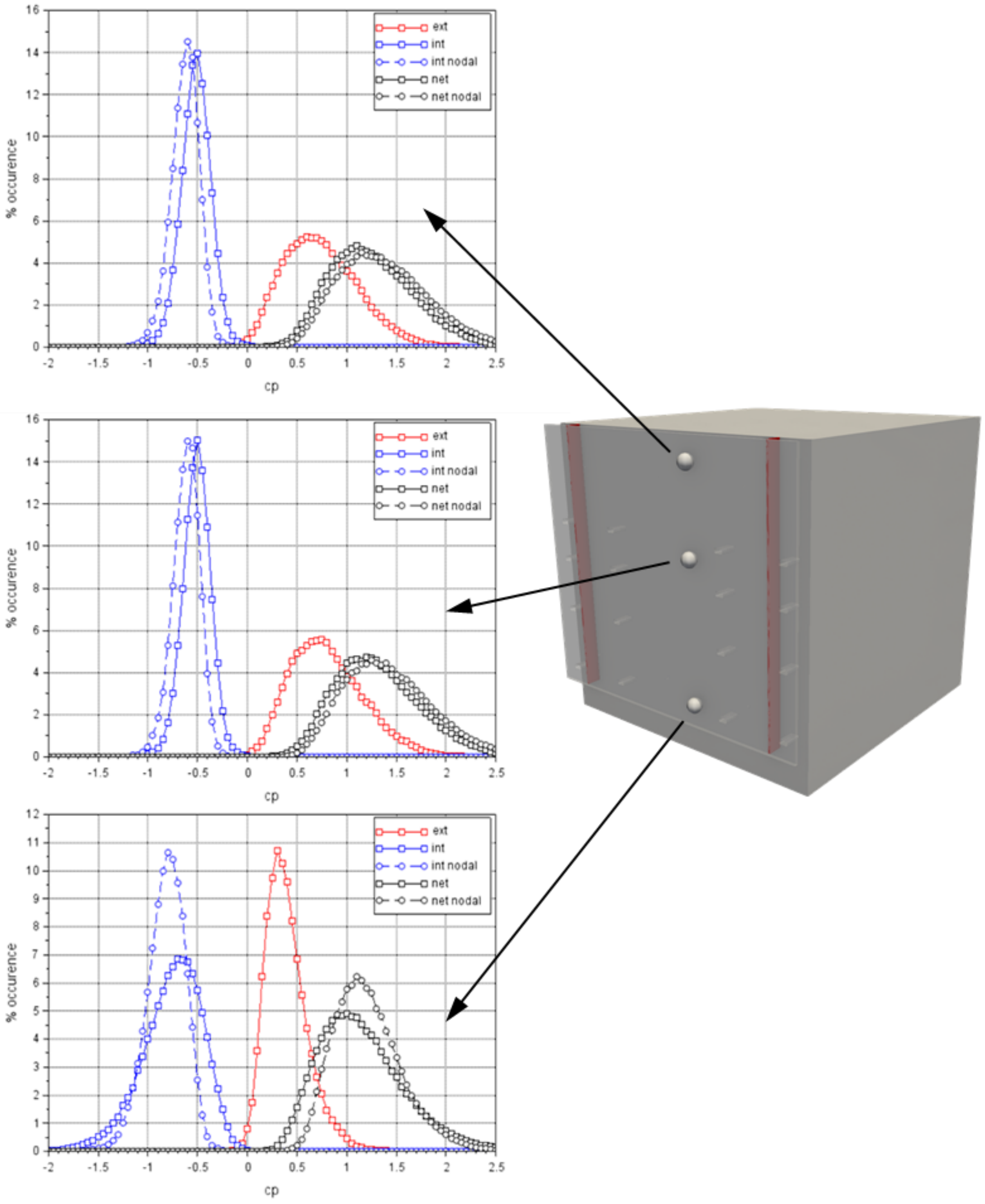

Figure 114 - PDF of the pressure coefficient, interior, exterior and net, at three points of the double-skin facade, comparison of calculated and measured values, model modified at the foot of the facade (configuration h_n_l_20_p_00_s_vert)

The figure shows that at the centre and top of the facade, the modification of the model results in a shift of the PDF towards lower pressure values, and a modification of the PDF of the pressure differential. This shift is in agreement with what could be observed on the profiles in Figure 113. At the foot of the facade, the modification of the model improves the appearance of the PDFs of the simulated signal, but they remain quite far from those measured in the wind tunnel.

Thus, although the proposed modification allows for a better restitution of the loads at the foot of the facade, it does not allow for a sufficiently detailed reproduction of the dynamics of the pressure balancing of the air space. In addition, this modification would require prior knowledge of the value of the reduction in the thickness of the air space to be applied. This parameter does not necessarily seem trivial to determine, even if a CFD pre-calculation seems to be able to give a good indication.

We now propose to observe the behaviour of the nodal model by changing the height of the building. Analysis of the measurements showed that this led to a radical change in the pressure balance of the air gap. The Figure 115 plots the internal pressure profile and the net differential, mean and peak, calculated by the nodal model, and compares them with the values measured in the wind tunnel.

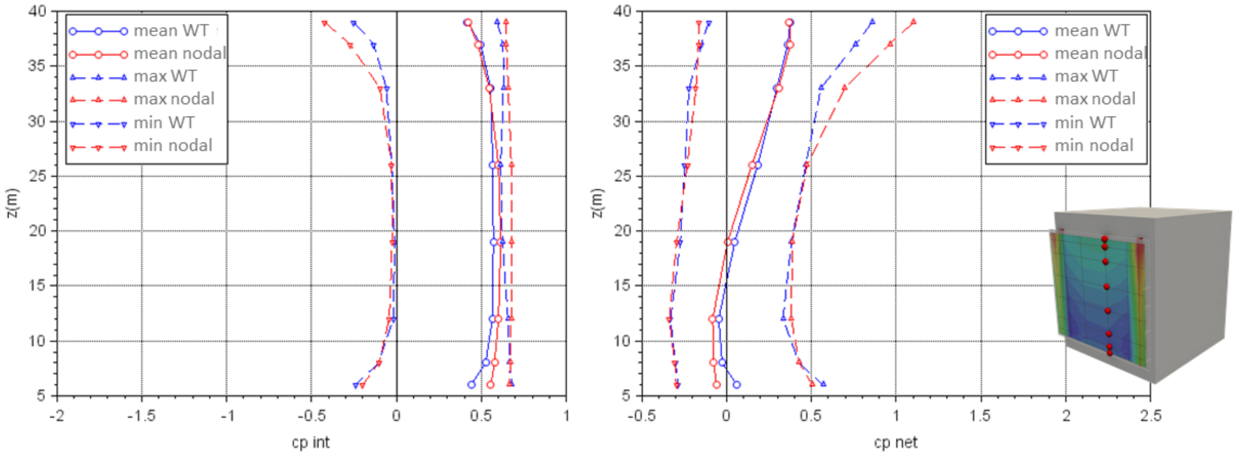

Figure 115 - mean and peak pressure coefficient profile, interior on the left and net on the right, comparison of calculated and measured values (configuration h_h_l_20_p_00_s_vert)

The figure again illustrates a radical change in the pressure balance in the air gap with increasing building height. Once again, the nodal model appears to be able to balance the pressure in the air space at a value comparable to that measured in the wind tunnel. The mean internal pressure $\overline{c_{p_{int}}}$ profile appears to be in agreement with the measurements over the entire height of the facade, although there is a slight discrepancy at the foot of the facade. The peak internal pressures $\widehat{c_{p_{int}}}$ are also in very good agreement with those that can be measured, once again demonstrating the ability of the nodal model to reproduce the dynamics of the pressure balance of the air space. However, there is a slight discrepancy in the minimum peak pressures at the top of the facade. Once again, this discrepancy can be attributed to the entrapment of the flow in the air gap, which is poorly reproduced by the model.

Interestingly, the profile of the pressure differential $c_{p_{net}}$ is in very good agreement with that measured in the wind tunnel. The mean value again shows a change in the sign of the mean net load between the upper and lower parts of the facade. The calculated peak pressure differential $\widehat{c_{p_{net}}}$ profiles are also very well reproduced, even though the maximum peak value calculated at the top of the facade is higher than that measured.

The Figure 116 provides a more in-depth analysis of the dynamic aspect by plotting the PDFs of the calculated pressure signals and comparing them with the wind tunnel measurements. The analysis is carried out at 3 points on the facade.

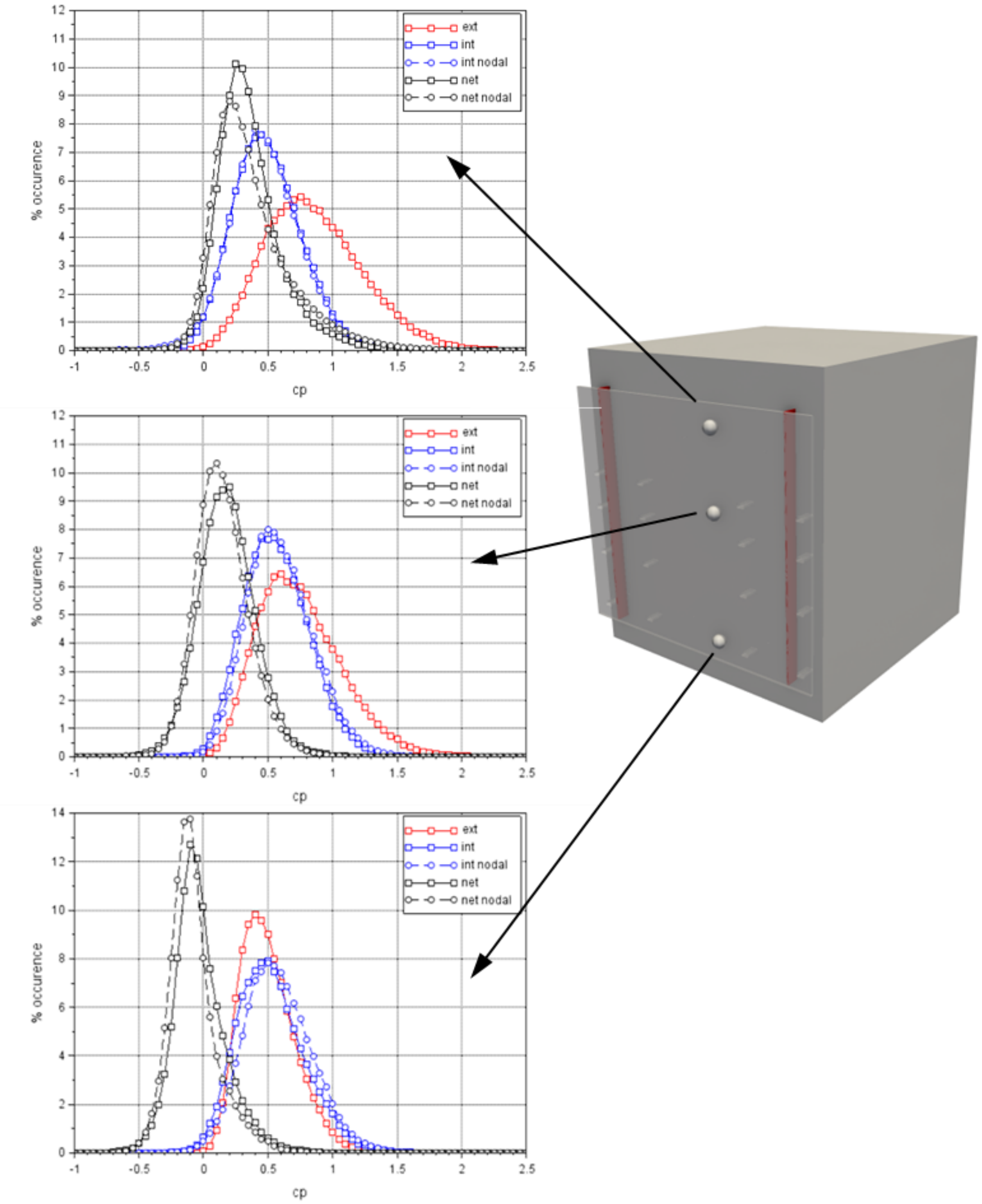

Figure 116 - PDF of the pressure coefficient, interior, exterior and net, at three points on the double-skin facade, comparison of calculated and measured values (configuration h_h_l_20_p_00_s_vert)

At the centre and top of the facade, analysis of the figure shows a superposition of the internal pressure PDFs with those measured. The model is therefore once again able to reproduce the dynamics of the pressure signal in the air gap very well. However, the calculated pressure differential PDFs are slightly different from those measured, despite the very good agreement of the internal pressure PDFs. Therefore, reproducing the dynamics of the internal pressure signal is not enough to reproduce the dynamics of the pressure differential. The fluctuations inside the air space must also be synchronised with the fluctuations on the outside.

At the foot of the facade, on the other hand, there is a slight deviation in the internal pressure PDF, while the pressure differential PDF is in better agreement with that measured.

Although the analysis highlighted discrepancies between the wind tunnel measurements and the values calculated by the model, it ultimately showed that the model was not only capable of reproducing the significant change in the pressure balance of the air gap with the change in the height of the building, but also, and above all, of reproducing a dynamic consistent with that measured. The model's main weakness lies in its inability to translate the effects of flow acceleration at the entrance to the air gap, and the associated increases in loads.

5.3.2 4-sided open skin

We are now interested in a geometric configuration with no segmentations. This moves away from the flat channel situation induced by the vertical segmentations. First, we look at a configuration with a level building. The Figure 117 plots the internal pressure profile and the net differential, mean and peak, calculated by the nodal model, and compares them with the values measured in the wind tunnel.

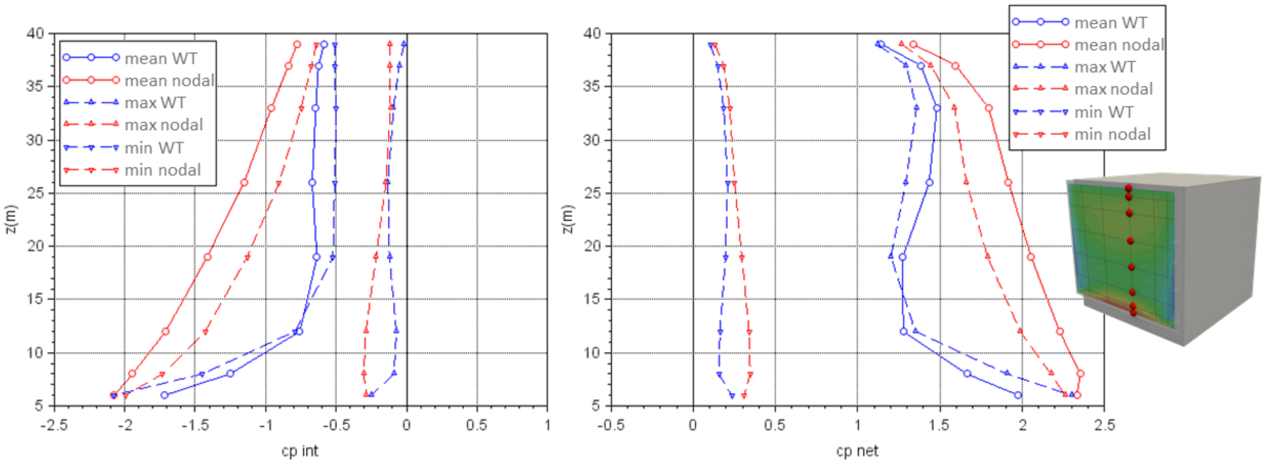

Figure 117 - mean and peak pressure coefficient profile, inside on the left and net on the right, comparison of calculated and measured values (configuration h_n_l_20_p_00_s_n)

Analysis of the figure shows a significant difference between the calculated and measured pressures in the air space, both for mean and peak values. Although the pressures at the top and bottom of the facade are of the same order of magnitude, the difference is mainly in the shape of the profile. Whereas in the measurements the pressure was more or less constant over the upper 2/3 of the air space, the calculated values show a pressure that changes along the entire length of the facade. The pressure inside the air space is then lower than that measured, resulting in a calculated net load that is significantly higher than that measured.

The Figure 118 maps the mean internal pressure coefficient $\overline{c_{p_{int}}}$ and the mean pressure differential $\overline{c_{p_{net}}}$ measured and calculated in this configuration to represent the two-dimensional nature of the pressure field.

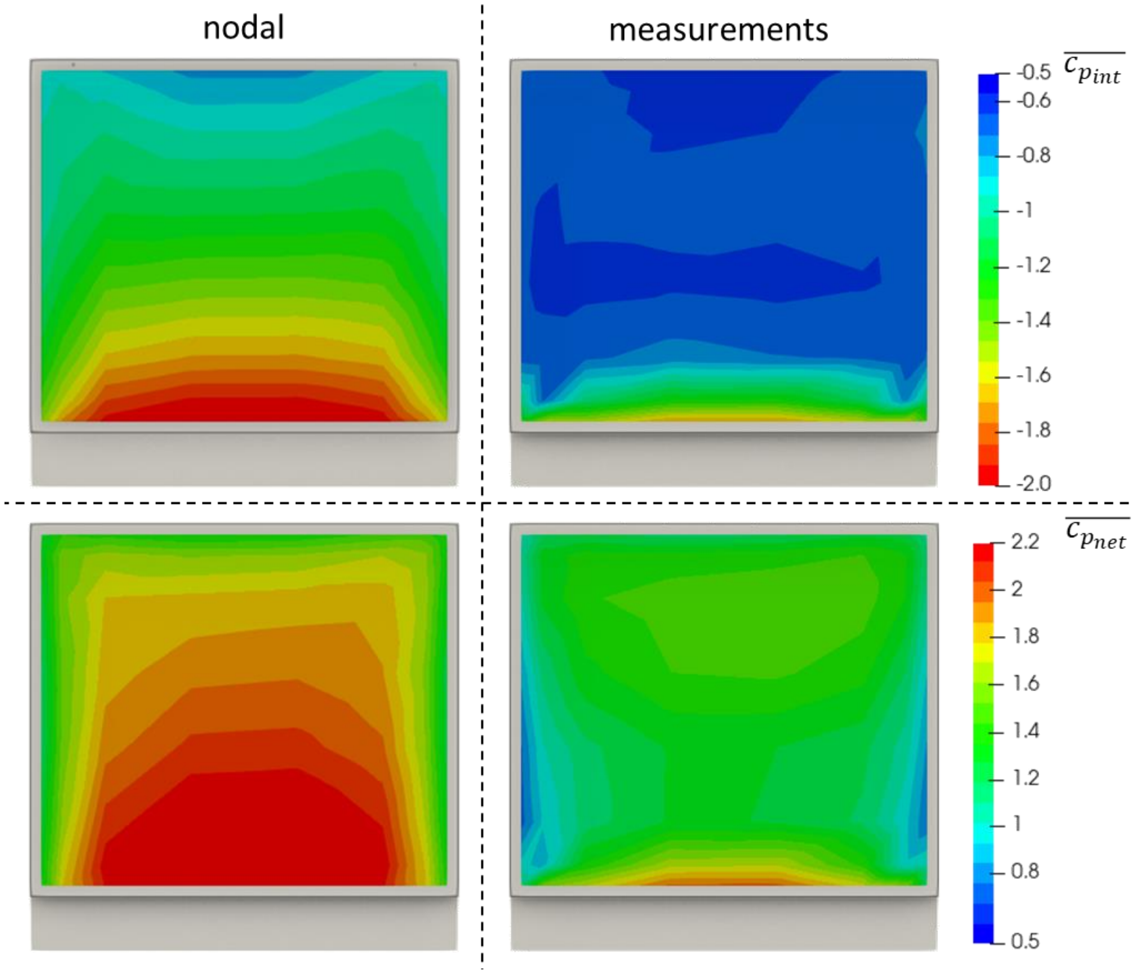

Figure 118 - mapping of mean pressure coefficient, internal (top) and net (bottom), comparison of calculated (left) and measured (right) values (configuration h_n_l_20_p_00_s_n)

Here again, there is a significant difference in the organisation of the calculated pressure field compared with that measured. While the model accurately reproduces the increase in loads at the foot of the facade due to air being forced inside the double skin, its effect is spread over a larger part of the facade, in contrast to what was observed in the case of a vertically segmented skin.

So the model does not seem to be able to correctly balance the pressure in the air gap from the three negative pressure edges and the single positive pressure edge.

This limitation of the model can be attributed to several factors:

-the difficulty of representing the two-dimensional and unsteady nature of the flow using a simple grid network

-failure to take account of the dynamics of the external flow at the entrance and exit of the channel

-flow inhomogeneity at flow entrapment

However, it is essentially the high dynamic of the flow in the air gap that seems to make the nodal modelling faulty in this configuration.

The Figure 119 plots the PDFs of the calculated pressure signals, and compares them with the wind tunnel measurements. The analysis is carried out at 3 points on the facade.

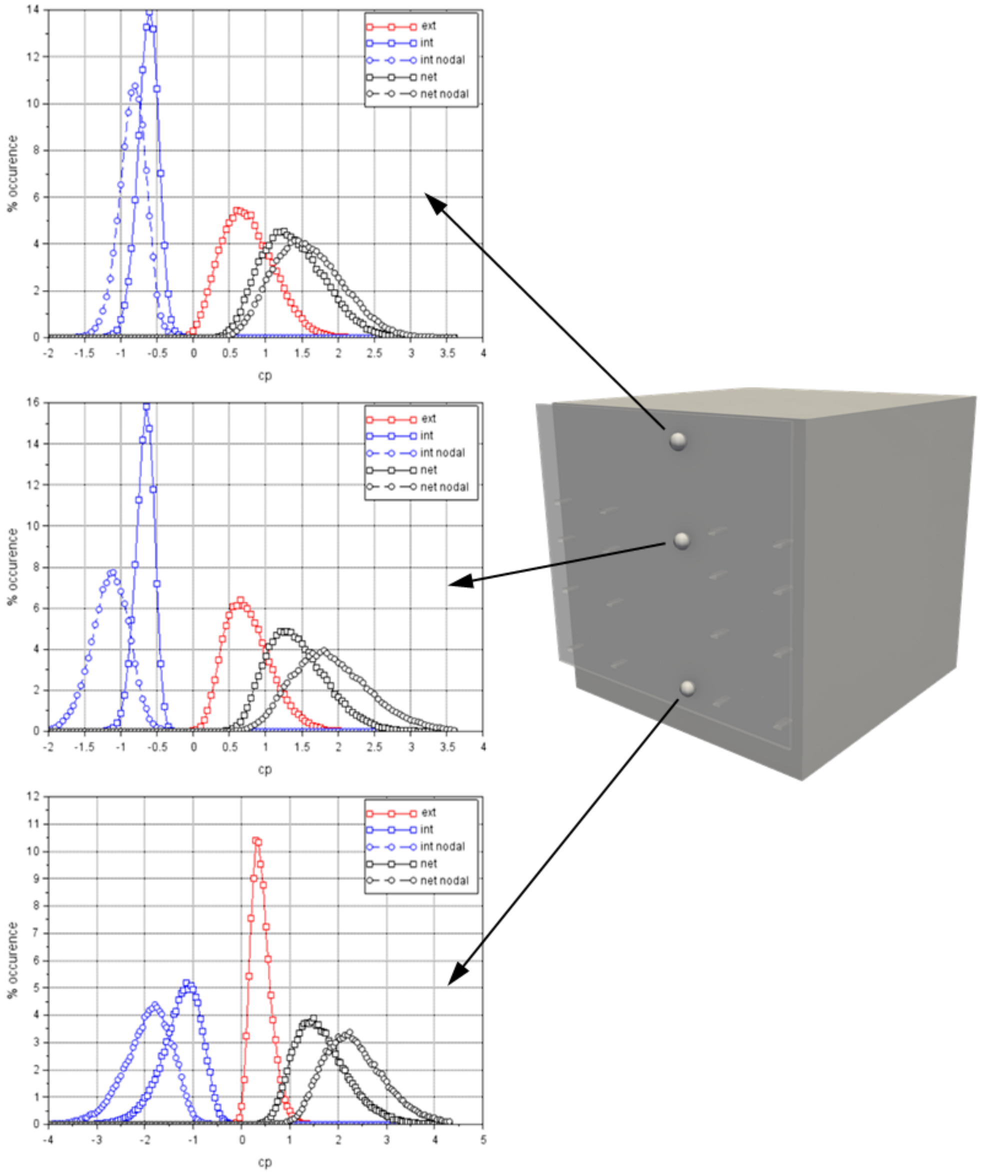

Figure 119 - PDF of the pressure coefficient, interior, exterior and net, at three points of the double-skin facade, comparison of calculated and measured values (configuration h_n_l_20_p_00_s_n)

The figure shows that in this configuration, the PDFs obtained by the nodal model are very different from those measured. Although qualitatively the model seems to be able to reproduce the evolution of the shape of the PDF between the top and the bottom of the facade, the comparison with the measurements shows that the model has difficulty in reproducing the correct dynamics of the pressure signal in the air gap for this configuration.

We now propose to study the case of the tall building, still with an uncut facade open on all 4 sides. The Figure 120 shows the internal pressure profile and the net, mean and peak differential, while Figure 121 maps the mean internal pressure coefficient $\overline{c_{p_{int}}}$ and mean pressure differential $\overline{c_{p_{net}}}$ measured and calculated.

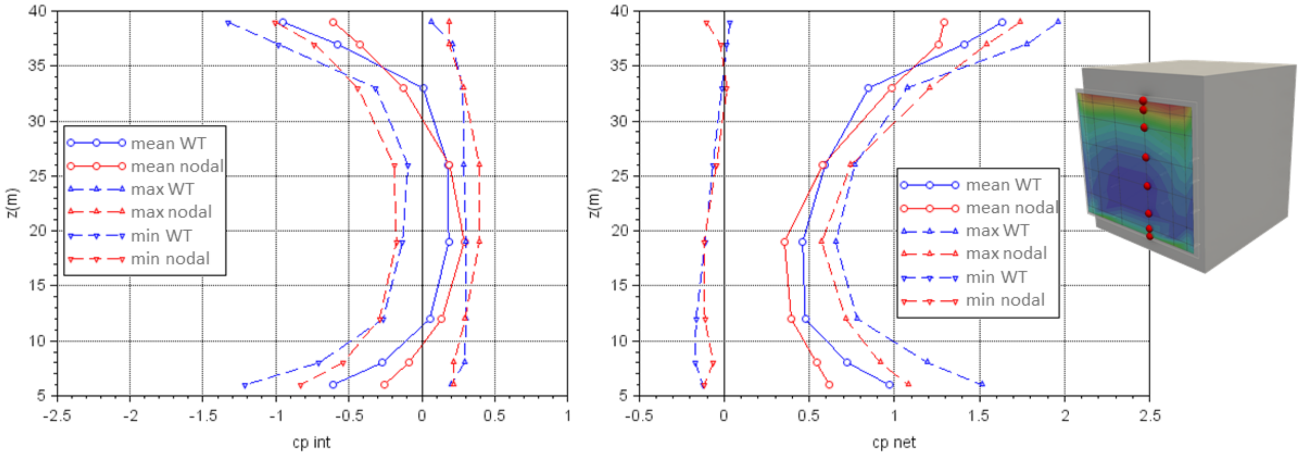

Figure 120 - average and peak pressure coefficient profile, interior on the left and net on the right, comparison of calculated and measured values (configuration h_h_l_20_p_00_s_n)

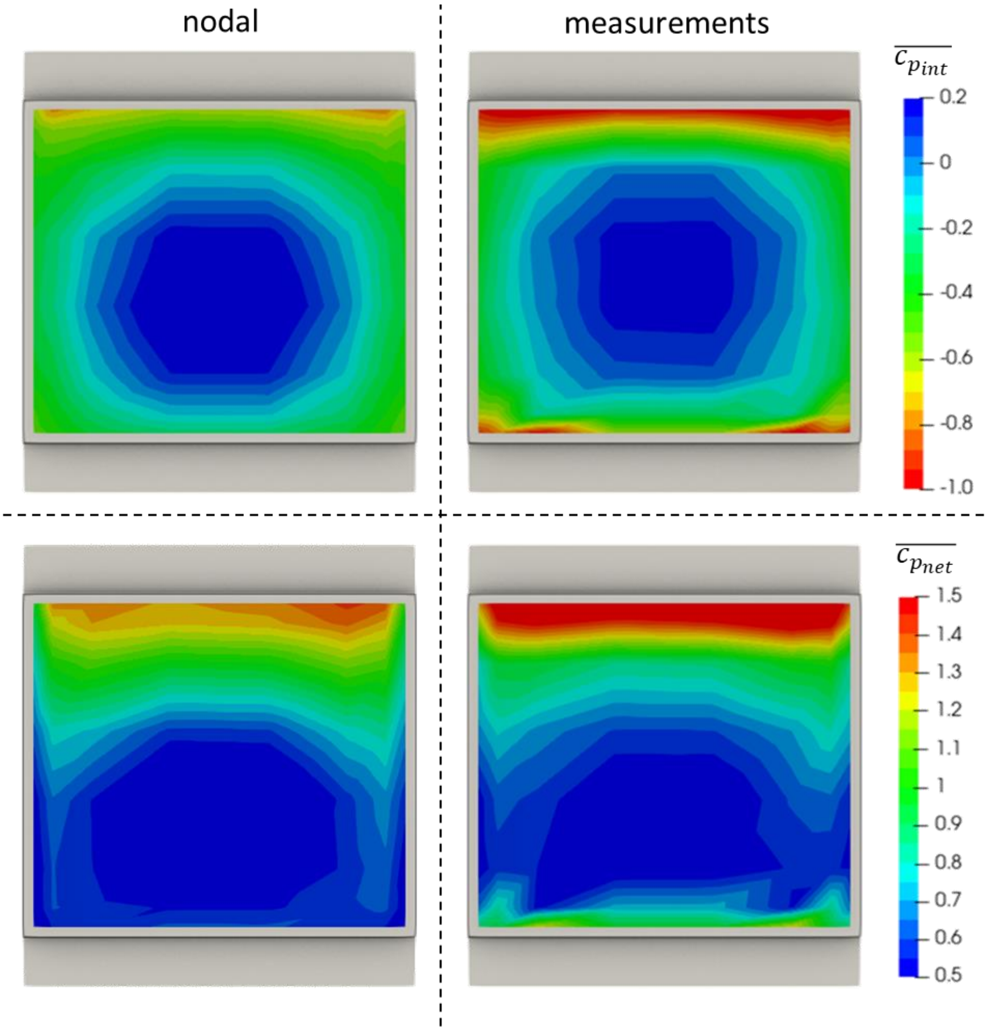

Figure 121 - mapping of mean pressure coefficient, internal (top) and net (bottom), comparison of calculated (left) and measured (right) values (configuration h_h_l_20_p_00_s_n)

The figures show a better reproduction of the evolution of the pressure calculated in the air space compared with the case of the level building. The model thus seems capable of predicting that the centre of the air gap will be under overpressure, while the periphery will be under negative pressure. The calculated pressure differential also looks satisfactory, although once again the high loads induced by the rushing flow in the air gap are not well represented by the model.

The Figure 122 plots the PDFs of the calculated pressure signals, and compares them with the wind tunnel measurements. The analysis is carried out at 3 points on the facade.

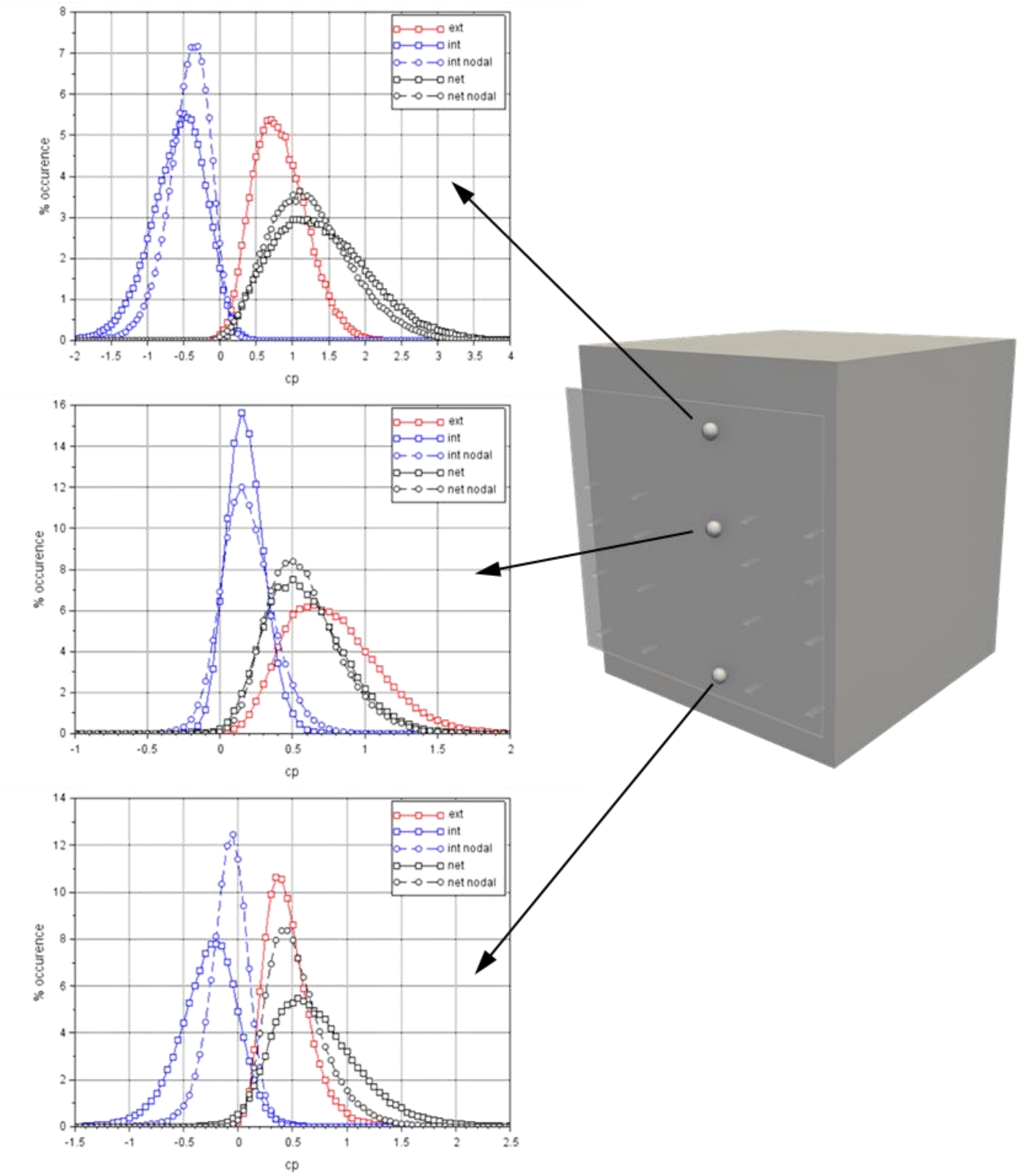

Figure 122 - PDF of the pressure coefficient, interior, exterior and net, at three points of the double-skin facade, comparison of calculated and measured values (configuration h_h_l_20_p_00_s_n)

The figure shows that at the centre of the facade, the PDF of the internal pressure simulated by the model is in fairly good agreement with that measured, even though the amplitude of the distribution seems wider. The PDF of the pressure differential is well reproduced. This is again due to the fact that in this configuration, the dynamics of the pressure differential are largely induced by the dynamics of the pressure signal on the outside of the double skin. At the top and bottom of the facade, however, the model does not seem to be able to reproduce all the signal dynamics. This is again due to the fact that the model cannot reproduce the effects of flow entrapment in the air space.

This configuration of a skin open over its 4 sides is therefore much more challenging for the nodal model than the configuration with vertical segmentations. The configuration of the level building, which generates very high flow dynamics in the air space, does not seem to be reproducible by the nodal model. However, the configuration with the high building, which generates a more reasonable dynamic, seems to be more favourable for the model to reproduce the pressure balance of the air gap.

5.3.3 Horizontally segmented skin

We are now interested in the case of a horizontally segmented skin. The analysis §4.3 showed that these segments, which cut off access to the upper or lower edge of the air gap, led to a significant change in pressure balance.

The Figure 123 to Figure 126 show maps of the mean internal pressure coefficient $\overline{c_{p_{int}}}$ and the mean pressure differential $\overline{c_{p_{net}}}$ measured and calculated for two building heights and the two positions of the horizontal segmentation. The Figure 127 plots the internal pressure profile and the net, mean and peak differential for the 4 configurations.

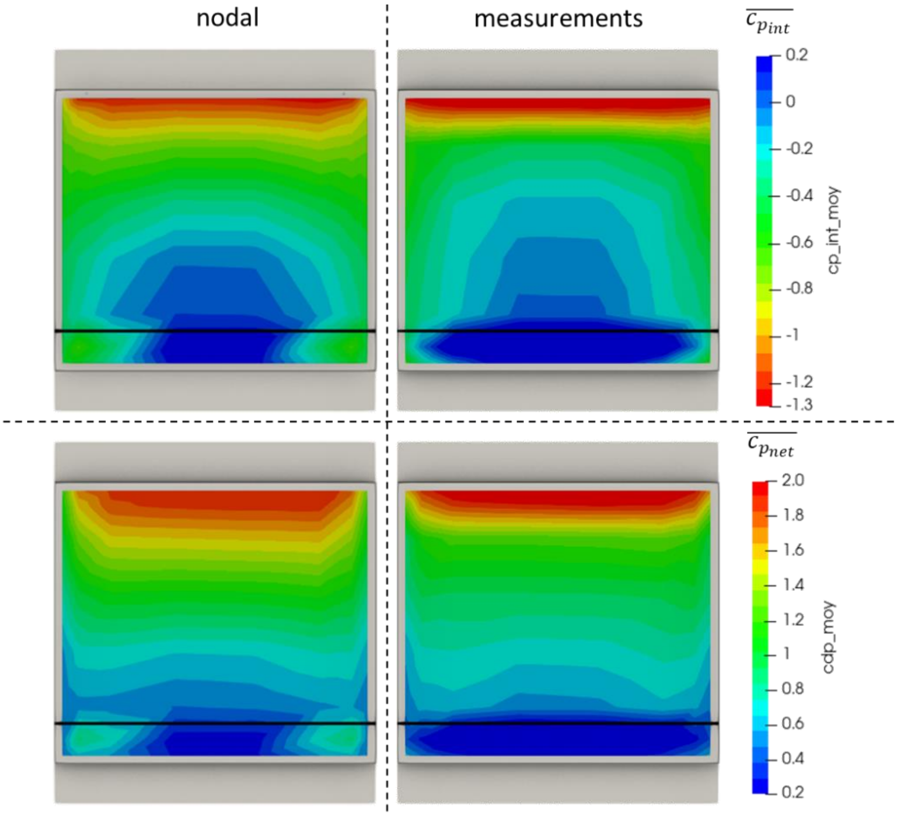

Figure 123 - mapping of mean pressure coefficient, internal (top) and net (bottom), comparison of calculated (left) and measured (right) values (configuration h_h_l_20_p_00_s_hb00)

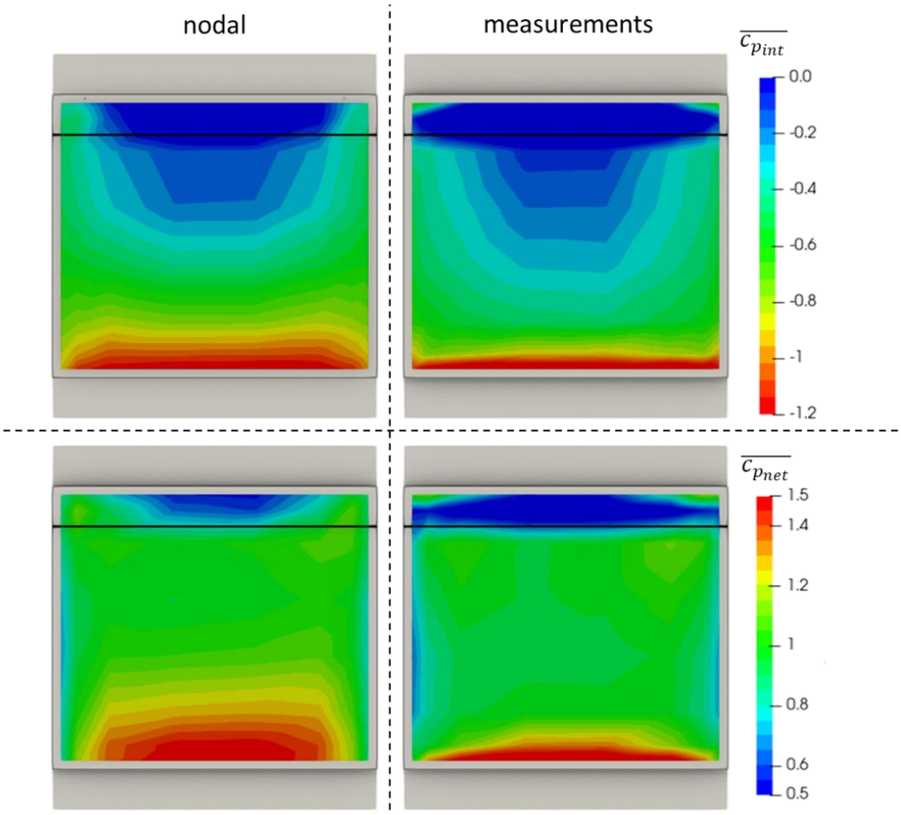

Figure 124 - Mapping of mean pressure coefficient, internal (top) and net (bottom), comparison of calculated (left) and measured (right) values (configuration h_h_l_20_p_00_s_hh00)

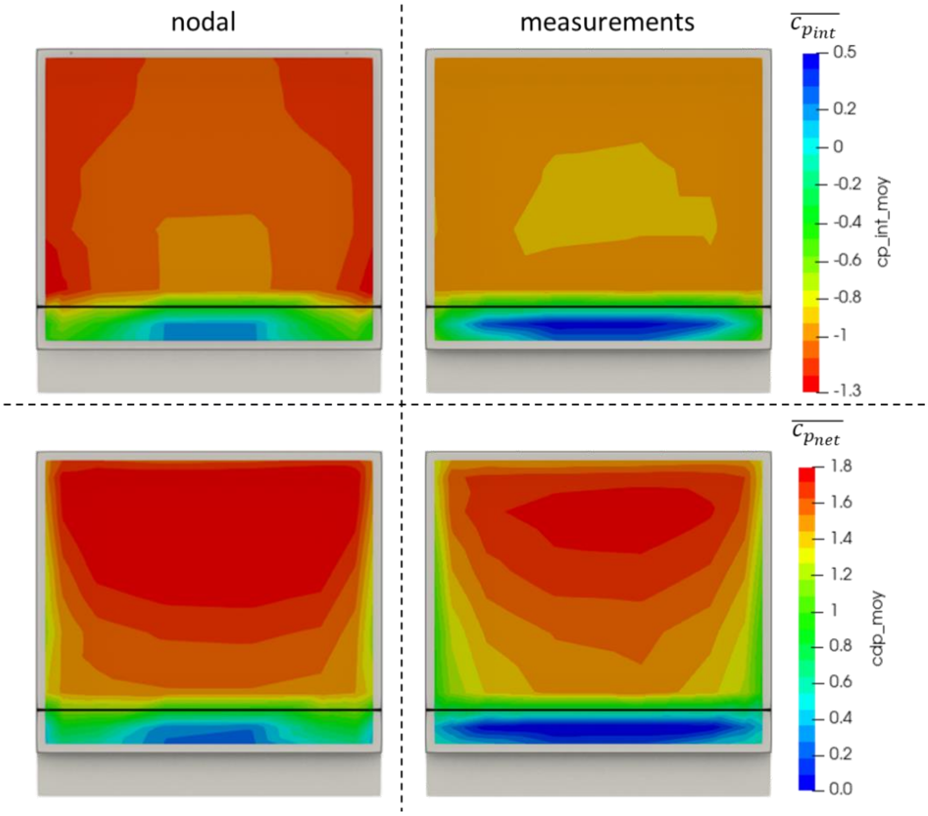

Figure 125 - Mapping of mean pressure coefficient, internal (top) and net (bottom), comparison of calculated (left) and measured (right) values (configuration h_n_l_20_p_00_s_hb00)

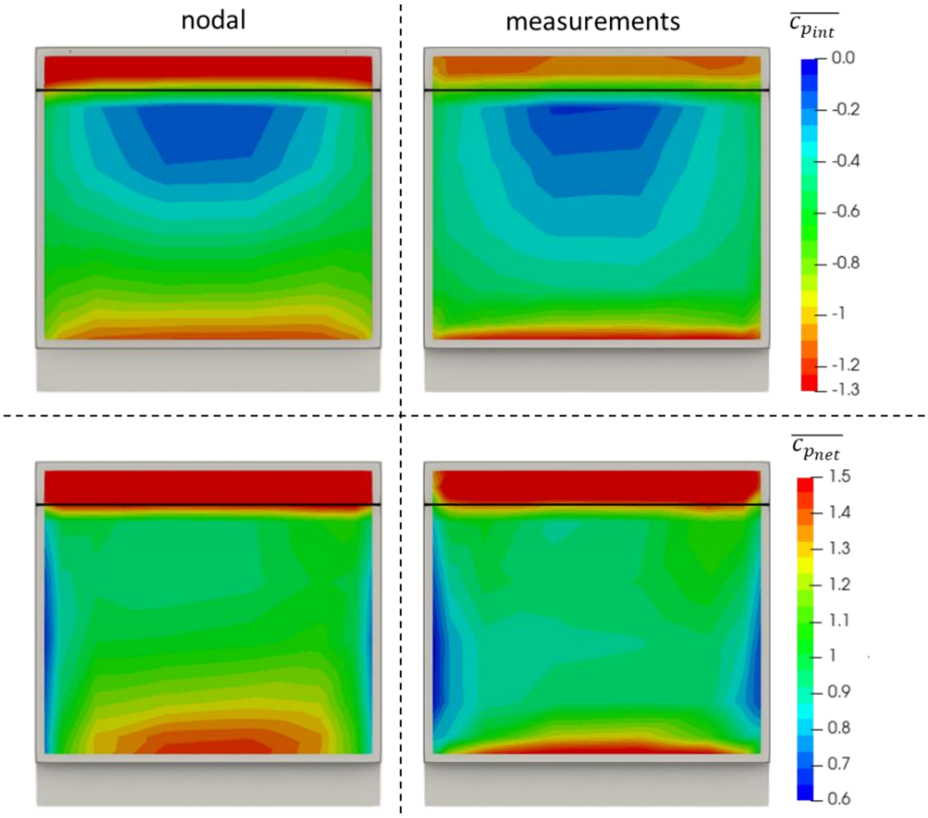

Figure 126 - mapping of mean pressure coefficient, internal (top) and net (bottom), comparison of calculated (left) and measured (right) values (configuration h_n_l_20_p_00_s_hh00)

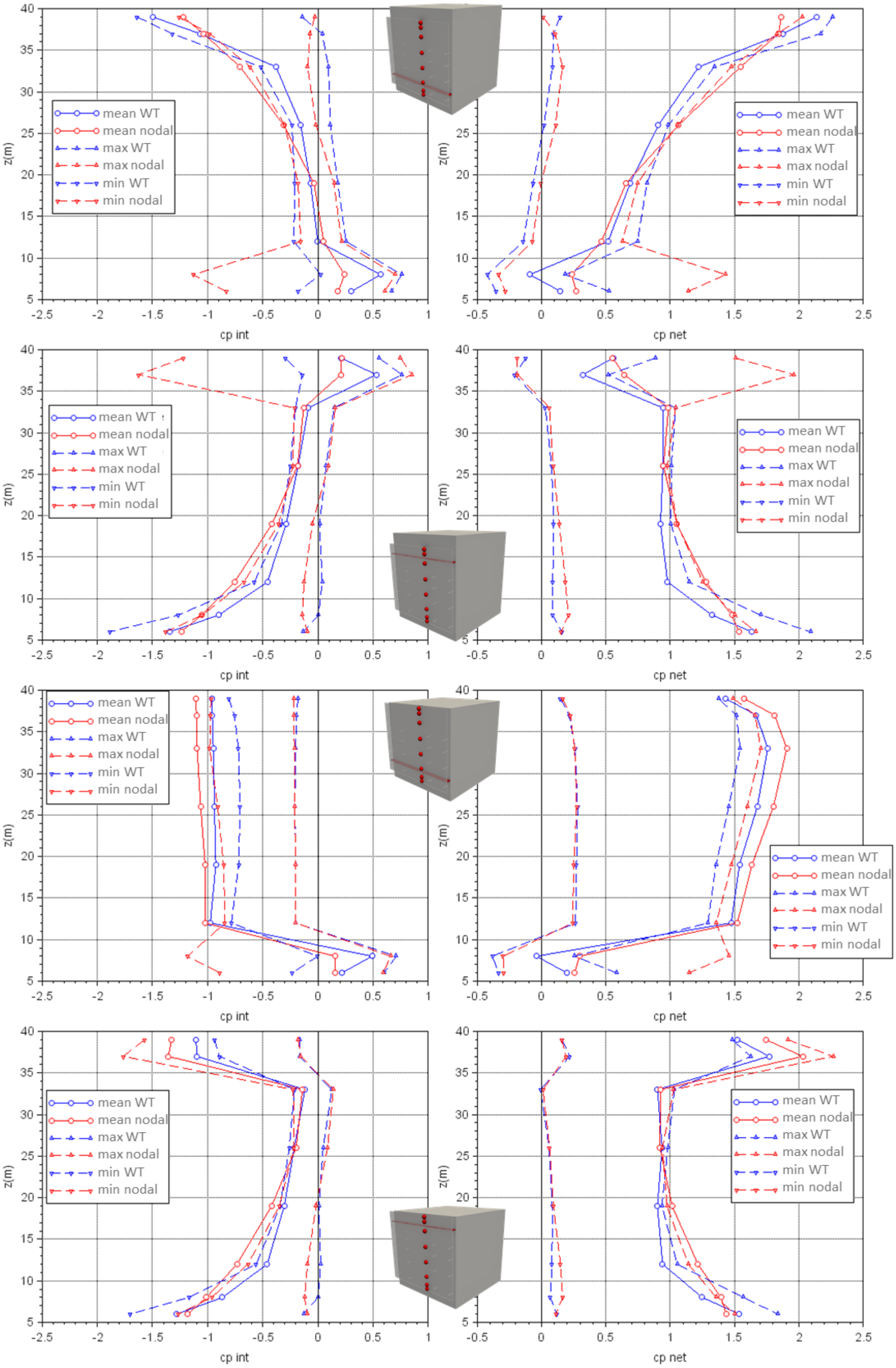

Figure 127 - mean and peak pressure coefficient profile, inside left and net right, comparison of calculated and measured values, from top to bottom: h_h_l_20_p_00_s_hb00, h_h_l_20_p_00_s_hh00, h_n_l_20_p_00_s_hb00, h_n_l_20_p_00_s_hh00

The maps of mean pressure coefficients obtained by the nodal model in these 4 configurations are qualitatively satisfactory. The model appears to be able to predict the significant variations in pressure balance induced by changes in building height or the presence of horizontal segmentation. In addition, the model seems able to reproduce the two-dimensional evolution of pressure, in the direction of the height and width of the facade, in a qualitatively satisfactory manner.

Quantitatively, the mean and peak pressure profiles show sometimes significant differences between the values obtained by the nodal model and those measured in the wind tunnel. Once again, the greatest discrepancies occurred at the edges of the facades, due to the model's difficulty in reproducing the effects of the flow becoming entangled in the air gap. While the deviations at these edges lead to calculated loads that are lower than those measured, at the centre of the facade the opposite is true, i.e. loads that are higher than those measured, which is quite safe.

For the two configurations with high segmentation, the skin is in compression on the lower part, and in depression on the lateral edges. Analysis of the measurements had shown that the flow would then rush in through the foot of the facade, and evacuate through the sides. The configuration is therefore close to that of a 4-sided open skin with a level building, a configuration that had failed the nodal model. Here we can see that the model performs better, even if the grid effects at the foot of the facade are once again quite visible.

The high-building configuration with low segmentation is similar, with flow entering from the top and exiting from the sides. The conclusions on model performance are fairly similar to the previous configurations.

Finally, for the configuration of the level building with low segmentation, the 3 sides of the double skin are in depression. This is the configuration that generates the lowest airflow in the air space. The calculated pressure profile is uniform throughout the height of the air space. The value of the internal pressure $c_{p_{int}}$ at the centre of the facade is lower than that measured, resulting in higher net loads $c_{p_{net}}$. It should be noted in passing that the ratio between the calculated peak values and the calculated mean values is similar to the ratio between the measured peak values and the measured mean values.

Generally speaking, and with the exception of the deviations highlighted for the mean values, which also apply to the peak values, the dynamics of the flow in the air gap appear to be well represented by the nodal model.

The results obtained in this configuration with 3 open sides are therefore more satisfactory than those obtained with the skin open on all 4 sides. The model appears to be capable of qualitatively determining the behaviour of pressure balancing according to the different geometric variations, even though there are still fairly large differences in terms of quantity, especially at the edge of the facade.

5.3.4 Porous skin

We now propose to study the possibility of modelling a porous skin using the nodal approach. We consider the case of a 15% porous skin, segmented vertically and backed by a building at level. This is one of the configurations studied §4.5.1 which showed a very significant impact of porosity on the pressure balance of the air space.

In order to take account of the effect of porosity, the nodal model is supplemented with new boundary conditions onto which we prescribe the pressures measured on the external face of the double-skin facade. These new boundary conditions are then linked to the calculation nodes by so-called "permeability" branches. These branches are only considered for the calculation nodes included in the porous zone of the facade. A schematic diagram is proposed Figure 128.

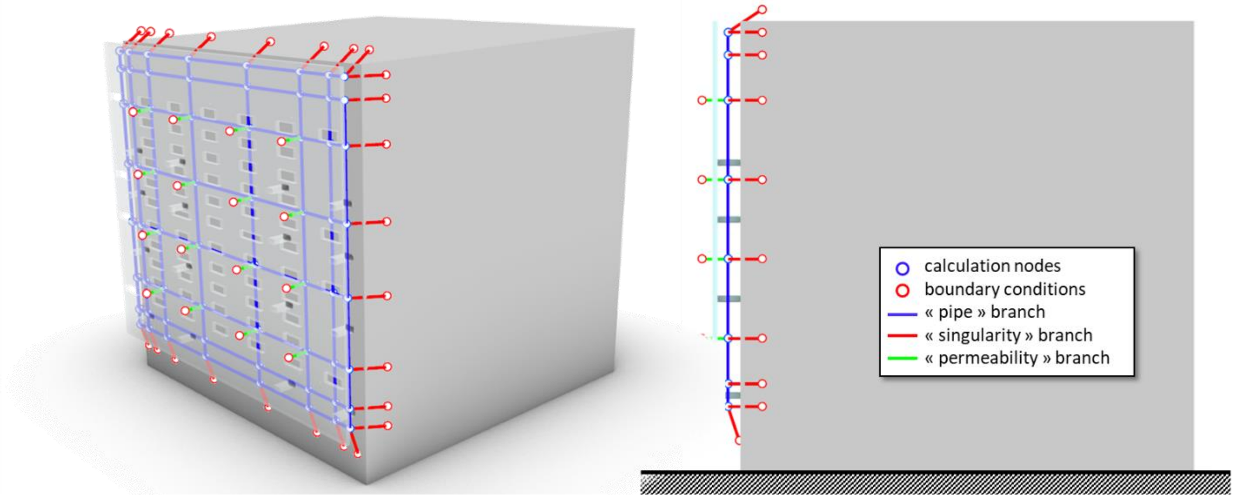

Figure 128 - adaptation of the nodal model to take account of porosity

The permeability branches correspond to a model proposed in the MATHIS [13] which simulates the flow of air through a porous surface. The model takes two parameters as input: the flow rate through the branch Q_{permea} as a function of the pressure delta Δp_{permea} applied across the branch. We propose to determine these parameters using a pressure loss coefficient:

$$\Delta p_{permea} = \frac{1}{2}\rho\xi_{permea}\left(\frac{Q_{permea}}{S_{permea}}\right)$$

With S_{permea} the area representative of the facade covered by the panel linking the calculation node to the boundary condition, and ξ_{permea} a pressure drop representative of the porosity. The latter can be evaluated, for example, using the Idel'Cik head loss charts [15]. These charts give the following values for a plate with holes $\xi_{permea} = 400$ with a porosity of 8%, and $\xi_{permea} = 100$ for a porosity of 15%.

The Figure 129 plots the profile of the pressure coefficient inside the air gap, as well as the pressure differential calculated for several values of ξ_{permea} and compares them with the values measured on a skin with a porosity of 15%.

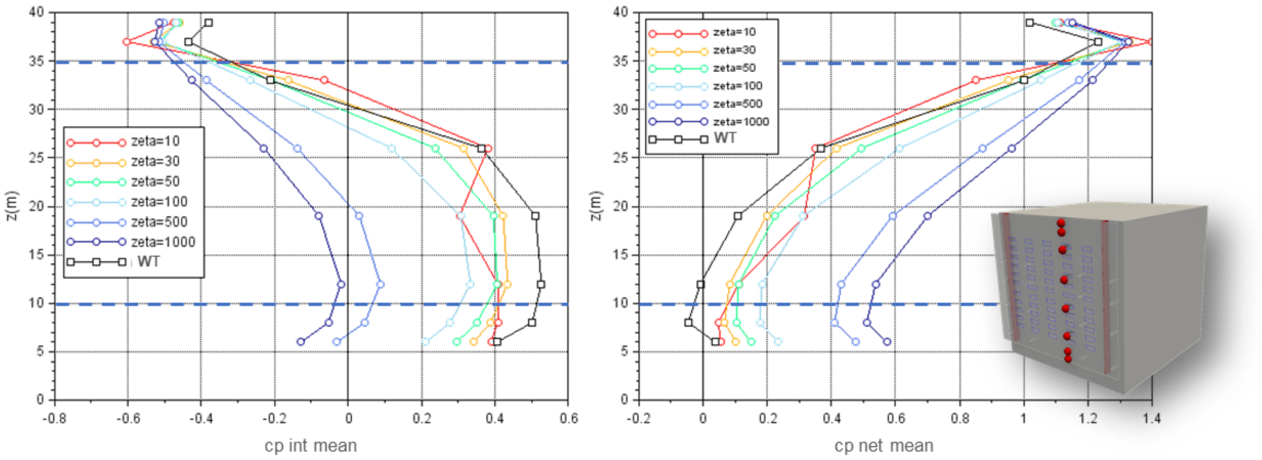

Figure 129 - profile of the mean pressure coefficient, internal on the left and net on the right, comparison with pressure measurements calculated for several values of ξ_{permea} (configuration h_n_l_20_p_15_s_vert)

The figure shows that the shape of the profiles is representative of those measured. The calculated profiles are progressively closer to those measured as the ξ_{permea} decreases, and therefore as porosity increases.

The theoretical value of ξ_{permea} for a porosity of 15% is $\xi_{permea} = 100$. The figure shows that this value is too high to be representative of the measured pressure profiles. This may be due to a limitation in the modelling of the boundary conditions, for which a static pressure is prescribed here, whereas the model expects a total pressure. In other words, these boundary conditions do not necessarily take into account the dynamic pressure of the flow on the outside of the air space. This dynamic pressure can encourage the flow to penetrate through the porosity of the facade. This may be why this porosity needs to be artificially reduced to "encourage the flow to penetrate" the air space via the porosity.

So the optimum value for the pressure loss coefficient to get as close as possible to the measurements seems to be $\xi_{permea} = 30$. Below this value, the figure shows that the pressure profile inside the air gap deviates from the measured profile, with a drop in pressure at the centre of the porous zone. In this case, the modelling bias would lead to too much flow being forced into the air gap, since in "reality", the flow will prefer to continue its course along the external facade, rather than penetrate the air gap. Excessive air circulation in the air space will then induce excessively high speeds, thus lowering the static pressure on the inside of the double skin.

These two modelling biases highlight the model's difficulty in accurately reproducing the competition between the inertia of the flow outside the air gap and the effects of porosity.

The Figure 130 plots the internal pressure profile and the net differential, mean and peak, calculated with $\xi_{permea} = 30$. The figure also shows the profiles calculated with a solid skin (already shown in Figure 111) in order to highlight the effect of porosity, and how the nodal code resituates it.

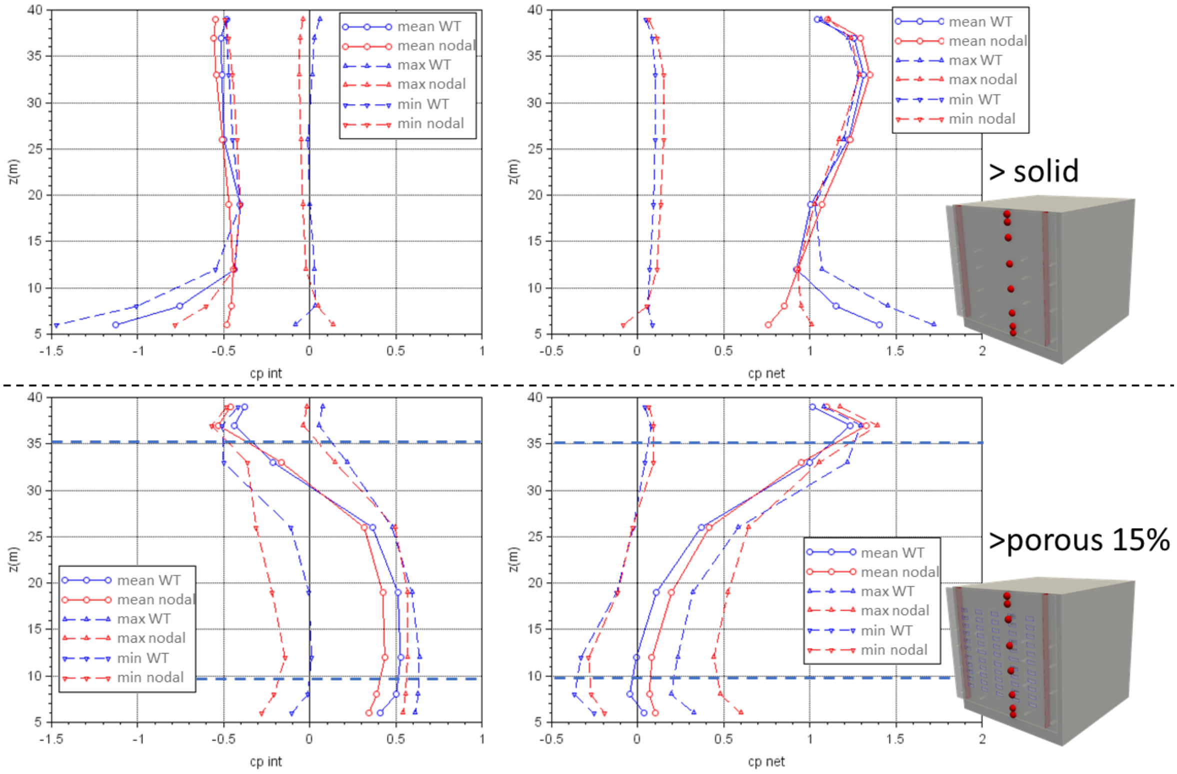

Figure 130 - profile of the mean and peak pressure coefficient, interior on the left and net on the right, comparison of calculated and measured values,
top: h_n_l_20_p_00_s_v; bottom: h_n_l_20_p_15_s_v

The figure shows that the nodal code is able to represent the radical change in pressure balance induced by the presence of porosities in the facade. The mean pressure profiles are well reproduced, even though the pressure in the air space is lower at the foot of the facade. This difference is amplified on the peak pressures, which has repercussions on the peak pressure differential, with higher peak loads at the foot of the facade. To complete the analysis of the signal dynamics the Figure 131 plots the PDFs of the pressure signals calculated at 3 points on the facade.

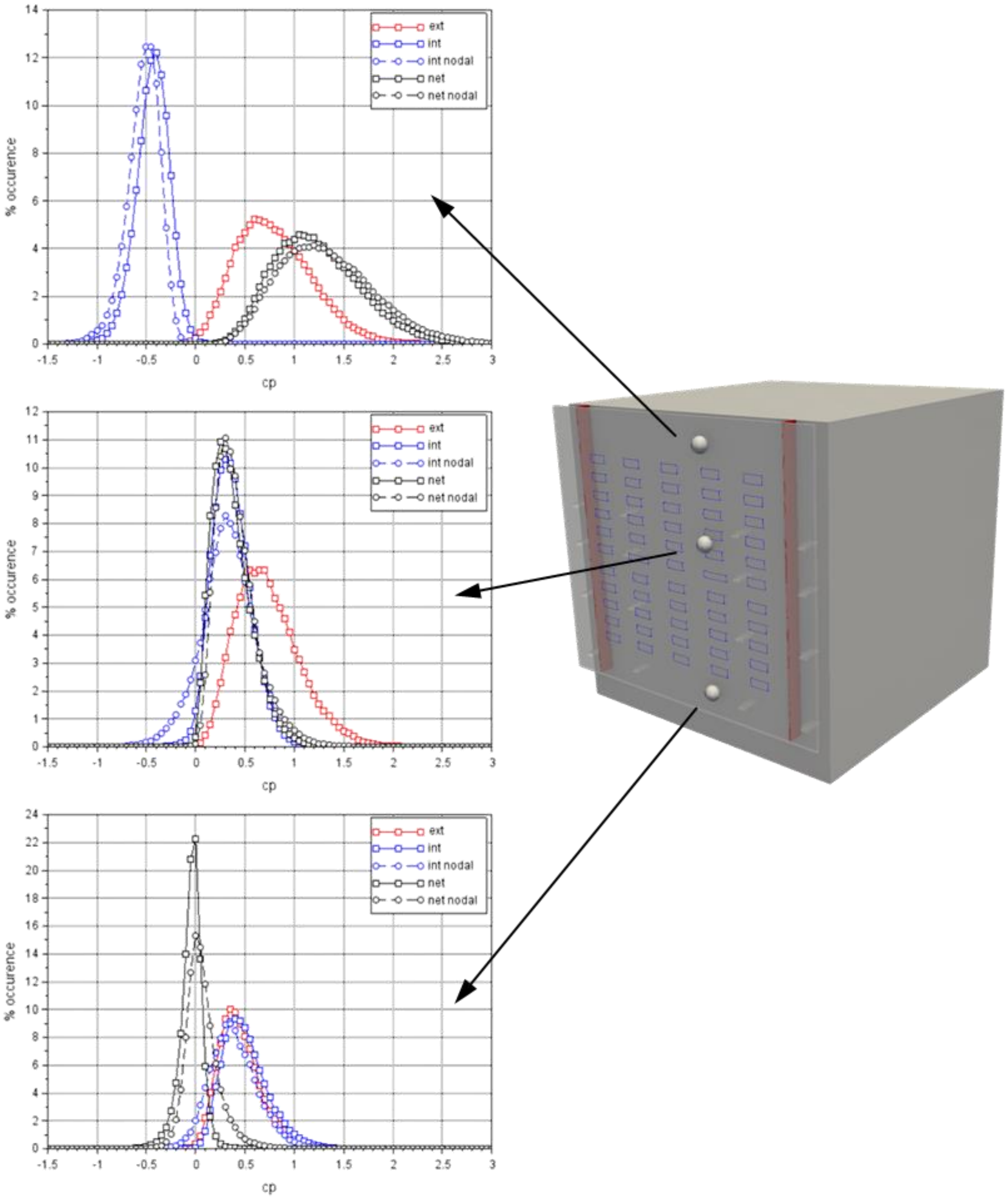

Figure 131 - PDF of the pressure coefficient, interior, exterior and net, at three points of the double-skin facade, comparison of calculated and measured values (configuration h_n_l_20_p_15_s_vert)

Once again, the model seems capable of qualitatively reproducing the evolution of the pressure PDF inside the air gap $c_{p_{int}}$ for the 3 measurement points, and the consequences on the PDF of the pressure differential $c_{p_{net}}$. Analysis of the PDFs in the porous zone reveals a problem in reproducing the tail of the distribution on the negative part of the PDF of the internal pressure $c_{p_{int}}$. This deviation in the distribution can be related to the lower peak pressures observed on the profile presented Figure 130. Symmetrically, this deviation in the internal pressure distribution has repercussions on the tail of the pressure differential distribution $c_{p_{net}}$which leads to higher peak loads.

This change in the internal pressure PDF can certainly be attributed once again to the modelling bias highlighted earlier. These very low pressures are probably associated with high velocities created very locally in time, as a result of air rushing into the air space, induced by very high pressure differentials between the top and bottom of the porous zone, which are also very localised in time. In "reality", due to the dynamics of the flow outside the double-skin facade, these events would certainly not lead to such a strong engulfment of the flow in the air space and the generation of these high speeds.

Thus, although the nodal code once again provides a good qualitative representation of the dynamics of pressure equilibration in the air gap in the presence of porosity, there are still some quantitative discrepancies. The biggest limitation in applying the model to this configuration is the choice of ξ_{permea} which is difficult to choose a priori, as it seems to depend not only on the porosity of the facade, but also on the dynamics of the flow on the external facade.

5.3.5 Fully cut porous skin

We propose to test the model on a final configuration, which is that of a double skin that is fully cut and porous. The measurements carried out in this configuration, presented in §4.5.3 had shown that pressure balancing did not depend on either the porosity of the skin or the height of the building, but only on fluctuations in the pressure applied by the wind on the outside of the overlapped area.

The Figure 130 plots the calculated average and peak internal pressure profile and net differential and compares them with the measured values.

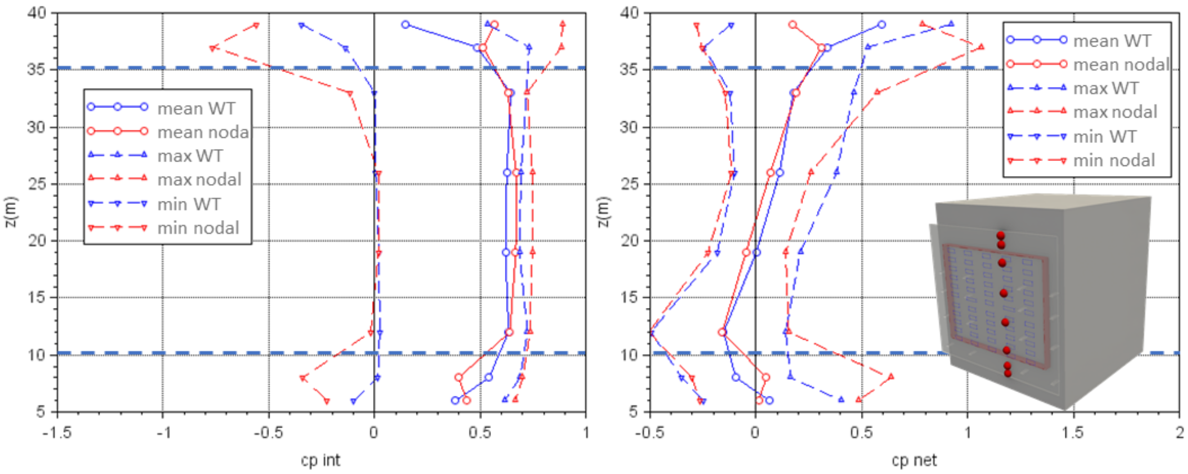

Figure 132 Profile of the average and peak pressure coefficient, interior on the left and net on the right, comparison of calculated and measured values, (configuration h_h_l_20_p_15_s_p)

The figure shows that the average pressure profile inside the air gap balances out at a value comparable to that measured in the wind tunnel. In particular, the mean differential pressure $\overline{cp_{net}}$ changes sign between the top and bottom of the facade, again in line with what was measured in the wind tunnel. Note that the pressure value at the centre of the porous zone is slightly higher than that measured in the wind tunnel. The dynamics of the pressure signal also appear to be well represented, with calculated peak pressures close to those measured in the wind tunnel. In order to explore these dynamics in more detail, the Figure 133 plots the PDFs of the signals measured at 3 points on the facade.

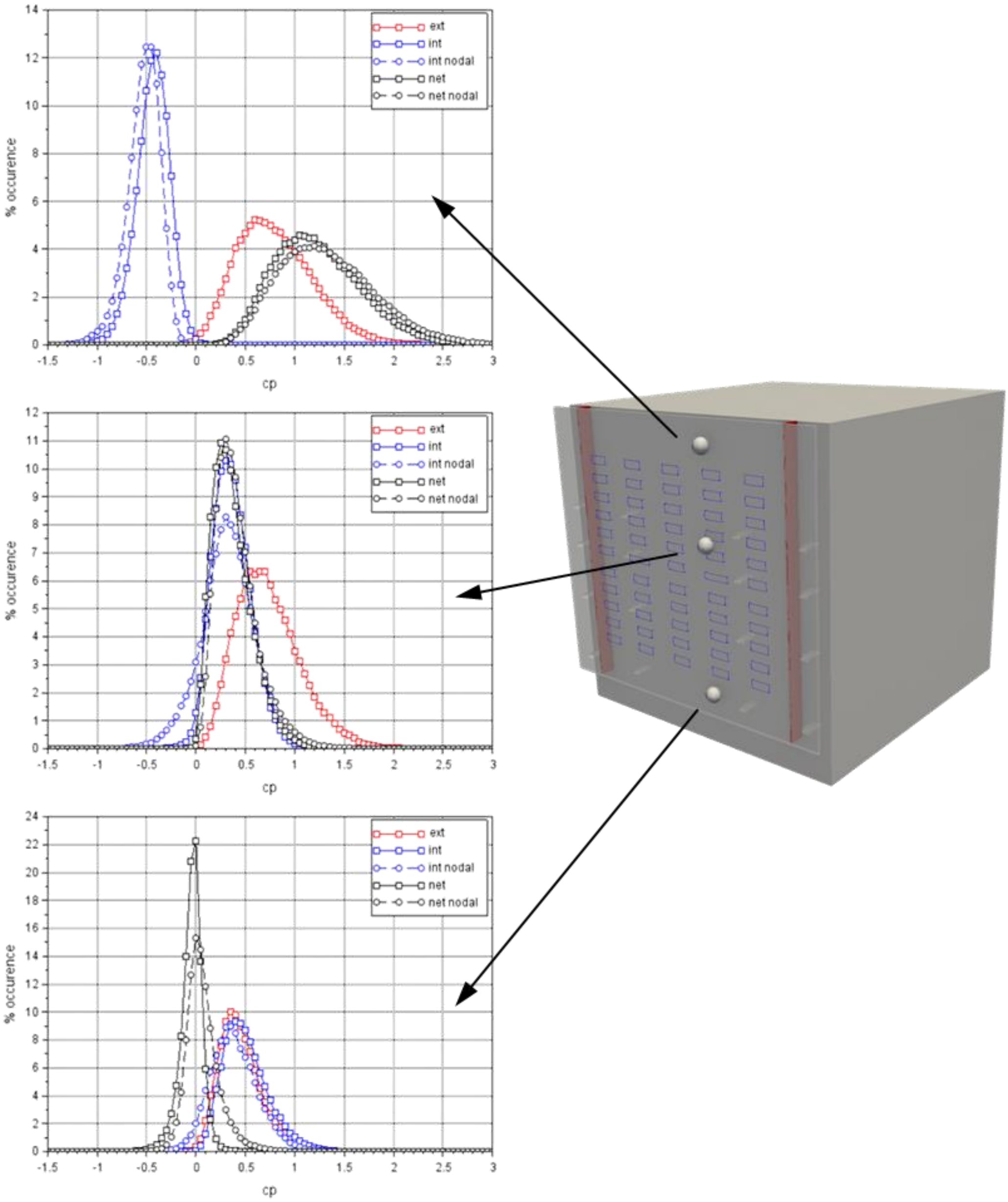

Figure 133 - PDF of the pressure coefficient, interior, exterior and net, at three points of the double-skin facade, comparison of calculated and measured values (configuration h_p_l_20_p_15_s_p)

Analysis of the figure shows that the nodal model is able to predict the shape of the internal pressure PDF $c_{p_{int}}$ but also the rather unusual change in shape of the pressure differential PDF $c_{p_{net}}$ between the top and bottom of the air gap. In addition to reproducing the shape of this PDF, the values are also quantitatively in very good agreement with what can be measured in the wind tunnel.

In this way, the nodal model appears to be perfectly capable of reproducing the instantaneous balancing of the pressure inside the air space of a porous double-skin facade that is completely intersected due to pressure fluctuations on the external face. It therefore allows a more accurate and controlled assessment of wind loads than the Eurocode could propose for this configuration, as shown Figure 99.

5.4 SUMMARY OF THE NODAL MODEL

As a reminder, the main advantage of using the nodal model is to be able to simulate the propagation of pressure fluctuations within the air gap, if this cannot be reproduced in the wind tunnel on models that are too small in scale. In this respect, the model's performance varies greatly depending on the geometric configurations investigated.

On geometric configurations where the flow dynamics inside the air gap are fairly low, the model seems to be capable of reproducing dynamic pressure balancing, with all its subtleties. The simulation of PDFs, both of the internal pressure signal and of the net pressure differential signal, shows fairly remarkable agreement with what has been measured in the wind tunnel. The tool is therefore of great interest for dimensioning configurations where the average loads are low, but the peak loads are non-negligible, and appear to respond to the dynamic balancing of pressure fluctuations at the various openings in the air gap.

However, the model appears to have serious limitations in certain flow configurations:

- first of all, it does a poor job of reproducing the loads induced by the inhomogeneities of the flow as it rushes through the air gap. The very nature of the nodal model makes it impossible to reproduce the accelerations generated by these inhomogeneities. Attempts to recreate these accelerations artificially, by reducing the thickness of the air space based on a priori knowledge of the flow, have been relatively unsuccessful, particularly with regard to the dynamic aspects of the pressure signal in the air space.

- it has difficulty in managing the strong flow dynamics within the air gap, particularly in the case of a 4-sided opening, where the air rushes in on the lower opening and is evacuated via the 3 other openings. The model's difficulty in predicting this configuration can be explained by a rather crude discretisation, in the form of a grid of ducts, of a 2D flow that is becoming too complex.

- Finally, the model has difficulty in reproducing air entrainment through the porosities of the double skin, because it does not take into account the competition between this entrainment through the porosities and the flow dynamics outside the facade.

This problem of reproducing the flow dynamics outside the double skin may also explain the differences in modelling mentioned in the previous points. In this sense, modelling tricks should certainly be used to improve the model's performance and thus increase its level of confidence.

In addition to its practical application, this work on the nodal model has also led to a better understanding of the mechanisms of pressure equalisation in the air gap, by exploring the limits of the model.

6 PRACTICAL APPLICATION TO THE WIND LOADS ASSESSEMENT OF DOUBLE-SKIN FACADES

The aim of this final part of the study is to return to the engineering problem of the wind load assessment of double-skin facades, and to develop strategies on the basis of the lessons learned from measurements on the reference experiment and the simulations carried out with the nodal model.

6.1 APPLICATION OF THE RESULTS OF THE STUDY TO THE ENGINEERING PROBLEM

Analysis of the measurements on the reference experiment showed that slight variations in the geometry of the building against which it was set, or in the geometry of the double-skin facade itself, could lead to very large variations in the wind loads on the double skin.

Given the infinite number of geometric combinations of buildings and double-skin facades that may exist in the existing or future building stock, it seems difficult to identify a generic rule that would cover all possible geometric configurations.

6.1.1 Conservative assessment

For a generic building, in the absence of any knowledge of how the pressure in the air space will balance out, a safe and dimensioning approach would be to consider the maximum possible load that could be applied to such a facade, in the worst possible configuration. In this sense, the analysis of loads obtained for all configurations taken together in section 4.7.1 has made it possible to draw up an initial outline of what such a major load case would be. It is shown schematically Figure 134.

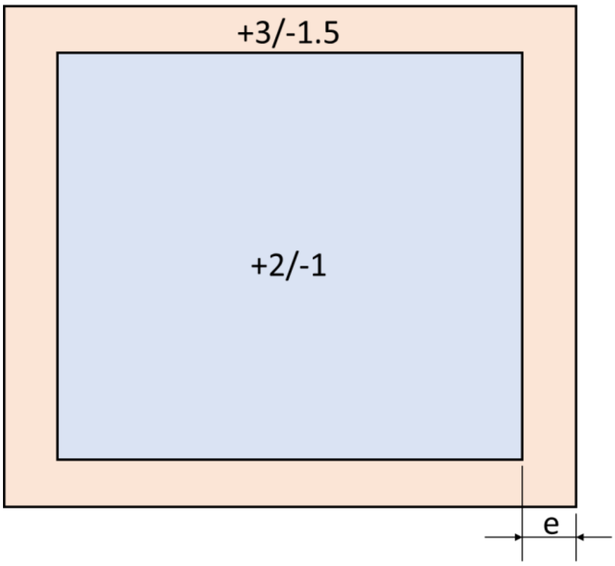

Figure 134 - definition of a major load case for double-skin facades

At the centre of the facade, a maximum peak compression of +2 and a peak pull-out of -1 are defined. They result from unfavourable configurations where the pressure in the air space has a sign opposite to that of the pressure on the external face of the double skin. Even if the Figure 103 showed a zone with lower loads in the centre of the facade, the analysis showed that it was difficult to define the contours of this zone, which depended heavily on the geometric configuration of the facade and the building against which it was leaning.

At the edge of the facade, a maximum peak compression of +3 and a peak pull-out of -1.5 are defined. The maximum compressions take into account the case of a feathered facade, which can then be assimilated to an acroterion, but also the effects of the flow becoming entangled in the air space, which locally increase the loads. Peak pull-outs correspond to configurations where the wind flow is grazing, and very locally generates high pressure differentials pushing the double skin away from the building facade.

It then remains to define the distance noted e of the edge to which these loads apply. This will depend both on the wind flow at the scale of the facade, but also on the flow at the scale of the air space. The value of e will then result from a combination of the thickness of the air space and the Eurocode requirements for facade design. We therefore propose :

$$e = \max\,(2a, \frac{b}{5})$$

With a the thickness of the blade, and b the largest dimension (height, width) of the facade.

This increased load case would therefore be able to safely and conservatively cover all the double-skin facade configurations that could be installed on a building. It should be noted that this load case is more severe than the one proposed in the SNFA sheet [11].

6.1.2 Optimising the wind loads

However, analysis of the measurements has shown that pressure balancing can greatly reduce these wind loads. It may therefore be worth proposing an optimised assessment, taking these lower loads into account, in order to reduce the construction cost of the double-skin facade. However, this assessment must be carried out safely.

The best approach for assessing wind loads remains direct measurement of the pressure differential in an Atmospheric Boundary Layer wind tunnel, with synchronous measurement of the pressure on each side of the double-skin facade, as carried out on the reference experiment. Once again, this implies being able to instrument the model correctly for pressure measurement without disturbing the pressure balance of the air space. This restricts the investigation to small-scale buildings, making it possible to propose a scale model compatible with the dimensions of the Atmospheric Boundary Layer wind tunnel.

If the size of the model does not allow the air space to be represented at a sufficiently large size to be instrumented with pressure taps, pressure balancing can be simulated in a hybrid way, using a nodal model and the pressure signals measured at the boundaries of the air space. The net pressure differential is then calculated by subtracting the pressure signal measured on the outer face of the double skin from the virtual pressure signal calculated in the air gap by the nodal model. However, the work carried out in this study has shown that this approach gives satisfactory results in a limited range of geometric configurations of the double-skin facade. Configurations with high flow dynamics in the air space, or with a 4-sided opening, caused the nodal model to fail in its ability to accurately assess peak loads.

This study made very little mention of the use of CFD-type numerical simulations to assess the pressure balance of the air gap, even though numerous illustrations of the flow have been obtained in this report using this approach. CFD is proving to be a very interesting way of qualitatively assessing the pressure balance of the air gap. In this respect, it is even more effective than the nodal approach, since it can detect complex flow configurations where the air gap has many openings. That said, the RANS CFD industrial approach proposes quantitative evaluations of loads that are often far removed from those measured in atmospheric boundary layer wind tunnels. Above all, RANS CFD is unable to reproduce unsteady pressure equalisation in the air space. This is a very serious limitation for wind load assessment, since peak pressure differentials cannot be evaluated correctly. Once again, unsteady CFD simulation (LES, DES, etc.) could provide an answer to this question, but at calculation costs that would certainly be prohibitive for considering an industrial application of the approach. Does this mean that CFD should be eliminated from the process of assessing loads on the double-skin facade? Quite the contrary. CFD offers a relevant visualisation of the flows, making it possible to anticipate how the pressure in the air gap will balance out, and thus propose an investigation method adapted to the wind tunnel measurement of peak loads, either by direct measurement on a model, or by a hybrid approach (wind tunnel measurement + nodal model).

It is therefore the combination of investigation methods that will make it possible to establish, on a case-by-case basis, the best wind dimensioning strategy for double-skin facades.

6.2 WIND DIMENSIONING STRATEGIES ACCORDING TO THE TYPE OF DOUBLE-SKIN FACADE

Once again, the best strategy for assessing wind loads on a double-skin facade remains direct wind tunnel assessment of the peak pressure differential, if the model allows pressure measurement of the air gap (scale of 1/100 or more).

If this is not the case, this paragraph sets out to establish a series of alternative wind loads assessment strategies, depending on the different types of double-skin facade.

6.2.1 Fully segmented double skin (watertight segmentation)

First, we consider the case of a fully segmented double skin, with perfectly watertight segmentation. A distinction is then made between the central part of the skin, which is closed at all 4 edges, and the part of the double skin that may be feathered at the edge of the facade.

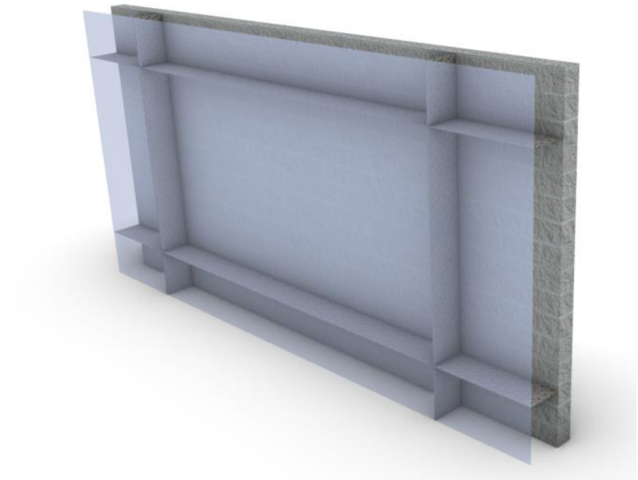

Figure 135 Completely watertight double-cut skin

There are two possible scenarios, depending on whether the skin is solid or porous:

1) Case of a solid skin

→*On the central section, which has been completely cut through:*

This case is similar to that of a normal building facade, and can be assessed using standard Eurocode evaluations. The pressure on the external face p_{ext} is then assessed using either the regulatory approach (Eurocode §7.2.2 [8]), or by wind tunnel measurement, whereas the internal pressure is taken from the regulations (Eurocode §7.2.9 [8]) equal to $p_{int} = +0.2 \cdot p_{dyn}$ or $p_{int} = -0.3 \cdot p_{dyn}$, with p_{dyn} the reference dynamic pressure at the facade height, so as to maximise the pressure differential p_{net}.

→*On the feathered part of the border :*

This case is similar to that of an acroterion within the meaning of the Eurocode and can be dimensioned as such (Eurocode §7.4.1 [8])

2) Porous skin

→*On the central section, which has been completely cut through:*

This case can be dealt with by calculating the pressure equilibrium of the cavity using a nodal model as described in §5.3.5. The pressures measured on the external face of the double skin are then used both as input data for the nodal model for pressure balancing in the air space and to calculate the peak pressure differential. This peak pressure differential can also be obtained using the regulatory approach (Eurocode §7.2.10 [8]), which proposes the following for this scenario $c_{p_{net}} = \frac{2}{3} c_{p_{ext}}$ for compression and $c_{p_{net}} = -\frac{1}{3} c_{p_{ext}}$ for pull-outs.

→*On the feathered part of the border :*

This case is similar to that of an acroterion within the meaning of the Eurocode and can be dimensioned as such (Eurocode §7.4.1 [8])

6.2.2 Double-skinned channel type (horizontal / vertical)

We now consider a skin segmented to form a horizontal or vertical channel.

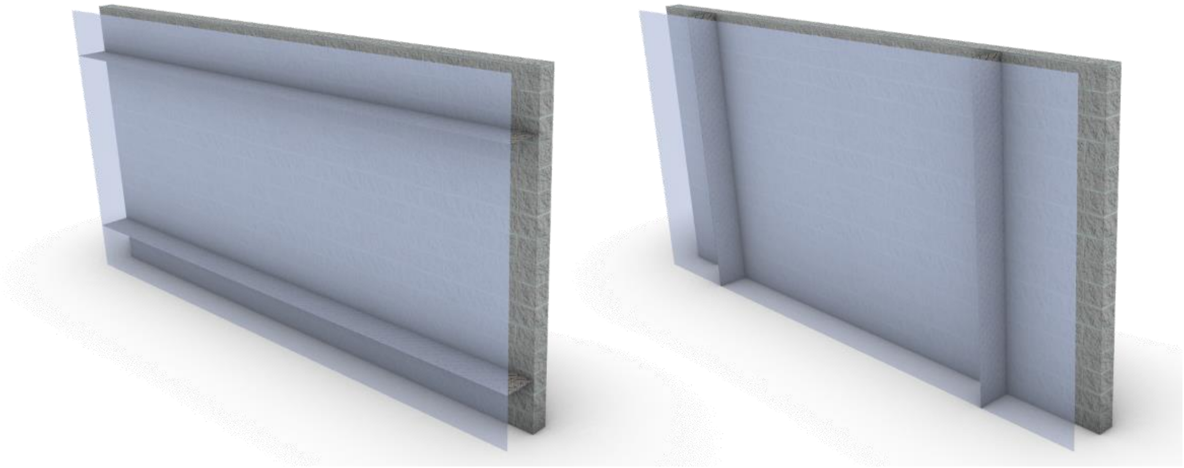

Figure 136 - Double-skinned, cut channel type

Once again, there are two cases depending on whether the skin is solid or porous:

1) Case of a solid skin

→*On the central part of the* channel*:*

This case can be dealt with by calculating the pressure equilibrium in the channel with a nodal model as carried out in §5.3.1. The pressures measured on the facade of the building, at the boundaries of the channel, are used as input data for the balancing model, which then produces a virtual pressure signal along the inside face of the double skin. The pressure measurements taken on the external face of the facade are then used to calculate the net pressure differentials.

In the case of high flow dynamics in the air gap (large pressure differential at the terminals, or high flow rates recorded in the nodal calculation), the study must be completed by an assessment of the effects of the flow becoming entangled in the air gap. This study can be carried out either by a complementary wind tunnel study, on a larger scale model of the air inlet, or by a CFD approach. This will enable an increase coefficient to be applied to the peak loads obtained using the nodal approach.

→On the feathered part of the border :

This case is similar to that of an acroterion within the meaning of the Eurocode and can be dimensioned as such (Eurocode §7.4.1 [8])

2) Porous skin

This case is similar to the one tested §5.3.4 and is more problematic to study. In this case, the nodal approach presented difficulties in reproducing the competition between the dynamics of the flow outside the facade and that penetrating through the pores. The simulation results showed a very strong dependence on the head loss coefficient ξ_{permea} on the porosity of the facade. This case must therefore be treated by including a sensitivity study on the coefficient ξ_{permea}coefficient, and using the most extreme case for the peak differential pressure $\widehat{p_{net}}$ then calculated. More conservatively, these porous skins can also be considered as solid, and can therefore be treated in the same way as the previous case.

6.2.3 Double skin open on 3 or 4 sides

We consider a skin open on 3 or 4 sides. This case is similar to the one studied in §5.3.2 and §5.3.3.

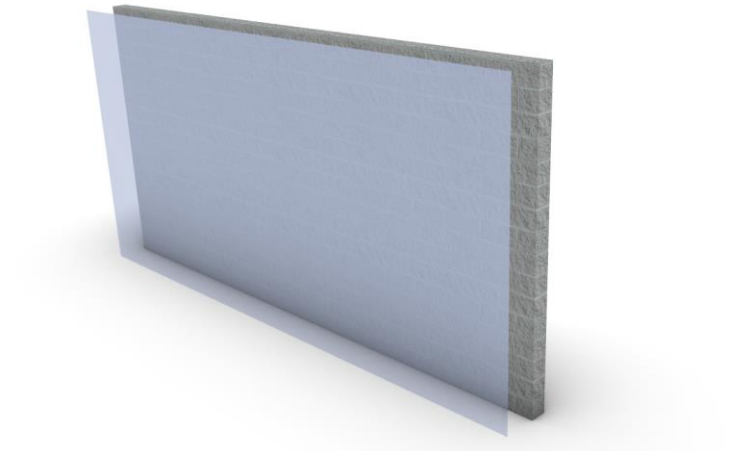

Figure 137- Double skin open on 4 sides

Two cases will be considered, depending on whether the flow dynamics in the air gap are low or high. This can be determined either by an initial nodal model, or by evaluating the flow using a CFD approach.

1) If dynamic is low

This case can be dealt with by calculating the pressure balance of the air gap using a nodal model, as described in §5.3.2 or §5.3.3. The study can then be completed by an assessment of the effects of flow entrapment in the air gap, as discussed for channel type double-skin façade.

2) If the dynamic is high

This is the most problematic case, and one for which the nodal approach has the greatest limitations. It is also the case most conducive to the generation of very high peak loads on the double skin, due to the very high flow dynamics. Therefore, if this case cannot be dealt with by wind tunnel measurements using a model of sufficient size to ensure a good representation of the air gap, the only alternative will be to consider the conservative load case presented in §.**Erreur ! Source du renvoi introuvable.**.

6.2.4 Summary

The Table 5 provides a visual summary of the different sizing strategies proposed in the previous paragraphs.

Facade type		**Strategy**	
		Regulatory (Eurocode)	Hybrid (WT measurement + nodal)
completely segemented	solid	🟩	🟦
	porous	🟩	🟦
Channel segmentation (horizontal, vertical)	solid	🟥	🟩 with channel inlet increase
	porous	🟥	🟧
Open on 3 or 4 sides	low dynamics	🟥	🟧
	hogh dynamics	🟥	🟥

level of confidence	🟦 very high	🟩 high	🟧 low	🟥 very low

Table 5 - Summary of alternative strategies to direct wind tunnel measurement depending on the type of double-skin facade

This table shows that the alternative strategies proposed only cover a small proportion of the possible configurations of double-skin facades. The cases not covered by these alternatives are also representative of the complexity of the flows generated on these facade elements, which are difficult to model using simplified approaches.

6.3 CONSIDERATIONS FOR THE DESIGN OF DOUBLE-SKIN FACADES WITH REGARD TO WIND LOADS

In the final part of his thesis, Vaglio proposes [1] recommendations for the design of double-skin facades with regard to wind loads. These facades can have several functions, including providing a ventilation process to cool the building. The aim is to generate a flow in the air space at relatively low wind speeds. In the light of the measurements carried out in this study, it is clear that encouraging such a dynamic flow in the air space can lead to the generation of considerable wind loads during a storm. Optimising the ventilation function may therefore be to the detriment of the facade's wind resistance.

The results of this study allow us to draw up a few recommendations, from the point of view of wind loads, leaving aside for the moment the other functions of the facade.

In order to limit wind loads, it is advised to try to partition the air space as much as possible and create porosity in the double skin, in order to balance the pressure on either side of the facade. As well as limiting the wind loads on the double skin, this configuration is relatively well controlled from the point of view of wind loads assessement, and the loads can therefore be assessed with sufficient confidence. However, this arrangement of the double-skin facade will only create limited circulation in the air space.

In order to create a more substantial convection movement, it may be useful to use vertical segmentations to create channels, and create air circulation through the pressure difference between the bottom and the top of the facade. This principle has been illustrated in this study on the configurations of the level building and the low-rise building, equipped with vertical segmentations. These configurations will therefore lead to higher loads on the double-skin facade, but these can be measured fairly accurately using the modelling strategies proposed in the previous paragraph.

Finally, it might be preferable to avoid installing air space with too many openings, either because of the absence of segmentations, or because of the presence of porosities which lead to competition between the internal and external flow dynamics. These configurations are relatively poorly mastered from the point of view of wind loads assessment, and would lead to having to rely on a very conservative load case.

These design choices must, of course, be set against the facade's other functions. Significant wind loads can be compensated for by reinforcing the structure, but at the cost of the project. It is therefore necessary to assess, on a case-by-case basis, the benefits of refining the assessment of wind loads. The conservative load case proposed in §**Erreur ! Source du renvoi introuvable.** may, for example, be compatible with a specification that does not require the structure to be lightened, and therefore does not require the assessment of loads to be refined.

Finally, there is the question of a double-skin facade with variable geometry, equipped with shutter systems that adjust according to wind conditions, either to ensure effective ventilation of the air space, or to reduce wind loads on the facade. So-called "bioclimatic" facades already exist, which can regulate the speed of the flow in the air space. However, such equipment raises the question of who bears responsibility in the event of a failure in the control system, which would prevent the facade from being placed in a safe position in the event of a gust of wind.

7 CONCLUSIONS AND OUTLOOK

The aim of this research is to study wind loads on double-skin facades.

The first part of the study presents a brief review of academic research on the subject and clearly sets out the associated engineering problem, i.e. the wind resistance of a double-skin facade to a 50-year storm. It highlights the need for a better understanding of the phenomenon of pressure balancing of the air space, which has a major impact on the wind loads of the double-skin facade. The engineering problem is essentially posed by the complexity of directly measuring the pressure differential on either side of the double-skin facade, on models that are too small to faithfully represent the flow in the air space.

The study is based on a reference experiment that enables the instantaneous pressure differential on either side of a large-scale double-skin facade to be measured in detail, against a cubic building. The model produced for the study has a number of modular features so that the effect of several geometric parameters on wind loads can be investigated. Measurements carried out in the Atmospheric Boundary Layer wind tunnel showed that small geometric variations could lead to large variations in wind loads on the double-skin facade. These effects, which are often counter-intuitive, have been explained using a detailed analysis of the measurements, supplemented by graphical representations of the flow resulting from numerical simulations.

The number of configurations investigated cannot claim to be an exhaustive representation of the installed base (or that to be built) of double-skin facades, as the combination of geometric parameters can be infinite. However, they are sufficiently numerous to illustrate the mechanisms responsible for pressure balancing of the air space, and their impact on the wind loads of the double-skin facade. Particular attention has been paid to the question of peak loads generated by atmospheric boundary layer turbulence. This aspect has been little studied in the literature, yet it lies at the heart of the engineering problem. These measurements could be supplemented if the geometric configurations representative of the installed base cannot be compared with the configurations dealt with during the study. The pressure measurements could also be supplemented by velocity measurements using laser velocimetry in the thickness of the air gap in order to confirm the flow structures described by the numerical simulation.

Analysis of the measurements showed that in most of the configurations tested, the pressure in the air space was directly related to the pressure fluctuations at its boundaries. This observation led the study to the use of a nodal model. This would enable the pressure signal in the air space to be virtually reconstructed from the pressure measurements taken at the terminals and on the external face of the double-skin facade. This model would then have a direct practical application for wind tunnel models where it is impossible to measure the pressure in the air gap.

Finally, modelling strategies for practical applications to industrial cases were proposed. These strategies have been deduced from analyses of measurements from the reference experiment, as well as from simulations carried out with the nodal model. Without claiming to cover all possible double-skin façade configurations, these strategies offer an initial practical approach to better understanding the wind dimensioning of these façades.

LIST OF REFERENCES

[1] J. C. Vaglio, "Aerophysics of double-skin . Sans cese preteondre pouvorie r eshausoitaoive a 'mensmebelde s conofingster cefacades: simulation-based determination of pressure coefficients for multi-story double-skin facades," 2015.

[2] H. J. Gerhardt and F. Janser, "Wind loads on wind permeable facades," *Journal of Wind Engineering & Industrial Aerodynamics,* vol. 53, pp. 37-48, 1995.

[3] F. Marques_da_Silva and M. Gloria_Gomes, "Gap inner pressures in multi-storey double skin facades," *Energy and Buildings,* vol. 40, p. 1553-1559, 2008.

[4] M. Jafari and A. Alipour, "Aerodynamic shape optimization of rectangular and elliptical double-skinfacades to mitigate wind-induced effects on tall buildings," *Journal of Wind Engineering & Industrial Aerodynamics,* vol. 213, 2021.

[5] G. Hu, S. Hassanli, K. C. S. Kwok and K. T. Tse, "Wind-induced responses of a tall building with a double-skin facade system," *Journal of Wind Engineering & Industrial Aerodynamics,* vol. 168, pp. 91-100, 2017.

[6] G. Hu, J. Song, S. Hassanli, R. Ong and K. C. S. Kwok, "The effects of a double-skin facade on the cladding pressure around a tall building," *Journal of Wind Engineering & Industrial Aerodynamics,* vol. 191, p. 239-251, 2019.

[7] F. H. Kemper and M. Feldmann, "Wind load assumptions for permeable cladding elements considering theinstallation context," *Journal of Wind Engineering & Industrial Aerodynamics,* vol. 184, p. 277-288, 2019.

[8] AFNOR, "Eurocode 1: Actions on structures. Part 1-4 General Actions - Wind Actions," 2005.

[9] G. Pomaranzi, N. Daniotti, P. Schito, L. Rosa and A. Zasso, "Experimental assessment of the effects of a porous double skin facadesystem on cladding loads," *Journal of Wind Engineering & Industrial Aerodynamics,* 2020.

[10] P. Skvorc and H. Kozmar, "The effect of wind characteristics on tall buildings with porousdouble-skin facades," *Journal of Building Engineering,* vol. 69, 2023.

[11] SNFA, "Fiche Technique n°45 Tableaux des Pressions de vent W50 applicables aux facades légères et déterminées selon l'Annexe Nationale NF EN 1991-1-4/NA," 2010.

[12] RAGE, "Façad multiple: Naturally ventilated double skin on the exterior," 2014.

[13] F. Demouge, "MATHIS: Technical Guide," 2019.

[14] G. Giovannelli and J. Guilhot, "Vitesse de ventilation naturelle dans la tranchée couverte Austerlitz-Tolbiac-Masséna," 2017.

[15] I. E. Idel'Cik, Memento des Pertes de Charges, Eyrolles, 1965.

[16] M. Rahiminejad and D. Khovalyg, "Review on ventilation rates in the ventilated air-spaces behind commonwall assemblies with external cladding," *Building and Environment,* vol. 190, 2021.

[17] V. Yellamraju, "Evaluation and design of double-skin facades for office buildings in hot climates," 2004.

[18] S. Matour, V. G. Hansen, R. Drogemuller and S. Omrani, *Adaptation of Double Skin Facade for warm climate from a wind harvesting perspective in tall buildings*.

ACKNOWLEDGEMENTS

This study was entirely financed by the CSTB Research & Development Department. The author would like to thank Hervé Charrue, Romain Mege and Nicolas Naville for their confidence in the allocation of the associated funding.

The author would also like to thank :

-Julien Rogé and Nicolas Pinoteau, for their trust and careful monitoring of this research work.

-Bruno Béliard and Patrice Metaireau, for producing the beautiful mockup of the reference experiment.

-Cyril Vachon, for his assistance during the wind tunnel tests.

-François Demouge, for his invaluable help in setting up the nodal model, and for his infinite wisdom in the delicate art of controlling head losses.

This report is dedicated to the memory of Gabriel Giovanelli, a
great master of pressure balancing.

-

CSTB
le futur en construction

Entreprise publique au service de ses clients et de l’intérêt général, le Centre Scientifique et Technique du Bâtiment a pour ambition d’imaginer les bâtiments et la ville de demain, en accompagnant et sécurisant les projets de construction et de rénovation durable, pour améliorer la qualité de vie de leurs usagers en anticipant les effets du réchauffement climatique.

Il exerce pour cela cinq activités-clés : la recherche et expertise, l’évaluation, les essais, la certification et la diffusion des connaissances. Il répond ainsi à trois missions principales, au service des acteurs de la construction et de l’intérêt général : créer des connaissances et les partager, accompagner l’innovation, sécuriser et valoriser la performance.

Scientific and technical centre for the building industry
Head office > 84 avenue Jean Jaurès - Champs-sur-Marne - 77447 Marne-la-Vallée cedex 2 - France
Tel: +33 (0)1 64 68 82 82 - www.cstb.fr
Marne-la-Vallée / Paris / Grenoble / Nantes / Sophia Antipolis